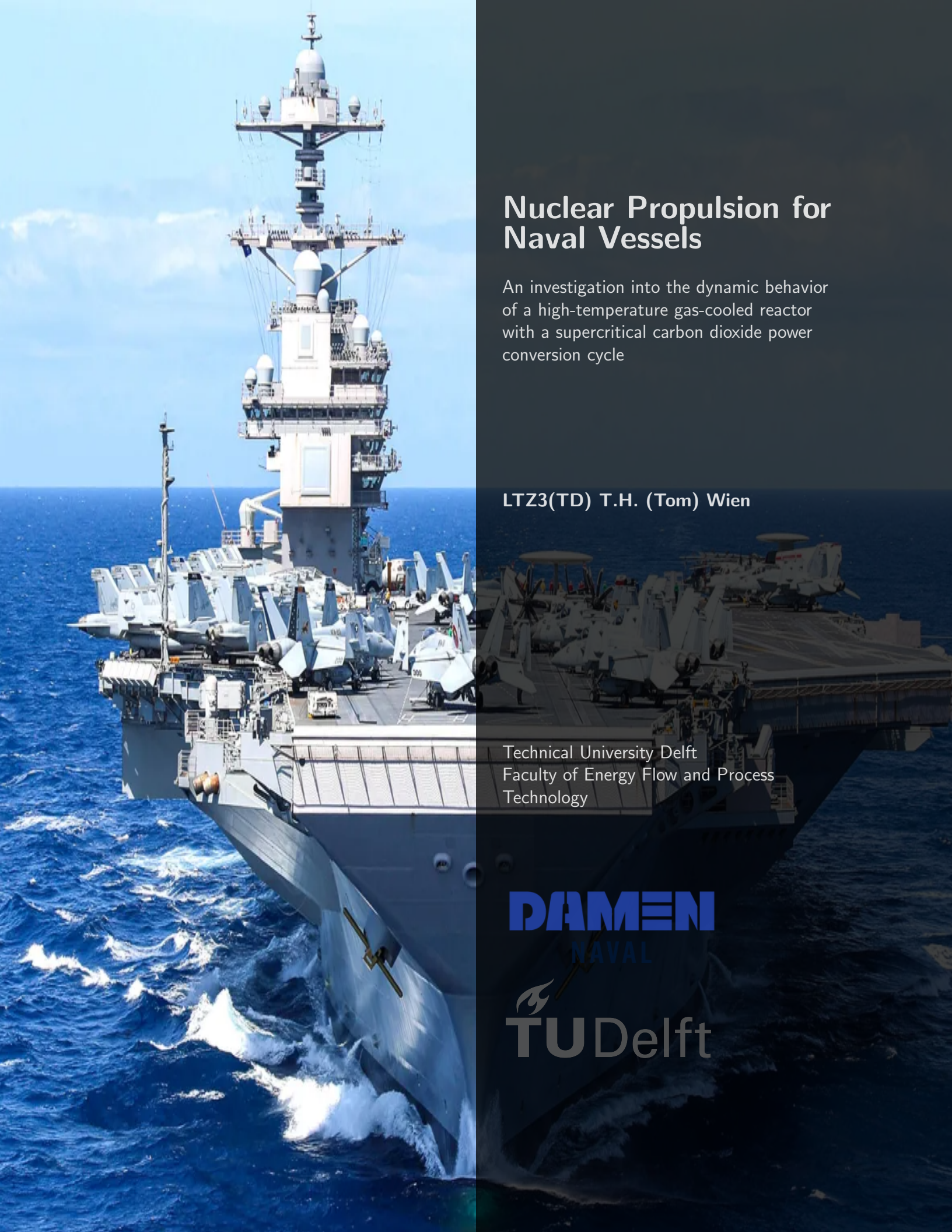

Nuclear Propulsion for Naval Vessels

An investigation into the dynamic behavior of a high-temperature gas-cooled reactor with a supercritical carbon dioxide power conversion cycle

LTZ3(TD) T.H. (Tom) Wien

Technical University Delft
Faculty of Energy Flow and Process Technology

DAMEN NAVAL

TU Delft

Nuclear Propulsion for Naval Vessels

An investigation into the dynamic behavior of a high-temperature gas-cooled reactor with a supercritical carbon dioxide power conversion cycle

by

LTZ3(TD) T.H. (Tom) Wien

A thesis for obtaining the MSc. degree in Mechanical Engineering,
with the specialization Energy Flow and Proccess Technology,
at the Delft University of Technology.

Student number:	5870682	
Date submitted:	December 8, 2024	
Place:	Delft	
Supervisors:	prof. dr. ir. R. Pecnik	TU Delft
	dr. ir. J.W.R. Peeters	TU Delft
	ir. G.-J. Meijn	Damen Naval

Image front page: The nuclear-powered aircraft carrier *USS Gerald R. Ford* [1]

Technische Universiteit Delft
Delft University of Technology

Abstract

There is currently a resurgence of interest in nuclear propulsion within the maritime sector, which is reflected by the ambition, as mentioned in the Dutch maritime sector report "No Guts, No Hollands Glorie", to develop a standardized, modular nuclear reactor for ship integration within 10 years. Nuclear energy has the potential to reduce the maritime sector's contribution to climate change, as it does not emit CO_2 during operation. Additionally, in contrary to many other renewable energy sources, nuclear energy offers a high-energy-density power source capable of providing sufficient energy for longer periods of operation. Not only would this improve the strategic autonomy of the Royal Netherlands Navy, but it would also be a solution for the increasing energy demands of additional unmanned systems or advanced combat systems, like high power radars and rail guns.

Implementing nuclear propulsion in future (naval) vessels presents challenges, particularly regarding the dynamic power profile of ships during operation. Land-based nuclear reactors typically operate as stable power sources, which contrasts with the fluctuating power demands of ships, especially naval vessels. This research aims to find a solution for these dynamic power requirements, without the use of energy storage capabilities, like batteries, for peak shaving capabilities.

Based on the expected implementation of a small modular reactor (SMR) by 2034, the Future Air Defender and the Amphibious Transport Ship were selected as potential vessel types of interest for the Royal Netherlands Navy to implement an SMR. Additionally, the high-temperature gas-cooled reactor (HTGR) and the supercritical carbon dioxide (sCO_2) recompression power conversion cycle were selected for the nuclear power plant. A dynamic model of the selected SMR and its energy conversion system has been developed to compare its ramp rate with those of conventional naval prime movers, such as diesel engines and gas turbines.

The simulation results indicate that the reactor dynamics alone are insufficient to meet common ramp rates of naval vessels, demonstrating that relying solely on reactor control is not a viable control strategy. However, the implementation of the turbine bypass valve, while operating the reactor at a constant load, provides dynamic power behaviour comparable with diesel engines and even gas turbines. Potential drawbacks include reduced cycle efficiency at part load, as well as significant pressure and temperature gradients within the heat exchangers. The unacceptable temperature increase at the reactor's inlet was addressed by incorporating a dump cooler into the primary circuit. This research therefore concludes that an HTGR, in combination with an sCO_2 cycle and a bypass valve, is capable to provide the dynamic power requirements of a naval vessel.

Nomenclature

Abbreviations

ARIS	Advanced Reactors Information System
ASWF	Anti-Submarine Warfare Frigates
ATS	Amphibious Transport Ship
B	Blower
BNI	Barber-Nichols Incorporated
BWR	Boiling Water Reactor
CL	Cooler
CSS	Combat Support Ship
DCL	Dump Cooler
FP	Full Power
FuAD	Future Air Defender
G	Generator
GFR	Gas-cooled Fast Reactor
HEU	High Enriched Uranium
HSC	High-end Surface Combatant
HTGR	High-Temperature Gas-cooled Reactor
HWR	Heavy Water Reactor
IAEA	International Atomic Energy Agency
IG	Ideal Gas
IHX	Intermediate Heat Exchanger
LCF	Luchtverdedigings- en commandofregat
LEU	Low Enriched Uranium
LFR	Lead-cooled Fast Reactor
LOL	Loss of Load
LPD	Landing Platform Dock
LTR	Low Temperature Recuperator
MC	Main Compressor
MOX	Mixed Oxide
MSR	Molten Salt Reactor
OPV	Ocean-going Patrol Vessel
ORC	Organic Rankine Cycle
P	Pump
PCHE	Printed Circuit Heat Exchanger
PKE	Point Kinetics Equation
PWR	Pressurized Water Reactor
R	Reactor
RC	Recompressor
RCCS	Reactor Cavity Cooling System
RNLN	Royal Netherlands Navy
RPV	Reactor Pressure Vessel
SCWR	Supercritical Water Reactor
SFR	Sodium-cooled Fast Reactor
SMR	Small Modular Reactor
STC	Sequential Turbocharging
SWR	Sodium Water Reaction
T	Turbine
TAC	Turbine Alternator Compressor
TRISO	Tristructural-Isotropic
TRL	Technology Readiness Level
TTD	Terminal Temperature Difference
VHTR	Very High Temperature Reactor
WNA	World Nuclear Association

Roman Symbols

A	Area	m^2
c	Population of delayed neutrons	$-$
c	Speed of light	$\frac{m}{s}$
C_d	Valve discharge coefficient	$-$
C_p	Specific heat capacity	$\frac{J}{kgK}$
C_v	Valve construction coefficient	m^2
d/D	Diameter	m
d_H	Hydraulic diameter	m
E	Energy	J
f	Friction factor	$-$
f	Function	$-$

f_{open}	Valve opening	$-$
F	Fission rate to power factor	$-$
g	Gravitational field strength	$\frac{m}{s^2}$
h	Convective heat transfer coefficient	$\frac{W}{m^2K}$
h	Enthalpy	$\frac{J}{kg}$
H	Height	m
H_c	Channel height	m
H_{rod}	Rod height	m
I	Inertia	$kg\,m^2$
k	Multiplication factor	$-$
k	Thermal conductivity	$\frac{W}{mK}$
L	Channel length	m
$\dot{m}$	Mass flow	$\frac{kg}{s}$
M	Mass	kg
MCF	Mass Correction Factor	$-$
n	Neutron population	$-$
n_s	Isentropic volume exponent	$-$
N	Atomic number density	$\frac{\#}{cm^3}$
N	Number of channels	$-$
N	Shaft speed	$RPM/\frac{rad}{s}$
NCF	Speed Correction Factor	$-$
Nu	Nusselt number	$-$
p	Perimeter	m
p	Pressure	Pa
P	Power	W
Pr	Prandtl number	$-$
$\dot{Q}$	Heat	W
r/R	Radius	m
R	Specific gas constant	$\frac{J}{kgK}$
Re	Reynolds number	$-$
s	Entropy	$\frac{J}{kgK}$
t	Time	s
t_e	Equivalent plate thickness	m
$t_{\frac{1}{2}}$	Radioactive half-life	s
T	Temperature	$K/°C$
u	Speed	$\frac{m}{s}$
U	Overall heat transfer coefficient	$\frac{W}{m^2K}$
v	Neutron velocity	$\frac{m}{s}$
v	Specific volume	$\frac{m^3}{kg}$
v_{rod}	Rod speed	$\frac{m}{s}$
V	Volume	m^3
Z	Compressibility factor	$-$

Greek Symbols

α	Reactivity feedback coefficient	$\frac{pcm}{K}$
β	Effective delayed neutron fraction	$-$
γ	Specific heat ratio	$-$
ϵ	Surface roughness	m
η	Efficiency	$-$
Λ	Prompt neutron generation time	s
λ	Radioactive decay constant	s^{-1}
μ	Dynamic viscosity	$\frac{Pa}{s}$
ν	Neutron velocity	$\frac{m}{s}$
π	Pressure ratio	$-$
ρ	Density	$\frac{kg}{m^3}$
ρ	Reactivity	$pcm/\$$
Σ	Macroscopic cross section	cm^{-1}
σ	Microscopic cross section	cm^2
τ	Nucleus mean lifetime	s
ϕ	Neutron flux	$\frac{n}{m^2s}$

Substances

Be	Beryllium
C	Carbon
CO_2	Carbon dioxide
D	Deuterium
He	Helium
I	Iodine
Pm	Promethium
Pu	Plutonium

Sm	Samarium
Th	Thorium
U	Uranium
UO_2	Uranium-dioxide
Xe	Xenon

Subscripts

a	Actual
B	Barrel
B	Blower
C	Compressor
c	Cold side of the heat transfer element
$corr$	Corrected
cp	CoolProp
CR	Central Reflector
cr	Critical
Do	Down comer
$elec$	Electrical
F	Fuel
gen	Generator
h	Hot side of the heat transfer element
I	Insulation
i/in	Inlet side
$isen$	Isentropic
M	Mass
n	The N'th heat transfer element
o/out	Outlet side
P	Pump
ref	Reference
Ri	Riser
RPV	Reactor Pressure Vessel
SR	Side Reflector
T	Turbine
w	Wall of the heat transfer element

Non-SI units

b	Barn	$10^{-28}\,\mathrm{m}^2$
eV	Electron volt	$1.602176 \times 10^{-19}\,\mathrm{J}$

List of Figures

List of Tables

Contents

1 Introduction to Nuclear Propulsion for Naval Vessels

1.1 Introduction

Nuclear propulsion has recently gained increasing interest within the maritime sector in the Netherlands and Europe. According to the Dutch maritime sector policy report "No Guts, No Hollands Glorie" published in 2023, nuclear energy can help reduce dependency on fossil fuels and provides a potential high-energy density source for ships without emitting carbon dioxide (CO_2). One of the project goals is to develop a standardized, modular nuclear reactor for ship integration within 10 years [2]. The resurgence of interest in nuclear propulsion for maritime applications comes at a crucial time when the global shipping industry is aiming to reduce its environmental impact. Recognizing the urgent need to lower dependence on fossil fuels and mitigate greenhouse gas emissions, the use of nuclear energy presents a promising solution. The Dutch maritime sector's focus on nuclear propulsion reflects a broader international trend towards cleaner and more sustainable energy sources for maritime applications.

Renewable energy sources, like wind and solar [3], and alternative fuels, like methanol [4], are investigated as a potential replacement of fossil fuels, but an issue arises looking at their energy densities. Compared to conventional fossil fuels, the energy and power densities of 'green' energies are significantly lower [5] [6]. The expectations are that, especially for naval vessels, the energy usage on ships will not decrease in the coming years. This is due to the implementation of drones and unmanned vessels, without even considering the possibility of adding additional weapon systems such as a rail gun [7]. On one hand, the energy demand is increasing while on the other hand, there's an energy density decrease which results in an energy mismatch problem. Nuclear energy could play a major role in solving this issue, as it offers one of the highest available energy densities.

Nuclear energy is not seen as a renewable energy source, due to the limited amount of uranium and thorium available on earth. Despite that, it is a low-carbon energy source that does not emit CO_2 during operation. Over the course of the life-cycle of nuclear power plants, they produce similar amounts of CO_2 per unit of electricity as wind, and one-third of the emissions per unit of electricity compared with solar [8]. As the maritime sector was responsible for 2.9% of the worldwide CO_2 emissions in 2018, and 3-4% of the EU's total CO_2 emissions [9], implementing this technology could contribute to lowering the maritime influence on climate change.

Operational advantages of nuclear propulsion for naval vessels include high energy density and ensuring sufficient power for long operation times, this way providing a reliable power source for various ship types. As a result, nuclear vessels can ensure high vessel speed without losing endurance, this way ensuring a high operational endurance due to the potential of staying at a location for long periods (regarding an energy perspective). Therefore, operational flexibility is improved as nuclear vessels can respond to crises more quickly and can operate longer with fewer logistics support compared to conventional vessels [10]. It is therefore no surprise nuclear energy has been used on vessels previously, especially on military ships.

Nuclear energy has been utilized for propulsion in military ships, such as aircraft carriers and submarines. China, France, India, Russia, the United Kingdom and the United States possess nuclear-powered naval vessels [11], and other countries like Australia [12] and Brazil [13] are currently in the process of developing nuclear naval vessels. These military ships benefit from energy independence for long operation times, which especially holds for air independent power sources for submarines. Moreover, merchant ships in countries like Germany, Japan, Russia and the United States have applied nuclear propulsion specifically for icebreakers and cargo ships [14].

1.2 Problem statement and research questions

Although nuclear energy has previously been used on ships, that does not mean the technology can be easily implemented in future (naval) ships. The biggest issue arises from the dynamic power profiles that ships, especially naval vessels, require during operation. Nuclear reactors are commonly used to operate as stable power sources, and operating ships fully on nuclear energy could lead to dynamic issues when the required power increases or decreases. Previous research on applying nuclear energy on ships [15] [16] [17] accounted for this dynamic behaviour by applying linear power increase/decrease limits based on values from literature (stating a power increase of e.g. 5%/min is the limit). These studies show that significant power peak shaving capabilities, such as batteries or fuel cells, are required to support the dynamic power behaviour of ships. Moreover, previous research has primarily focused on ship types like container ships and dredgers, which have more stable power profiles than naval vessels. To ensure that nuclear energy can be applied as a power source for naval vessels, the dynamic power behaviour of nuclear power plants must be investigated, leading to the following research question:

How can a nuclear power plant be implemented in a naval vessel to supply the required dynamic power behaviour?

To answer this research question, multiple sub questions were formulated in order to analyse different aspects of this question. These sub-questions are:

1. *What naval vessels are of interest for the Royal Netherlands Navy for the implementation of nuclear technology?*
2. *What are the dynamic power behaviour requirements for the selected naval vessels?*
3. *Which reactor type proves the most suitable for integration into a naval vessel?*
4. *Which power conversion cycle, in combination with the selected nuclear reactor, is the most suitable onboard of a naval vessel?*
5. *Which control strategy should be selected to improve the dynamic power behaviour of a maritime nuclear power plant?*
6. *What are the dynamic limitations of the selected nuclear reactor?*
7. *What are the dynamic limitations of the selected power conversion cycle?*

This research question, along with the associated sub-questions, will be addressed through a combination of a literature study and a designed model. The literature review was performed to assist in initial design choices, ensuring alignment with recent developments in nuclear reactors, power conversion cycles and control configurations. Based on these findings, a novel modelling approach was applied for dynamically modelling a nuclear power plat installation. In this way, this research contributes to the preliminary design phase of nuclear propulsion for (naval) vessels by providing initial insights into whether the dynamic capabilities of a naval vessel can be achieved with a nuclear power plant.

1.3 Thesis outline

The thesis is organised as follows:

- In Section 2 the literature research will be presented. Here, the vessels of interest for the Royal Netherlands Navy, the propulsion layout and dynamic power requirements of a naval vessel will be determined. In addition, different nuclear reactors will be investigated and compared with each other. The power conversion cycles, and required heat exchangers, will be discussed. Finally, the power dynamics of the reactor and the control configurations of the cycle will be investigated.
- In Section 3 the layout of a nuclear power plant, specifically designed for a naval vessel, will be presented, Here, the selected nuclear reactor type, power conversion cycle and control method will be combined into one detailed plant configuration.
- In Section 4 the detailed plant configuration is modeled and the respective sub-models are further described, providing the equations and assumptions related to each of the sub-models.
- In Section 5 each component of the model will be validated.
- In Section 6 an overview is provided of the required control loops for stable plant operation, followed by the selected control methods and their implementation.
- In Section 7 a number of scenarios are proposed that will be used to highlight the dynamic capabilities of the nuclear power plant. The results of each scenario are presented and discussed.
- In Section 8 a general discussion is presented, reflecting on the choices made regarding the selection of the nuclear power plant and the created model.
- In Section 9 the problem statement is revisited, answering the individual sub-questions, leading to the answering of the main research question posed in this thesis.
- In Section 10 research recommendations based on the current work and topics for further research are presented.

2 Literature research

2.1 Vessel considerations for nuclear propulsion

2.1.1 Propulsion types

The implementation of nuclear energy on a maritime vessel is impacted by the type of propulsion method used on the vessel. Before investigating the dynamic power requirements of the vessel, it is important to examine the most common types of (naval) propulsion, review the propulsion types previously used on nuclear ships, and ultimately select a specific propulsion type to serve as the basis for this nuclear power plant. After the selection of this propulsion type, a short investigation towards the vessels of interest for the Royal Netherlands Navy will be performed. Finally, the dynamic power requirements of naval vessels will be determined as reference conditions for the nuclear power plant installation.

2.1.1.1 General propulsion types

Geertsma [18] states there are different propulsion and power generation types for naval (vessels). For propulsion types a distinction is made between mechanical, electrical and hybrid propulsion, of which an overview is presented in Figure 1. In the case of mechanical propulsion, one or more combustion engines are connected directly or through a gearbox to a propeller. An additional engine, in combination with a generator, is required to provide electrical power for the hotel load of the vessel. With electrical propulsion one or more electric motors are connected to a propeller directly, which are provided power by solely an engine and generator installation. Hybrid propulsion is a combination of the previous two, using one or more combustion engines and electric machines connected directly or through a gearbox to a propeller. The distinction between power generation is neglected, as nuclear energy was assumed to be the solely power source for this research.

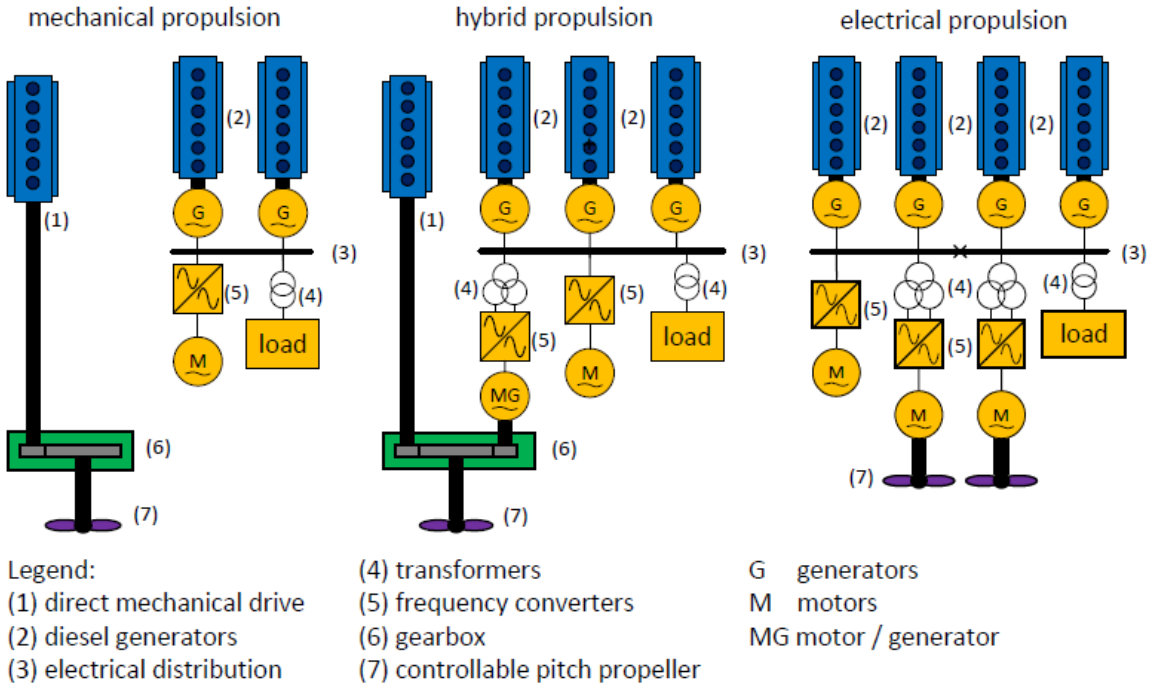

Figure 1: Propulsion layouts for mechanical, hybrid and electrical [18]

2.1.1.2 Propulsion for nuclear energy

Historically, there have been many cases where nuclear energy has been used for ship propulsion. The method of implementation is however not consistent as multiple propulsion types have been used. Looking at submarines, it is stated that Russia, the USA and the UK rely on mechanical propulsion while France and China use the turbines to generate electricity for propulsion [19]. The nuclear Russian Kirov class cruisers applied a steam propulsion system turning two shafts therefore applying mechanical propulsion as propulsion type [20]. The four nuclear merchant ships that were used as cargo ships all applied mechanical propulsion [19] (Appendix A1 provides additional information about merchant nuclear vessels). Historically it therefore seems mechanical propulsion was favoured as propulsion type, however the implementation of electrical propulsion was limited at the time most of these ships were in operation and could (partly) suggest why electrical/hybrid propulsion was not implemented.

Nuclear energy has been actively considered in recent ship design studies. Full electrical propulsion was preferred, as it adds flexibility for placement of the reactor and the motor separately from each other in the ship, not being limited by a mechanical connection. Removing the main shaft would also free up space in the ship [21]. Houtkoop [22] also favours electrical propulsion as it gives the option of adding batteries to the power generation of the ship. These batteries could be used for enhanced load response and peak shaving purposes. Energy storage also benefits the implementation of electrical propulsion.

Overall, the historical use of mechanical propulsion does not seem to be the favoured option for future nuclear vessels. The flexibility benefits of system placement, the possibility of adding batteries for load following and an expected increase in electrical desires for sensors and advanced weapon systems determined that electrical propulsion was deemed the favoured option for nuclear ship designs. For simplicity, full electrical propulsion was selected, but additional complexities could be added in further (electrical) propulsion designs.

2.1.2 Vessels of interest

2.1.2.1 Future ships for the Royal Netherlands Navy

The past few years, more budget of the Dutch government went towards Defence purposes [23]. Besides many other purposes, the budget is going towards replacing and expanding the current fleet. Multiple replacement projects are currently ongoing and these will be investigated to see which ships have potential for implementation of nuclear propulsion. It was decided to look solely at these projects, as this is the only public information about the replacement and expansion of the Dutch Navy. Nuclear energy could be of interest for additional future projects, but as information about these projects is not available at the time of writing, other futuristic ideas will be neglected.

An overview of the current projects regarding the expansion and replacement of the Dutch Navy can be seen in Table 1 [24]. Table 1 shows that multiple projects are already under construction, under contract or under tendering, indicating specific information is already available for these projects. Regarding the two projects under construction, the combat support ship (CSS) and the Vlissingenklasse, both projects have selected to not implement nuclear propulsion and are therefore not of interest. For the Anti-Submarine Warfare Frigates (ASWF) project, which is currently under construction, the main contractor Damen Naval has already decided to implement another propulsion method by signing a contract with MAN for diesel engines and generators [25]. For the replacement of the submarines, the tendering process has been evaluated and for now the French company Naval Group was selected as main contractor [26], but all the proposed designs did not implement nuclear propulsion. It has also been decided that the eight support vessels will implement methanol as fuel source [27].

Although seven projects are listed in this table, it is not realistic to assume all projects could be of interest for nuclear propulsion. Only the Future Air Defender (FuAD) and the Amphibious Transport Ship (ATS) project are current projects of the Royal Netherlands Navy that could be of interest for implementation of a nuclear reactor. To the writer's knowledge these projects have not selected a definitive propulsion method and the ship types are of interest looking at historical use of nuclear propulsion and their ship size. Even in the case when a maritime small modular reactor (SMR) will not be designed on time, these ship types could implement a nuclear power plant at a later moment. If during the design phase the implementation of an SMR is considered, then during a midlife update the SMR could be implemented. It is therefore that both these projects will be further investigated to see if nuclear propulsion could be a feasible option.

Table 1: Replacement and expanding project for the Royal Netherlands Navy [24]

Type	Name	Number	Project phase	Delivery year
Supply ship	Combat Support Ship	1	Construction	2025
Mine countermeasures	Vlissingenklasse	6	Construction	2025
Frigates	Anti-Submarine Warfare Frigates	2	Contract	2029
Support vessel	Seagoing and diving vessels	8	Preparation	2030?
Submarines	Replacement Walrusklasse	4	Tendering	2034
Frigates	Future Air Defender	4?	Preparation	2034?
Transport/patrol	Amphibious Transport Ship	6?	Preparation	2035?

2.1.2.2 Future Air Defender

The aim for the Future Air Defender (FuAD) project is to achieve a replacement for the Air Defence and Command Frigate (Luchtverdedigings- en commandofregat, LCF) of the Dutch Navy. As this project is still in its preparation phase, it is difficult to determine what the required power and energy demands are. For this reason, the assumption is made that the power and energy requirements are similar to High-end Surface Combatant (HSC) described by Sapra et al. [28], as the design focus of this ship is similar to the purpose of the FuAD.

In Figure 2 an overview is given of the power and energy requirements at specific ship speeds for the high-end surface combatant. The energy requirements depend on a yearly operational profile of the ship. For example, if the ship is operating almost all the time at 10 knots, then it is expected that at 10 knots the most amount of energy is required. Even if at higher speeds significantly more power is required the operational duration at these power levels is shorter and therefore the overall energy requirement is lower. It can be seen that for the HSC at around 18 knots, 500 MWh of energy is required, which is the most for all ship speeds. The required power at that moment is 8 MW. Although less energy is used at higher ship speeds, around 400 MWh at 28 knots, the power demand can be significantly higher, topping at 28 MW. This maximum power depends strongly on the desired maximum ship speed and can increase significantly if the maximum ship speed is slightly increased after 28 knots. It could be desired for the FuAD to ensure higher top speeds, for example for operating in carrier strike groups, but as no clear information is present about these desires it was assumed the top speed is 28 knots. At lower ship speeds a lot of energy is required, as at 0 knots more than 400 MWh is required with a power need of 1.1 MW [28]. This is the result of the hotel load of the ship, which must always be provided even when the ship is laying for anchor or staying in the harbour. The current installation of the HSC contains a fuel capacity of 700 m^3 [28].

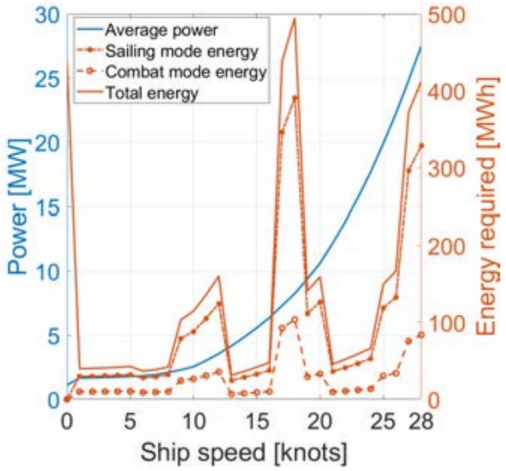

Figure 2: Average power and energy requirements for the high-end surface combatant (HSC) [28]

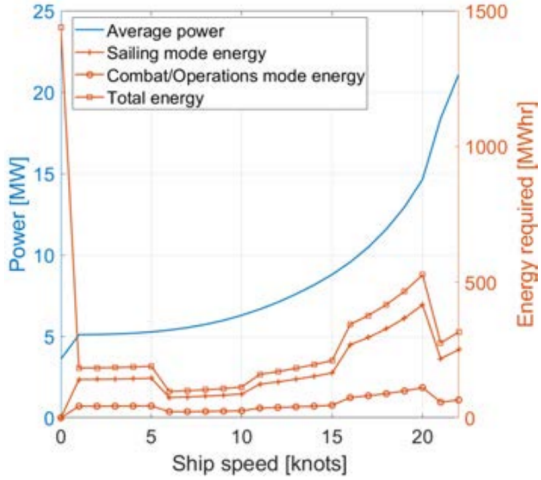

Figure 3: Average power and energy requirements for the landing platform dock (LPD) [28]

2.1.2.3 Amphibious Transport Ship

The ambition for the Amphibious Transport Ship (ATS) project, previously known as LPX project [29], is to replace the current landing platform docks (LPD) and the ocean-going patrol vessels (OPV). The ATS will therefore be a combination between a transport and patrol vessel. As this project is still in its preparation phase, it is difficult to determine what the required power and energy demands are. For this reason, the assumption is made that the power and energy requirements are similar to the LPD described by Sapra et al. [28]. The power and energy requirements compared to the vessel's speed can be seen in Figure 3.

In contrast to the HSC, the energy requirement of the LPD tops when it's laying for anchor or staying in the harbour. At 0 knots the energy required is almost 1500 MWh and the power required is 3.6 MW [28]. The highest amount of energy during sailing is required at 20 knots which is 500 MWh and at this point 15 MW of power is required. At the top speed of the LPD, the energy required lowers to 300 MWh, but the power need increases to 21 MW. The current installation of the LPD accounts for a fuel capacity of 7700 m^3, out of which 1500 m^3 is used for its own onboard power requirements [28].

2.1.3 Dynamic power requirements for naval vessels

2.1.3.1 Limiting dynamic system

As discussed in Section 2.1 electrical propulsion was selected as the preferred propulsion method, which means that all the energy produced by the nuclear reactor is directly converted to electricity before it is used by other (sub)systems on the vessel. The power requirements within a vessel are determined by the propulsion of the vessel and by the hotel load, which includes all the non-propulsion (sub)systems. All these loads are connected to the vessel's grid, but the impact of each system may differ greatly in the amount of electric power required and the intensity of their use. If the power demand of a (sub)system is small compared to the power of a single diesel generator, or if the dynamic power variations of a (sub)system are sufficiently small, these can be neglected with respect to the overall load response of the prime mover.

In reality, most hotel loads are relatively small in power size or have such a small dynamic power variation that these can be neglected. The propulsion load therefore requires in general the majority of the installed

power and the acceleration of the vessel therefore determines the dynamic requirements of a naval vessel. The impact of waves could also contribute to significant power changes, but this impact will be neglected within this research. The propulsion load, and thus the dynamic acceleration of a vessel, is based on the power provided by the prime movers. This means that not the vessel itself, nor the operational desires of the captain, are the limiting factor for the dynamic power demand, but the prime movers determine the dynamic requirements of a vessel. For naval vessels, there are in general two types of prime movers, which are a diesel engine and a gas turbine. By investigating the rates at which power can be increased or decreased of the diesel engine and the gas turbine, the current dynamic power behaviour of a naval vessel can be determined.

2.1.3.2 Diesel Engine

To investigate the dynamic power behaviour of a diesel engine, the four-stroke diesel engine MAN V28/33D STC (sequential turbocharging) was chosen as this is a common diesel engine for naval purposes (the ASWF will implement these engine types [25]) and MAN provides the required data for most of their diesel engines [30]. The MAN V28/33D STC is a marine engine designed to provide propulsion for ship types like frigates, amphibious and logistic ships. The name of the engine is related to its technical properties as it has a 28 cm cylinder bore and a 33 cm piston stroke. It can contain 12, 16 or 20 cylinders which can produce a maximum of 500 kW per cylinder, therefore ranging between the 6 and 10 MW, at a maximum operating speed of 1000 rpm. The dynamic power behaviour of the diesel engine can be determined by looking at the ramp limits given by the manufacturer. In Figure 4 specific acceleration times for several operations can be seen. Several manoeuvre types can be seen which cover full ahead, stop and full astern. The black lines are normal manoeuvre acceleration times and the blue lines are emergency manoeuvre acceleration times. Although it can be argued that the blue lines are feasible for the engine, it is not specifically stated how many cycles the engine can endure before the maintenance of the engine increases. Therefore, during operation the normal manoeuvre lines are maintained and these will therefore indicate the dynamic limits that can be achieved with a diesel engine.

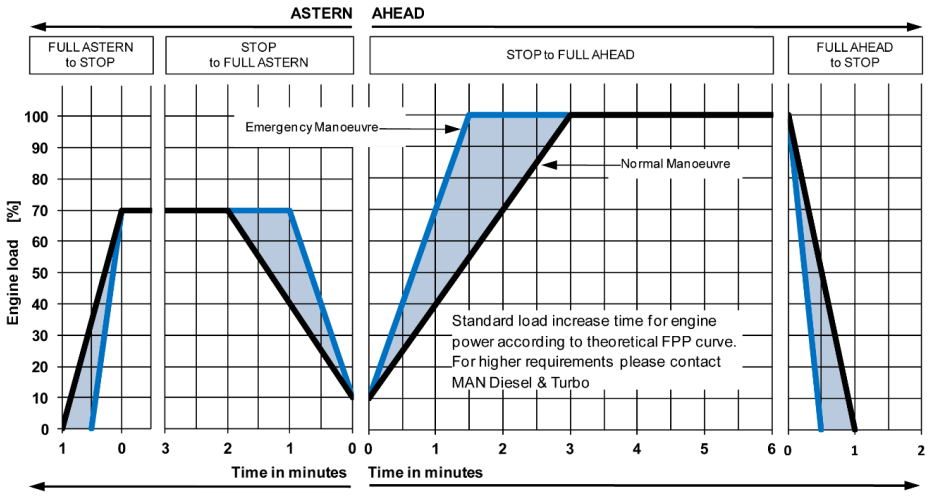

Figure 4: The specific acceleration times for the MAN V28/33D STC diesel engine [31]

Figure 4 shows that for full astern, the accelerations are slower or equal compared to sailing full ahead. It is assumed that for nuclear power, the power generation when sailing ahead or sailing astern will not differ, and for this reason only the ahead manoeuvres will be investigated as these are the more challenging power changes. The figure shows that when the stop to full ahead manoeuvre takes place, the engine load changes linear from 10% to 100% in 3 minutes, showing a 30%/min increase. In the case of the manoeuvre from full ahead to a stop situation, the load changes from 100% to 0% in 1 minute indicating a 100%/min decrease.

2.1.3.3 Gas Turbines

Another common prime mover for naval applications is the gas turbine. To investigate the dynamic power behaviour of the gas turbine, the GE LM2500 was selected as this is a common gas turbine for naval purposes (for example the current German F125 frigates [32] and the Arleigh Burke-Class Destroyers for the United States Navy [33] apply the GE LM2500 GT). The LM2500 is a gas turbine that is used for ship types like patrol boats, corvettes, frigates, destroyers, cruisers, cargo ships, and aircraft carriers [34] and is therefore applicable for the research case. Specific data about the dynamic power behaviour of the LM2500 for naval applications is not publicly available and could not be used as a dynamic power reference. It was therefore assumed that the dynamic power behaviour of the naval type LM2500 is similar to the dynamic power behaviour of the industry type LM2500, which provides more publicly available data. It is stated that for all the LM2500 models the ramp rate is 30 MW/min [35]. The lowest rated LM2500 model has the highest ramp rate and has in this configuration a net output of 33.5 MW. The available data makes no distinction between increase and decrease ramp rates, and these are therefore assumed to be equal. The ramp rate of the gas turbine that will be used for comparison is therefore equal to 30 MW/min for a 33.5 MW rated gas turbine, which is equal to 90%/min.

2.1.4 Conclusion vessel considerations

Historically, mechanical propulsion has been used as propulsion type for nuclear vessels. However, new designs have favoured the use of electrical propulsion as this improves flexibility, reduces the needed volume of the shaft and adds the possibility of batteries for load following conditions. It was therefore decided to implement a full electrical propulsion system for the nuclear power plant.

Multiple projects about the replacement of vessels for the Royal Netherlands Navy were investigated. Of all these projects, only the Future Air Defender (FuAD) and Amphibious Transport Ship (ATS) were deemed feasible for nuclear propulsion. After investigating the power profiles of the FuAD and the ATS, it seems that the most amount of energy is not needed at full power. For the FuAD the most amount of energy (500 MWh) is used at 18 knots and 8 MW of power. For the ATS, the most amount of energy (1500 MWh) is used at 0 knots and 1.1 MW. Compared to the max power needs of these vessels, 28 MW for the FuAD and 21 MW for the ATS, this means that the most amount of energy is used at low part load. It is therefore crucial, for efficient power consumption, that the efficiency at part load is considered during the design of the nuclear power plant.

To investigate the dynamic behaviour of these ships, it was determined that the prime movers are dynamically the limiting factor for a naval vessel. The diesel engine and gas turbine were selected for further investigation as these are two common naval vessel prime movers. The MAN V28/33D STC, a common naval diesel engine, and the GE LM2500, a common naval gas turbine, were selected for determining the dynamic requirements. Looking at the characteristics of this diesel engine, a power increase of 30%/min could be realized between 10—100% of full power and a power decrease can be realized of 100%/min from full power to full stop. The gas turbine achieves faster overall dynamic power behaviour compared to the diesel engine, as it can reach a ramp rate of 90%/min. However, no distinction was made between increase and decrease ramp rates and these are therefore assumed equal. This results in the ramp rate of the diesel engine being slightly faster when a power decrease is desired. Overall, the dynamic behaviour of these two prime movers will be compared with the dynamic power behaviour of the nuclear power plant to determine if nuclear energy could fulfill, or come close to, the current dynamic requirements for naval vessels.

2.2 Nuclear energy

This section will give a short introduction towards the use of nuclear energy, and general concepts of reactor analysis. At first the process of radioactive decay will be explained. Neutron interactions, focusing specifically on fission, will be discussed next. Finally, the concept of reactivity and its importance for dynamic reactor control will be explained.

2.2.1 Radioactive decay

The stability of nuclides present in the universe differs. Unstable nuclides can undergo a spontaneous transformation into a different nuclide while emitting energetic particles, which is called radioactive decay [36]. Reasons for this occurrence could be an imbalance between the amount of neutrons and protons within the nuclide, or an energy imbalance that creates the need for the nucleus to emit the excess energy in order to obtain greater stability [37]. The decay process leads to another nuclide, but if this nuclide is still unstable, this nuclide can further decay until a stable nuclide is reached, resulting in a so-called decay chain. There are different types of decay of which α decay (emitting a helium nucleus), β decay (emitting an electron or positron) and γ decay (emitting a photon) are the most common [36]. All natural decay reactions result in a net positive output of energy. This creation of energy in any nuclear reaction follows Einstein's postulate of mass-energy equivalence, stated in Equation 1 [38]. From this postulate, and the knowledge of the decay reactions producing energy, a result is that the mass of the products in a nuclear reaction is lower than the mass of the reactants, as the mass is converted into energy.

$$E = mc^2 \tag{1}$$

2.2.2 Neutron interactions

In contrary to protons and electrons, which are positively and negatively charged, a neutron has no charge or is, as the name suggests, neutral. Neutrons are responsible for many types of nuclear reactions, for which an overview can be seen in Figure 5. These interactions can be categorized in two groups, which are scattering and absorption. In practice, not all neutron interactions will take place as frequent as others. The probability of a specific neutron interaction with a type of material can be calculated based on a nuclear cross-section. A distinction can be made between the microscopic cross-section σ [cm^2], the probability of neutron interaction with only a single nucleus, and the macroscopic cross-section Σ [cm^{-1}], the probability of neutron interaction with a chunk of material, which are related to each other by the atomic number density of the material N [#/cm^3] [36]. These cross-section can be applied for every type of neutron interaction, and so the total cross-section Σ_t can be determined as the cross-section of neutron absorption Σ_a and scattering Σ_s added together, presented in Equation 2. The cross-sections of absorption and scattering can be further divided into more specific neutron interactions to give details over a specific type of neutron interaction.

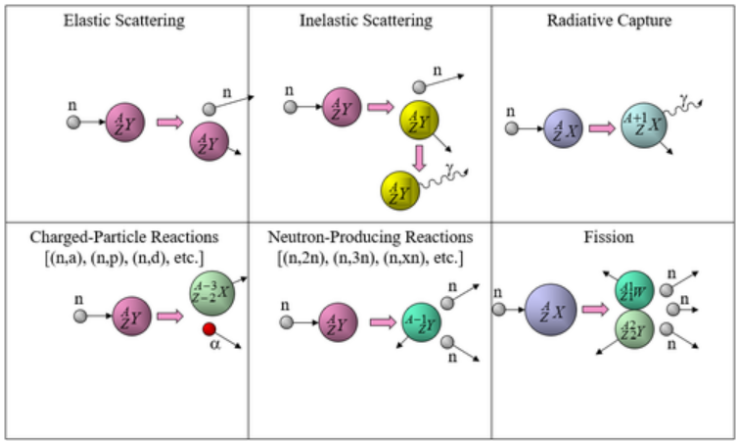

Figure 5: Types of neutron interactions [39]

$$\Sigma_t = \Sigma_s + \Sigma_a = N\sigma_s + N\sigma_a \tag{2}$$

2.2.2.1 Fission

All these neutron interactions play a role in using nuclear energy, but their significance is different. The energy released in a nuclear reactor comes from neutron interactions resulting in fission, and therefore more attention will be given to this specific neutron interaction. Nuclear energy can be created from the principle of fission and fusion. Where the principle of fission accounts for the splitting of atoms to create energy, fusion applies the concept of combining atoms into a single atom to create energy. Currently, all commercial operated nuclear power reactors rely on the principle of fission, so for this reason fusion will be ignored. Nuclear reactors are devices in which controlled nuclear fission chain reactions can be maintained. Here, a fission reaction occurs where neutrons are used to induce splitting of heavy nuclei into smaller nuclei, releasing energy and several additional neutrons. These neutrons can then be used in multiple further fission reactions [36]. An overview of a fission process can be seen in Figure 6.

The total amount of energy per fission is around 200 MeV, but the energy released during a fission reaction is distributed among several reaction products, of which not all can be used as useful energy. The most significant part of the energy (80%) is kinetic energy of fission fragments, which are most present at the location where fission occurs. However, some energy appears as kinetic energy of neutrons (3%) and gammas (4%). These have relatively long distant ranges and will result in energy being distributed over the full core of the reactor, including the shielding. All these energy sources are instantaneous, but some fission energy (4%) appears in the form of heat generated by the decay of radioactive fission products. Even after shutdown, but also during operation, heat will be produced caused by the decay of fission products into other products. This amount can be significant, as it is around 4% of the heat generated during operation. It is therefore important that even after shutdown the reactor is cooled to prevent a temperature increase. The final two sources of energy distribution are the neutrinos (5%) and other non fission reactions due to neutron capture (4%). Due to the distribution of the energy produced by fission over multiple reaction products, not all energy by fission can be used effectively. The effective heat per fission depends on the isotopes used in the fuel, and can therefore differ based on the core composition used in a specific reactor. [36]

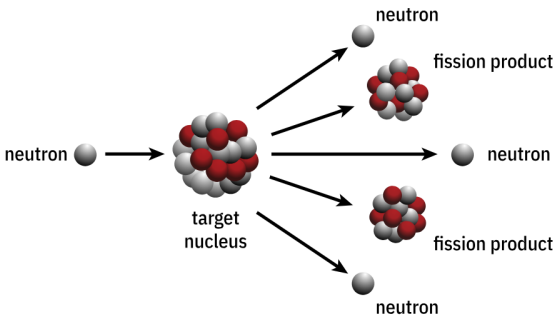

Figure 6: Nuclear fission reaction [40]

2.2.2.2 Nuclear fuel materials

It is not possible for all types of materials to undergo fission. A distinction can be made between fissile and fertile materials, where fissile materials contains isotopes like $^{233}\mathrm{U}$, $^{235}\mathrm{U}$, $^{239}\mathrm{Pu}$ and $^{241}\mathrm{Pu}$ [36] [41]. These fissile materials can undergo fission by capturing neutrons in a thermal spectrum [41]. Of the fissile isotopes only $^{235}\mathrm{U}$ is found in nature. Natural uranium is however composed primarily of $^{238}\mathrm{U}$, only containing 0.711% $^{235}\mathrm{U}$ [36]. Multiple reactors need higher enriched uranium (higher percentage of $^{235}\mathrm{U}$) of around 3-5% to operate efficiently, so enriching is applied. Besides enriching, another process to achieve fissile materials is breeding, in which neutron capture is applied to isotopes that can produce fissile materials. The isotopes that can undergo neutron capture to produce fissile materials are called fertile isotopes, of which $^{232}\mathrm{Th}$ and $^{238}\mathrm{U}$ are of interest due to the abundant supply throughout the world. These fertile isotopes will respectively convert into fissile $^{233}\mathrm{U}$ and $^{239}\mathrm{Pu}$ [36]. In the case of fast reactors other isotopes can be used as fuel which are: $^{232}\mathrm{Th}$, $^{238}\mathrm{U}$, $^{240}\mathrm{Pu}$ and $^{242}\mathrm{Pu}$, but these are not called fissile but fissionable isotopes [36].

Uranium fuel containing around 3-5% of $^{235}\mathrm{U}$ is called low enriched uranium (LEU). Due to proliferation risks, it is required for nuclear reactors to operate with LEU up to a 20% enrichment as anything above 20% can be used for building nuclear weapons and is determined as highly enriched uranium (HEU) [42]. Although civilian reactors are not allowed to use HEU, an exception can be made for defence purposes. Some naval reactors use HEU up to 97 percent of $^{235}\mathrm{U}$ as this provides enough reactivity to override xenon poison dead time. It also ensures reactor compactness, a higher fuel burnup and the possibility for a single fuel loading for the operational time of the ship [43]. However, this research will focus solely on reactors using LEU. As the maritime sector aims to develop a standardized nuclear reactor, it would be wise to prioritize a reactor design that is permissible for both civilian and naval applications.

Reactors run on materials like uranium, plutonium and thorium. Of these materials, only plutonium is not a naturally occurring element, as it is created as a by-product during nuclear operations. Uranium is nowadays used mostly a fuel material, but there is significant interest in the development of thorium as fuel. Thorium is abundantly available on earth, it reduces the total amount of radioactive waste, lowers the amount of long-lived waste products (as the formation of plutonium is less likely during this process) and increases proliferation resistance [15]. However, a downside of thorium is that it is not fissile and therefore a nuclear reaction will not spontaneously happen. A solution for this problem is to start the reactor with another fissile material, such as $^{235}\mathrm{U}$ or $^{239}\mathrm{Pu}$.

2.2.2.3 Fission products

After the occurrence of a fission reaction in general two fission products occur. The specific fission products are not constantly the same two fragments as a hundred different fission products can occur. The products can have mass numbers ranging from 70 to 170, but these different mass numbers are not created equally. The probability that a fission fragment is a specific nuclide with mass number A is determined by the fission chain yield presented in Figure 7 [44]. As can be seen, the four fuel isotopes $^{233}_{92}\mathrm{U}$, $^{235}_{92}\mathrm{U}$, $^{239}_{94}\mathrm{Pu}$ and $^{241}_{94}\mathrm{Pu}$ have similar yield curves, whereas the yield curves of the plutonium isotopes are slightly shifted towards the higher masses compared to the uranium isotopes curves. It can be seen that it is far more likely to obtain mass numbers of around 100 and 140 (occurring around 6.5% of all fission reactions) than obtaining two fission products with a symmetric splitting (both products with a mass number of around 118) which only occurs 0.01% of all fission reactions.

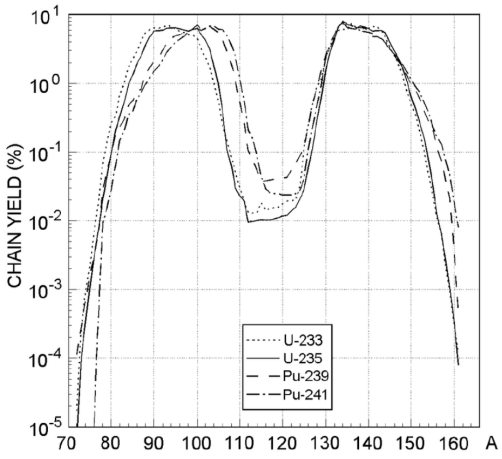

Figure 7: Fission chain yield of $^{233}_{92}\mathrm{U}$, $^{235}_{92}\mathrm{U}$, $^{239}_{94}\mathrm{Pu}$ and $^{241}_{94}\mathrm{Pu}$ [44]

Some attention should be given to some specific fission products, which are xenon (Xe) and samarium (Sm). These products are of interest as they can affect reactor operation significantly due to their large absorption cross-section. As a result, neutrons can be absorbed by the xenon and samarium, lowering the amount of neutrons available for fission, which is called fission product poisoning [36]. In the worst case, too much Xe and/or Sm is present in a reactor, resulting in a reactor where the amount of neutrons is too low to result in enough fission reactions, a so-called dead reactor. The reactors can stay dead for hours or days, depending on how much Xe and/or Sm is present. As can be seen in Figure 7, these products, with A = 135 and 149, are likely to occur, but can also be the result of decay from other isotopes. Xenon can decay further into other isotopes with a

smaller absorption cross-section, therefore lowering the amount of neutrons absorbed, but samarium is a stable isotope and can only be removed by neutron capture. Although samarium has a smaller absorption cross-section than xenon, and thus has a less impact on the absorption of neutrons, due to its stability it can build up to significant concentrations, even after the shutdown of a reactor [36]. It must be noted that the concern for a dead reactor is primarily an issue for thermal reactors [36] [45]. The absorption cross-section of fission products rapidly decline for neutron energies above 1 eV. As thermal reactors are operating with neutron energies below 1 eV they do not benefit from this decrease in absorption cross-section, while fast reactors operate with higher neutron energies and therefore do benefit from this absorption cross-section reduction [36].

2.2.3 Nuclear reactor analysis

For nuclear reactor analysis it is important to track the amounts of neutrons generated and absorbed in the reactor. These neutrons are responsible for the fission process and should therefore be sufficiently present in the reactor. A way of analysing the neutrons in the reactor is by applying the multiplication factor k. This is defined as the number of neutrons in one generation divided by the number of neutrons in the preceding generation [36]. If k is equal to 1 the amount of neutrons stays constant during operation and the reactor is called critical. In the case $\mathrm{k} < 1$ then the number of neutrons is decreasing and the reactor is subcritical. In the case of $\mathrm{k} > 1$ the number of neutrons is increasing and the reactor is supercritical. There are multiple ways of determining the multiplication factor k, for example the four- or six-factor formula [36], but a more convenient parameter for dynamic reactor analysis is core reactivity ρ. Reactivity measures the deviation of the core multiplication factor from unity and is typically measured in units of dollars or percent per delayed neutron fraction. It is defined according to Equation 3 [36].

$$\rho(t) = \frac{k(t) - 1}{k(t)} \tag{3}$$

During operation of the reactor, the reactivity of the reactor will change due to external and internal phenomena. External phenomena are mostly related to raising or lowering the control rods (although other control methods are used in specific reactor designs, which will be explained in Section 2.8), but there are many internal phenomena having an effect on the power of a reactor. Feedback phenomena like fuel or moderator temperature changes have a short-term (timescale: $<$ s) effect on the reactor, while Xe or Sm have a longer time effect (timescale: hours to days) [46]. Feedback effects, due to for example fuel burnup, could also take multiple weeks or years before having a significant effect on the reactor [36] [47]. To ensure criticality can be maintained, these feedback phenomena must be compensated, which could be for example achieved in short time by raising the control rods or by refuelling the wasted fuel for long term feedback effects. However, these feedback effects could also be beneficial in maintaining a safe and stable reactor. For example, if designed properly, a temperature increase of a reactor will result in a negative reactivity, lowering the criticality and so the amount of fission reactions occurring. As a result the temperature would lower, this way ensuring self-regulation of the reactor and thus inherent safety [36].

There are multiple feedback phenomena that have an effect on the reactivity, but for short term reactivity feedback the most important is the increase of fuel temperature. To assess this reactivity feedback a coefficient of reactivity is determined as presented in Equation 4 [36]. Here, α is the reactivity coefficient and T is the temperature resulting in a reactivity change. The fuel temperature coefficient of reactivity is principally determined by the Doppler effect [36]. The Doppler effect reflects the change in neutron cross-section for the uranium fuel material by Doppler broadening. Therefore, as the fuel temperature changes the amount of absorbed neutrons changes, impacting the reactivity of the reactor [47].

$$\alpha_T = \frac{\delta\rho}{\delta T} \tag{4}$$

2.3 Nuclear Reactor Technologies

2.3.1 Introduction nuclear reactors

Nuclear reactors are used all over the world for energy production. In 2022 there were a total of 437 reactors in operation in 32 countries. This resulted in a capacity of 394 GWe, producing around 10% of the world's electricity [48] and around 25% of the world's clean electricity. In the Netherlands, nuclear energy is responsible for only 3.3% of the energy generation, which comes from a single 485 MWe reactor operating at Borssele, but there are projects ongoing to increase the number of reactors in the Netherlands [49] [50]. Although traditionally the amount of nuclear energy has been provided by large nuclear power plants, there are developments ongoing towards smaller nuclear reactors, the so-called small modular reactors (SMRs). These SMRs are also of interest for maritime applications as they have a lower power capacity and are smaller in size compared to traditional nuclear power plants. SMRs are defined as having a power capacity up to 300 MWe per unit, which is around a third of the normal capacity of traditional nuclear power plants, but there are also even smaller reactors, so called microreactors operating below the 10 MWe power level [51]. An overview and size comparison is presented in Figure 8. At the time of writing over 80 designs and concepts for SMRs and microreactors are known, but only four are in advanced stages of construction [52], showing the need for development and additional research.

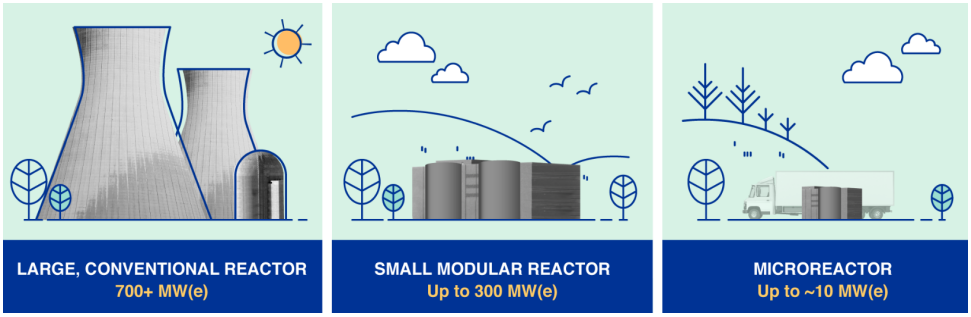

Figure 8: Power and sizing difference between the classification of nuclear reactors [51]

2.3.2 Nuclear energy production

2.3.2.1 General overview nuclear power plant

A general overview of a nuclear reactor can be seen in Figure 9. This overview is based on the layout of the pressurized water reactor as this is the most common reactor type in the world [49]. The nuclear fuel is present within the fuel rods positioned in the center of the reactor. These rods are enclosed by a moderator (in the case of a thermal reactor) which slows down the neutrons from a fast to thermal energy spectrum. Control rods are implemented for controlling the amount of fission reactions and thus the amount of heat produced in a reactor. The created heat must be removed from the reactor core by a cooling medium, which transfers the heat to a secondary circuit by a heat exchanger. Surrounding the reactor core is a reflector which scatters neutrons back towards the core, ensuring less neutrons escape to the surroundings. Finally, the reactor core is surrounded by a shield to minimize radiation reaching personnel, the environment and equipment near the reactor [53].

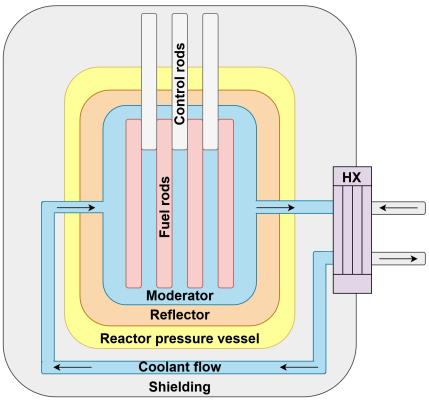

Figure 9: Simplified overview of a nuclear reactor

A general overview of a nuclear power plant can be seen in Figure 10. In total, two loops are present, the primary connected to the reactor, and the secondary to the turbomachinery and cooling installation. The heat produced in the nuclear reactor is transferred by the primary loop to the heat exchanger, which in the case of Figure 10 will create steam in a steam generator. This steam will spin the turbine and the connected generator will convert this mechanical energy into electrical energy. The steam will further be cooled by a condenser to ensure liquid water enters the secondary loop again for further heating. The reason for the two loop construction relates to the risk of radioactive material being transferred in the first loop and the second loops limits the radioactive material being transferred through the turbine and condenser. Besides, the primary loop operates under high pressure to ensure the conversion to steam is limited improving heat transfer properties. As the primary loop can contain radioactive material, this has to be shielded from the outside and must be part of the containment structure, which ensures that in any circumstance radioactive material cannot contact the outside environment.

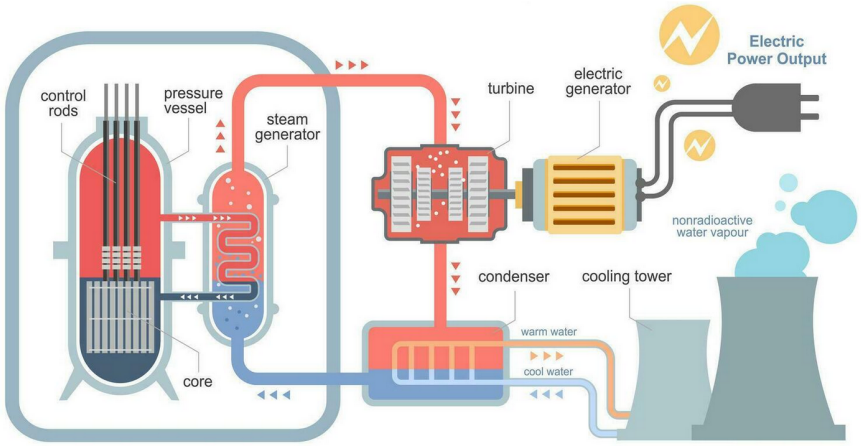

Figure 10: General overview of a pressurized water reactor installation [54]

2.3.2.2 Nuclear fuel

There are different kinds of fuel types for nuclear reactors which can apply uranium and/or plutonium as fuel material. By far the most widely used nuclear fuel type is uranium dioxide (UO_2), with enriched ^{235}U. Only some heavy water and graphite moderated reactors can use natural uranium as fuel, therefore limiting the need for enrichment. In addition, in some power reactors, the by-product ^{239}Pu is mixed with enriched uranium in the form of a mixed oxide (MOX) fuel [53]. In Figure 11 a generic fuel element of a reactor can be seen. This element consist of a zirconium-tin alloy tube and within this cladding tube the fuel pellets are present. At the top of the fuel pellet an open volume is present (the plenum) which prevents damage from over pressure due to gases released from the fuel [55]. Another noteworthy fuel type is the tristructural-isotropic (TRISO) layered particle [55]. This fuel has been specifically made for higher temperature environments, which can be found in the very high temperature reactor (VHTR) [55] [56], and can be used for temperatures up to 1600°C [45]. This TRISO fuel is a 1 mm diameter sphere containing a kernel of fuel surrounded by three layers of carbon and one layer of silicon carbide. Each layer has a specific function, as can be seen in Figure 12. As all these particles are self protected by

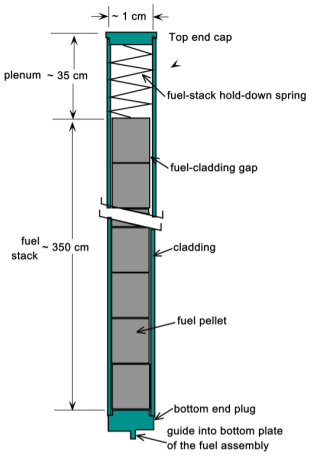

Figure 11: Generic fuel element of a LWR [55]

several layers, there is less risk of a single point failure regarding damage to the fuel, enhancing the safety of this fuel type [57]. Due to the small size of these particles, the fuel forms applying TRISO particles can differ in geometry. For high-temperature gas-cooled reactors there are in general two options in core geometry, which are a prismatic core and a pebble-bed core (see Appendix A2 for a concept design). Both use TRISO particles, but the difference in geometry results in differences regarding size and type of operation [57].

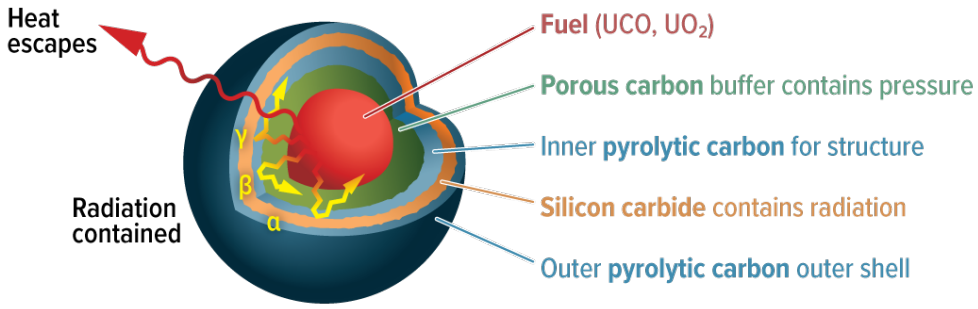

Figure 12: Structure of a TRISO particle [58]

2.3.2.3 Moderator

In a thermal reactor the fast fission neutrons lose their kinetic energy primarily through elastic scattering with the moderator. The moderator is a nucleus with a small mass number, as these are favourable for lowering the energy with each occurrence of elastic scattering [53]. The amount of times elastic scattering has to occur before the desired energy level is reached is not constant and is dependent on the material of the moderator. In Table 2 different types of materials can be seen and the required amount of elastic scatterings n before the energy level is lowered from 2 MeV to 0.025 eV [53], showing which types of materials are favourable for acting as a moderator. It can be seen that water and deuterium (D) need the lowest amount of scattering before the desired energy level is reached. It is therefore that these two materials are used worldwide in light water reactors (water) and heavy water reactors (deuterium). However, a liquid moderator is not always applied and therefore other moderators like solid graphite (carbon) are used in many gas type reactor. Also Beryllium (oxide) has been proposed as moderator [53].

Table 2: The number of scatterings (n) needed to slow a neutron down from 2 MeV to 0.025 eV [53]

Material	A	n
H	1	18.2
H_2O	1 & 16	19.8
D	2	25.1
D_2O	2 & 16	35.7
He	4	42.8
Be	9	88.1
C	12	115
U^{238}	238	2172

2.3.2.4 Reflector

Most nuclear reactors have a reflector which surrounds the core, but a reflector could also be present in the center of the core. The reflector is made of a material that has a high neutron scattering property (and preferably also a low neutron absorption property). Common reflector materials are graphite, beryllium, water, and natural uranium [59]. Due to this high scattering property, the reflector reflects some neutrons back into the core, which would otherwise have leaked from the reactor. This effect improves the neutron economy in the reactor and reduces the amount of fuel needed to achieve criticality [53]. A reflector is also applied to increase the thermal neutron flux density near the edges of the core. As a result, the power at the edge increases, thereby decreasing the difference between the peak and average power density in the core. This ensures a more uniform power profile across the core which is beneficial for power generation and heat transfer [53].

2.3.2.5 Control rods

The control rods present in the reactor are for, as the name suggests, controlling the rate of fission in the nuclear reactor. A general layout of these rods can be seen in Figure 13. By raising or lowering these rods, the criticality of the reactor changes. The rods are made of materials like boron or hafnium, which are materials that have a large absorption cross-section. This way the control rods can absorb neutrons, preventing the neutrons from causing fission [61]. A distinction is made between regulating rods, which are responsible for changing reactor power, and safety rods, which are only present for reactor shutdowns and other emergencies [53]. During reactor operation the composition of the fuel changes due to the burn up of fissile material. This results in more negative reactivity and to compensate this (as it is desired to maintain criticality) another negative reactivity must be removed. One way of realizing this is by withdrawing the control rods, but other control methods are also applied.

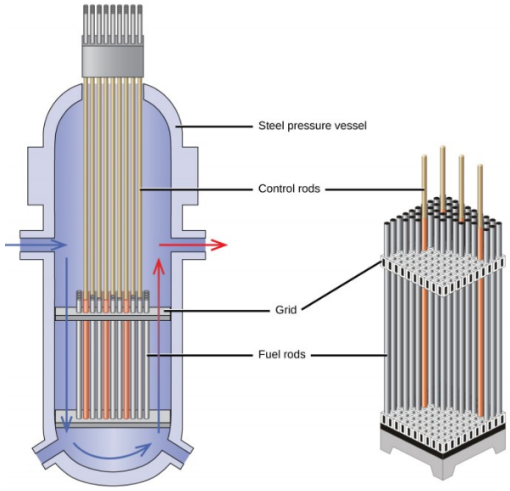

Figure 13: Rods in a reactor [60]

2.3.2.6 Reactor vessel

Surrounding the nuclear reactor is the reactor vessel, which is called a reactor pressure vessel (RPV) if it works under high pressure. An example of a RPV is presented in Figure 14, indicating that the RPV contains everything belonging to the reactor core. The RPV is designed to protect the reactor from outside influences and is an additional safety barrier from keeping radioactive material away from the outside environment. The RPV also guides the coolant through the core of the reactor to ensure heat transfer occurs. Besides, the RPV includes the mechanism for raising or lowering the control rods and allows for instrumentation to be added directly in the core to monitor the operating conditions. [53]

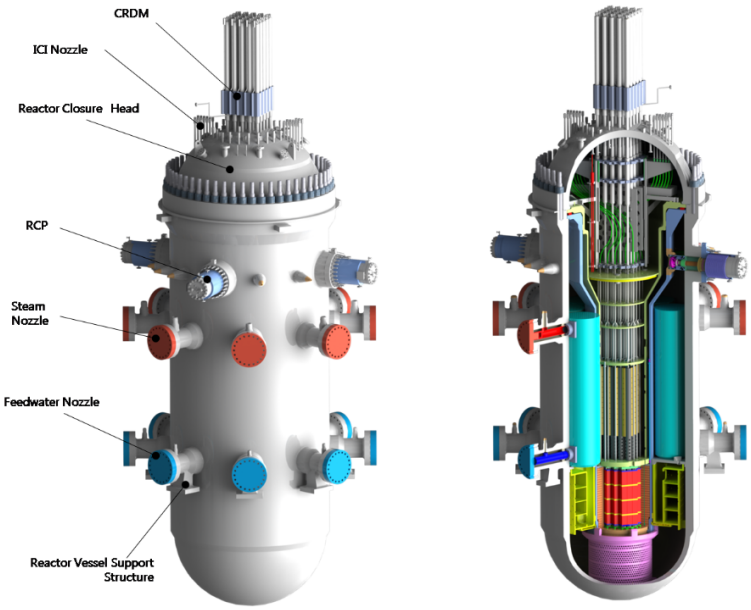

Figure 14: Outside and inside of the reactor pressure vessel of the South Korean SMART SMR [62]

2.3.2.7 Shielding

Personnel operating with nuclear reactors, and the environment of the nuclear power plant, must be protected against radiation from the nuclear reactions. To ensure radiation is partially stopped before entering the human body, shielding is applied. This shielding is based on the type of radiations, of which an overview can be seen in Figure 15. In this figure it can be seen that α- and β-particles cannot easily penetrate materials, and for this reason during shielding calculations only γ-rays and neutrons are considered as they have strong penetration capabilities. For shielding radiation, the material type has a significant impact on the protection of radiation. In general, it is not possible to select a single material that can protect against γ-rays and neutrons due to the reason that materials with high amounts of protons perform better in minimizing γ-ray radiation, while the materials with a low amount of protons are more efficient for blocking neurons. In addition, the shielding should be capable to protect against fast and thermal neutrons, containing different energy levels. As a result, a mixture with both heavy and light nuclei is necessary for efficient shielding to make sure personnel is protected against both γ-rays and neutrons with a broad energy spectrum. [64]

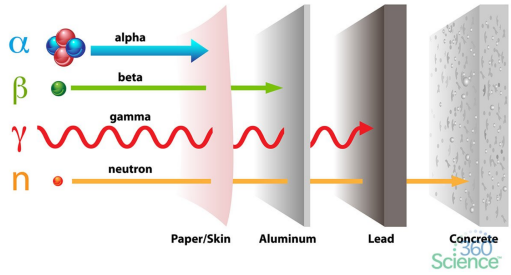

Figure 15: Types of radiation and the impact of shielding with different materials [63]

2.4 Reactor types

2.4.1 Overview reactor types

There are different nuclear reactor designs used worldwide for energy production. A distinction can be made between their generation type, gen. I until gen. IV, of which an overview is presented in Figure 16. The first ever build reactors are gen. I reactors, but these are not commonly used anymore and are mostly replaced by the generation II, III and III+ reactor types. These generations all have similar reactor concept designs, but later generations have added more passive safe and redundant systems, while also improving plant economics. The last type of nuclear reactors, generation IV, contains new concept designs, mainly created to improve efficiency, safety and economics while minimizing waste production and the proliferation risk [56]. These reactors are currently in their design and testing phase and are expected to be operational in the coming decade.

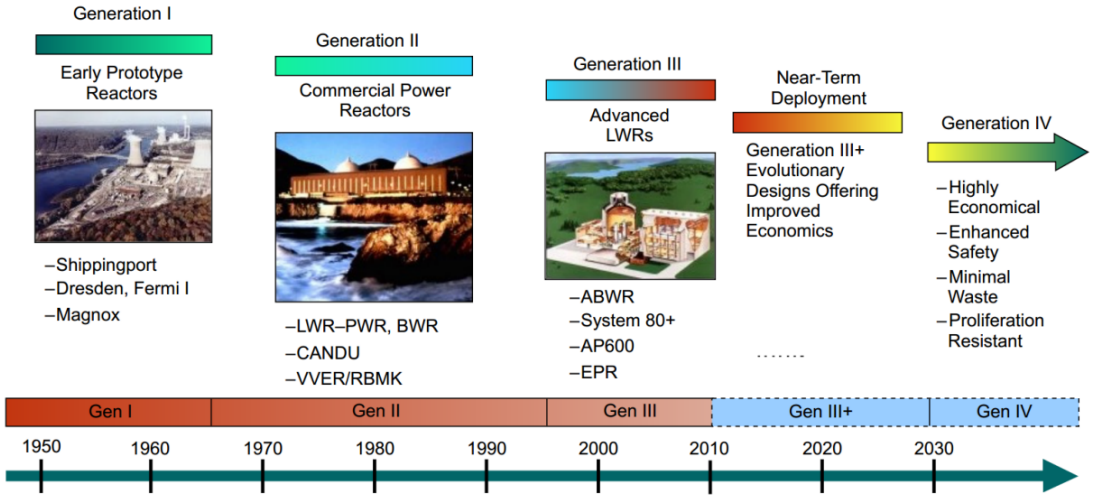

Figure 16: Different generations of nuclear reactors [65]

2.4.2 Selection method

To investigate the potential of implementing nuclear energy on ships, multiple reactor designs must be investigated. Gen. I reactors were prototype reactors and as they are not used anymore, this generation will not be investigated. The further reactor generations will be considered for maritime implementation. Here, no distinction will be made between gen. II, III and III+ reactors, as they have similar concept designs. If such a reactor was implemented on ships, a specific reactor design will have to be selected that has sufficient safety features, and would therefore probably be a gen. III or III+ reactor type.

For the gen. II, III and III+ reactors, only the pressurized water reactor (PWR) will be investigated, and reactors like the boiling water (BWR) and heavy water (HWR) will be neglected. The assumption is made that if almost every nuclear ship in history has used PWRs, and not the other technologies present at that time, the PWR is not only the superior gen. II, III and III+ reactor type for maritime application, but it is also the reactor type with the most maritime experience, making it the favoured reactor type of these generations. A pre-selection will also be made for the gen. IV reactors types. The delivery year of the FuAD and the ATS, which were selected in Section 2.1.2.1 as projects of interest, is set around 2035. It is therefore not of interest to investigate nuclear reactors that are expected to be unavailable at that time.

2.4.2.1 Technology readiness level reactors

The different reactor technologies of the gen. IV reactors are all in different readiness phases and it is therefore important to look at their technology readiness level (TRL) before comparing the technologies. The reactors that are part of the gen. IV reactors are the very high temperature reactor (VHTR), the sodium-cooled fast reactor (SFR), the supercritical water reactor (SCWR), the molten salt reactor (MSR), the lead-cooled fast reactor (LFR) and the gas cooled fast reactor (GFR) [66]. The gen. IV international forum [66] investigated the future outlook of these reactors in 2014. Although this research is slightly outdated, this is the latest research investigating all the gen. IV reactors at the same time. Figure 17 present the timelines and belonging phases for each reactor type. Here, a distinction is made between three phases namely [66]:

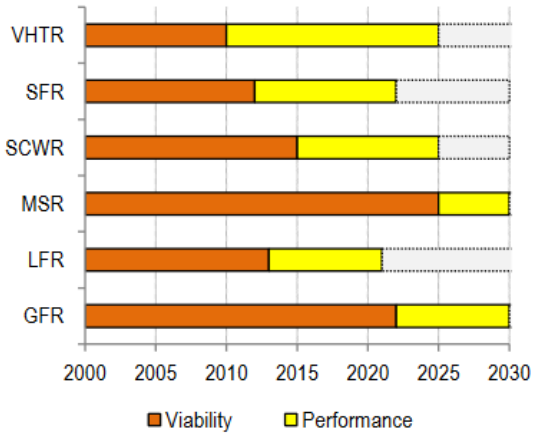

Figure 17: Outlook gen. IV reactors [66]

- *The viability phase, when basic concepts are tested,*
- *The performance phase, when processes, phenomena and materials are verified and optimised,*
- *The demonstration phase, when detailed design is completed and licensing, construction and operation of the system are carried out. Expected to take atleast 10 years.*

At first the different TRLs must be determined, which has been done by applying the TRL scale of the "Rijksdient voor Ondernemend Nederland" [67]. Here they state four phases are present:

- *Discovery phase: TRL 1, 2 and 3,*
- *Development phase: TRL 4, 5 and 6,*

- *Demonstration phase: TRL 7 and 8,*
- *Deployment phase: TRL 9.*

Based on the TRLs for each phase and the phases presented in Figure 17 at the moment of 2014, the TRLs of the reactors were determined. However, some small changes will be made to update the TRLs based on 2014 data to current values. TRL results of both methods are presented in Table 3. The updated TRL values are determined based on the following reasoning. Looking at the Advanced Reactors Information System (ARIS) [68] most reactor designs part of the SCWR, GFR and MSR are still in the conceptual design phase. It can therefore only be concluded that these reactor types are still in the development phase and for this reason were given a TRL of 4-6. The TRLs for the SFR and LFR, based on the data of Figure 17, seem appropriate to current reactor developments and were therefore not changed. For both reactor types there are already reactors under construction, or in operation, at large conventional reactor level (for example; LFR: BREST, SFR: BN-series [69]). In addition, historically these reactor types been tried on maritime vessels, although implementation was not successful [70] [71]. A final change will be made towards the TRL of the VHTR. The TRL of the VHTR, based on Figure 17, is lower than expected looking at the current developments for the VHTR. The predecessor of the VHTR (the High-Temperature Gas-cooled Reactor (HTGR)) has already been successfully operated for land based applications. For example, the High Temperature Test Reactor (HTTR) is currently in operation in Japan [72] and the HTR-PM is currently within the latest stages of construction in China [68]. It could be that the TRL of the VHTR is lower due to the fact that a big distinction is made between the developments of the HTGR and VHTR. It could be that the TRL of the VHTR is lower than expected due to the fact that the aim for operating at temperatures above 1000°C is not realised. However, the HTGR shows that the realisation of lower output temperatures is closer than stated in Figure 17. In addition, it seems that most reactor designs applying an HTGR or VHTR construction make no distinction between these two categories (ARIS [68] defines them as gas cooled reactors). It was therefore decided to increase the TRL of the VHTR to 7-8, as the influence of the HTGR is included within this reactor type.

Table 3: Technology readiness level for gen. IV reactors

Reactor type	TRL [56]	TRL adjustment
SFR	7-8	7-8
LFR	7-8	7-8
VHTR	6-7	7-8
SCWR	6-7	4-6
GFR	5-6	4-6
MSR	3-4	4-6

Based on the TRLs of different gen. IV reactors, as presented in Table 3, it was decided that the SCWR, GFR and MSR are not of interest due to their low TRL. Still, further research could consider these reactor types if significant progress is made, as some of these reactor types are of interest for maritime implementation [15] [19]. This initial selection therefore determines that the following four reactor technologies will be investigated:

1. Pressurized Water Reactor (PWR) (gen. II, III and III+),
2. Very High Temperature Reactor (VHTR) (gen. IV),
3. Lead-cooled Fast Reactor (LFR) (gen. IV),
4. Sodium-cooled Fast Reactor (SFR) (gen. IV).

2.4.2.2 Criteria assessment

To identify the most suitable reactor type for maritime implementation among the four selected options, an investigation will examine the operational characteristics of each reactor. A criteria-based assessment will enable a comparison across reactor types. These criteria are divided into four main categories: overall performance, dynamic performance, safety and maritime feasibility. Each category includes several sub-criteria, which will be explained before assessing each reactor type.

Overall performance
The overall performance of a reactor type is crucial, as it provides insights into which reactor might be most suitable for maritime implementation. This can also indicate which reactor type(s) companies may find worthwhile for investment and further development. To evaluate this criterion, factors such as economics, efficiency, and application versatility will be examined. Economics are essential, as economic feasibility has historically posed significant challenges to (maritime) reactor implementation. High efficiency reduces waste for a given power output and allows for lower reactor output to achieve the same electrical power. Finally, versatile applications increase the reactor's potential for various implementations. A multipurpose reactor type could leverage the advantages of collaboration across multiple companies and sectors, thereby accelerating its development.

Dynamic performance
To achieve the power transients required in naval applications, a reactor optimized for dynamic performance could be advantageous. To assess this dynamic capability, the load-following range and ramp rate will be examined alongside susceptibility to reactor poisoning. The load-following range indicates the power levels at which the reactor can operate relative to its full power, while the ramp rate shows how quickly the reactor can transition between these levels. Susceptibility to reactor poisoning reflects how potential poisoning might impact reactor operation. If the reactor is highly susceptible, negative reactivity could limit the occurrence of enough fission reactions, potentially leading to reactor shutdown. As explained in Section 2.2.2.3 this is mostly an issue for thermal reactors.

Safety
Safety is another critical criterion, as the reactor must ensure the safety of both crew and environment, not only during normal operation, but also in accident scenarios and during maintenance. To evaluate this criterion, neutron spectrum, pressure and temperature levels, and design aspects will be assessed. Here, a fast neutron spectrum is considered less safe due to the increased complexity of reactor control. Additionally, elevated pressure or temperature levels decrease reactor safety, as it must rely on robust containment and high-temperature materials that could fail. Finally, design aspects like passive systems that enhance safety in emergencies and the use of dangerous materials will also be investigated. While no single sub-criterion alone deems a reactor type unsafe, excessive levels across multiple criteria will determine a reactor unsuitable for implementation.

Maritime feasibility
The final criterion for reactor selection is maritime feasibility. Since most nuclear reactors are designed for land-based applications, successful implementation to a maritime environment is not guaranteed. For a maritime reactor, minimizing weight and volume is essential, as available space on ships is limited, and excessive weight can lead to reduced speed and manoeuvrability, as more power is required to maintain performance. As only information is available about the sizing and weight of reactor pressure vessels, a comparison will be made between these different RPVs related to their power output. Additionally, the reactor type must offer a sufficient amount of SMR designs within the appropriate power range. Based on selected ship types, SMR designs below 50 MWe were deemed acceptable. Even if a reactor performs well in other criteria, it cannot be considered suitable for near-term maritime implementation if it only operates effectively at large power outputs.

2.4.3 Reactor investigation

2.4.3.1 Pressurized Water Reactor

At the end of the year 2022, just over 70% of all operable reactors (307 out of the 437 worldwide reactors) were pressurized water reactors (PWR) [49]. Besides, historically almost all nuclear driven ships have implemented a PWR as reactor type [14]. This not only shows the importance of this technology for the current nuclear sector, but also indicates a lot of experience has been made operating this type of reactor (at sea). PWRs operate within a thermal spectrum and apply UO_2 as fuel material although sometimes a MOX fuel structure is applied [68]. In Figure 18 a general concept of a PWR can be seen. Here, heat is transferred to a steam generator by pressurized water. A pressurizer, present within the primary circuit, controls the system pressure to ensure enough water stays liquid. The steam produced in the second loop will be directed to the turbine generators to produce electricity. It is then cooled in the condenser and continues as inlet water for the secondary loop [73]. PWRs currently in operation produce a coolant outlet stream of 315-330°C and due to these lower outlet temperatures, the efficiency of this reactor is lower than gen. IV reactors, ranging between 25-35% for SMR designs [74].

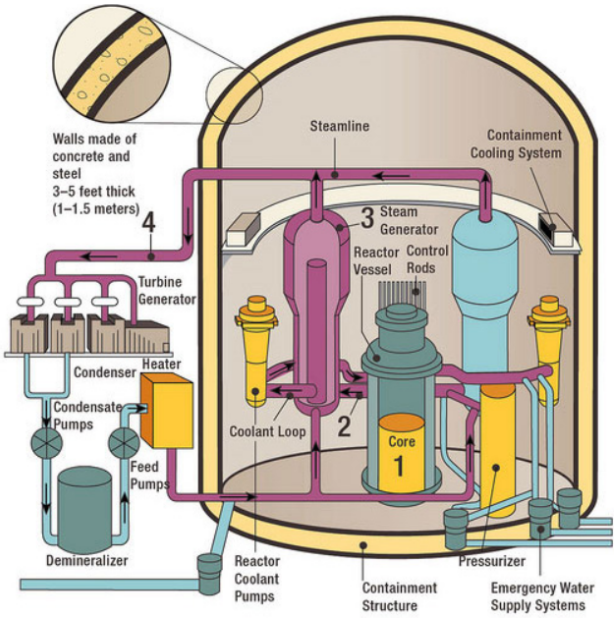

Figure 18: General concept of the PWR [73]

As the PWR contains multiple reactor designs for maritime purposes, the load following range and ramp rate are improved compared to land-based reactors. In general for PWR SMRs a load following range of 20-100% is applicable [45] [75] [76] [77], but some specific maritime models could operate within the 10-100% range [76]. The most common ramp rate for a PWR is 6%/min [45] [76] [77], but specific maritime reactors could reach 10%/min [45].

As most PWRs use ordinary water, and as this is a non-toxic medium, it does not bring concerns about worker exposure to hazardous materials and also simplifies maintenance operations. On the contrary, PWRs operate under high pressures, and the reactor coolant pressure ranges conventionally between 15-16 MPa [68]. This could result in issues when leakage occurs or when damage is inflicted during combat situations. On the other side, operational safety tests and decades of successful operation across multiple different PWR installations, show that this technology is reliable and safe for operation.

In Appendix A3 the sizing and weight values can be seen for specific PWR reactors. Based on the average value of PWR below 50 MWe, the following average sizing and weight values were selected: 12.5 m^3/MWe and 5.4 tonne/MWe. In addition, it is shown that for maritime applications the relative sizing is lower than land-based power plants, as this is 5.7 m^3/MWe.

There are multiple PWRs created in the SMR size range. In total 29 SMRs are currently designed applying PWR technology, of which 8 are specifically designed for maritime purposes. Of these reactors 8 designs range within the desired power ranges of the selected vessels [45].

2.4.3.2 Very High Temperature Reactor

The very high temperature reactor (VHTR), part of the gen. IV reactors, is the next step in the development of high-temperature gas-cooled reactors (HTGR). The VHTR is a graphite-moderated reactor operating on the thermal neutron spectrum [56] focused on maximizing safety and thermal efficiency, the latter by having a high outlet temperature. This high temperature ensures it can operate a hydrogen production plant, visible in Figure 19, and that it can be used to generate electricity at high efficiencies [55] [56]. It is therefore deemed a reactor type that contains significant economic improvements compared to PWRs [78]. In addition, the high outlet temperature and hydrogen production possibility could also be of interest for the decarbonization of the industry sector, a sector deemed hard to decarbonize due to the required heat at high temperatures.

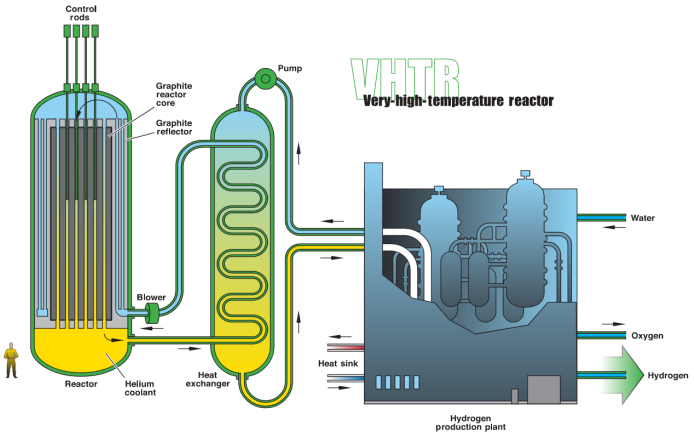

Figure 19: General concept of the VHTR [56]

The VHTR has two typical reactor configurations, namely: the pebble bed and the prismatic block (see Appendix A2 for a concept design) [56]. There is a difference between these two configurations regarding the shape of the fuel geometry, but the technical basis is for both configurations the same. It has a graphite core structure and low power density [56]. The heat created in the core is transferred by helium to the secondary cycle. Here, another working medium drives a turbine for generating electricity or produces hydrogen.

The fuel used in the VHTR is the earlier mentioned TRISO fuel, also for SMR designs [45]. Within this TRISO particles most of the time UO_2, is used, but there are also designs applying MOX and UCO [68]. The TRISO fuel is especially designed to function in the high operating temperatures of the VHTR as it can withstand temperatures up to 1600°C [45]. Regarding the fuel cycle is the VHTR able to support alternative fuel cycles such as U-Pu, Pu, MOX and U-Th [56] even regarding SMR designs [45].

The VHTR can supply heat over a range of core outlet temperatures between 700°C and 850°C [45] [56], but future designs could even produce outlet temperatures of more than 1000°C [56]. This high outlet temperature also results in higher efficiencies compared to PWRs. Efficiencies are stated between 40-50 % for large power SMRs [45] [74], but for smaller power SMRs the efficiency lowers to 33-45% [45]. The operating pressure of specific reactor designs differ between the 4-9 MPa.

There is limited information available about the load following capabilities of a VHTR. Only a few specific designs present the load following range; the XE-100 and the PBMR are between 40-100%, whereas the SC-HTGR can achieve a range of 20-100% [45] [76]. It is therefore assumed that in general the VHTR can achieve a 30-100% load following range. The ramp rate also differs between these designs, as the XE-100 achieves 3%/min [77] and the SC-HTGR and GTHTR300C achieve 5%/min. However, the Holosquad (Holosgen) achieves a significantly faster ramp rate, equal to 10%/min. It is therefore assumed the general ramp rate of the VHTR is the average of these four, which is 6%/min.

The VHTR is an inherent and passively safe reactors, because it has a low power density coupled with the high heat capacity of graphite. In some cases a reactor cavity cooling system (RCCS) is applied, which is capa-

ble to avoid core melting due to overheating as the RCCS is capable of passively removing heat from the RPV with radiation and (natural) convection techniques [79]. However, the high temperature of the VHTR could result in material issues, which has been the reason several alloys are created for high temperature environments. Noteworthy is that most materials contain a high chromium weight fraction for oxidation resistance. At elevated temperatures, these materials are able to form a chromium rich oxide on their surface, which protects around corrosion [80]. The radiation dose for the workers operating a VHTR is very low due to the inert coolant helium and corrosion issues are limited. Furthermore, operational safety tests on existing smaller versions of HTGRs, have been performed successfully making it feasible for operation [81].

In Appendix A3 the sizing and weight values can be seen for specific VHTR reactors. Based on the average value of these reactors the following sizing and weight values were selected: 37.8 m^3/MWe and 16.3 tonne/MWe for VHTR SMRs having a power output lower than 50 MWe. This is significantly higher than conventional PWRs, which is expected as the VHTR has a lower power density for enhanced safety features. It should be noted that these values are based on only 4 specific reactor models and actual values could therefore differ significantly.

There are multiple HTGR/VHTR created in the SMR size range. In total 20 reactors are designed applying HTGR/VHTR technology, of which 5 are so called microreactors. Of this reactor 11 designs seem appropriate for the desired power range. [45]

2.4.3.3 Lead-cooled Fast Reactor

The Lead-cooled fast reactor (LFR) is a member of the gen. IV nuclear reactors and an overview is presented in Figure 20. It is a fast neutron reactor applying molten lead or lead-bismuth as a coolant medium. This way it can achieve high outlet temperatures, resulting in that the LFR can be used for efficient electricity production but also for industrial heating processes. In addition, the LFR can also be used as a breeding reactor for converting fertile materials into fissile materials [56]. The LFR was top-ranked among the other gen. IV reactors regarding sustainability, due to its closed cycle, and proliferation risk, due to employing a long life core [82]. Applying lead as coolant, the reactors can operate on low-pressures of 1 bar [68] while still ensuring very good thermodynamic properties. In a pool or loop configuration, the liquid lead flows through the reactor core, transporting the thermal energy produced by fission reactions to a heat exchanger. A secondary loop drives a turbine for electricity generation. [56]

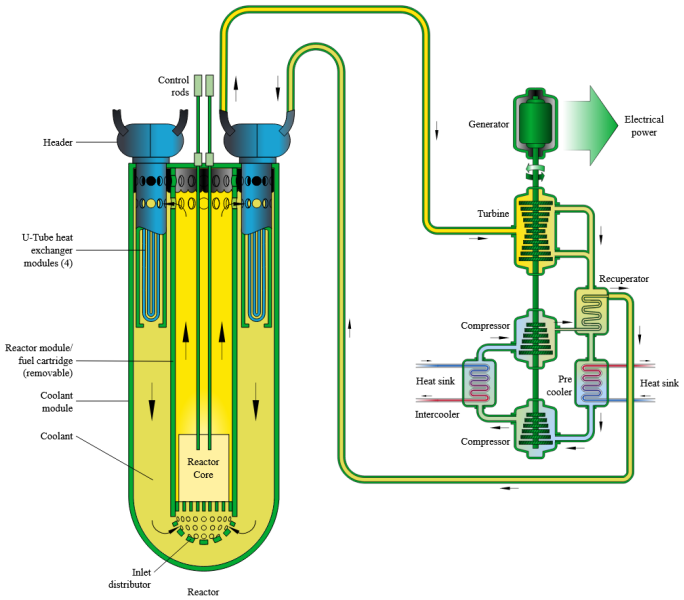

Figure 20: General concept of the LFR [56]

LFRs can apply a wide range of fuel types, applying conventional UO_2, or MOX, but also fuel types like UN (uranium nitride) or PuN (plutonium nitride) [68]. The coolant outlet temperature belonging to an LFR ranges between the 480-540°C [45] [74], although a few specific reactor designs presented within ARIS [68] indicate the range is wider, ranging between 390-650°C. This high outlet temperature results that designs above 100 MWe can achieve efficiencies of 35-47%, but SMR designs have an efficiency of 30-35% [45] [74].

The LFR is deemed the reactor type with the best overall load following capabilities compared to other SMR types [75], but the load following range of these reactors differ significantly between specific designs. The W-LFR has a load following range between 65-125 % [68], while the LFR-AS-200 has a load following range of 20-100% [68]. Ismael et al. [75] even state a range of 0-100% can be achieved. They also state a ramp rate of 10% min can be achieved [75], which corresponds with the ramp rate of the W-LFR [68] [45].

An important feature of the LFR is the enhanced safety that results from the choice of molten lead as a chemically inert and low-pressure coolant [56]. Still, lead is a toxic coolant, so protections are needed for workers when dealing with spills, especially during maintenance [81]. In addition, lead has a high melting point (330°C) so freeze prevention will be a necessary part of the design [81]. During maintenance of the reactor this high melting point should be still realised, which resulted in issues for the Russian Alfa-class submarine. Coolant activation could also result in the production of radioactive toxic polonium-210 [81].

In Appendix A3 the sizing and weight values can be seen for specific LFR reactors. Based on the average value of these reactors the following sizing and weight values were selected: 8.56 m^3/MWe and 5.58 tonne/MWe for LFR SMRs having a power output lower than 50 MWe. It should be noted that these values are based on only two specific reactor models and actual values could therefore differ significantly. There are several LFRs created in the SMR size range. In total 8 SMRs are designed applying LFR technology, but only three are in the operating range for the selected vessels [68] [74].

2.4.3.4 Sodium-cooled Fast Reactor

A sodium-cooled fast reactor (SFR) is a fast reactor type part of the gen. IV reactors. Multiple SFRs have been operated successfully, especially by Russia, and this technology has also been applied on a submarine, although not successfully, by the USA. Prior SFRs have been shown to be operable, but the capacity factors were very low due to operation issues [81]. SFRs have been seen as a promising technology regarding actinide management, reusing spent reactor fuel and utilizing the U-238 resources at earth [82] [83], but only if overall economics are improved [82] which are deemed significantly worse than PWR SMRs [78]. The SFR operates on the principle of using liquid sodium as a coolant within a closed-loop design. In this system, liquid sodium circulates through a primary reactor pool, which can be seen in Figure 21. The sodium absorbs the heat of the reactor and transfers this through a heat exchanger to another working medium, which eventually drives a turbine for electricity generation [56] [81].

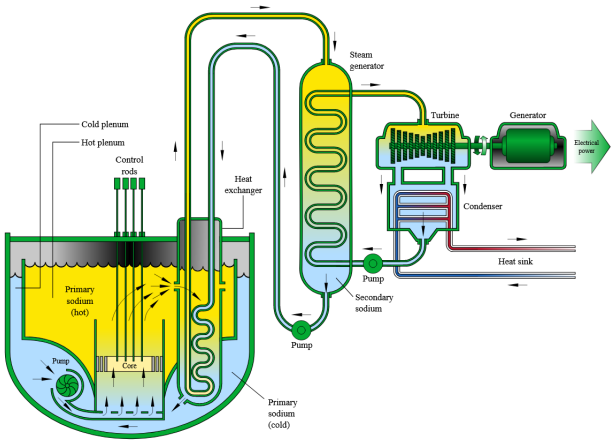

Figure 21: General concept of the SFR [56]

SFRs can apply MOX as fuel type, but also apply a U-zr (uranium-zirconium) fuel type [68]. It is possible for fast neutrons in the reactor to efficiently breed fissile material from fertile material, this way contributing to a sustainable and efficient nuclear energy system [56] [81].

Operating on sodium, it ensures the SFR can have a high power density while operating at low pressures between 1-6 bar [56]. The outlet temperature of the reactor ranges between the 475°C and 550°C [68] [45] [56]. This higher outlet temperature, compared to PWRs, results in higher efficiencies of 30-35% for SMR designs [45].

There is limited information available about the load following capabilities of a SFR. It is stated that the 4S SMR can achieve a 0-100% load following range [68], but the load following range of the BN-800 (2100 MWth) is given as 17-100% [82]. Ismael et al. [75] state that SFRs can operate with a load following range of 20-100% and it is therefore assumed the general load following range is 15-100%. Ismael et al. [75] state the ramp rate of an SFR is equal to 1-2%/min and as no other information was available this ramp rate was selected.

While no oxygen is present in the reactor's environment, this way preventing corrosion, sodium reacts chemically with air and water resulting in dangerous sodium water reactions (SWR). It therefore requires a sealed coolant system for additional protection [56] [83]. In addition, sodium also reacts with CO_2 if the reaction temperature is around 600°C resulting in an auto ignition reaction. Although this reaction is less intense than reactions with water or air, it still lowers the safety of adding a potential supercritical carbon dioxide power conversion cycle [83]. Engineering solutions have adequately addressed both of these concerns at conventional SFRs around the world [81] by for example applying a nitrogen or helium gas Brayton cycles as power conversion method [83], but concerns arise when operating this technology in a maritime environment.

In Appendix A3 the sizing and weight values can be seen for specific SFR reactors. Based on the average value of these reactors the following sizing and weight values were selected for SFR SMRs below 50 MWe: 92.6 m^3/MWe and 8.6 tonne/MWe. It should be noted that these values are of one specific reactor model and actual values could therefore differ significantly. This limited information is the result of the existence of only 4 sodium type SMRs of which 3 designs are of interest of the selected naval vessels [45] [74].

2.4.3.5 Overview nuclear reactor types

Table 4: Overview of the investigated nuclear reactors. * = limited data available (at SMR level)

Reactor type	PWR	VHTR	LFR	SFR
Overall performance	+/−	++	+/−	+/−
Economics*	+	++	+/−	−−
Efficiency at SMR size [%]	25-35	33-45	30-35	30-35
Application versatility	−	++	++	+
Dynamic performance	+/−	+/−	++	+
Load following range [% of FP]	20-100	30-100	20-100	15-100*
Load response rate [%/min]	6	6	10	2*
Susceptibility to reactor poisoning [-]	High	High	Low	Low
Safety	+	+	−	−
Neutron spectrum [-]	Thermal	Thermal	Fast	Fast
Primary circuit pressure [MPa]	15-16	4-9	0.1	0.1-0.6
Primary circuit temperature [°C]	315-330	700-850	480-540	475-550
Design aspects [-]	+/−	+	−	−−
Maritime feasibility	++	+	+/−	−−
Weight for SMR < 50 MWe [tonne/MWe]	5.4	16.3*	5.58*	8.6*
Sizing for SMR < 50 MWe [m^3/MWe]	12.5	37.8*	8.56*	92.6*
SMRs designs [-]	29	20	8	4
SMRs within desired power range [-]	8	11	3	3
Ranking	2	1	3	4

In this analysis four reactor types were investigated: the pressurized water reactor (PWR), very high temperature reactor (VHTR), lead-cooled fast reactor (LFR) and sodium-cooled fast reactor (SFR). Each of these reactors have potential for maritime purposes, but only one will be selected. In Table 4 an overview is given of the investigated criteria and the results for the respective reactor type.

For the two fast reactors, the LFR and the SFR, both have been tried for implementation on naval vessels, but in both cases this was not successful. Looking at Table 4 it seems that reactor dynamics are better than conventional PWRs, as the load following range is wider or similar, load response rates are higher for the LFR and fast reactors are less susceptible to poisoning. In addition, the higher efficiency and potential for multiple application purposes, compared to PWRs, indicate their interest. However, the safety of these reactors is lower as the LFR uses molten lead, which is toxic and brings additional maintenance and operational issues. The SFR uses sodium, which could create a fire when it reacts with air or water. In addition, compared to the PWR and the VHTR, limited information is available about these reactors, economics are (likely) worse and there are fewer SMRs in development at the moment, resulting in the conclusion that both fast reactors are not ready for maritime implementation. Both fast reactor were therefore deemed as not optimal for maritime environments.

Looking at the PWR, this is the most used reactor type for conventional and maritime reactors, resulting in a lot of real-world operational experience. Not only would this improve the implementation and design phase, but it also means operational safety standards can be met with an acceptable amount of risk. On the other hand has the VHTR not been implemented for maritime purposes, but its safety is theoretically better due to a lower pressure environment, helium as inert cooling medium and the potential of a passive cooling system. The economics and efficiency are also better for the VHTR, which is partly the result of its higher outlet temperature. In contrary, the dynamic power behaviour for the PWR is slightly better than the VHTR. This difference is negligible when realizing that maritime PWRs give special focus on dynamic power behaviour, and a maritime design of a VHTR could improve these values. Regarding sizing and weight is the PWR the most optimal for implementation for maritime applications, but here again an aim for implementing gen. IV technologies on vessels could lower their relative sizing and weight.

In summary, the PWR and VHTR reactors are closely matched in operational capabilities, with valid arguments supporting each option. However, as a gen. IV reactor, the VHTR is designed to offer improvements in multiple areas, and ongoing advancements may address its current limitations compared to the PWR. By focusing on maritime adaptations, designers could further enhance the VHTR's dynamic performance and optimize its size and weight to come closer to the performance of the PWR. Given that the VHTR either meets or exceeds the PWR in most other criteria, it is the preferred choice for this research. This selection would not only enhance operational capabilities, but also promote strategic autonomy. Furthermore, with its potential applications across various sectors, the VHTR offers promising opportunities for cross-sector collaboration, which could accelerate its development and improve short time feasibility.

2.5 Power conversion units

The heat created by a nuclear reactor cannot be used directly for propulsion or auxiliary loads. To convert this heat to electrical energy, power conversion steps must be applied for creating useful energy. Power conversion can be performed using different types of thermodynamic cycles. At first two common conversion cycles, the Rankine and Brayton cycle, will be investigated. Here, a comparison will be made between common different mediums available for power conversion which are air, helium, nitrogen, steam and supercritical carbon dioxide. Based on several criteria like sizing, efficiency and load following, a selection will be made which conversion cycle is the best option for a maritime nuclear reactor.

2.5.1 Rankine cycle

2.5.1.1 General cycle operation

The Rankine cycle is a thermodynamic cycle, which converts heat into mechanical energy. It is used worldwide mostly as a steam cycle in coal, gas, geothermal, nuclear and solar thermal power plants [84]. To ensure heat is converted into mechanical work, the Rankine cycle has four main steps; compression, heat addition, expansion, and heat rejection. These steps can be seen in Figure 22 in which the T-s diagram is visible. In this figure the 4 main steps of an ideal Rankine cycle can be seen as [84]:

1. Isentropic compression (1-2), putting water under pressure by a pump without adding or removing heat.
2. Isobaric heat addition (2-3), converting water into steam by adding heat from an energy source.
3. Isentropic expansion (3-4), converting thermal energy in mechanical work by expanding steam in a turbine.
4. Isobaric condensation (4-1), converting the steam back into water by removing heat through a condenser.

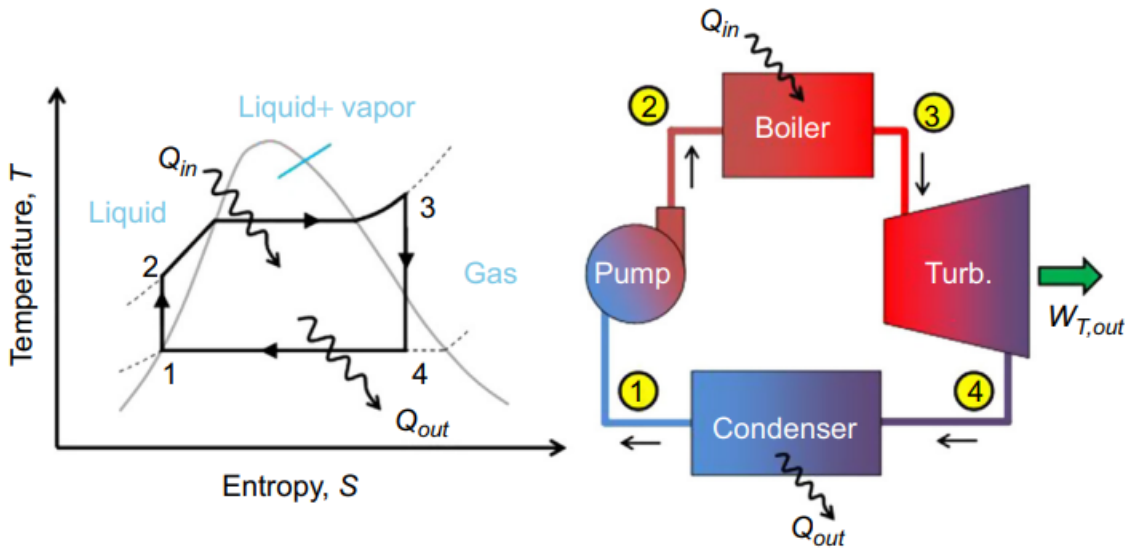

Figure 22: T-s diagram and component overview of a Rankine cycle [85]

Instead of steam is it also possible to use organic fluids for power conversion, which occurs in the so-called Organic Rankine Cycle (ORC). The heat source of the cycle is in general the determining factor for the cycle selection, as ORCs are suitable for low/medium temperature and small heat sources, while steam is the best option for medium/high temperature and large heat sources [86]. The reason for this is the low critical temperature of commonly used organic fluids (T<300°C). In addition, the high temperature heat source will easily cause decomposition of most regular organic fluids [86]. This leads to the conclusion that the ORC is not deemed an attractive option for the high temperature conditions of a nuclear power conversion cycle, which operates at higher temperatures above 300°C. However, the ORC is commonly used for effectively transporting waste heat, this way improving overall cycle efficiency. It is therefore that the ORC has already been implemented on ships to convert low temperature waste heat into power [86]. It could therefore be a beneficial addition, but is less relevant as a conversion cycle for the primary heat source.

2.5.1.2 Current use

Currently, most nuclear power plants in operation use PWRs or BWRs, which apply steam turbines for producing electricity. Nuclear turbines usually operate with main steam pressures between 4.9 to 6.9 MPa and because of this relative low steam pressure the volume flow per power output is up to 5 times larger than of fossil fired power plants, resulting in larger components for nuclear power plants [84]. In addition, the efficiency of conventional nuclear power plants is lower than for example coal burning plants, which is the result of the lower output temperatures belonging to conventional nuclear plants [84]. The Rankine cycle is still a commonly used power conversion cycle in SMR designs [68] [87]. As PWRs operate at lower outlet temperatures than gen. IV reactors, and steam cycles still outperform helium and supercritical carbon dioxide cycles in terms of efficiency at lower output temperatures, Rankine cycles are still favoured for SMR applying PWR technology [87]. Operating experience is also a factor in selecting a Rankine cycle [83].

2.5.2 Brayton Cycle

2.5.2.1 General cycle operation

The Brayton cycle is a thermodynamic cycle that is mostly used in modern gas turbine engines, such as those used in aircraft propulsion, power generation, and some industrial applications. With respect to nuclear reactors is the Brayton cycle the most studied for application at gen. IV reactors. The cycle can be run as an open system if it operates on air, but can also reuse the exhaust gases in a closed cycle. The thermodynamic steps belonging to a Brayton cycle can be seen in Figure 23 and contain the 4 following steps:

1. Isentropic compression (1-2), the compressor compresses the gases without adding or removing heat.
2. Isobaric heat addition (2-3), under constant pressure the gases are heated by an external energy source.
3. Isentropic expansion (3-4), high temperatures gases expand in a turbine to produce mechanical work.
4. Isobaric condensation (4-1), gases enter a heat exchanger, which removes heat and lowers the temperature. In the open Brayton cycle the gases are rejected into the atmosphere.

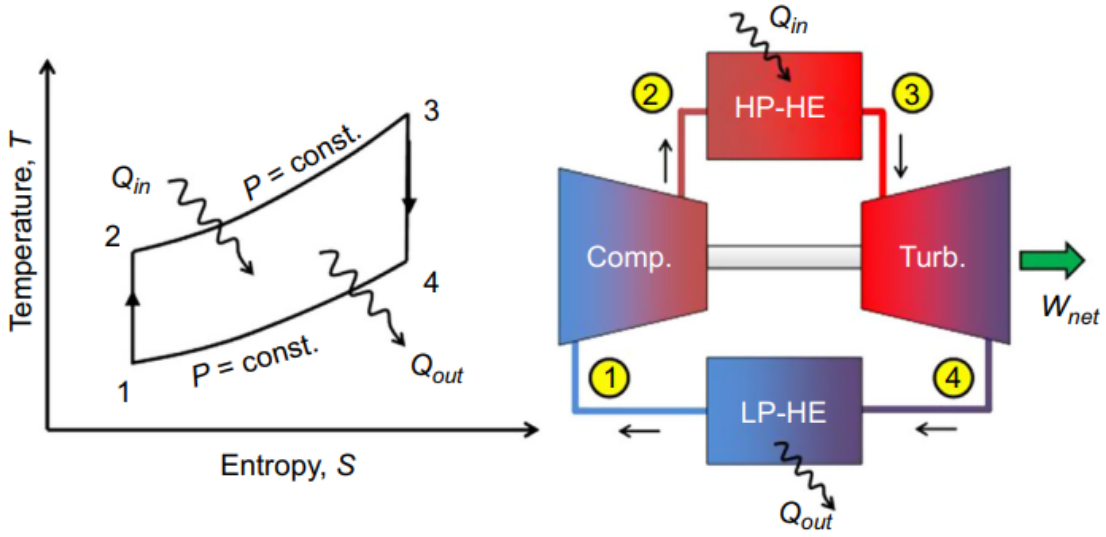

Figure 23: T-s diagram and component overview of a Brayton cycle [85]

2.5.2.2 Open and closed cycle

The Brayton cycle can be implemented as an open or closed cycle configuration. The open Brayton cycle involves the continuous intake of fresh air from the environment. The closed Brayton cycle operates within a closed loop in which the working fluid undergoes the same steps as the open cycle, but it is contained within the system. This means additional systems must be added for cooling the medium, but results in more control over the working conditions and specific type of fluid.

The open Brayton cycle does not seem appropriate for power conversion of a nuclear power plant implemented in a maritime environment as this cycle configuration is limited to using air as working fluid. The environment of a maritime vessel contains high amounts of moisture and traces of salt [15], resulting in an additional need for air filtration systems to ensure no fouling and corrosion occurs [88]. In addition, the environment of a vessel ensures sufficient cooling capacity is present, minimizing the beneficial aspect of an open Brayton cycle which does not require cooling capacity [15]. The use of different working fluids with favourable thermal and transport properties compared to air, makes the closed cycle also the favoured option [88]. Finally, specifically for naval vessels, the open cycle ensures thermal signatures are elevated due to the outlet of heated air, increasing the chance of detection by enemy thermal sensors. It was therefore decided that for a naval vessel the open Brayton cycle is not the preferred option.

2.5.2.3 Working media

The most common type of fluids for the Brayton cycle are air, helium, nitrogen and supercritical carbon dioxide (sCO_2) [88]. As air is mainly used in the open Brayton cycle, which was not deemed beneficial, air will be neglected. The other three working fluids will be shortly covered.

Helium is an ideal gas, which makes it a beneficial fluid for reactor cooling under high temperature conditions [88]. Especially in the case of a direct driven power conversion cycle connected to a nuclear reactor, helium could increase overall safety regarding radiation issues within the whole power conversion cycle. As it is a non-corrosive and non-toxic gas, the maintenance and operational lifetime of components is beneficial compared to other working fluids [89]. Furthermore, helium has a high thermal conductivity and can therefore realize efficient heat exchange within power cycles or reactor cooling [88] [90]. However, helium is costly and not abundant at earth and could therefore result in feasibility issue regarding economic effectiveness or large scale implementation. Other disadvantages are high leakage rate and the need for multiple turbomachinery stages for an effective cycle design [88].

Nitrogen is another medium proposed in Brayton cycles [83] [91] [92]. As the composition and properties of nitrogen are similar to air, the experience of conventional air gas turbines increases its technological feasibility [88]. Furthermore, as nitrogen is inert, it is proposed as a power conversion cycle for SFRs to prevent a dangerous sodium water reaction [91] [92] [93]. However, the poor heat transfer properties and high pressure losses, result in lower cycle performance compared to other working fluids [88]. Furthermore, nitriding and embrittlement of materials at high temperatures limit the potential for implementation in an HTGR/VHTR [88].

Supercritical carbon dioxide (sCO_2) systems for converting heat to power are of interest due to their high efficiency [88] [94] [95] [96], operational flexibility [94] and low volume to power ratio [88] [95] [96]. Besides, CO_2 is abundant, low cost, non-toxic, non-flammable and thermally stable at high temperatures [88] [97], making it a feasible option for heat to power conversion from high temperature heat sources [88] [94]. Although CO_2 is more chemically stable than steam, CO_2 is not an inert gas like helium and therefore corrosion issues may occur, especially under high temperature operating conditions [88] [89].

2.5.2.4 Current use

The open air Brayton cycle is already in operation in many fields like aerospace and power industries, proofing it is a working and matured technology [98]. It is also proposed as power conversion cycle for land-based PWR SMRs [98]. On the other hand, there is a lot of research into closed cycles especially for gen. IV reactors and multiple SMRs designs aim to implement such a cycle. The company OKLO is developing the 1.5 MWe SFR Aurora, which will apply an sCO_2 Brayton cycle as power conversion system [98]. The GT-MHR, part of the HTGRs, applies a helium gas turbine system [89]. Another HTGR, the GT-HTR also applies a helium gas turbine in which a recuperated cycle without intercooling was applied [89]. The SFR ARC-100 applies an sCO_2 Brayton cycle in its design, as this lowers the risk of a SWR [83].

2.5.3 Direct and indirect drive

Besides the type of conversion cycle, there is also a difference between a direct and indirect drive option. During the direct drive option, the fluid entering the turbomachinery is directed through the reactor core, while in the case of an indirect drive a secondary cycle is present. In this case a heat exchanger separates the primary reactor cycle and the secondary turbomachinery cycle. The difference between the direct and indirect drive can be seen in Figure 24.

The indirect drive is favourable due to the flexibility of different working fluids between the primary and secondary circuit. As the direct approach is limited to the medium used for cooling the reactor, limitations occur for the fluid type within the power conversion cycle. Implementation of the direct approach would also result in fluids entering the turbomachinery directly after leaving the reactor core, which could result in radiation issues along the total system. Although an inert medium like helium could be used for cooling, reducing the risk of radiation within the whole system, safety risks increase with the direct option. Probably the whole power conversion system should be shielded against the risk of radiation leakage, increasing the size and weight of the power plant. The indirect approach could however also produce safety issues related to heat exchanger puncture [99] and therefore the need for shielding the whole power conversion cycle must first be investigated more properly. Finally, with the direct approach, the turbomachinery should be able to operate in circumstances where the fluid is irradiated, which could impact its performance or maintenance needs.

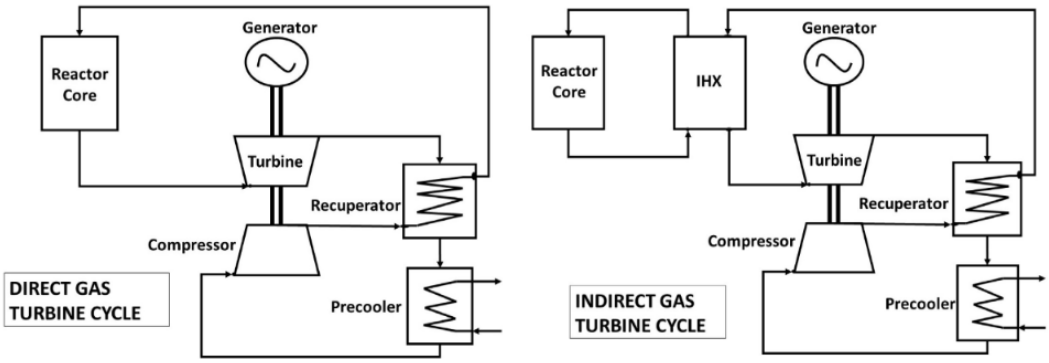

Figure 24: Direct and indirect drive for a nuclear power conversion cycle [88]

Overall, to ensure flexibility in conversion medium and to ensure safety for the whole power conversion cycle, the choice was made to implement an indirect cycle approach for the power conversion cycle. Still the direct approach connected to a nuclear reactor has been investigated in literature [100] [101] and should not be excluded in further research as it could be that the direct cycle is beneficial regarding dynamic power behaviour due to operating without an additional heat exchanger (which lowers the total thermal mass).

2.5.4 Efficiency

2.5.4.1 Impact medium and outlet temperature

The efficiency of the different power conversion cycles is of importance for economically viable power systems, reducing the amount of nuclear waste needed for power production and lowering the required power output of the reactor as more efficient energy is realized. From a thermodynamic perspective, higher operating temperatures are desirable to achieve a higher thermal to electric conversion efficiency [102]. This is also presented in Equation 5, which shows the theoretical equation for the Carnot efficiency. In Figure 25 the efficiencies can be seen for the steam, helium (He) and supercritical carbon dioxide (sCO_2) cycles compared to the turbine inlet temperature. Another possible medium in the Brayton cycle is nitrogen. The efficiencies of this cycle have been investigated and Ahn et al. [83] added this efficiency in a similar figure. There it seems that nitrogen cycles operate slightly more efficient than helium cycles at temperatures below 650°C and slightly below helium cycles above turbine inlet temperatures of 650°C.

$$\eta = 1 - \frac{T_{cold}}{T_{hot}} \tag{5}$$

Furthermore, in Figure 25 it can be seen that the sCO_2 cycle has an overall higher efficiency than the helium cycle, while the steam cycle has the lowest efficiency at higher temperatures. In the same figure the general pressures and operating temperatures from several reactor types can be seen. Looking at the reactor technologies, only the VHTR is capable of operating in the inlet turbine temperature range that belongs to the highest cycle efficiencies. After the VHTR, the highest cycle efficiencies are realised for the MSR and GFR, but in general the gen. IV reactors all operate at higher efficiencies ranges compared to conventional PWRs. However, it must also be noted that when operating in the temperature range of PWRs, at lower outlet temperatures below 400°C, the superheated steam cycle still outperforms helium and sCO_2 cycles regarding efficiency [87].

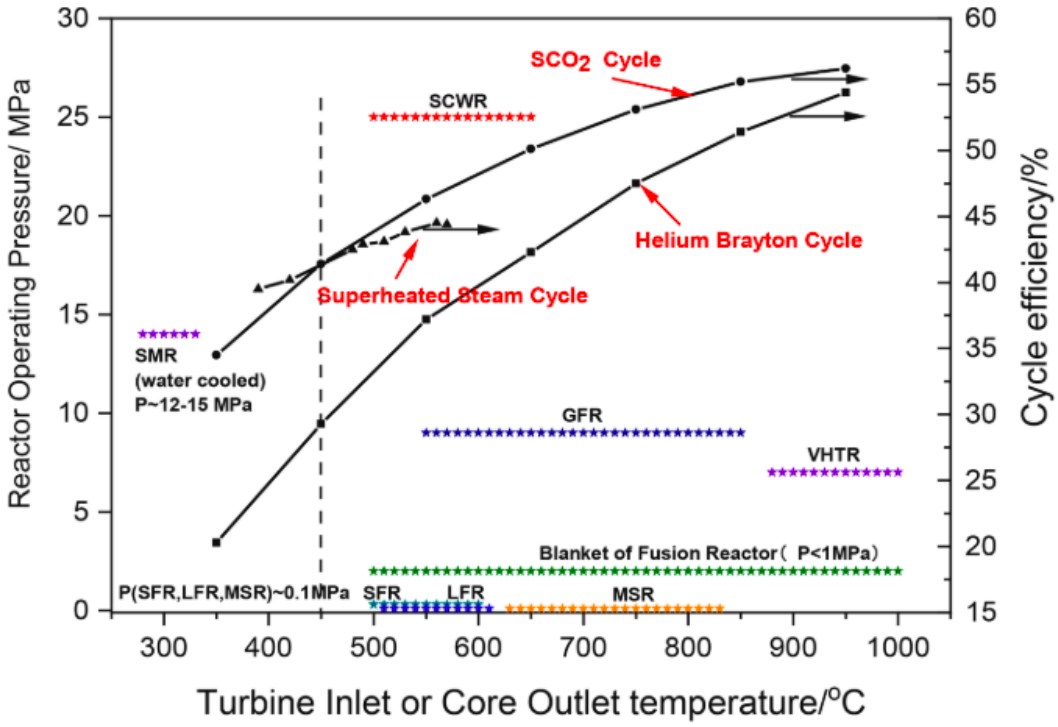

Figure 25: General cycle efficiencies for steam, helium and supercritical carbon dioxide compared to the turbine inlet temperature and operating ranges of different reactor technologies [103]

2.5.4.2 Part-load operation

Gad-Briggs et al. [104] investigated the efficiency during part load operation of a helium Brayton cycle when coupled to a gen. IV nuclear power plant, specifically a GFR and VHTR. The results are presented in Figure 26 and show that operating at a part load of 50% reduces the efficiency by 10%. However, a more drastic efficiency loss is observed when part load drops to even lower percentages, as at 15% full power the cycle efficiency is only 20%. As naval vessels often operate for extended periods at low part loads, as presented in Section 2.1, this efficiency drop impacts the total efficiency of the vessel. If it is desired to maintain a high efficiency during the operational lifetime of the vessel, it would be advisable to strive for the highest full power efficiency, as this would result in a better overall efficiency performance at part load.

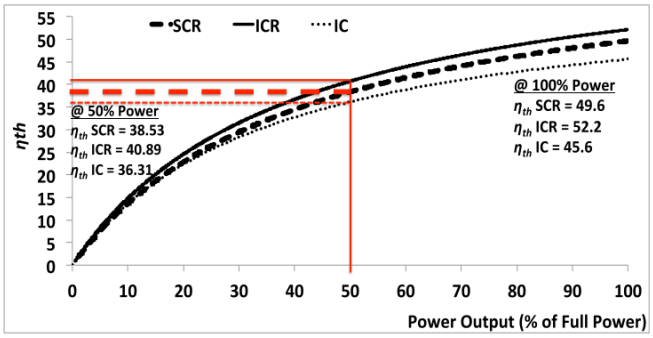

Figure 26: Part load efficiency belonging to three different helium Brayton cycles: a simple cycle recuperated (SCR), intercooled cycle recuperated (ICR) and intercooled cycle without recuperation (IC) [104]

2.5.4.3 Power sizing considerations

Another consideration impacting the efficiency is the absolute power output of the cycle. As the power of the conversion cycle increases, the total cycle efficiency increases mainly due to turbomachinery efficiency increases [83] [89]. The major reason for the turbomachinery efficiency reduction due to smaller power sizes is because of the increased losses due to irreversibility in the turbomachinery [83]. The irreversibility generated in the turbine is related to the turbine's surface and the power generation is related towards the volume of the turbine. Therefore, as the total power output of the cycle increases, more volume is needed to produce this power. This results in a lower surface to volume ratio, which reduces the irreversibility generation and will result in an increased turbomachinery efficiency [89] [98]. Ahn et al. [83] researched the decrease in efficiency related to the power size for a 150 MWe power conversion cycle belonging to an SFR. Figure 27 shows that the sCO_2 cycle still achieves the highest efficiency, but it also lowers the least in efficiency when a small power conversion cycle is applied [83]. However, the calculations of Ahn et al. [83] are not fully explained and a 5% isentropic efficiency drop was identically assumed for all cycle types. In addition, they investigate specific cycle layouts, where the recompression cycle is investigated for the sCO_2 cycle, but a reheating and intercooling combination is investigated for the helium cycle. This could influence the outcome of their research. Still, it is of importance to investigate the efficiency drop due to smaller turbomachinery sizing, as power sizes belonging for maritime applications are even lower than the investigated power output in Ahn et al. [83].

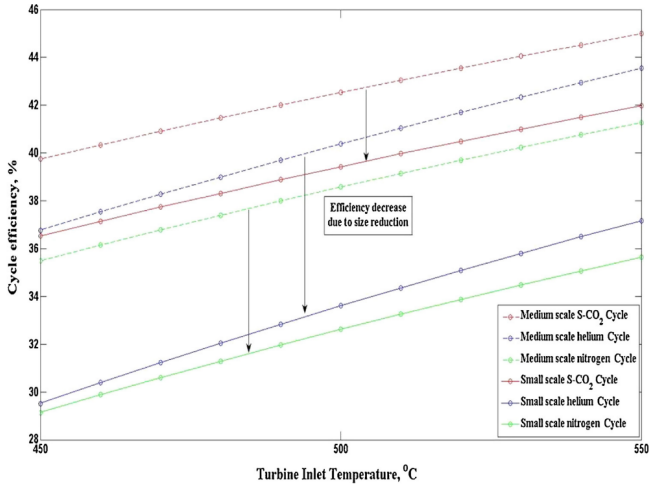

Figure 27: Efficiency decrease due to smaller power conversion cycles for supercritical carbon dioxide, helium and nitrogen [83]

2.5.5 Turbomachinery sizing

It is important to compare the different conversion cycles based on their sizing, as limited space is available on ships. In Figure 28 a general size comparison can be seen for steam, helium and supercritical carbon dioxide turbines [98] [103] [105]. The volume difference, especially between the steam and the other types of turbines, is significant and should therefore be considered before implementation on a (naval) vessel. The exact volume difference between the different cycles is not certain as the sCO_2 is deemed 4 times smaller [87], or 10 times smaller [101] than the steam Rankine cycle. It is however certain that a Brayton cycle, and especially an sCO_2 conversion cycle, is much smaller than a steam Rankine cycle. Although Figure 28 can be a little exaggerated, it does represent clearly which cycle is smaller in size compared to the others.

Yoon et al. [106], state that the total volume of turbomachinery needed for an sCO_2 conversion cycle is 1.4 m^3, while connected to a 330 MWth PWR. This small turbomachinery sizing is also noticeable within the design of KAIST, presented in Figure 29. Here, a 36 MWth PWR is connected to an sCO_2 cycle, which produces 12.5 MWe. All the components for power production are present within Figure 29, showing only a container size of 7.0x3.7x3.8 meter is required. Overall it can only be concluded that, looking purely on a size perspective, an sCO_2 power conversion cycle would be the most beneficial for maritime applications.

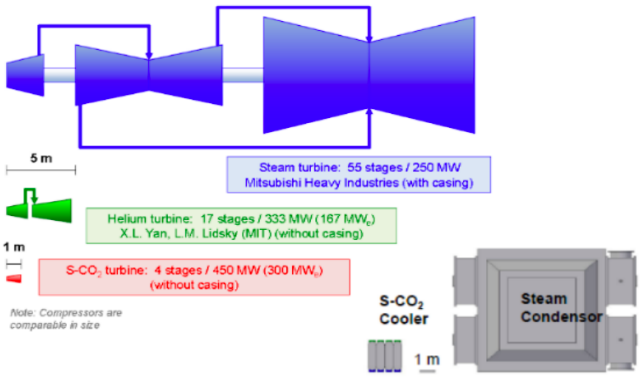

Figure 28: Size comparison between turbines for steam, helium and supercritical carbon dioxide [98]

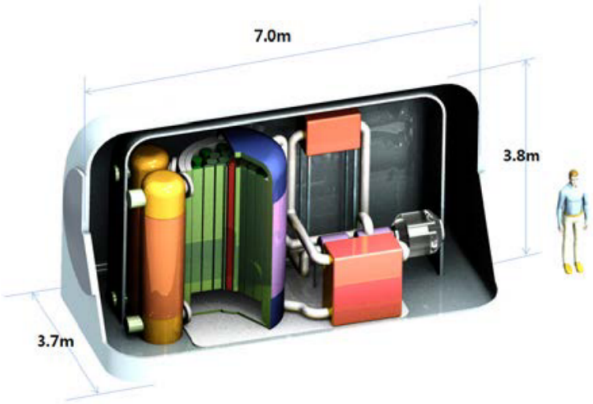

Figure 29: Cycle design of a 36 MWth PWR and 12.5 MWe sCO_2 cycle [107] [108]

2.5.6 Load following

2.5.6.1 Rankine cycle

Salazar et al. [109] investigated the operational flexibility of several power conversion methods, including coal power plants applying a steam Rankine cycle. Ramping rates of these power plants are in the range of 0.5-8%/min [109], but ramp rates between 3-6%/min are also mentioned for steam cycles [84]. In addition, Salazar et al. [109] showed that start up times for coal power plants are also significantly slower than gas turbines. The specific startup time depends strongly on how long the shutdown time was prior to the start, as lower metal temperatures result in longer start-up times [109]. However, Spelling et al. [110] suggest that start up times can be reduced if the steam turbine can be kept hot during idle periods. Spelling et al. [110] state that heat blankets will have the most significant impact on keeping a higher temperature in the casing of the turbine, this way reducing the thermal stress during cold startup time.

2.5.6.2 Brayton cycle

Ming et al. [101] analyse the transient possibilities of a 5 MWth direct sCO_2 conversion cycle. The results of applying a combined inventory and bypass control, further explained in Section 2.9, can be seen in Figure 30. Although the reactor output stayed constant, the system still achieved a net power output of 0 MWe as all the produced heat by the reactor is taken away by the cooler, and all the power generated by the turbine is used to drive the compressor [101]. The results show that a 0% power output can be realised after a transient duration of 920 seconds, resulting in a power decrease speed of 6.52%/min [101]. Bong et al. [95], report for a similar case a 5%/min power transient, but this occurred when applying inventory control. The simulations of Ming et al. [101] also show that the power increase takes more time before it achieves full power, as the full transient duration takes 3200 seconds, achieving a transient speed of 1.88%/min. However, as can be seen in Figure 30 this slower transient is determined by the power increase after already achieving a 60% of full power level, indicating that the transient speed is not linear.

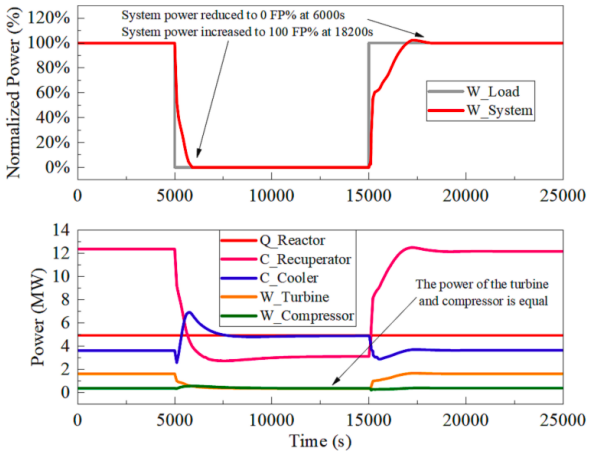

Figure 30: Normalized power output during a load change of 100–0-100 % [101]

Carstens [111] investigated a 600 MWth nuclear indirect sCO_2 power conversion cycle. The transient possibilities of this cycle were investigated for a loss of load (LOL) scenario, of which the results are presented in Figures 31 and 32. Due to the generator loosing its power almost immediately a power imbalance occurs over the shaft, resulting in an increase in shaft speed. The bypass control added to this cycle will however result in a decrease in turbine power output, this way stabilizing the shaft speed after a few seconds. The results show that even in a loss of load scenario, the shaft speed increase can be limited to a 30% increase, with appropriate bypass control, suggesting fast power transients can be achieved under normal operating conditions. However, these results predict faster power transients than presented by Ming et al. [101] and Bong et al. [95]. This contradiction could be (partially) explained due to the difference in cycle configuration, as Carstens [111] applies an indirect sCO_2 cycle, which could be dynamically beneficial from the direct cycle configuration.

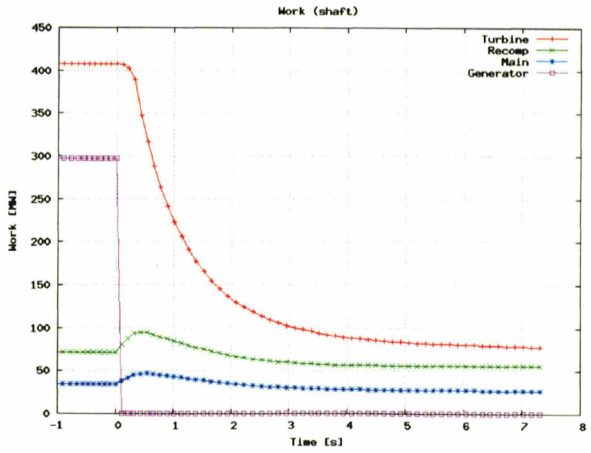

Figure 31: Power transients of several components during a loss of load scenario [111]

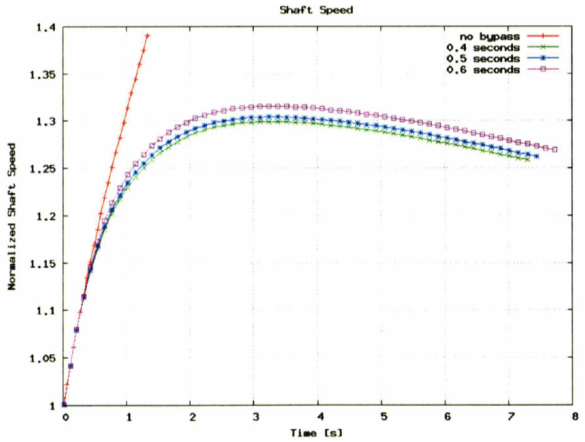

Figure 32: Shaft speed during a loss of load scenario for different bypass reaction times [111]

2.5.7 Cycle selection

There are many power conversion cycle types for converting the thermal heat of a nuclear reactor into feasible electrical energy. The steam Rankine cycle is commonly used for nuclear power plants, but it is compared to the Brayton cycle larger, has a lower efficiency at high temperatures and does not contain dynamical benefits. It was therefore not selected as appropriate power conversion cycle for nuclear maritime reactors. Still, the organic Rankine cycle could be an attractive addition for efficiency improvement regarding the use of waste heat.

The Brayton cycle was selected as the most useful power conversion cycle, but this cycle contains multiple specific configurations. At first, the open Brayton cycle was not deemed an attractive option for naval vessels as it limits flexibility of the fluid choice to air and increases thermal signatures of the naval vessel. In addition, the direct drive option was also not deemed beneficial as this increases safety risks due to radiated fluid entering turbomachinery, increases the amount of shielding needed as the turbomachinery components must be shielded, lowers the flexibility choice of a cycle fluid to the cooling fluid used in the reactor and probably results in lower power transients. The indirect closed Brayton cycle was therefore selected as power conversion cycle.

The fluid used in this cycle impacts the overall cycle performance drastically. Nitrogen is not of interest as it lacks significant cycle improvements compared to air and is not effectively applicable as power conversion cycle for high temperature reactors. Between supercritical carbon dioxide (sCO_2) and helium, sCO_2 seems to be the favoured cycle medium for an HTGR/VHTR due to an improved efficiency and smaller cycle sizing. In addition, sufficient research into this fluid type is performed, especially in combination with nuclear reactors, which makes it the most beneficial fluid medium for a nuclear power conversion cycle on a maritime vessel.

2.6 Supercritical carbon dioxide power conversion cycle

2.6.1 Thermodynamic properties

Supercritical carbon dioxide cycles are of interest due to two main reasons. At first, the fluid properties near the critical point of CO_2 (30.98 °C and 73.77 bar [91]) ensure that an efficient and small cycle can be designed [85] [94], which is the result of having a liquid-like density and a gas-like viscosity near the critical point [94]. Secondly, the nearly ambient critical temperature of CO_2 ensures that sCO_2 power cycles can be used for multiple different heat sources, like waste heat recovery or nuclear power [85]. In Figure 33 the T-h diagram of several isobars of CO_2 are presented near the critical point. Not only is the supercritical region present, the thermodynamic behaviour of CO_2 is also visible. It is shown that the enthalpy changes significantly near the critical point of CO_2, while temperature stays relative constant. Equation 6 presents the calculation for the specific heat capacity, which indicates that near the critical point the specific heat capacity increases drastically. This low slope near the critical point, and thus high specific heat capacity, results in a compression process where energy can be added to the fluid while incurring a little increase in fluid temperature [85]. This reduces the amount of work required to increase the pressure of sCO_2, therefore improving the overall cycle efficiency.

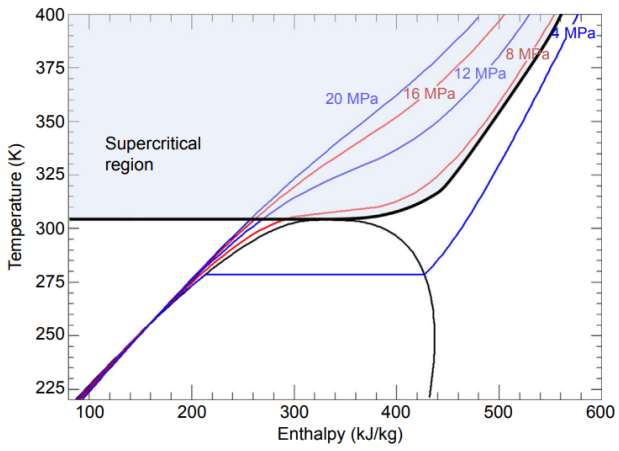

Figure 33: T-h diagram of several isobars near the critical point of CO_2 [85]

$$C_p = \left.\frac{\delta h}{\delta T}\right|_{\mathrm{p}} \tag{6}$$

All other fluids are also able to operate in supercritical regions, but these regions are far from operating conditions that can be achieved within conventional cycle limits [85]. The main advantage of CO_2 compared to these fluids is that its critical temperature is near ambient temperature. For comparison, water turns supercritical above a temperature of 374.3 °C and a pressure of 22.1 MPa [112], which increases the complexity of achieving and operating in its supercritical region.

2.6.2 Turbomachinery considerations

2.6.2.1 Shaft configuration

There are different types of shaft configurations possible for a power conversion cycle of which an overview has been presented in Figure 34. In general, the turbomachinery shaft configurations can be classified into three types [113]: 1) The most simple and compact configuration is the so called Turbine-Alternator-Compressor (TAC). This single shaft configuration represents the compressors, turbine and an alternator/generator as coaxial [85]. 2) Turbine-Generator and Turbine-Compressor (TG-TC). This shaft configuration uses one shaft for a turbine driving the generator while another shaft is used for a turbine driving the compressors [113]. 3) The last configuration, the so called "TG-C", uses a turbine for driving the generator while a motor drives the compressor with another shaft [113]. For simplicity, the TAC shaft configuration was chosen for implementation as this is the simplest and widely used [85], but other shaft configurations could be beneficial for implementation on a naval vessel. Further research must be done towards comparing the (dis)advantages of different shaft configurations for optimal performance.

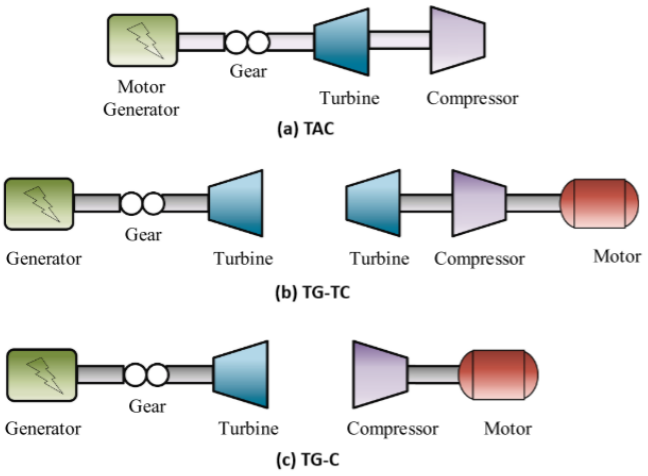

Figure 34: Typical shaft configurations [113]

2.6.2.2 Axial or radial turbomachinery

For the selection of turbomachinery at first a choice must be made on the type of turbomachinery of which a distinction can be made between centrifugal/radial or axial flow turbomachinery. Brun et al. [85] present a range for different turbomachinery characteristics in Figure 35. It shows, that for power levels of a naval vessel it is not recommended to implement axial flow compressors. Although single stage axial turbines could be beneficial according to this figure at power levels around 10 MWe, the question arises if this would be advisable. Brun et al. [85] state that it is expected that the most efficient configuration for the turbine and recompressor transitions from radial to axial at 30 MWe and 100 MWe, respectively. For the main compressor it is expected that at all power scales a radial compressor is used as this compressor type is better for regions where gas properties are closer to the critical point [85]. As the maximum required power output for a naval vessel is around 28 MWe, as described in Section 2.1, it was decided to implement a radial design for the main compressor, recompressor and the turbine.

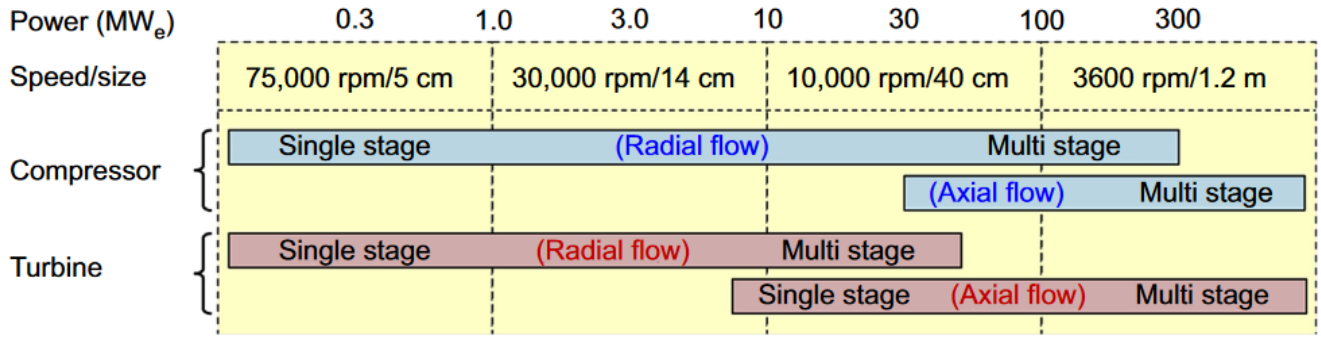

Figure 35: General sizing and performance characteristics of sCO_2 turbomachinery [85]

2.6.3 Cycle considerations

To improve the overall cycle performance of a Brayton cycle, additional components can be added. The most common components added to a power conversion cycle are a recuperator, a reheater and/or an intercooler. It is possible to add multiple of these components to a cycle, or use a combination of several components for the total cycle configuration. This final cycle configuration all depends on the specific working conditions of the cycle and therefore many possible cycle configurations are possible. Brun et al. [85] state that the indirect recompression and reheat cycle are the most efficient cycle configurations for sCO_2 power conversion cycles, while Dostal [105] argues that the recompression cycle is more beneficial due to its simplicity. In addition, Dostal [105] states that re-heating more than one stage is economically unattractive, limiting the possibility of improving the efficiency of the cycle. Although there are many different sCO_2 cycle configurations considered in literature, it seems the recompression cycle is the most considered due to its large efficiency and relative simplicity [85] [105] [111] and was therefore selected for this research.

2.6.3.1 Recompression cycle

The most common sCO_2 Brayton cycle is the recompression cycle, which is presented in Figure 36. This cycle is based on the most basic sCO_2 cycle, namely the recuperator cycle. As this cycle only applies a recuperator, it has a lower efficiency than cycles implementing additional intercoolers or reheaters [87]. However, by adding an additional compressor, and belonging recuperator, the efficiency can be increased without increasing complexity drastically [87]. Dostal [105] and Carstens [111] state that the recompression cycle is the most efficient cycle architecture for an sCO_2 cycle, while still retaining simplicity. It was argued that inter-cooling is not attractive for this type of cycle as it offers a very modest efficiency improvement while increasing complexity. This lack of efficiency improvement is the result of the pinch point problem in sCO_2 [88]. The pinch point problem occurs at the point in the heat exchanger where the temperature difference is the smallest and in this region the heat transfer of sCO_2 is less effective compared to other Brayton cycles.

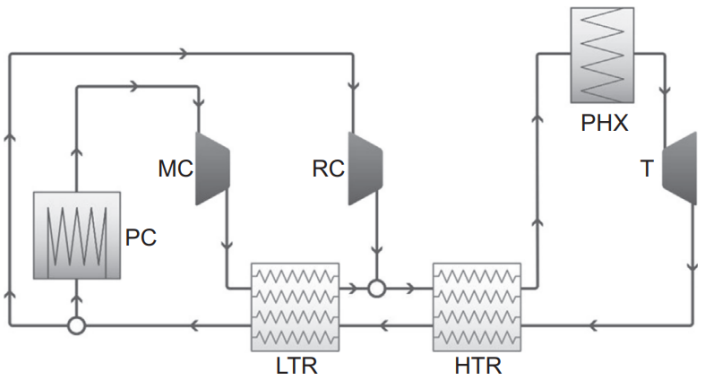

Figure 36: Overview of the recompression cycle [85]

However, the recompression cycle is probably not suitable for all types of purposes as for waste heat recovery the recompression cycle is unsuitable due to the relatively small specific work, the slight temperature difference in the heater and the lower heat recovery from the exhaust gas [97]. In addition, for fossil fueled power plants the cycle is also not beneficial due to small temperature window used for heat addition. Still, for the purpose of a nuclear reactor, it is a favoured cycle configuration as this contains a large temperature window in which heat is added to the secondary cycle [85] [105].

2.6.3.2 Efficiency considerations

For an sCO_2 cycle, it is stated that an optimized cycle efficiency can be achieved at a pressure ratio between 2.4 and 2.8 [87] [92] [106] [114]. As the pressure ratio of the system is related to the turbomachinery design, it is of importance to select turbomachinery with the right pressure ratio. Turbomachinery with a smaller pressure ratio can still be favoured, but than a multi-stage compression or expansion process should be considered. Furthermore, the split ratio is also an important parameter in the recompression Brayton cycle. As it can be used to balance the heat capacity on both sides of the LTR, it is an important parameter in improving cycle efficiency [92]. It is defined as the amount of mass flow rate going through the main compressor compared to the total mass flow rate entering the turbine [92]. For an efficient sCO_2 Brayton cycle, the split ratio ranges around 0.65-0.7 [92].

2.7 Heat exchangers

2.7.1 Printed Circuit Heat Exchanger

The physical size of a Brayton cycle can be roughly estimated based on the heat exchanger volume which occupies the major portion of the system [83]. This indicates the extreme importance of a heat exchanger when implementing a Brayton cycle on a nuclear vessel where space is limited. There are multiple types of heat exchangers available, but the Printed Circuit Heat Exchanger (PCHE), visible in Figure 37, is widely adopted as suitable heat exchanger choice for power conversion cycles [91] [113] [116], especially for next generation nuclear reactors using cooling mediums as helium or sCO_2 [111] [117] [118] [119]. In these power conversion cycles the PCHE is mostly used for the recuperator, intercooler, heater and cooler, although for the last two sometimes shell-and-tube heat exchangers are used [113]. From a size perspective, the recuperator is responsible for the most amount of heat exchanger volume needed in a conversion cycle [91] and the effective design of a PCHE could lower the needed volume compared to shell and tube heat exchangers as the PCHE only needs 20% of the volume for the same heat load capabilities [118]. In addition, the PCHE is able to withstand high pressures and high temperatures [111] [113], while still being highly effective [91] [117]. Due to their lower mass and higher heat transfer coefficients compared to shell-and-tube heat exchangers, PCHEs also have faster dynamic responses [119]. Overall, the PCHE is the best suitable heat exchanger type for a nuclear power installation implemented on a maritime vessel.

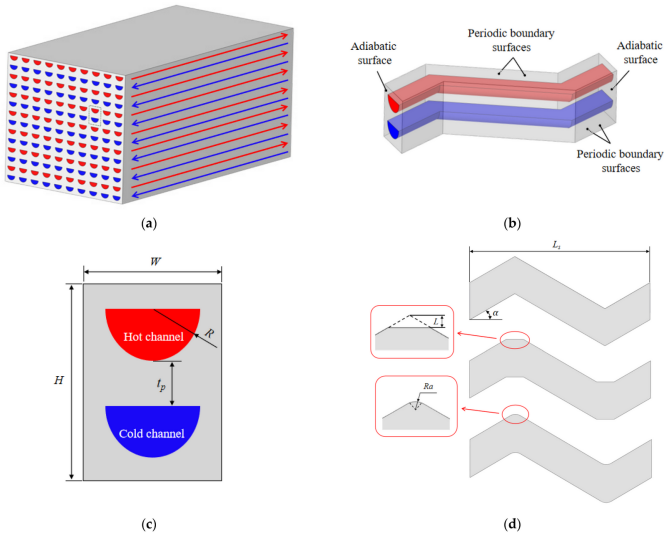

Figure 37: Schematic structure of a printed circuit heat exchanger with a wavy channel geometry [115]

The PCHE contains multiple layers stacked on each other and each plate contains multiple semicircular channels for the hot and cold fluids, this way ensuring optimal heat transfer due to increased heat transfer area. There are different types of PCHEs which can differ based on the channel type. The most basic PCHE contains straight channels for the hot and cold channels. Other advanced concepts can apply wavy channels which are more superior to straight channels PCHEs as wavy channels increase heat transfer performance. However, the pressure drop along these advanced channels increases compared to straight channels [117]. Still, if the pressure drop is manageable in the overall power conversion design, wavy channels can reduce the amount of heat exchanger volume needed as the overall heat transfer coefficient is twice as high compared to straight channels [120].

2.7.2 PCHE sizing and operating conditions

Limited information is available about the practical design of PCHEs, but Bennett et al. [121] investigated the parameter ranges of typical PCHEs. The most important parameters for straight channel PCHEs are stated in Table 5 and the belonging geometry areas can be seen in Figure 38. In addition, they state that the two most common material types are Stainless Steel 316L and Inconel Alloy 617 [121]. Olumayegun et al. [91] also state that there are limits to the overall module size of a PCHE as it is possible to produce modules with sizes up to 900 mm in width, 900 mm in height and 2500 mm. Regarding PCHEs the length is parallel with the flow direction of the fluids. In the study of Olumayegun et al. [91] a nitrogen power conversion cycle belonging to a 500 MWth SFR was investigated. Here, the recuperator needed 63 modules, resulting in a total heat transfer duty of 1100 MW and a total heat exchanger volume of 119 m^3. In the thesis of Chen [120] a 600 MW PCHE applying helium was modelled, which resulted in a needed total volume of 52 m^3.

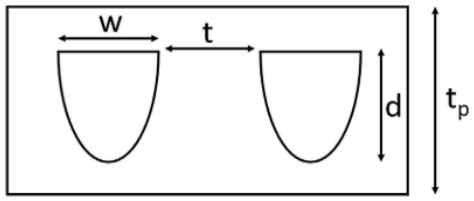

Figure 38: Design geometry for corresponding values belonging to a PCHE [121]

Table 5: Range values for the different parameters for straight channel printed circuit heat exchangers [121]

Parameter	Low value	High value
Channel depth (d) [mm]	0.6	1.5
Channel width (w) [mm]	0.8	3
Wall thickness (t) [mm]	0.6	1.2
Plate thickness (t_p) [mm]	1.6	2.4
Hot inlet temperature [K]	430.15	852.15
Cold inlet temperature [K]	303.15	558.71
Hot inlet pressure [MPa]	2.2	9.26
Cold inlet pressure [MPa]	6.5	22.5
Channel mass flow rate [kg/s]	0.000017	0.00034

For a nuclear power conversion cycle implemented on a naval vessel, the printed circuit heat exchanger (PCHE) is selected. Not only is the PCHE able to withstand high pressures and high temperatures, but compared to shell and tube heat exchangers needs the PCHE only 20% of the volume and also results in faster dynamic responses. Compared to straight channel PCHEs are wavy channel PCHEs beneficial regarding heat transfer. This reduces the volume needed for the heat exchanger, but wavy channels increase the pressure drop in the heat exchangers. Finally, there are design limitations regarding the production of PCHE, but it is possible to produce PCHE modules with sizes up to 900 mm in width, 900 mm in height and 2500 mm in length if desired.

2.8 Dynamic limitations of nuclear reactors

There are many aspects that influence the dynamics of nuclear reactors. As limited information is available about the dynamic characteristics of specific nuclear reactors, a general investigation has been performed towards the aspects affecting nuclear dynamics. This includes control methods for power regulations, physical aspects affecting power dynamics, thermal safety limitations and general plant considerations regarding load following.

2.8.1 Power control methods

There are many ways of controlling the power output and power distribution within nuclear reactors, and each reactor type has its own specific control methods. In addition, most reactor types apply a combination of different control methods, making it difficult to state a typical control configuration for each reactor type. Therefore, the most common control methods will be investigated, which are: control rods, soluble neutron absorbers, coolant flow rate, burnable poisons, physical mechanism for reactivity control and fuel management.

2.8.1.1 Control rods

Control rods are the most common control method for nuclear reactors [36]. As explained in Section 2.3.2.5 raising or lowering the control rods changes the criticality of the reactor. The rods are made of materials like hafnium or boron, which are materials that can absorb neutrons, preventing the neutrons from causing fission in the fuel [61]. It is however stated by Atkinson et al. [122] that control rods tend to remove neutrons from the top or bottom of the core. This affects the power distribution and uniformity of the core, and therefore the aim should be to use the control rods as little as possible. To compensate the effect of a change in power distribution by control rods, the reactor has a difference between enrichment across the length of the reactor, which in combination with the control rods ensures a more uniform power profile [122]. However, a reduced enrichment across some parts of the core reduces the overall lifetime of the core. Other control options should therefore be added to ensure a uniform power distribution while not limiting the operational lifetime of the reactor [122].

2.8.1.2 Soluble neutron absorber

Another control method, used commonly in water type reactors like the PWR, is by changing the boron concentration in the coolant/moderator. This boron concentration acts as a soluble neutron absorber and thus by increasing the boron concentration in the water more neutrons are absorbed by the boron instead of the fuel, resulting in a uniform reactivity decrease within the reactor. To reverse the effect, the water has to be treated to remove the boron, which is slow and costly and creates radioactive waste [123]. It is therefore used mainly to counteract reactivity changes due to intermediate and long term processes like fuel burn up [53] [124], ensuring excessive movement of the control rods can be avoided [53]. Although less applicable to gas cooled reactors, the concept of adding a neutron absorber to the coolant can still be used. For example, the advanced gas cooled reactor (AGR) applies CO_2 as coolant during normal operation. This reactor has a back-up safety system which injects nitrogen in the channels of the reactor core [125]. As nitrogen is a much better neutron absorber than CO_2 the amount of fission reactions taking place would lower, showing the possibility of adding a soluble neutron absorber for power control.

2.8.1.3 Coolant flow rate

Another control method is controlling the coolant flow rate by using the recirculation pumps. This controlling method is effectively implemented in some BWRs and is applied in combination with control rods. The recirculation controlling method takes advantage of the negative reactivity feedback based on the coolant temperature. As the coolant flow rate is increased, the temperature is reduced, which will increase overall reactivity

and therefore power production [124]. The opposite occurs when the cooling rate is decreased. This controlling method is suitable for load following in the power range interval of 60—100% and within this region fast ramp rates up to 10%/min can be achieved by only using this control method. Below 60% rated power, load following cannot only be realised by recirculation controlling and additional rod control is required [124].

2.8.1.4 Burnable poisons

Burnable poisons are materials like boron and gadolinium [126] intentionally introduced into the reactor to absorb neutrons without undergoing fission themselves. They can be mixed with the fuel in the form of compounds or pellets, or they can be placed in separate rods among the fuel rods [122] [126]. As the reactor operates, the poison absorbs neutrons, reducing the overall reactivity of the core. Over time, as the reactor operates, the burnable poisons are themselves "burned up" and will gradually lose their effectiveness at absorbing neutrons [122]. This allows the reactor's reactivity to increase over time, compensating for the depletion of fissile material (which induces a negative reactivity). Burnable poisons are therefore long-term reactivity control methods [53] and result that reactivity during the reactor's operating lifetime is more constant. They can also act to ensure a uniform power distribution within the reactor core. Burnable poisons compensate for the fuel depletion within the reactor, allowing other control methods to be solely used for short time power control.

2.8.1.5 Mechanical systems

Reactivity control systems of nuclear reactors could include physical mechanisms for adjusting the geometry of the core, such as mechanisms for adjusting the reflectors in the reactor. This has been investigated in for example the design of the U-battery. Due to its small annular core, the centre reflector contains the area with the highest thermal flux [126]. Physically removing the central reflector could therefore act as a variable reactivity control mechanism. Preliminary results show that by applying a variable height inner reflector, the dependence of the control rods for reactivity control due to fuel depletion reduces [126]. However, this control method increases the complexity of the reactor significantly and Atkinson et al. [126] also note that removing the inner reflector results in additional neutron leakage from the reactor.

2.8.1.6 Fuel management

The final control method used in reactor control is based on fuel management of the reactor. Some reactors contain systems which can influence the distribution of fuel within the core during operation, this way optimizing power output and managing reactivity. One of these reactors is the pebble bed reactor, part of the VHTRs. As explained in Section 2.4.3.2 the pebble bed reactor applies small pebbles as fuel. The design of the reactor allows the possibility to continuously deploy newly fresh fuel within the reactor core and by using several pebble inlet positions at the top of the core, the pebble distribution over the core can be influenced [127]. The power profile in the radial direction can be controlled by placing pebbles with different fuel enrichment at a different radial starting position [127]. Another advantage of these pebbles is the possibility of recycling used pebbles to control the power distribution while not needing burnable poison materials [127]. This can be done by placing fresh pebbles in the outer region of the core while placing recycled pebbles in the centre of the core [127]. Other reactor types may not have this flexibility during operation, but in the design phase fuel management strategies could also influence the overall reactivity within the reactor.

2.8.2 Physical aspects

Power transients of a nuclear power plant also have impact on several physical aspects of the reactor. The most important phenomena are a change in fuel, moderator or coolant temperature, the increase of fission poisoning and the fuel burnup. A well-designed reactor will have a negative reactivity feedback regarding a

temperature increase of different materials. An increase in temperature due to a power transient could therefore result in a negative reactivity feedback. As a negative reactivity impacts the power increase, this could limit the power transients of the reactor [36]. A higher concentration of fission products, like xenon and samarium, decreases the amount of neutrons that undergo fission reactions within the fuel. As a power change impacts the concentration of fission products [36] [128] it is important to limit the power change in such a way that the amount of fission products stay limited and a dead reactor is avoided. Fission products need time to decay into more stable, less affecting, fission products. This could result that after a significant power increase/decrease, the reactor needs time before it can undergo another significant power increase, as otherwise the amount of fission products could be too high to even ensure a power output from the reactor. Finally, the amount of fuel burnup also impacts the reactor dynamics, as the allowed/achievable power transient rate for reactors drops as the length of the fuel cycle increases [124]. At the start of the fuel cycle the reactor would be capable of achieving faster power transients than at the end of the cycle [124], limiting the operational capabilities of such a reactor. This could result that the refuelling time of a maritime nuclear reactor must be shortened if certain power dynamics must be achieved during the full operation time.

2.8.3 Thermal aspects

During power changes, it is important to ensure that the material within the reactor is not damaged. Maximum temperature values for materials like the fuel, cladding or coolant should be maintained during power transients to prevent material degradation or in the worst case material damage [47]. The result of a power change is that the heat through the materials and the temperature of the materials itself will change significantly. Irregular power distribution in the fuel blocks can therefore result in different operating conditions within the reactor. For example, Figure 39 presents the power distribution within a fuel block of the U-battery. As the power density within the fuel block could differ between 0.7 and 2.5 MW/m^3 the heat flux within the fuel block will not be constant [129]. Beside irregularities within the whole fuel block of a nuclear reactor, there is also a difference between the temperature distribution within the fuel elements itself. The temperature within the fuel element could differ significantly and wall temperatures are not a representation of the center of the fuel [47]. Calculating the inner temperature of the fuel elements, at a location within the fuel block that encounters the highest heat flux, is therefore essential in preventing material damage.

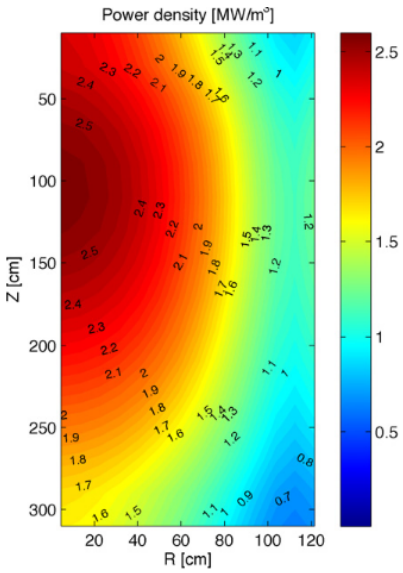

Figure 39: Steady-state power density of the U-Battery at full power [129]

2.8.4 Plant performance considerations

There are also some considerations that the operator of a nuclear reactor must consider regarding the dynamic use of a reactor. A slower ramp rate would limit the material stress and fatigue of the materials within the reactor and as a result there are lower maintenance costs and more load cycles achievable [124]. The economic impact of load following for a nuclear power plants is therefore an additional concern for dynamic power transients. Nuclear power plants that operate in load following mode could reduce the average load factor by more than 10% [124]. This is less of an issue looking at a whole nuclear power plant fleet of a country, as not all the power plants will operate in load following mode [124]. However, if the economic impact of a single nuclear power plant is determined, or if the whole fleet is operating in load following mode, then load following could reduce economical feasibility. Loisel et al. [130] argue against this and state that a load following reactor could

be capable of providing higher load factors than reactors intended for baseload operation. If the power plant would only operate on baseload, the power output would be lower than maximum power, as it is not possible to operate at full power for long operation times [130]. Load following could therefore temporarily act at higher power outputs than constant baseload operation, which could improve the overall load factor of the reactor, compensating operating at lower power outputs.

Regulations also influence the load following capabilities of a reactor. According to European regulations from 2001, reactors must be able to operate continuously between 50-100% of rated power with a 3-5%/min rate of change regarding the electrical output [124] [131]. During an emergency, the reactor should be capable of achieving a rate of change of 20%/min [124]. However, this is only allowed with fresh fuel, as when the reactor is through 90% of its fuel, it is not allowed to change significantly in operating power [123].

2.9 Power conversion cycle control

2.9.1 Dynamic control strategies

To safely and effectively control the dynamic power load on the conversion cycle, multiple control strategies can be applied. For closed cycle configurations there are in general three main control strategies which can be used (in combination) to control the cycle power output. These are bypass control, inventory control and temperature control [94] [95] [105]. The control strategies will be investigated further to understand their working and their potential benefits. Between the three main control categories, there are many different specific control strategy configurations available. Due to the large number of possible configurations, and the difference in complexity between these strategies, a general control analysis was performed.

2.9.1.1 Bypass control

With bypass control, the power output is controlled by controlling the mass flow rate through the turbine as this is directly related to the power created by the system [105]. When the bypass valve is opened, some high pressure working fluid is transferred to the low pressure side [105] resulting in a reduction of mass flow in the direction of the turbine. This not only lowers the mass flow rate through the turbine, but also reduces the expansion ratio. Sometimes the bypass flow is split into multiple streams, in which for example one of the outlet streams will be mixed at the turbine outlet and the other at the pre-cooler inlet [105], but this all depends on the specific cycle configuration and location of the bypass valve. The main advantage of bypass control over other control options is its capability to deal with rapid power changes due to fast power dynamics [105].

2.9.1.2 Inventory control

Inventory control uses a storage tank to temporarily store the working fluid from the cycle. Fluid present within the tank cannot produce power and storing fluid will thus result in a cycle power decrease. If a power increase is desired, then the working fluid can enter the cycle from the storage tanks. This control strategy ensures that pressure ratio remains relatively unchanged, and as the cycle efficiency is effected by the pressure within the system, this ensures a stable cycle efficiency during part load [105]. There are however some drawbacks for inventory control. First, additional volume is needed as storage tanks must be added to the system [105]. Secondly, system stability issues could be the result due to local pressure gradients caused by the temporary storage and return of the fluid [95] [101]. Another drawback is the finite capacity of the storage tanks, which limits the rate of power change. Once the pressure in the vessel reaches the compressor outlet pressure the power cannot be further decreased, limiting the control range of inventory control [105].

2.9.1.3 Inlet temperature control

The last control option is by changing the turbine inlet temperature. In contrary to the previous control strategies, the mass flow is kept constant across the turbine [105]. Instead, the inlet temperature of the fluid is adjusted, which can be realised by changing the reactor power output. This approach is therefore dynamically limited to the dynamics of the reactor. The change in power output level of the reactor, and the change in turbine inlet temperature, will also result in a change in other temperatures and pressures around the cycle as these are influenced by the temperature of the fluid leaving the turbine [105]. This approach is suited mainly for nuclear power plants operating at baseload, which is not the case for a nuclear power plant on a naval vessel. Solely implementing inlet temperature control as a control strategy, and therefore limiting the dynamic change of the power conversion cycle to the dynamics of the nuclear reactor, is therefore not deemed an attractive option for nuclear propulsion.

2.9.2 Comparison of control strategies

2.9.2.1 Efficiency

Each control strategy has its own specific impact on the total cycle efficiency. In Figure 40 the impact of different control strategies, on the efficiency of a helium power conversion cycle, is displayed. Bypass control, reactor outlet temperature control, or a combination of the two results in a significant efficiency decrease when operating at part load. Inventory control ensures a more stable efficiency level and only drops significantly in efficiency at part load below 40% full power. However, these results are based on a helium Brayton cycle and as CO_2 is not an ideal gas the results could differ [105]. Moisseytsev et al. [132] investigated the behaviour of different control strategies for a 400 MWe nuclear power plant using sCO_2 as working fluid. When the system operated between the 50-90% of its nominal power, inventory control maximized cycle efficiency. However, in an operating range above the 90% of the nominal power, the bypass resulted in a more suitable control strategy [132]. Overall, it seems that regarding efficiency at part load, inventory control is the preferred option.

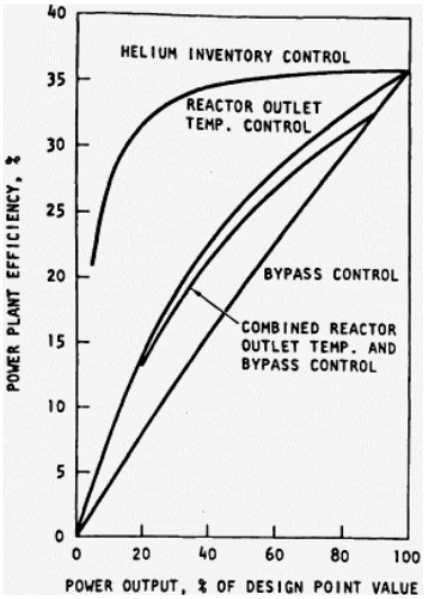

Figure 40: Impact of the control strategy on the cycle efficiency during part load [105]

2.9.2.2 Dynamic behaviour

Dostal [105] states that there is a difference between the dynamic behaviour of the three main control strategies. According to his research, bypass control is able to accomplish a 10% load step change, which neither inventory nor temperature control are capable of [105]. Temperature inlet control is limited by the change in reactor output and according to Dostal this control strategy can achieve a load rate change of 5%/min. An explicit value for the rate of change for inventory control is not mentioned, but an order of fastest to slowest control schemes is given as bypass control, inventory control and lastly temperature (reactor) control [101] [105] [111].

2.9.3 Control configurations

For the control of a recompression cycle, there are multiple configurations possible, each with its own benefits and disadvantages. An overview of common control options for a recompression cycle is presented in Figure 41. Here, the grey valves are throttle valves, used for ensuring a stable cycle operation, the red valves are bypass valves, used for bypassing a certain component and blue valves are valves used for cooling the waste heat of the cycle. In addition, an example location is given for an inventory tank. It must be noted, that this is not a fully inclusive configuration option and multiple other control configurations are present within literature [105] [111] [133]. To determine which control configuration will be selected, an initial comparison will be made between several common control configurations.

2.9.3.1 Bypass valves

There are multiple possible locations for a bypass valve, which are presented in Figure 41 as red valves. At first, a turbine bypass valve (V4) can be placed, which passes the outlet flow of the heater to the inlet of the HTR. This is a common bypass valve in Rankine cycles [111], but this valve produces a large thermal shock due to the large temperature difference around the turbine [105]. Another bypass option is between the inlet of the heater and the inlet of the HTR (V14 + V4), which is a common location for helium Brayton cycles [111]. The temperature difference between these two points is less and results in a lower thermal shock. Finally, the sCO_2 recompression cycle has the possibility of another bypass valve located between the LTR and HTR (V7). The temperature difference at this location is the smallest, as it is equal to the heat exchanger terminal temperature difference. Although this location is a favoured sCO_2 recompression cycle option, it also contains a lot of uncertainties regarding practical implementation [111].

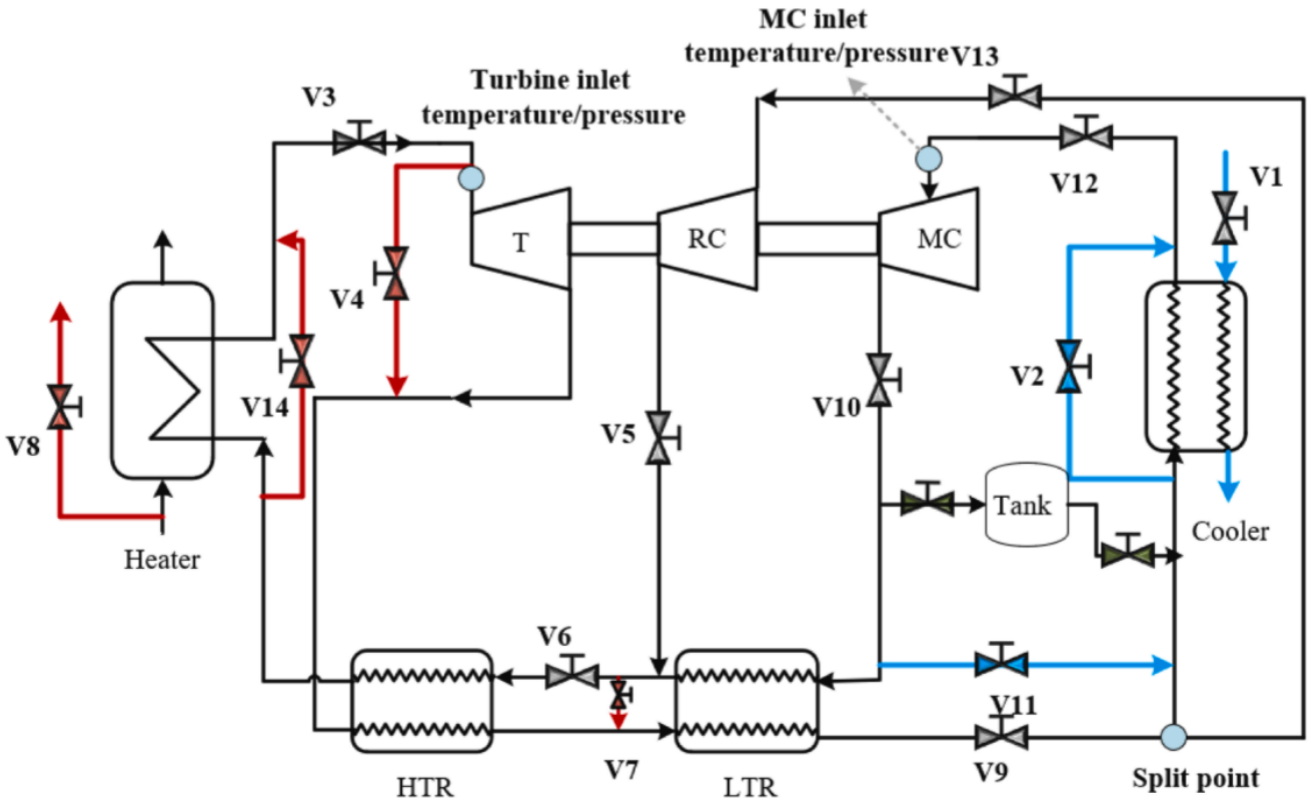

Figure 41: Control overview of a recompression cycle [113]

2.9.3.2 Inventory control

According to Dostal [105] there are two common methods of applying inventory control. In both cases the flow enters the storage tanks at the outlet of the compressor, as the inlet should be at the highest pressure point within the circuit [105]. A difference occurs between the outlet of the storage tanks [104] [105]. The first outlet option is before the inlet of the cooler [105] as presented in Figure 41, this way passing the turbine first as it will enter the compressor again. Another option would be to connect the outlet of the tank to the same point as the inlet, but this would require an additional (smaller) compressor in the system [104] [105]. Both options indicate that after storage of the fluid, the fluid must at least enter a compressor again before it can enter the turbine, ensuring the fluid keeps a high enough operating pressure.

2.9.4 Control method selection

For controlling a Brayton power conversion cycle there are in general three control strategies which are: bypass, inventory and temperature control. Bypass control is deemed faster than inventory control, which is in its place is faster than temperature control. Although bypass control is dynamically favoured, the efficiency drop at part load is significant during bypass and temperature control, while inventory control manages a more efficient power control. It is for this reason that a combination between bypass and inventory control is an attractive control choice, as this benefits the stability of efficiency from the inventory control, but also the dynamics of the bypass control. However, as this research focuses on the dynamic possibilities of a nuclear power plant, optimal part load cycle efficiency will be neglected. Therefore, looking solely at optimal cycle dynamics, bypass control is deemed the superior control strategy.

3 Nuclear power plant design

3.1 Plant sizing

In Section 2.1 it was decided that for the RNLN, the FuAD and the ATS projects are of interest for nuclear propulsion. Based on an energy analysis of similar vessel types, the important power levels are determined for these projects. Table 6 provides an overview of the power requirements for the FuAD and the ATS at some important power levels as percentage of full power (FP). These power levels all refer to the electrical power requirements due to the choice for full electrical propulsion.

Table 6: Important power values for the FuAD and the ATS

	FuAD		ATS	
Parameter	**MWe**	**% of FP**	**MWe**	**% of FP**
Max power sailing	28	100	21	100
Min power sailing	2	7.1	5	23.8
Power at max energy	8	28.6	14	66.7
Power in harbour	1.1	3.9	3.6	17.1

Based on Sections 2.4 and 2.5 the most suitable nuclear power plant for a naval vessel should contain an HTGR in combination with an sCO_2 recompression power conversion cycle. To design such installation, it is important to consider the required power levels to accurately represent a propulsion system for a naval vessel. As two vessels of interest are selected, and only one power conversion cycle can be designed for this research, both use cases must be considered for the sizing of the installation.

It was decided to implement multiple separate nuclear power plants on board of the naval vessels. Naval vessels operate long durations at low power outputs, as presented in Table 6, and the efficiency of a nuclear power plant decreases significantly at part load, as indicated by Figures 26 and 40. Multiple nuclear power plants present the opportunity to individually operate each installation at its desired power output. It could therefore be decided to shutdown a few installations and run a single installation at full power, providing the required power output at a high cycle efficiency. In addition, an increased number of separate power plants improves the redundancy of the vessel. Even if one power plant is damaged, then other installations could still provide power to the vessel, improving the vessel's resilience.

Firstly, between the FuAD and the ATS, the most amount of energy is used at power levels of 8 MWe and 14 MWe respectively. The design aim for the nuclear power plant is therefore to produce a power output between 7-8 MWe. This provides the possibility for the FuAD to operate at full power with one installation, while the ATS could use two installations at full power to produce the desired power at max energy consumption.

Secondly, the maximum power levels of both vessels should be achieved by a combined number of nuclear power plants. The choice for a 7-8 MWe power range of a single nuclear power plant results for the ATS in the need of 3 installations to provide the desired 21 MWe. The FuAD needs 4 nuclear power plants to provide at least the required 28 MWe. This increases the maximum power level of the FuAD, but this was only deemed beneficial as additional power output could be used for achieving higher ship speeds or implementing larger sensor and weapon systems.

Finally, it is not only of importance to achieve the required maximum power, but also the minimum required power. For both vessels, the minimum required power output occurs when staying within the harbour. Although it could be argued that this power consumption could be provided by the harbour energy infrastructure, it was decided to account for the worst case scenario, which means a (single) nuclear power plant should be able to provide these power levels on its own. Between the FuAD and the ATS, the lowest amount of power that is needed occurs when the FuAD is staying within the harbour, requiring a power of 1.1 MWe. It was decided that a single nuclear power plant should be able to provide 10% part load energy, as then at least a power of 1.1 MWe could be provided to the vessel.

3.2 Overall cycle design

Before a detailed design of each component is given, at first a general overview of the designed nuclear recompression cycle will be explained, which is visible in Figure 42. The recompression cycle applies a nuclear reactor (R) as heat source, using helium as working medium. To ensure sufficient pressure is realized within the primary circuit, a blower (B) is added. The primary circuit also contains a dump cooler (DCL), which can be activated or neglected with a valve (V5). The heat present within the helium will be transferred by the intermediate heat exchanger (IHX) to the sCO_2 cycle. The sCO_2 cycle applies a single stage turbine (T), but adds an additional separate compression stage, resulting in a main compressor (MC) and a re-compressor (RC). These turbomachinery are all connected to a single shaft, which also drives the generator (G). For optimal cycle efficiency, two recuperators will be placed after each compressor, resulting in a low and high temperature recuperator (LTR and HTR). A cooler (CL) must be implemented to transfer leftover heat from the cycle to the seawater. To ensure sufficient mass flow from the seawater is entering the coolers, two pumps (P) are added to the system. Finally, multiple valves have been added to the system. Here, V1-V4 are throttle valves, which are used for maintaining a safe and stable cycle pressure, while V6 is a bypass valve used for controlling the cycle power. In reality, the different components are connected with several pipes, but it is at this research phase not possible to make an estimation about the specific layout of such a system within a naval vessel. It was therefore decided to neglect the impact of pipes on the system, which is a common assumption [116] [134].

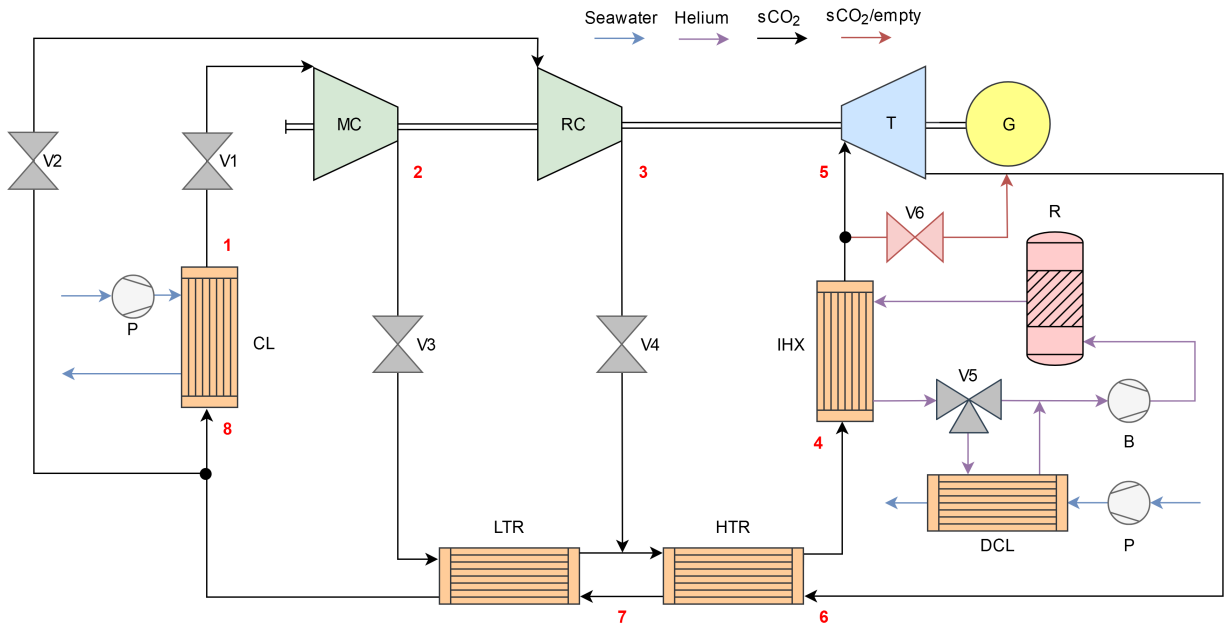

Figure 42: Schematic overview of the designed recompression cycle with a nuclear reactor

3.3 Reactor selection

For implementation of the HTGR, it is of importance, looking at the aim of this study, that the selected reactor will be within the right power range of a naval vessel, but also that enough design values are available in literature for modelling purposes. Based on Figure 25, it is expected that an HTGR in combination with an sCO_2 power conversion cycle, should achieve an efficiency between 40-50%. A desired cycle power output of 7-8 MWe, therefore results in a required thermal power output of 14-20 MWth. A potential HTGR that could provide the desired power amount is the so-called U-battery. The most publicly developed design of the U-battery contains a power output of 10 MWth [136] of which general reactor values are presented in Table 7. In addition, this specific reactor model contains enough public information for model implementation [99] [135] [136] therefore making it a feasible reactor choice for this research. A single 10 MWth reactor will not provide the required power output for naval propulsion, so it was therefore decided to combine two single 10 MWth U-battery as power source for one power conversion cycle, resulting in a 20 MWth power source for a single power conversion cycle. The two reactors will be modelled individually, but by equally splitting the fluid streams leaving the IHX, and mixing the fluid streams leaving the reactors before entering the IHX again, a 20 MWth power source design can be realised.

Table 7: Design values of the U-battery [135]. Mass flow is calculated based on an enthalpy balance at full power.

Parameter	Value
Capacity [MWth]	10
Core layout	Prismatic
Moderator	Graphite
Coolant	Helium
Fuel type	UO_2 (TRISO)
Inlet temperature [°C]	400
Outlet temperature [°C]	750
Pressure [bar]	40
Mass flow [kg/s]	5.5

The U-battery is a reactor still in its design phase and therefore different designs are present within literature [99] [136]. In Figures 43 and 44 a schematic overview can be seen of the selected design of the U-battery. Based on the design of Ding et al. [99] and the material sizing and operating conditions of Atkinson et al. [122], the vertical cross-section was created. At the reactor inlet, the helium will rise between the barrel and RPV before going downwards through the multiple coolant channels within the hexagonal fuel blocks. Here, heat transfer will occur, which results in heated helium leaving the RPV at the bottom of the reactor. As the barrel is not capable to withstand temperatures above 425°C [136], this outlet stream must be insulated.

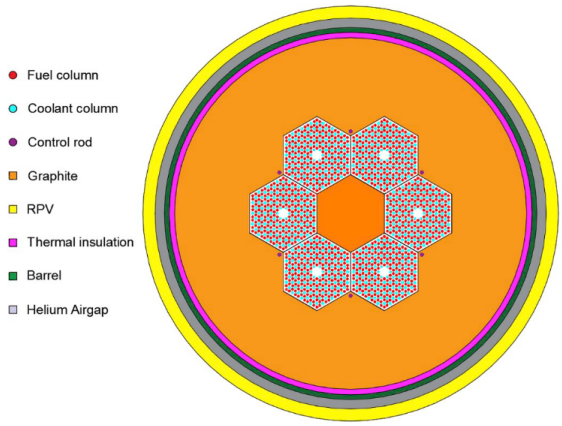

Figure 43: Schematic horizontal cross-section of the U-battery [122]

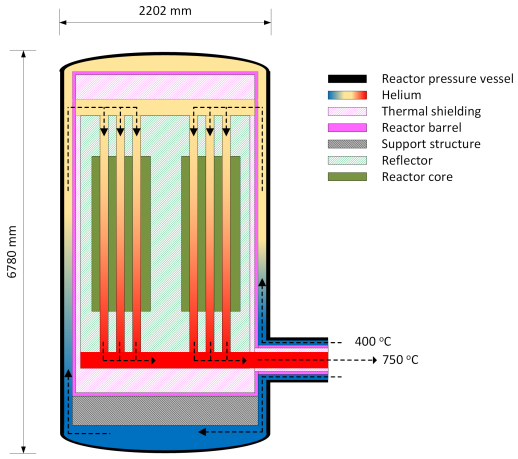

Figure 44: Schematic vertical cross-section of the U-battery, based on the work of Atkinson et al. [122] and Ding et al. [99]. Image not drawn to scale.

3.4 Power conversion cycle

For implementation of the power conversion cycle, at first an efficient power conversion cycle must be designed. This cycle is designed based on the recompression cycle and uses the following assumptions:

1. Seawater inlet temperature equal to 35°C,
2. Heat exchanger terminal temperature difference equal to 10°C,
3. Helium inlet temperature within the reactor equal to 400°C,
4. A pressure ratio of 2.5,
5. Shaft speed equal to 20,000 RPM,
6. Design turbomachinery efficiency equal to 84.9% for the compressor and 91.9% for the turbine,
7. Lower cycle pressure equal to 90 bar.

At first, to account for the worst case scenario, a seawater temperature of 35°C was chosen. Naval vessels operate globally, and should therefore be capable to operate in any conditions. In the worst conditions, seawater temperatures could rise to 35°C [137], so this value was selected as input temperature for the cooling.

Multiple heat exchangers are present in the power conversion cycle. The terminal temperature difference (TTD) of a heat exchanger has a significant impact on the total design of the heat exchanger. Based on the work of Olumayegun et al. [91] the TTD was set to 10°C. A smaller TTD could be achieved, but this increases the total needed volume of a heat exchanger drastically. A more optimal cycle design could decrease the TTD for some heat exchangers present within the cycle, but this can only be determined if a full detailed ship design is available, as otherwise heat exchanger sizing limitations are not known.

The helium inlet temperature for the U-battery was selected at 400°C [135]. Although this value could be increased, a higher inlet temperature would result in material temperatures exceeding safety limits. In normal operating conditions, the barrel of the reactor, which is made of steel, should keep a temperature below 425°C as otherwise graphitization of steel starts to occur [136]. A helium inlet temperature of 400°C therefore applies a safety margin of 25°C for the materials which are in direct contact with the inlet stream.

Due to a lack of time, it is not possible to perform a full sCO_2 turbomachinery design, and therefore the turbomachinery design values presented by Oh et al. [108] were selected, which are a pressure ratio of 2.5 for the turbomachinery and the cycle. As this falls within the efficient pressure ratio range of an sCO_2 power conversion cycle, as explained in Section 2.6.3.2, this was set to the pressure ratio of the designed cycle. Furthermore, the shaft speed of Oh et al. [108] was set to 20,000 RPM, which was deemed within reason by looking at Figure 34 and was therefore used for the designed cycle. The efficiency of the applied turbomachinery is assumed equal to the turbomachinery efficiency applied by Oh et al. [108], which results in 84.9% for the main- and recompressor and 91.9% for the turbine. Scaling will affect turbomachinery efficiency, but as this effect is small, as explained in Section A8, it is neglected.

A pressure of 90 bar was selected as lower cycle pressure. As this pressure is far away from the pressure of the critical point, small pressure changes would not immediately result in phase changes. In addition, a 90 bar lower cycle pressure would result, in combination with a pressure ratio of 2.5, in a higher cycle pressure of 225 bar. Olumayegun et al. [134] apply a maximum pressure of 250 bar for their designed sCO_2 cycle, showing that the selected pressures are within safety margins.

It is further assumed for the cycle design that no pressure losses occur over the heat exchangers. As this is the case in reality, the actual design points will differ slightly from the calculated points during the simulation. With these boundary conditions, the operating points of the cycle can be determined. To calculate each operating point, only two thermophysical properties must be known, as CoolProp is capable to determine each other needed property. The number of the operating points relate to the cycle points presented in Figure 42. To determine the thermophysical properties of each operating point (P), the following steps are applied:

1. The lower and higher cycle pressure are known, which results that at least one thermophysical property is known for each design point.
2. A water temperature of 35°C, and a TTD of 10°C results in a temperature of 45°C at P1 [1].
3. The efficiency of the main compressor, and the enthalpy at point 1, determine the enthalpy at P2.
4. The temperature at the outlet of the LTR should be 10°C higher than P2, resulting in the temperature at P8.
5. The efficiency of the recompressor, and the enthalpy at P8, determine the enthalpy in P3.
6. The temperature at the inlet of the LTR should be 10°C higher than P3, resulting in the temperature at P7.
7. The reactor inlet temperature of 400°C, and a TTD of 10°C result in the temperature at P4.
8. P5 and P6 are limited by the overall mass flow of the system. Maximum mass flow is desirable, as more power is than produced in the turbine, but there are two limitations to the maximum amount of mass flow in the power conversion cycle. First, the heat of the reactor is limited to 20 MWth, limiting the amount of heat entering the secondary cycle. The temperature of P5 is therefore related to the cycle mass flow, as a higher mass flow would result in a lower temperature in P5. As the turbine characteristic is set, the temperature in P6 is directly influenced by the conditions in P5. If the temperature in P6 should account for the TTD with P4, this means P5 must at least contain a certain temperature (and thus limited mass flow) so that the TTD between P4 and P6 is satisfied. Secondly, the HTR provides the temperature increase from P3 to P4 due to leftover heat provided by the enthalpy change between P6 and P7. If P6 would drop lower due to an increased cycle flow, then the enthalpy difference between P6 and P7 could drop below the enthalpy difference between P3 and P4, realizing P4 cannot be achieved by the recuperator. To satisfy both conditions, the model calculates the maximum mass flow in which both conditions are still valid and this way determines the temperature in P5 and thus P6.
9. The split ratio has an influence on the total cycle efficiency. To ensure optimal cycle efficiency, the difference in heat over the LTR should be set to 0, as then all the heat available is effectively transferred. The enthalpy difference between P2-3 and P7-8 should therefore be compensated in different mass flows. The split ratio is determined such that the total amount of energy at both sides is equal.

Applying all the above mentioned steps ensures that the thermophysical properties of each point in the power conversion cycle is known. This results in the T-s and p-h diagram of the designed cycle, which are presented in Figures 45 and 46. Furthermore, the cycle mass flow was determined equal to 114.78 kg/s. The split ratio was calculated as 0.71, which is similar to design values used in literature, as explained in Section 2.6.3.2. A full design overview of the power conversion cycle is presented in Table 8.

[1] This inlet temperature at the main compressor is relatively high compared to common main compressor inlet temperatures for power conversion cycles. Appendix A4 shows the impact of this assumption on the cycle performance.

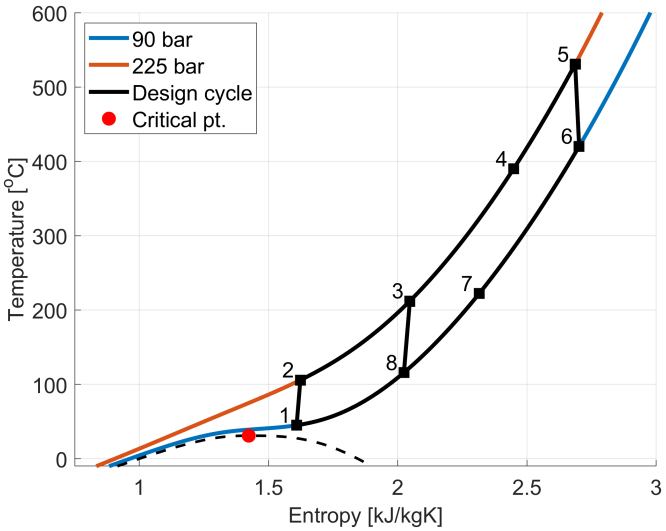

Figure 45: T-s diagram of the designed cycle

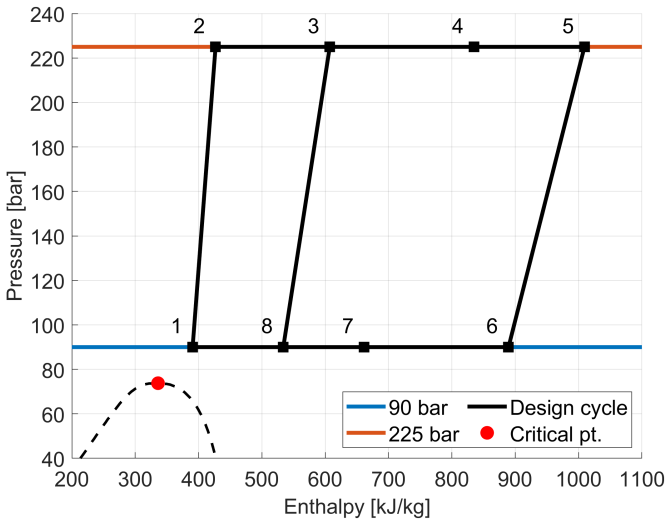

Figure 46: P-h diagram of the designed cycle

Table 8: Design values of the power conversion cycle

Parameter	Value
Working fluid	Supercritical carbon dioxide (sCO_2)
Cycle type	Indirect recompression
Turbomachinery type	Radial/centrifugal
Thermal power [MWth]	20.0
Electrical power [MWe]	7.9
Efficiency [%]	39.5
Shaft speed [RPM]	20,000
Cycle pressure [bar]	90–225
Cycle mass flow [kg/s]	114.78
Split ratio [-]	0.71
Seawater inlet temperature [°C]	35
Heat exchanger terminal temperature difference [°C]	10

3.5 Heat exchanger design

To implement the several heat exchangers, beforehand the sizing of the heat exchanger must be determined. As explained in Section 2.7, has the wavy channelled PCHE a higher heat transfer capability compared to other types of heat exchangers, resulting in a smaller required heat exchanger size. As a vessel has limited space available, this type of HX was selected for all the heat exchangers present within the power conversion cycle. As the wavy PCHE of Marchionni et al. [138] is based on experimental data, it was decided to use as much of the same design parameters of this PCHE. The total sizing of the PCHE is limited by the sizing limits stated by Olumayegun et al. [91], described in detail in Section 2.7. In addition, a mass flow channel limit was stated equal to 0.001 kg/s, which is similar to values of the experimental heat exchanger used in Marchionni et al. [138]. This value exceeds the maximum value stated by Bennet et al. [121] as described in Section 2.7. Further research should validate these limits, but for this research the data of the experimental heat exchanger were applied.

The pressures losses over the heat exchanger cannot be excessive, as otherwise the power conversion cycle would lose its pressure. It is therefore of importance, that during the design of the heat exchangers, the pressures losses are limited, which was realised based on the following reasoning. The design compression ratio of the compressors is equal to 2.5, while for the turbine the design expansion ratio is 2.44 [108]. This is not equal due to the pressure losses present over the heat exchangers and the heat exchanger pressure losses should therefore not exceed the difference between these pressure ratios. Fully flowing through the whole cycle, the sCO_2 passes six times through a heat exchanger[2]. Applying an expansion ratio of 2.44 on the higher cycle pressure of 225 bar, results in a lower cycle pressure of 92.2 bar, which is 2.2 bar above the designed lower cycle pressure. The overall heat exchanger pressure losses should therefore not exceed 2.2 bar. In addition, to ensure that the effect on flow entering and leaving the channels is negligible on the heat transfer of the heat exchangers, the length of the PCHE should be maintained a certain minimum value. It was decided to not lower the length of the PCHE to 0.4 m, but further research should validate this assumption.

The limitation of mass flow through a channel has a significant impact on the Reynolds number of the flow within the channels, as the mass flow impacts the fluid velocity. This has the most influence in the heat exchanger design of the IHX. The limitation in channel mass flow rate of the sCO_2 will enforce a low channel mass flow rate at the helium side, resulting in lower Reynolds number. This effect must be accounted for by changing the diameter of the channels, as this changes area of the channel and thus the flow velocity. Otherwise, Reynolds number would drop below values of a turbulence region, limiting effective heat transfer at the helium side. Therefore, the diameter of the heat exchanger of the IHX has been adjusted in such a way that the Reynolds number stays above 2300 among all the nodes of the heat exchanger. The same phenomena occurs at the cooler regarding the side of water, but the diameter of the channel would drop below practical values of PCHE before a turbulence region would be realised. Therefore, laminar flow regions are present in the water channels, which has been accounted for in linear friction factor relations and constant Nusselt number.

As the cycle design points are determined, the input and output conditions for each heat exchanger are known. Based on an iterative process of manually changing the length, the channel diameter and the amount of channels, a design was selected, which results in the desired output conditions with acceptable mass channel flows and pressure losses. The results of this heat exchanger design are presented in Tables 9 and 10. The lower channel diameter of the IHX, used for ensuring a turbulence flow region, ensures that the pressure drop over the channel is significantly higher compared to the other heat exchangers. Although the pressure drop of sCO_2 is 0.56 bar, the lower pressure drop in the other heat exchangers ensures that the total cycle pressure drop is equal to 1.92 bar, which complies with the previously mentioned 2.2 bar and was therefore deemed acceptable.

Table 9: General heat exchanger values

Parameter	Value
Material	Stainless steel 316 L [138]
Density [kg/m^3]	8000 [139]
Specific heat capacity [J/kgK]	500 [139]
Thermal conductivity [W/mK]	15 [139]
Width wall [mm]	0.75 [121]
Plate thickness [mm]	1.8 [121]
Channel surface roughness	neglected [138]

[2]The path of the sCO_2 through the cycle is: MC $\rightarrow$ LTR $\rightarrow$ HTR $\rightarrow$ IHX $\rightarrow$ T $\rightarrow$ HTR $\rightarrow$ LTR $\rightarrow$ CL $\rightarrow$ MC. sCO_2 flow entering the main compressor will therefore encounter six heat exchangers before a full cycle is completed.

Table 10: Printed circuit heat exchanger design values

Parameter	IHX	HTR	LTR	CL
Heat transfer duty [MW]	20.00	26.17	14.68	11.48
Fluid, hot/cold side [-]	He/sCO_2	sCO_2/sCO_2	sCO_2/sCO_2	sCO_2/Water
Mass flow, hot/cold side [kg/s]	11.01/114.78	114.78/114.78	114.78/81.28	81.28/108.83
Channel diameter [mm]	1.40	2.00	2.00	2.00
Module width [mm]	899	899	899	899
Module height [mm]	495	810	639	603
Module length [mm]	400	1450	1460	990
Volume [m^3]	0.178	1.056	0.839	0.537
Number of channels per row [-]	418	327	327	327
Number of rows [-]	275	450	355	335
Hot side inlet/outlet temp. [°C]	750/400	420/222	222/116	116/45
Cold side inlet/outlet temp. [°C]	390/531	212/390	105/212	35/55
Hot/cold side pressure loss [kPa]	72.86/56.69	48.60/17.28	49.78/8.95	10.42/8.22
Hot/cold side channel flow [g/s]	0.096/0.99	0.78/0.78	0.99/0.70	0.74/0.99

3.6 Control valves

There are many valves used in a power conversion cycle, but in general they can be classified as throttle or bypass valves. Throttle valves are used for "throttling" the mass flow. Due to valve resistance a pressure drop will occur over the valve, and by controlling the opening of the valve the resistance and thus outlet pressure can be controlled. Bypass valves are used, as the name suggests, to bypass a certain component. By opening the valve the flow will (partially) skip a certain component. For this research the valves presented in Figure 42 were selected, in which the throttle valves are displayed in grey and the bypass valve in red.

The throttle valves before the main and recompressor (V1 and V2) are applied to control the inlet pressure of the compressors and ensure an efficient operating region is realised. The throttle valve after the main compressor (V3) controls the maximum cycle pressure to 250 bar to prevent cycle damage [134]. It is also possible to control the pressure by controlling the mass flow through the compressor, but this was deemed too complex for this research purpose. An additional throttle valve is installed after the recompressor (V4). Carstens [111] states that the recompressor can produce higher pressures than pressures realised after the main compressor and LTR. If there is a large pressure difference between the two incoming streams at the mixer, then flow reversal can occur, which could result in system failure [140]. To prevent this possible failure, V4 is placed after the recompressor and limits the pressure of the recompressor to the pressure after the LTR.

There are multiple possible bypass valve locations of which a few are presented in Figure 41. The most common bypass valve location in power conversion cycles, is the so-called turbine bypass valve [111] of which the location is presented in Figure 42. Dostal [105] argues that this valve produces a thermal shock due to the large temperature difference before and after the turbine, and therefore proposes other bypass locations. It is however not clear which exact bypass valve would be the most realistic and beneficial regarding a prevention of thermal shock. For example, Carstens [111] argues that the bypass valve should be placed between the HTR and LTR, as here the smallest temperature difference occurs, but it is also stated that questions arise about the technical feasibility of such a valve. The turbine bypass is a realistic option that has been effectively used before and was therefore selected for this research. Further research could focus on comparing multiple bypass locations to determine the most optimal bypass location.

4 Modelling method

4.1 Overview

To investigate if a nuclear power plant can provide the required dynamic power behaviour of a naval vessel, a model will be created. As the current research phase on this subject is in a starting phase, a model could give preliminary results to indicate if power dynamics could be realised. In addition, a model is required as linear assumptions regarding the dynamic limitations are not sufficient. This section will explain the method applied for designing the dynamic model.

Figure 47 presents an overview of the created Simulink model of the nuclear supercritical carbon dioxide recompression cycle, indicating the most important subsystems and parameters within the model. Here, several thermodynamic states are present, which present a combination of mass flow, pressure and enthalpy for a specific substance. As these substances enter a subsystem, the thermodynamic state changes (partially) based on the system characteristics. As can be seen, the model is limited to the switchboard of the naval vessel and specifics regarding the propulsion system has been neglected for this research, but were further investigated by Wien and Meijn [141].

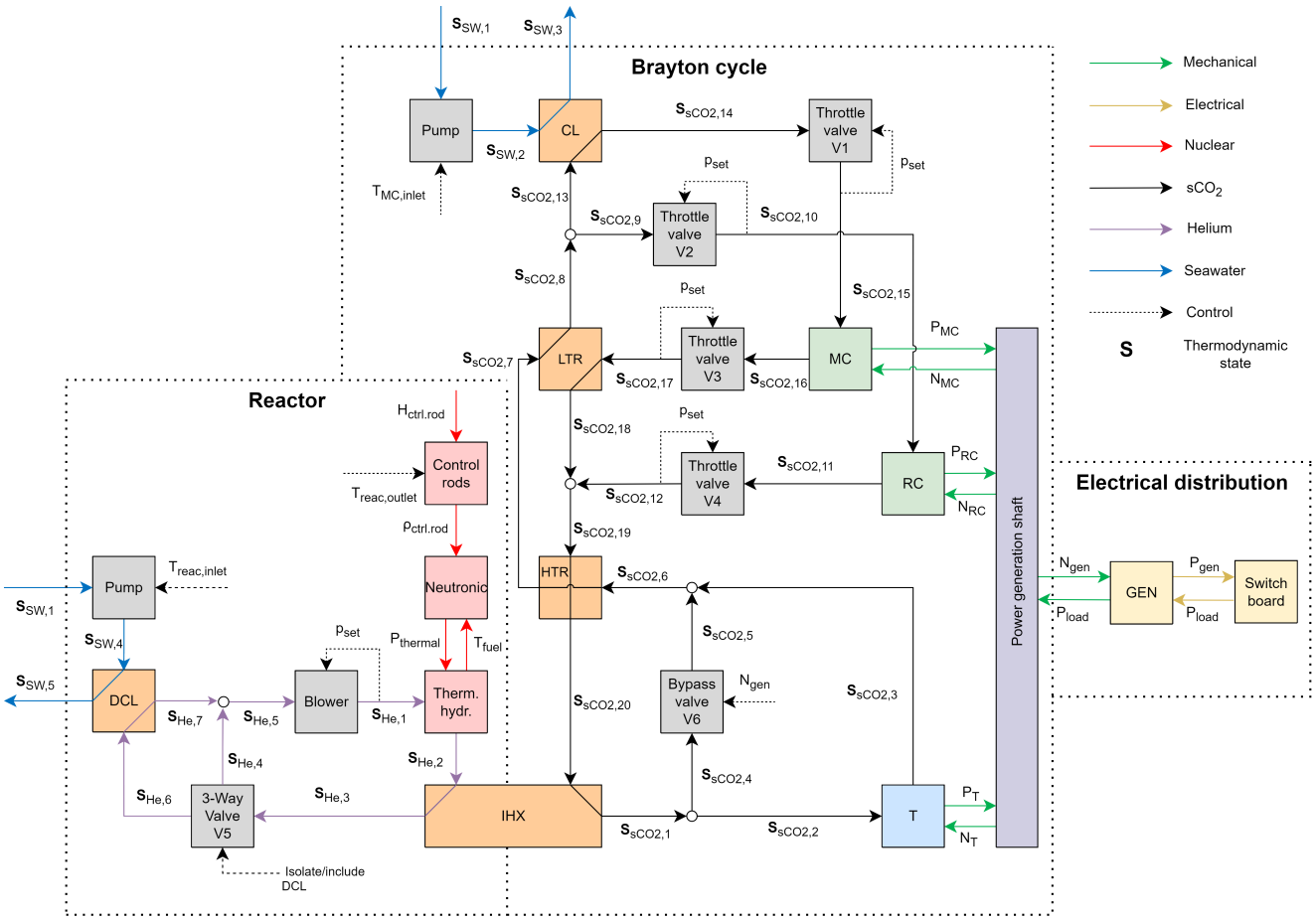

Figure 47: Schematic overview of the created model

At first in Section 4.2 the choices within the Simulink environment will be explained. The applied filters within the model are explained in Section 4.3, while Section 4.4 explains the calculation of different thermodynamic properties. Section 4.5 discusses the neutronics model for the nuclear reactor, which contains neutron kinetics, reactivity and reactivity feedback, followed by the thermal hydraulics in Section 4.6. After this, the heat exchanger model will be explained in Section 4.7. The turbomachinery model will be explained in Section 4.8, which discusses the used performance maps and the applied correction equations. Finally, the model for the shaft speed and the modelling of the valves will be explained in Section 4.9 and Section 4.10 respectively.

4.2 Simulink environment

The Simulink environment presents the possibility for dynamic power simulations, but to use this environment multiple solver choices must be made. At first, it was decided to implement variable time steps within the simulation. Due to the complexity of the model, running the model at small constant time intervals is not possible, as this would make the model user unfriendly. Small time steps are needed in Simulink to accurately calculate the small disturbances that occur when the power demand changes, but are not required when power stays relatively constant. It was decided to use a relative tolerance equal to 10^{-6} for the variable time step as this was deemed accurate enough, while not impacting simulation time drastically.

Furthermore, to solve the differential equations within the model, the ordinary differential equation (ode) solver ode23tb (stiff/TR-BDF2) was selected. The heat exchangers used in the model apply a counter flow modelling structure, resulting that the first node at the hot side is in contact with the last node of the cold side and vice versa. As multiple heat exchangers are present within the whole system, which also interact with other components, a stiff environment is created for solving the multiple differential equations. The ode23tb is created specifically for a stiff modelling construction and was therefore deemed sufficient as ode-solver. Other solving settings were deemed not influential for the simulation results or were put on automatic Simulink settings.

4.3 Filter

Filters are added to the model to ensure a stable model is realised. Within the model there are several parameters that are connected within a loop. The Simulink model applies variable time steps to ensure the relative tolerance stays within 10^{-6}. However, this presents an issue within the approach created for this model. Simulink determines the relative tolerance based on the change of several "states". By monitoring the change of these states, and measuring the relative tolerance, the variable time step is changed to ensure accurate calculations are performed. There are several "state" blocks that Simulink can monitor, but the most commonly used is an integrator block. If a certain equation contains an integration step, then Simulink is capable to monitor this process. The three parameters that occurs in a loop within the model are mass flow, pressure and enthalpy. Of these variables, only enthalpy is constantly calculated according to equations that contain an integration step. Small changes within mass flow or pressure are therefore not accurately monitored by Simulink. This results in not accurately changing the variable time step, even when pressure changes exceed the relative tolerance value, resulting in simulation issues.

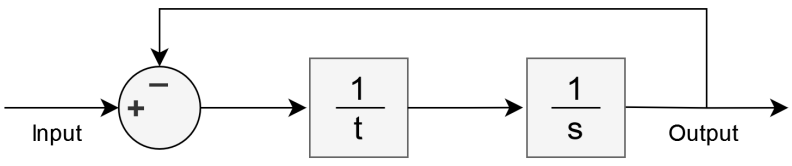

Figure 48: First-order low pass filter

To prevent this issue a first order low pass filter has been applied between each cycle loop for mass flow and pressure, as presented in Figure 48. As this filter contains an integration step, Simulink is capable to track changes during the simulation. A low pass filter was added as this ignores quick changes, while ensuring that large changes are accounted for. The time interval t for these filters has been arbitrary set to 1 second, and seems to not influence the outcome of the simulation significantly.

4.4 Thermodynamic properties

During the simulation of the power conversion cycle, several thermodynamic properties must be calculated. These properties could differ significantly, especially for a supercritical fluid as CO_2. It was decided to implement the CoolProp application to determine these thermodynamic properties as it is accurate enough for this research purpose and is free to use. The designed model will have three main parameters that will transport information to other subsystems, namely mass flow, pressure and enthalpy. If in any of the following equations other thermodynamic property parameters must be used, CoolProp will be applied. CoolProp can be used if there are two known thermodynamic properties, so for example the temperature can be determined if the thermodynamic properties pressure and enthalpy are known, which is stated in Equation 7.

$$T = f_{cp}(h, p) \tag{7}$$

However, directly calling CoolProp from Simulink for each time a thermodynamic property is needed, slows down the simulation drastically. To improve simulation speed, without losing significant accuracy, it was decided to calculate the thermodynamic properties before running the simulation and store them in a dataset. For a range of different pressures and enthalpies, a dataset for each thermodynamic properties is generated. Datasets can be easily used with Lookup Tables in Simulink and require negligible simulation time. Although simulation time is improved significantly, a potential drawback in accuracy occurs, as interpolation must occur between the beforehand generated data points. After comparison with original CoolProp values, this decrease in accuracy was deemed acceptable as values differed in the range of 10^{-3}. Appendix A5 presents an overview regarding the range and step size of the different datasets for the Lookup Tables.

4.5 Reactor neutronics

4.5.1 Neutron kinetics

To describe the neutron kinetics of the nuclear reactor, multiple approaches can be used, which could differ significantly for different reactor types or modelling purposes [46] [142]. One of the common modelling approaches is the point-kinetics model, which has been used not only to describe the reactor dynamics in SMRs [47] [143], but also specifically for gen. IV reactor types like the HTGR/VHTR [118] [144] [145] [146]. Qiu et al. [145] stated that this approach can be used for the VHTR due to that the selected 5 MWth Mi-HTR has a low output power and small reactor volume. This makes the point-kinetics model a suitable method for the selected research case.

The Point Kinetic (PK) model assumes that the spatial dependence of the diffusion model can be described by a single spatial shape, removing the spatial dependence of the diffusion model [36]. The neutron density at each point of the nuclear reactor core therefore only varies with time [142]. This makes it a less accurate and reliable model than developing a 3D reactor model, but it lowers the model complexity and computational time needed as the PK model only contains ordinary differential equations. Still, according to Wang et al. [142] the PK model still performs well in cases where the local neutron disturbance is not significant or close to criticality, which could be the reason Qiu et al. [145] mentioned that the model can be implemented for small power size VHTRs. Close to criticality does not refer to models created for accident simulations, as in those simulations

criticality could change significantly. In addition, Atkinson et al. [147] applied the PK model for the transient simulation of the U-battery as they also deemed it a feasible model with acceptable levels of accuracy. As the accuracy of the PK is still applicable for small size power reactors, in which the criticality does not change significantly, the PK model can be used for the purpose of this study.

Within the point-kinetics models there is a distinction between several methods; the one-energy-group point kinetics, multi-energy-group-point kinetics, the one-energy-group multi-region kinetics and the multi-energy-group multi region kinetics [46]. Although all these approaches have been used for modelling reactor dynamics [46], the one-energy-group point kinetics is the simplest, yet still used widely in literature [47] [118] [143] [144] [145] [146] [148] and will therefore be selected. Within this method there is a distinction between the amount of delayed neutron groups, based on the half-lives of the precursor nuclides, applied in the PK model. The current method implements the six groups of delayed neutrons as this seems the most complete model approach [36] [53] [118] [144] [145] [146] [149], but other approaches simplify this by combining it to a single delayed neutron group [47] [143] [148].

The derivation from the neutron diffusion equations to the applicable Point Kinetic equations (PKEs) for modelling has been done multiple times in literature. The specifics of this derivation can be found in Duderstadt and Hamilton [36]. The most common notation of the PKEs, considering the six groups of delayed neutrons, is presented in Equations 8 and 9 [36] [46] [53] [145] [149] [150].

$$\frac{dn}{dt} = \frac{\rho - \beta}{\Lambda} n + \sum_{j=1}^{6} \lambda_j c_j \tag{8}$$

$$\frac{dc_j}{dt} = \frac{\beta_j}{\Lambda} n - \lambda_j c_j, \text{ with j = 1,2, ... 6} \tag{9}$$

In these equations n is the population of prompt neutrons, c is the population of delayed neutron precursor nuclides, ρ is the reactivity of the system, β is the effective delayed neutron fraction, λ is the effective decay constant of delayed neutron precursors and Λ is the prompt neutron generation time. The PKEs can also be expressed in terms of the reactor's thermal power, which can be done by replacing the population of prompt neutrons in Equations 8 and 9 with the thermal power of the reactor [143] [144] by applying equation 10 [150].

$$P = F\Sigma_F \phi V = F\Sigma_F n v V \tag{10}$$

In Equation 10 F is the conversion factor from fission rate to power, Σ_F is the macroscopic fission cross-section, ϕ is the neutron flux, v is the neutron velocity and V is the reactor volume [150]. This equation shows that the power created within the fuel rods is directly related to the amount of prompt neutrons.

For the U-battery, the neutronic analysis was performed with Serpent by Atkinson et al. [147]. Serpent is capable to provide the required neutronic values for the point kinetics, which are presented in Table 11. These values will be used in the PKEs to model the selected 10 MWth U-battery.

Table 11: Input values used in the Point Kinetic equations for the U-battery [147]

Group	1	2	3	4	5	6
Delayed neutron fraction (β_i)	0.000205	0.001088	0.001039	0.002886	0.000851	0.000292
Decay constant (λ_i)	0.012493	0.031668	0.109361	0.317295	1.349730	8.659060

4.5.2 Reactivity

To control the power output of the U-battery, the reactivity of the reactor must be controlled. As explained in Section 2.8, there are many different ways of controlling the reactivity of a nuclear reactor, but for the U-battery it was decided to control the reactivity by lowering/raising the control rods [122]. The reactivity of the reactor is related to the height of the control rods according to Figure 49 [126], which has been acquired by using the WebPlotDigitizer tool [151]. As the height of the rods is limited to a minimum of 0 meters and a maximum of 1.6 meters [126], this also means that the reactivity is limited to certain values. After modelling the U-battery, it was determined that it is not possible to provide the full 0-100% power range control of the reactor by using a single control rods. This complies with the results of Atkinson et al. [122], which propose to use 6 control rods for reactor control. It was therefore decided to also use 6 control rods for reactivity control. All the controls rods will be raised or lowered at the same time and will thus operate at the same height at all times. Although the designed model will not account for reactivity differences within the reactor, the principle of raising and lowering the control together ensures that a more symmetrical power profile is ensured across the core [122].

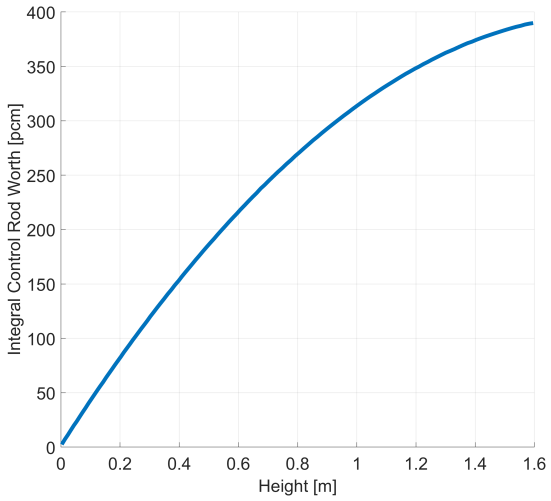

Figure 49: Reactivity effect on the U-battery due to the height of a single control rod [126]

As the reactivity is a function of the height of the control rod H_{rod}, controlling the height by changing the speed of the control rods v_{rod} can ensure reactivity control, and thus power control. This is presented in Equation 11. In this equation the height of the rods at the start of the simulation H_{t_0} is determined based on the required power output of the reactor at the start of the simulation. For this research, the initial rod height was set to 1.3 m for full power, as this provides margin in the operating region of the reactor.

$$H_{rod} = H_{t_0} + v_{rod}\, t \rightarrow \rho = f_{map}(H_{rod}) \rightarrow P = f(\rho) \tag{11}$$

Atkinson et al. [126] state that if a single control rod is fully withdrawn at a constant speed of 120 seconds, a controlled and stable power increase is achieved. As the height of the rod itself is 1.6 m, this results in a rod velocity of 0.0133 m/s. As the simulation applies 6 control rods, it was decided to limit the rod speed during the simulation to a sixth of this value, thus $v_{rod,max} = \pm$ 0.0022 m/s. This limitation in control speed limits the dynamics of the reactor, but is of importance to ensure the reactor does not enter the prompt critical region. Further research should focus on validating this limitation, or should focus on designing a reactor that can operate with faster reactivity changes.

4.5.3 Reactivity feedback

In Section 2.2.3 an explanation has been given for the impact of several phenomena on the reactivity of the reactor, which could impact the reactor dynamics. In general, multiple reactivity feedback types are applied in models such as; the Doppler effect [47] [144] [146], changes in material temperatures [118] [143] [144], changes in reactor power [47] [146], changes in pressure of the primary coolant [143], and finally external reactivity impacted by changing the control rod height [118] [143] [144] [146]. Although not present in models found within literature, reactivity feedback due to poisoning could also be of interest for further studies [36].

At the time of writing only data surrounding the temperature feedback of the fuel for the U-battery was present in literature, and it is therefore decided that only fuel temperature reactivity feedback will be applied in the model. Although this is only a single feedback effect, Kitcher et al. [47] state that the contribution of the Doppler effect, and thus the change in fuel temperature, on the reactivity is the most dominant in short time transient operations. Other feedback phenomena may have larger feedback coefficients than the Doppler effect, but the almost instantaneous reaction of the fuel temperature on a power change makes the Doppler effect the most dominant feedback contribution [47]. The addition of this reactivity feedback can be seen in Equation 12, in which the total reactivity is changed by the external reactivity (ρ_{rod}) and an increase or decrease in fuel temperature (ρ_{T_f}).

$$\rho(t) = \rho_{rod} + \rho_{Tf} = \rho_{rod} + \alpha_{Tf}(T_f - T_{f,0}) \tag{12}$$

In this equation the reactivity changes based on a temperature difference of the fuel (T_f) compared to a reference fuel temperature ($T_{f,0}$). This temperature change is multiplied by the negative reactivity feedback coefficient of the fuel (α_{Tf}). As a result the reactivity will lower when the temperature increases of the reactor, therefore ensuring a more inherent safe reactor. For the U-battery, the negative feedback coefficient is equal to -4.26 pcm/K [147]. Unfortunately, the reference fuel temperature belonging to this value was not present within literature. It was therefore decided to let the reactor model of the U-battery run at full power without any reactivity feedback. As a result, the temperature of the fuel reached a steady state at 1131 K, which was selected as reference fuel temperature in further simulations.

4.6 Reactor thermal-hydraulics

4.6.1 Thermal hydraulics scheme

When modelling the thermal hydraulics of a nuclear reactor it is of importance to not only connect the generated thermal heat in the fuel elements to the power conversion system, but also to investigate the temperature behaviour of reactor components during dynamic simulations. For this study it has been decided to implement a 1D lumped thermal hydraulics approach for the modelling of the U-battery. The 1D lumped thermal hydraulics approach has been used successfully in literature to simulate dynamic heat transfer conditions within an HTGR/VHTR [126] [152] [153] and is therefore deemed an appropriate modelling approach for this research case. The thermal hydraulics model is based on the equivalent heat transfer model used for the U-battery by Atkinson et al. [126], which can be seen in Figure 50, and the hexagonal fuel shape structure of a prismatic HTGR, which is presented in Figure 52.

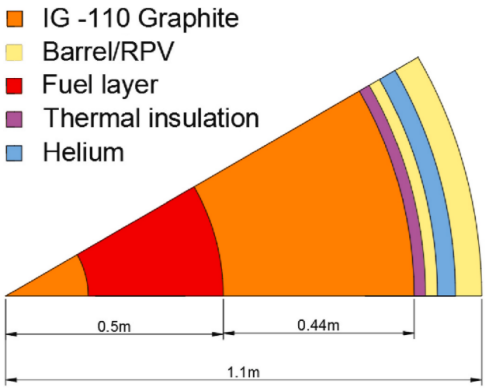

Figure 50: Heat transfer model used for the U-battery [126]

Figure 51 presents the structure of the 1D lumped heat transfer model. Each block contains its own heat transfer equation in which the difference between the heat input and output will result in a temperature change. The equations used for each block are described in Equations 13-21. In these equations M is the mass of the block, C_p the specific heat capacity, T the temperature, U the overall heat transfer coefficient, A the overall heat transfer area between two blocks, $\dot{Q}$ is the heat input from the point kinetics equation, $\dot{m}$ is the mass flow and h is the enthalpy. In addition, the following subscripts are used; F: fuel, M: moderator, CR: central reflector, SR: side reflector, I: insulation, B: barrel, RPV: reactor pressure vessel, Ri: coolant riser and Do: coolant down comer. Here, material parameter values used within the U-battery are stated in Tables 12-14.

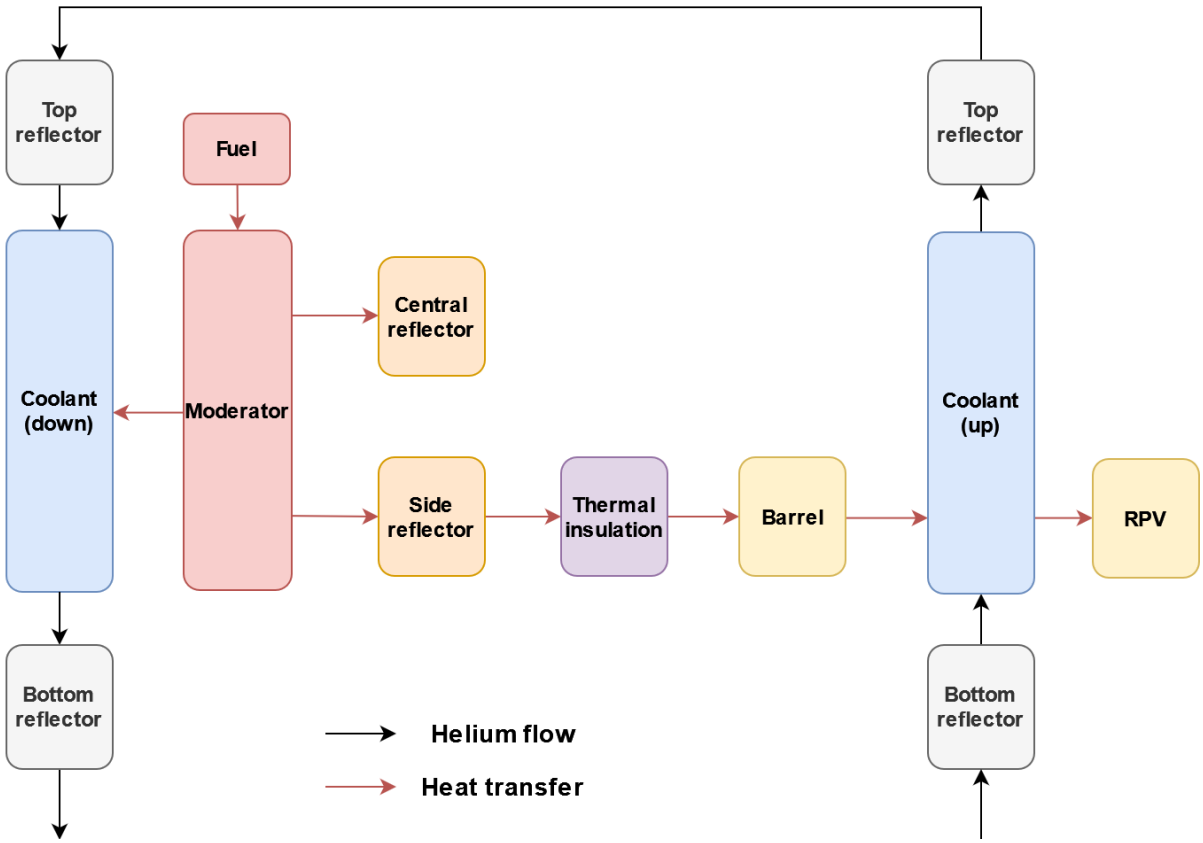

Figure 51: Schematic diagram of the lumped thermal hydraulics of the U-battery

Fuel: $$M_F C_{p,F} \frac{dT_F}{dt} = \dot{Q} - U_{F,M} A_{F,M} (T_F - T_M) \tag{13}$$

Moderator: $$M_M C_{p,M} \frac{dT_M}{dt} = U_{F,M} A_{F,M} (T_F - T_M) - U_{M,R} A_{M,R} (T_M - T_R) - U_{M,Do} A_{M,Do} (T_M - T_{Do}) \tag{14}$$

Central reflector: $$M_{CR} C_{p,CR} \frac{dT_{CR}}{dt} = U_{M,CR} A_{M,CR} (T_M - T_{CR}) \tag{15}$$

Side reflector: $$M_{SR} C_{p,SR} \frac{dT_{SR}}{dt} = U_{M,SR} A_{M,SR} (T_M - T_{SR}) - U_{SR,I} A_{SR,I} (T_{SR} - T_I) \tag{16}$$

Insulation: $$M_I C_{p,I} \frac{dT_I}{dt} = U_{R,I} A_{R,I} (T_R - T_I) - U_{I,B} A_{I,B} (T_I - T_B) \tag{17}$$

Barrel: $$M_B C_{p,B} \frac{dT_B}{dt} = U_{I,B} A_{I,B} (T_I - T_B) - U_{B,Ri} A_{B,Ri} (T_B - T_{Ri}) \tag{18}$$

RPV: $$M_{RPV} C_{p,RPV} \frac{dT_{RPV}}{dt} = U_{Ri,RPV} A_{Ri,RPV} (T_{Ri} - T_{RPV}) \tag{19}$$

Riser: $$M_{Ri} C_{p,Ri} \frac{dT_{Ri}}{dt} = U_{B,Ri} A_{B,Ri} (T_B - T_{Ri}) - U_{Ri,RPV} A_{Ri,RPV} (T_{Ri} - T_{RPV}) + \dot{m}_{in} h_{in} - \dot{m}_{out} h_{out} \tag{20}$$

Down comer: $$M_{Do} C_{p,Do} \frac{dT_{Do}}{dt} = U_{M,Do} A_{M,Do} (T_M - T_{Do}) + \dot{m}_{in} h_{in} - \dot{m}_{out} h_{out} \tag{21}$$

Temperature changes, or irradiation, within the materials of the reactor will affect the material property values. Density, thermal conductivity and specific heat capacity are dependent on the material conditions, but for this research it was assumed these properties do not change as detailed information was missing in literature. This assumption complies with the approach stated by Atkinson et al. [147]. As thermal conductivity is constant during the simulation, and the sizing of the reactor stays constant, the heat transfer coefficient for conduction is also constant. However, in the case when convection plays a part within the heat transfer, the overall heat transfer coefficient must be calculated as flow regimes could differ during power transients.

The thermal structure presented in Figure 51 applied on the U-battery must account for the cylindrical structure of the reactor, as presented in Figure 50. Therefore, to calculate the overall heat transfer coefficients U_x and the heat transfer area A_x of the different materials x, Equations 22 and 23 are applied [154].

$$\frac{1}{U_x A_x} = \frac{ln(r_{out,x}/r_{in,x})}{2\pi k_x H} + \frac{1}{2\pi r_{out,x} h H} \tag{22}$$

$$h = \frac{Nu\, k}{d_H} \tag{23}$$

Equation 22, accounts for the process of conduction and convection, of which the latter is only applicable if the material is in contact with helium. The physical sizing of the cylinder is implemented by the outside and inside radius r of the cylinder and its height H. The convective heat transfer coefficient h can be calculated by the thermal conductivity k, hydraulic diameter d_H and the Nusselt number Nu as described in Equation 23 [154]. The Nusselt number will be calculated by applying the Gnielinski relation presented in Equation 27 [118] [154], which is a relation between the Prandtl number Pr, according to Equation 24, the Reynolds number Re, according to Equation 25 and the friction factor f, calculated by applying the Petukhov relation presented in Equation 26 [118]. These relations are applied as it is assumed that a smooth pipe approach is applicable for the channels within the hexagonal fuel blocks and the flow between the cylindrical shape of the barrel and RPV.

$$Pr = \frac{C_p \mu}{k} \tag{24}$$

$$Re = \frac{\rho\, u\, d_H}{\mu} \tag{25}$$

$$f = (0.79\log(Re) - 1.64)^{-2} \tag{26}$$

$$Nu = \frac{(\frac{f}{8})(Re - 1000)Pr}{1 + 12.7(Pr^{\frac{2}{3}} - 1)\sqrt{\frac{f}{8}}}\ , 2300 < Re < 5 \cdot 10^6,\ 0.5 < Pr < 2000 \tag{27}$$

In these equations the specific heat capacity C_p, the viscosity μ, the density ρ, the speed u and the hydraulic diameter d_H are used for calculating these dimensionless numbers. Here, the hydraulic diameter must be calculated for the circular cooling channels within the fuel block, and the cylindrical channel between the barrel and RPV. The hydraulic diameter is equal to the area of the channel A divided by its perimeter p. For the circular channels this results in that the hydraulic diameter is equal to the diameter of the channel, while for the cylindrical channel Equation 28 is used [155].

$$d_H = \frac{4A}{p} = \frac{4(\pi r_{out}^2 - \pi r_{in}^2)}{(2\pi r_{out} + 2\pi r_{in})} = 2(r_{out} - r_{in}) \tag{28}$$

Table 12: Horizontal sizing of the U-battery [126]

Reactor part	Inside radius [cm]	Outside radius [cm]
Central reflector	0	19
Matrix layer	19	50
Side reflector	50	94
Thermal insulation	94	97
Barrel	97	101
RPV	106	110

Table 13: Vertical sizing of the U-battery [126]

Reactor part	Height [cm]
Active core	320
Top/bottom reflector	50

Table 14: Properties of the materials within the U-battery

Reactor part	Specific heat capacity [J/kgK]	Thermal conductivity [W/mK]	Density [kg/m^3]
Fuel element	1473 [156]	65.4 [156]	1650 [156]
Central reflector	720 [136]	133 [136]	1800 [136]
Matrix layer	720*	133*	1750 [122]
Side reflector	720 [136]	133 [136]	1800 [136]
Thermal insulation	1200 [157]	0.23 [135]	3200 [122]
Barrel	557 [158]	19.8 [158]	8000 [122]
RPV	557 [158]	19.8 [158]	8000 [122]

* assumed equal to the reflector as similar types of materials are used

4.6.2 Reactor matrix

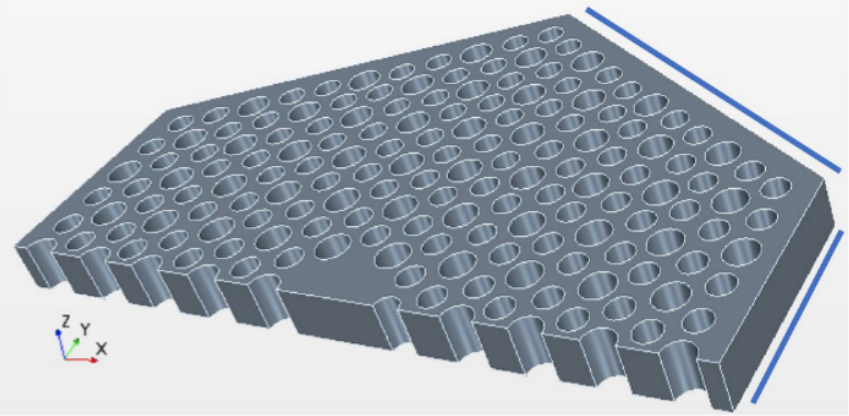

Figure 52: Half of a fuel block, with the side reflector position highlighted by the blue lines [122]

Looking at Figure 51, the matrix of the reactor is a material element that connects to multiple other components. modelling this component is therefore of essence, but complexity arises due to the hexagonal shape of the fuel block and the multiple fuel and coolant channels present within the block, visible in Figure 52 and Table 15. A single coolant channel is surrounded by 6 fuel channels, resulting in each coolant channel carrying approximately two times the heat generated in a single fuel element [156]. The graphite matrix surrounds each channel for heat transfer and structure, as presented in Figure 53. Due to the different fuel channels spread over the fuel, the temperature at a local channel level would differ, as the temperature would be higher around the fuel channels, but also on a total component level will the matrix temperature be higher at the inside of the fuel block compared to its outside. As it is not possible to accurately determine this temperature distribution with a 1D model, it is assumed the heat transfer of the hexagonal block can be modelled as presented in Figure 53. This assumption makes it possible to consider the hexagonal shape as a cylinder with multiple layers and the matrix temperature can be determined at the place of the red ring. This temperature is then also assumed to be equal to the matrix temperature for the heat transfer between the matrix and the reflectors. In Figure 53 three different radii are visible. After applying hexagonal geometry relations, it was determined that the shortest distance between the coolant channel and the fuel channel is equal to 4.51 mm. As a result, the coolant radius R_c was determined equal to 7.94 mm, the matrix radius R_m equal to 12.45 mm and the fuel radius R_f equal to 18.8 mm. These values will be used for the 1D heat transfer model of the fuel, matrix and coolant channel.

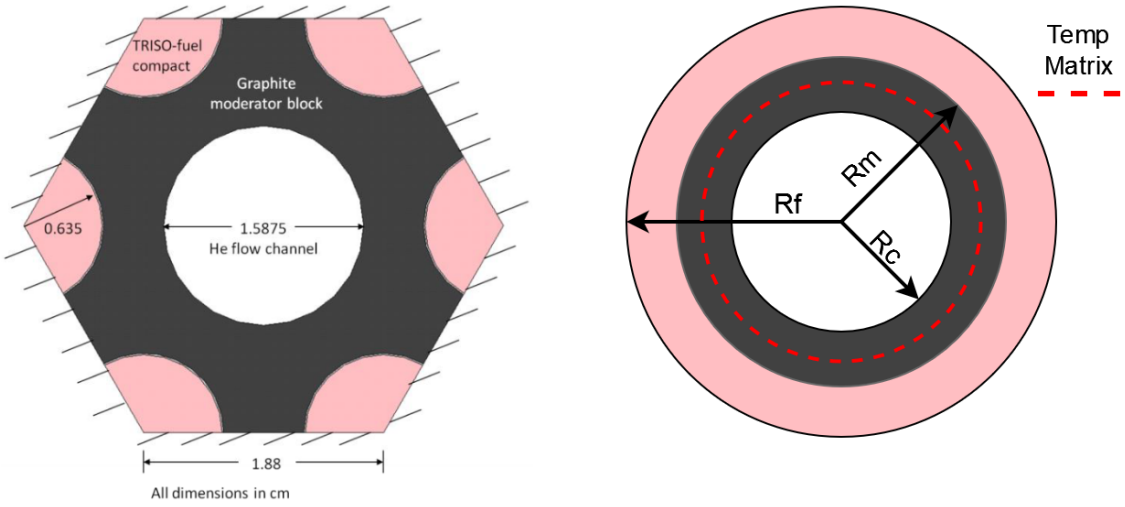

Figure 53: Schematic overview hexagonal fuel block (left) [159], and the modelled fuel block (right)

Table 15: Parameters per hexagonal fuel block [99]

Parameter	Value
Block width	36 cm
Block height	80 cm
Amount of fuel channels	210
Amount of coolant channels	108
Diameter helium channel	1.588 cm [3]
Diameter fuel channel	1.27 cm

[3] Near the center of the fuel block smaller coolants channels are applied, which have a diameter of 1.27 cm [156]. This is however neglected within this research.

4.6.3 Pressure losses and blower

As the helium is flowing through the reactor, a pressure drop will be the result due to friction losses in the channels and the height difference within the reactor. The pressure losses occur at six blocks in the reactor model through which the helium is flowing, visible in Figure 51. The grey blocks contain only a pressure drop, while the blue blocks contain heat transfer and pressure losses. The pressure losses in these blocks have been calculated according to the pressure loss due to the height and the friction, in which the latter uses the Petukhov relation for calculating the friction factor, presented in Equation 26. The pressure drop Δp can be calculated according to Equations 29-31 [118].

$$\Delta p = \Delta p_{height} + \Delta p_{friction} \tag{29}$$

$$\Delta p_{height} = \rho g \Delta H \tag{30}$$

$$\Delta p_{friction} = \frac{\rho f u^2 H}{2 d_H} \tag{31}$$

These pressure losses occur in the primary circuit, and to ensure the required pressure level in maintained, a blower is added to the primary circuit. The blower is designed as a steady state pump. The power input into the blower is calculated according to Equation 32 [91].

$$P = \dot{m}_{He}(h_{out} - h_{in}) \tag{32}$$

The isentropic efficiency of the blower can be calculated according to Equation 33.

$$\eta = \frac{h_{out,isen} - h_{in}}{h_{out} - h_{in}} \tag{33}$$

For an isentropic process in the blower, the first law for a closed system undergoing a reversible process holds: [91]

$$h_{out,isen} - h_{in} = \frac{p_{out} - p_{in}}{\rho_{in}}. \tag{34}$$

Assuming a blower efficiency equal to 82% [91], and stating that the outlet pressure of the blower should be equal to the design pressure of the reactor, 40 bar, ensures that the outlet enthalpy and required pump power can be calculated. It was assumed that this required pump power is electrical and will be provided by the power conversion cycle itself. In reality another energy source, like a battery or emergency diesel generator, should be used to ensure a system failure does not result in a loss of pressure within the reactor.

4.7 Heat Exchanger

4.7.1 Node and geometrical structure

As stated before, the heat exchanger is of the essence in the dynamic modelling of nuclear power plant. As described in Section 2.7 the wavy Printed Circuit Heat Exchanger (PCHE) was selected as suitable heat exchanger type for the selected power conversion cycle. For dynamically modelling the PCHE, the LMTD method is deemed not feasible due to the low accuracy during dynamic changes [113]. It is therefore common to split the model of the heat exchanger into several nodes and apply a 1D finite volume method [91] [105] [111] [113] [116] [117] [118] [133] [140]. Based on the dynamic PCHE model created by Ming et al. [118] and Trinh [140] the heat transfer in the heat exchanger will be calculated. This model applies the approach in which only two channels (one hot and one cold) are modelled. These channels will be separated by the wall of the heat exchanger and will also be divided into several nodes n along the length of the channel, to ensure accurate property calculations. The schematic structure is presented in Figure 54.

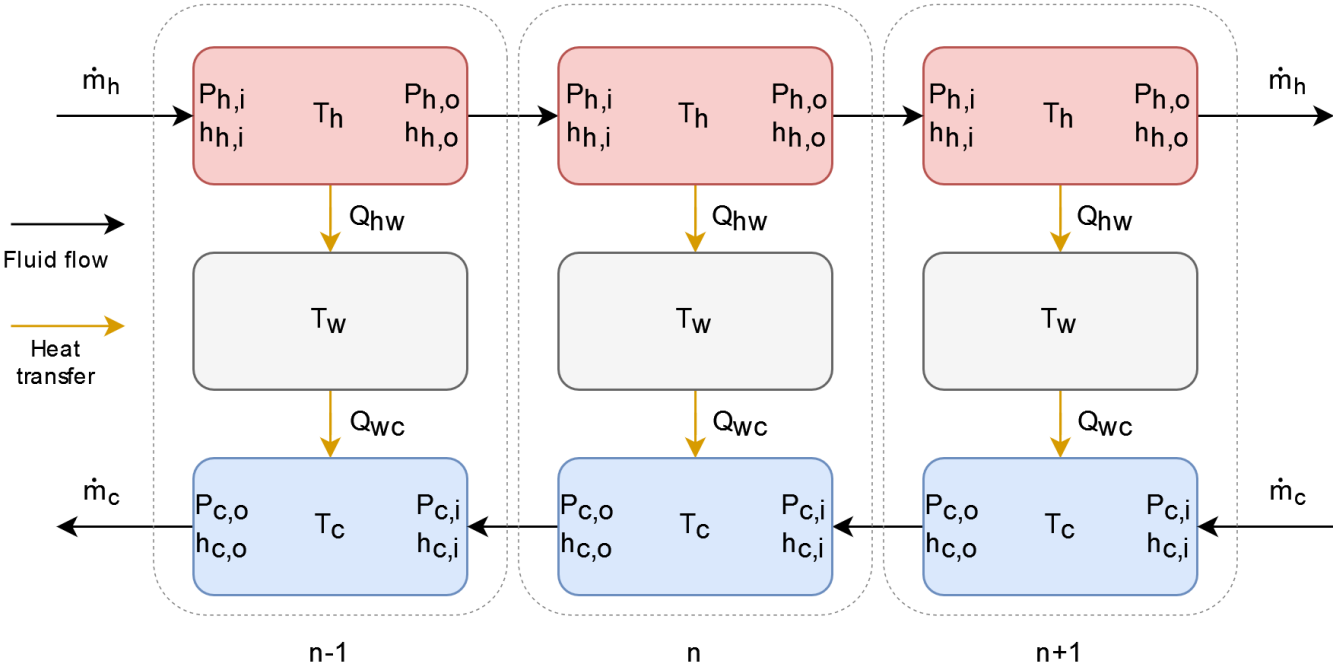

Figure 54: Node division of the 1D heat exchanger model

First, the geometric structure parameters of the heat exchanger will be applied to calculate the hydraulic diameter d_H and the equivalent plate thickness t_e [118]. This was done according to Equations 35 and 36.

$$d_H = \frac{4\pi d^2}{8(\pi\frac{d}{2} + d)} \tag{35}$$

$$t_e = H_c - \frac{\pi}{8}d \tag{36}$$

In these equations the diameter d of the channel and the height H_c between the channels are used. The dynamic equations of the heat transfer element are formed according to the mass balance, energy balance, and simplified momentum balance equations. It is stated in Equation 37 that mass will not be created nor destroyed, so the mass flow out of the channel will be the same as the mass flow entering the channel [118]. As stated in Equation 38, the total mass flow through the heat exchanger will be equally divided by the amount of hot or cold channels N which results in the mass flow through one channel of the heat exchanger.

$$\dot{m}_{i,n} = \dot{m}_{o,n} \tag{37}$$

$$\dot{m}_{chan} = \frac{\dot{m}_{tot}}{N} \tag{38}$$

For the energy balance within the channels, the following conservation equations are applied on each node for the hot h and cold c channel:

$$M_h \frac{dh_{h,o}}{dt} \approx M_h \frac{dh_h}{dt} = \dot{m}_{h,i}h_{h,i} - \dot{m}_{h,o}h_{h,o} - \dot{Q}_{hw}, \tag{39}$$

$$M_c \frac{dh_{c,o}}{dt} \approx M_c \frac{dh_c}{dt} = \dot{m}_{c,i}h_{c,i} - \dot{m}_{c,o}h_{c,o} + \dot{Q}_{wc}. \tag{40}$$

In these equations h_i and h_o are the enthalpy of the inlet and outlet fluids. Here, the assumption is made that, due to the implementation of several nodes, the enthalpy within the node will not change significantly, as otherwise it could not have been stated that dh/dt is equal to dh_o/dt. Furthermore, M_h and M_c are the mass of the fluid in the hot and cold side of the heat exchanger, which can be calculated by Equations 41 and 42. Here, the cross-sectional area of the channel is multiplied by the channel length of the node L_n, which is equal to the total channel length divided by the amount of nodes, and the density of the fluid in the channel ρ_n. [118]

$$M_{h,n} = \frac{\pi}{8} d^2 L_n \rho_{h,n} \tag{41}$$

$$M_{c,n} = \frac{\pi}{8} d^2 L_n \rho_{c,n} \tag{42}$$

4.7.2 Heat transfer and pressure loss

The heat transfer Q between these two channels occurs between the hot channel and the wall $Q_{hw,n}$ and between the wall and the cold channel $Q_{wc,n}$ according to the following equations: [118]

$$Q_{hw,n} = U_{h,n} A_{h,n} (T_{h,n} - T_{w,n}), \tag{43}$$

$$Q_{wc,n} = U_{c,n} A_{c,n} (T_{w,n} - T_{c,n}). \tag{44}$$

In these equations the heat transfer area A is equal to the circumference of the semicircular channel multiplied by the length of the node, as stated in Equation 45 [118].

$$A_{h,n} = A_{c,n} = L_n (\frac{\pi}{2} + 1) d \tag{45}$$

In Equation 43 and 44 the temperature of the fluid in the heat transfer elements ($T_{h,n}$ or $T_{c,n}$) is equal to the average temperature between the inlet and outlet temperature of the node. To calculate the wall temperature $T_{w,n}$ of the heat exchanger the energy conservation equation is applied on the wall as presented in Equations 46 and 47 [118].

$$M_{w,n} C_{w,n} \frac{dT_{w,n}}{dt} = \dot{Q}_{hw,n} - \dot{Q}_{wc,n} \tag{46}$$

$$M_{w,n} = (H_c d - \frac{\pi}{8} d^2) L_n \rho_w \tag{47}$$

To calculate the overall heat transfer coefficients $U_{h,n}$ and $U_{c,n}$ the following Equations are applied [118] [154]:

$$\frac{1}{U} = \frac{1}{h} + \frac{t_e}{k_w}, \text{ with} \tag{48}$$

$$h_h = \frac{Nu_{h,n} k_{h,n}}{d_H}, \; h_c = \frac{Nu_{c,n} k_{c,n}}{d_H}. \tag{49}$$

The convective heat transfer coefficient h can be calculated with Equations 48 and 49, which relates the thermal conductivity k_n, hydraulic diameters d_H and the Nusselt number Nu. For these equations, the Nusselt number must be known when convection occurs. Marchionni et al. [138] base there 1D channel PCHE model on experimental data of a wavy channel heat exchanger. To account for the difference between a straight and wavy channelled heat exchanger, correction factors are applied in the calculation of the friction factor and Nusselt number. The friction factor is calculated according to Serghides solution, presented in Equation 50. This solution is an approximation of the Colebrook–White equation and is valid for a turbulent regime (Re_D

$>$ 2300) [138][4]. Marchionni et al. [138] state that the pressure drop in a wavy channel is larger than in a straight channel PCHE. To account for the use of a wavy channel PCHE the correction factor C_1 has been introduced, which was determined equal to 1.1 based on experimental data [138]. As the heat transfer in a wavy channel heat exchanger is also larger compared to a straight channel, an additional correction factor C_2 has been implemented for the Gnielinski equation, which was determined to be equal to 1.2 [138]. The used Gnielinski equation by Marchionni et al. [138] is stated in Equation 53. These equations for the friction factor and Nusselt number were implemented in the model to simulate a wavy channel PCHE. Other Nusselt relations, especially for other types of PCHE, are also applied in literature of which an overview can be seen in Wang et al. [113]. These relations could be considered in further research as there is not one definite relation for PCHE channels.

$$f = C_1 \frac{1}{4} \left(4.781 - \frac{(A - 4.781)^2}{B - 2A + 4.781} \right)^{-2}, \text{ with} \tag{50}$$

$$A = -2log_{10} \left(\frac{\epsilon/D}{3.7} + \frac{12}{Re_D} \right), \tag{51}$$

$$B = -2log_{10} \left(\frac{\epsilon/D}{3.7} + \frac{2.51A}{Re_D} \right). \tag{52}$$

$$Nu = C_2 \frac{(\frac{f}{2})(Re - 1000)Pr}{1 + 12.7(Pr^{\frac{2}{3}} - 1)\sqrt{\frac{f}{2}}} \tag{53}$$

Within these equations, the quantities A and B are dependent on the roughness of the channels ϵ, the diameter of the channel D and the Reynolds number. However, as stated in Table 9 the roughness of the channels is neglected, reducing the impact of the factor ϵ/D. Prandtl and Reynolds number are calculated for each node according to Equations 24 and 25 respectively.

The pressure drop Δp along the channels can be calculated according to Equations 54-56 [118] [160].

$$\Delta p_n = p_{n,i} - p_{n,o} = \frac{f \rho_n u_n^2 L_n}{2 d_H} \tag{54}$$

$$\Delta p_h = \sum_i^n \Delta p_{h,n} \tag{55}$$

$$\Delta p_c = \sum_i^n \Delta p_{c,n} \tag{56}$$

Fouling could impact the heat transfer coefficient during operation, which could be addressed with a fouling resistance factor during the heat transfer calculation. However, in this case the fouling resistance was neglected. As the purity of CO_2 is high, fouling is less of an issue compared to other substances and can therefore be neglected [117], but this could be improved in further studies.

[4] The equations stated by Marchionni are using the Fanning friction factor, instead of the previous used Darcy–Weisbach friction factor. For fully clarity; the Darcy–Weisbach friction factor is 4 times larger than the Fanning friction factor. Before using these equations in the model, the equations were corrected for this difference.

4.8 Turbomachinery

Due to the fast response time of the turbomachinery, compared with the heat exchangers and reactor, it is common to neglect the response time of turbomachinery in modelling approaches. It is therefore proposed to apply steady-state models for the turbomachinery [85] [113] [116] [134]. There are multiple approaches for simulating steady state turbomachinery, which differ in complexity. A simple modelling approach applies constant compression and expansion ratio, and efficiencies, for the turbomachinery during the simulation. Although this approach has been used in literature [91] [119], it can be argued that this approach is not suitable for a transient power simulation in which the operating conditions and performance of turbomachinery changes significantly.

Another approach is by using performance maps of the turbomachinery for a more realistic turbomachinery performance [94] [116] [118] [133]. This method requires the compressor and turbine map of the belonging turbomachinery. Furthermore, the use of performance maps within the modelling approach can also differ. If the model uses the performance maps directly (without correction) than these are called Fixed Performance Parameter (FPP) models [116]. However, during the power transient, the operating conditions (temperature and pressure) can differ significantly from the design conditions of the performance map. This change in operating conditions could result in different turbomachinery performance compared to values presented in the performance map. Correction equations can be used to account for this difference in operating conditions, and models using this correction approach, before using the performance maps, are called Corrected Performance Parameter (CPP) models [116]. It is expected that the operating conditions will differ significantly during the power transients of a naval vessel, and therefore it was decided to focus on implementing a CPP turbomachinery model. At first, Section 4.8.1 will explain the realization of the performance maps for the turbomachinery and Section 4.8.2 will explain the used correction equations within the CPP model. In Section 4.8.3 the general modelling approach for the turbomachinery will be explained, which will use the obtained performance maps and correction equations as data input for performance parameter calculations.

4.8.1 Performance maps

Performance maps are capable to determine the performance of turbomachinery, the pressure ratio and efficiency, based on the corresponding shaft speed and mass flow. The Korean research institute KAIST has developed an in-house code for simulating sCO_2 turbomachinery, which is capable to create the required performance maps for centrifugal sCO_2 compressors and turbines. As the maps created by Oh et al. [108] are for a 12.5 MWe power conversion cycle, these maps are within range of the desired power range for the naval vessels. A normalization method can therefore be applied to correct the small change between the desired power output of the turbomachinery. The performance maps of the KAIST installation can be seen in Appendix A6, which have been obtained by using the WebPlotDigitizer tool [151].

For normalizing the performance maps, there are four parameters which must be converted. These are the mass flow, shaft speed, pressure ratio and efficiency. Pressure ratio and efficiency are dimensionless numbers, and are there for constant during the normalization approach [161]. The mass flow and shaft speed do however change based on their respective dimensionless numbers [161], but for this normalization approach, shaft speed was also assumed constant with the power conversion cycle of Oh et al. [108]. This is solely for the reason that the compressor and turbine are not normalized at the same rate. As Oh et al. [108] only use one compressor, while the designed cycle implements two compressors, a normalization in shaft speed would result in a mismatch between the shaft speeds of compressors and the turbine. This issue can only be solved if a fundamental turbomachinery design study is executed, and therefore the assumption is made that shaft speed is constant for this preliminary design analysis.

In reality there are limitations to these normalization relations as size effects of the turbomachinery impact the optimal mass flow rate, power and efficiency of a turbine [162]. Small turbomachinery always have lower efficiencies than larger geometrically similar machines [163]. However, as the reference power output and the scaled power output are within the same range, the assumption is made that these size effects can be neglected. An indication about the effect of scaling on efficiency has been made in Appendix A8, which shows the effect is negligible for the difference between the referenced and scaled power output.

Overall, the obtained performance maps of Oh et al. [108] and the normalization approach, result in the performance maps for the designed turbomachinery. These maps are visible in Figures 55-57. The performance maps obtained from the KAIST research group are 3D data sets, containing mass flow rate, shaft speed and either pressure ratio or efficiency. The turbomachinery model is created in such a way that mass flow rate and shaft speed are input values for the Simulink model and the performance maps therefore produce the pressure ratio and efficiency. The maps are however limited in their use case, as only specific speed lines are given and the dataset obtained from the WebPlotDigitizer tool is limited to scattered data points. To ensure smooth simulation times in Simulink, it was decided to produce the maps in such a way that 3D interpolation can happen with the input of mass flow rate and shaft speed.

To ensure 3D interpolation can happen smoothly, the function scatteredInterpolant of Matlab was used for interpolating within a certain meshgrid. Beside interpolation, extrapolation was also added to the model. The obtained performance maps have operating areas that do not contain data points. For example. above the surge line of a compressor there are no data points available as operating above the surge line is not recommended for a compressor. Still, for modelling, it could be beneficial that the model is capable to acquire at least a value in these unknown areas. Although it would not be realistic to operate for long times above the surge line, the model would not crash immediately due to unknown values provided. As the specific values around these operating points are not known, some estimates have been made on which interpolation and extrapolation method is preferred.

In Appendix A9 a comparison between the different inter-/extrapolation methods was made and natural interpolation and boundary extrapolation were chosen as preferred methods for creation of the performance maps. As a result the performance maps displayed in Figures A33-A35 were created and selected as input for the created Simulink model. Within this Simulink model, interpolation must still occur between the three input structures (mass flow, shaft speed and a choice between pressure ratio or efficiency). By applying the 2D Lookup Table of Simulink interpolation occurs between the mass flow and shaft speed to achieve the desired pressure ratio or efficiency. For this interpolation method, linear point-slope interpolation was selected, which is further explained in Appendix A9.

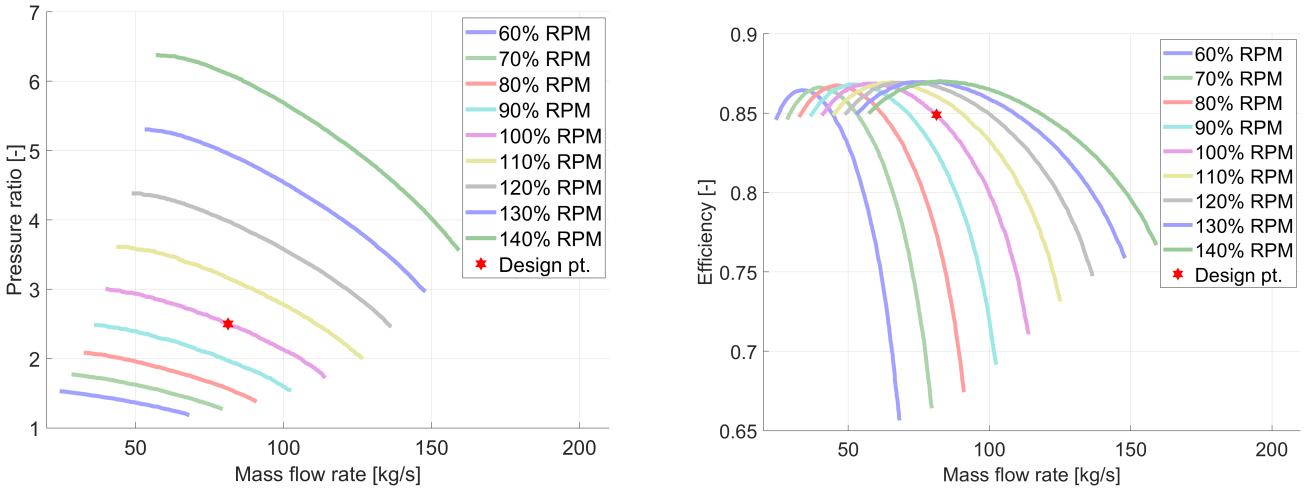

Figure 55: Main compressor performance maps

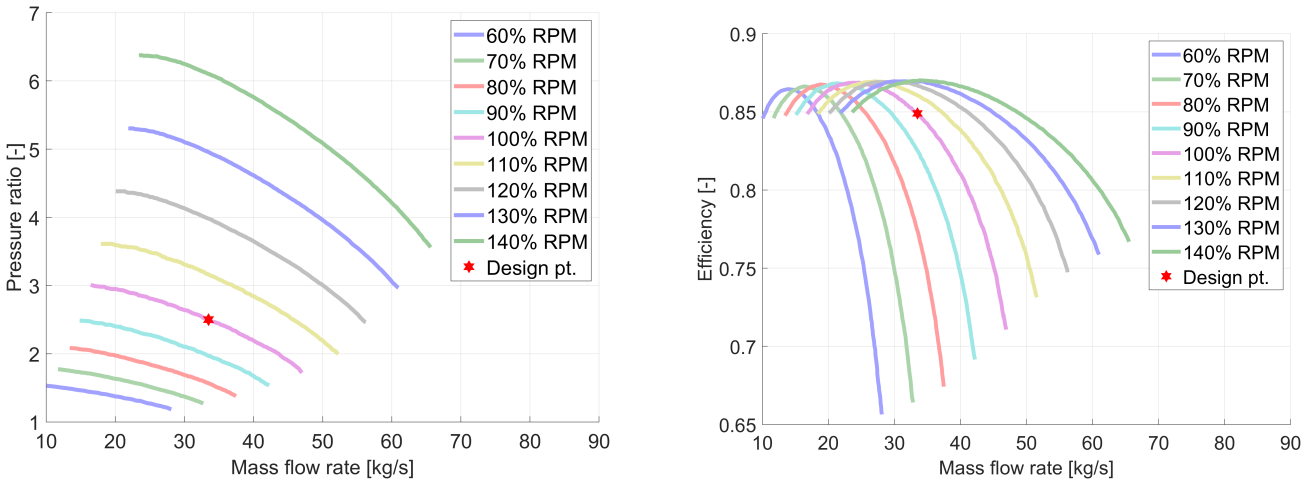

Figure 56: Recompressor performance maps

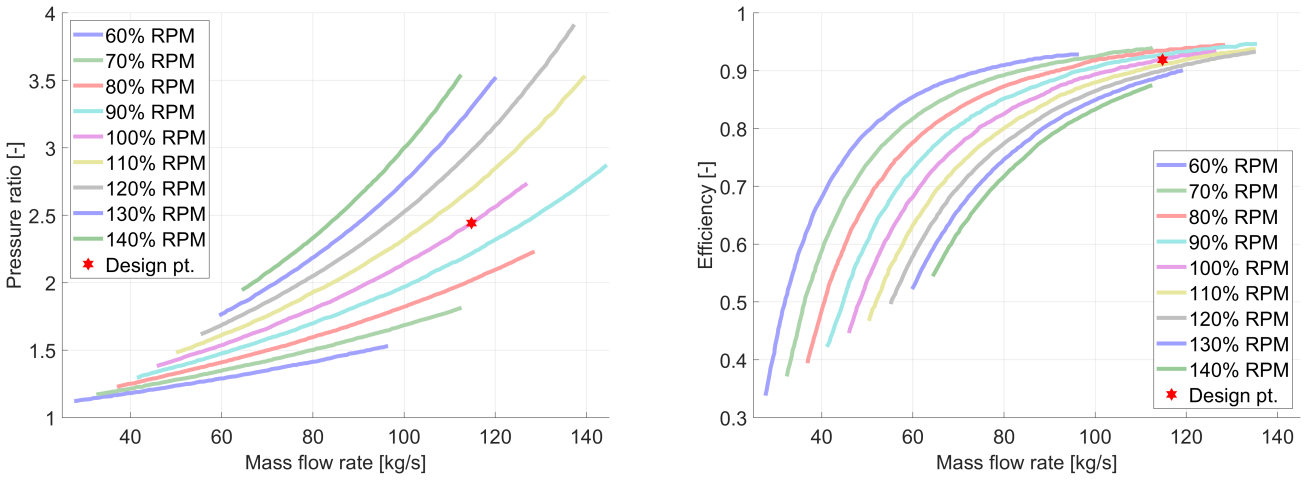

Figure 57: Turbine performance maps

4.8.2 Correction equations

Using a performance map ensures a more realistic performance simulation of the turbomachinery. However, it is also possible that inlet conditions like pressure and temperature change compared to the design values of the performance map. To account for these changes in pressure and temperature, correction models are applied to correct turbomachinery performance. These equations, or so-called similitude models, are able to correct the actual inlet temperature and pressure with the reference pressure and temperature of the performance maps, and therefore ensure that the maps are still applicable in off-design conditions.

There are 5 types of similitude models used for correcting the inlet conditions with the reference conditions of the performance maps. The relation between these different similitude models can be seen in Figure 58 and the equations used for correcting the enthalpy rise, the shaft speed and the mass flow can be seen in Table 16. In these equations, the temperature T, pressure p, specific gas constant R, the specific heat ratio γ and the compressibility factor Z are used. All the correction equations are based on the Ideal Gas (IG) approach and relate the reference ref conditions to the actual a conditions. Glassman reformulated the IG equations with critical temperature and pressure as inputs for non-ideal gas situation. This was done as the critical conditions account for specific heat ratio variations between the different temperatures and pressures, while the IG approach assumes a constant specific heat ratio [165]. The critical condition can be calculated according to Equation 57 and 58 [165].

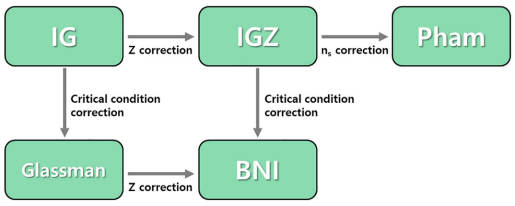

Figure 58: Relation correction equations [164]

$$Z_{cr}T_{cr} = ZT\left(\frac{1+\gamma}{2}\right)^{-1} \tag{57}$$

$$p_{cr} = p\left(\frac{1+\gamma}{2}\right)^{-\frac{\gamma}{\gamma-1}} \tag{58}$$

From these two methods, a compressibility correction can also be added. For the ideal gas case this results in the IGZ correction equations. The Barber-Nichols Inc. (BNI) correction equations applies the compressibility correction on the Glassman equations [165]. The compressibility correction is applied by adding the compressibility factor to the correction equations, which can be calculated by Equation 59.

$$Z = \frac{p}{\rho RT} \tag{59}$$

Table 16: Overview for the correction equations used in turbomachinery performance [116] [165][5]

Model	Δh_{corr}	N_{corr}	$\dot{m}_{corr}$
IG	$(\Delta h\frac{1}{\gamma RT})_a(\gamma RT)_{ref}$	$(N\frac{1}{\sqrt{\gamma RT}})_a(\sqrt{\gamma RT})_{ref}$	$(\dot{m}\frac{\sqrt{\gamma RT}}{\gamma p})_a(\frac{\gamma p}{\sqrt{\gamma RT}})_{ref}$
IGZ	$(\Delta h\frac{1}{\gamma RZT})_a(\gamma RZT)_{ref}$	$(N\frac{1}{\sqrt{\gamma RZT}})_a(\sqrt{\gamma RZT})_{ref}$	$(\dot{m}\frac{\sqrt{\gamma RZT}}{\gamma p})_a(\frac{\gamma p}{\sqrt{\gamma RZT}})_{ref}$
Glassman	$(\Delta h\frac{1}{\gamma RT_{cr}})_a(\gamma RT_{cr})_{ref}$	$(N\frac{1}{\sqrt{\gamma RT_{cr}}})_a(\sqrt{\gamma RT_{cr}})_{ref}$	$(\dot{m}\frac{\sqrt{\gamma RT_{cr}}}{\gamma p_{cr}})_a(\frac{\gamma p_{cr}}{\sqrt{\gamma RT_{cr}}})_{ref}$
BNI	$(\Delta h\frac{1}{\gamma RZ_{cr}T_{cr}})_a(\gamma RZ_{cr}T_{cr})_{ref}$	$(N\frac{1}{\sqrt{\gamma RZ_{cr}T_{cr}}})_a(\sqrt{\gamma RZ_{cr}T_{cr}})_{ref}$	$(\dot{m}\frac{\sqrt{\gamma RZ_{cr}T_{cr}}}{\gamma p_{cr}})_a(\frac{\gamma p_{cr}}{\sqrt{\gamma RZ_{cr}T_{cr}}})_{ref}$
Pham	$(\Delta h\frac{1}{n_sRZT})_a(n_sRZT)_{ref}$	$(N\frac{1}{\sqrt{n_sRT}})_a(\sqrt{n_sRT})_{ref}$	$(\dot{m}\frac{\sqrt{n_sRZT}}{n_sp})_a(\frac{n_sp}{\sqrt{n_sRZT}})_{ref}$

[5] Alsawy [116] neglects the critical compressibility factor at the Glassman and BNI equations, but Jeong et al. [164] and Pham et al. [165] (atleast for BNI) both apply the compressibility factor for these type of correction equations.

The fifth similitude method of Pham et al. [165] corrects the specific heat ratio with the isentropic volume exponent n_s compared the IGZ method. This isentropic volume exponent is defined in Equation 60 and for the ideal gas case n_s is equal to γ [165]. Here v is the specific volume of the fluid. The Pham method is the desired method for this use case. Not only do Jeong et al. [164] compare all these methods, and show that the Pham methods results in low error margins, but also Nederstigt and Pecnik [166] favour the use of the isentropic exponent in sCO_2 analysis, which is only used in the method of Pham. The importance of the isentropic exponent for sCO_2 can be seen in Figure 59. Here, the isentropic exponent differs drastically around the critical point of CO_2. Nederstigt and Pecnik [166] also present this change in isentropic exponent near the critical point, but also indicate that further from the critical point the isentropic exponent changes less. This means that for the main compressor (close to the critical point) the changes in isentropic exponent are expected to differ significantly, while for the turbine (far from the critical point) the changes are negligible.

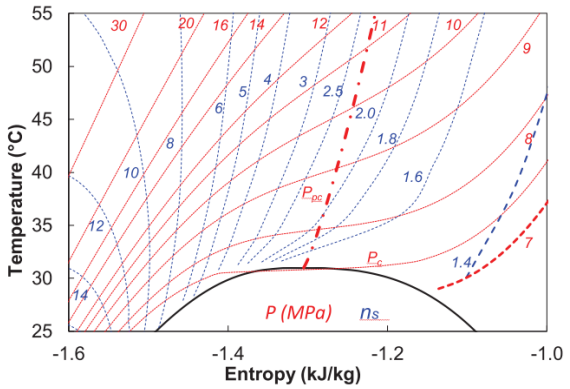

Figure 59: Isentropic exponent around the critical point of CO_2 [165]

$$n_s = -\gamma \frac{v}{p} \frac{\partial p}{\partial v}\bigg|_T \tag{60}$$

The pressure ratio obtained from the performance maps, using the corrected mass flow and shaft speed, is however still not the actual pressure ratio for off-design operating conditions. The actual pressure ratio can be obtained by the pressure ratio correction Equations 61 and 62, which should be used for the compressors and turbine respectively [116] [165]. To indicate the impact of the correction equations, Appendix A10 shows a comparison between using or neglecting the correction equations. It was shown that applying the Pham correction equations presented in Table 16 and the pressure ratio correction equations 61 and 62 is beneficial for accurately calculating turbomachinery performance.

$$\pi_{corr} = \left(1 + \frac{n_{s,ref} - 1}{n_{s,a} - 1}\left(\pi_a^{\frac{n_{s,a}-1}{n_{s,a}}} - 1\right)\right)^{\frac{n_{s,ref}}{n_{s,ref}-1}} \text{, for compressors.} \tag{61}$$

$$\pi_{corr} = \left(1 - \frac{n_{s,ref} - 1}{n_{s,a} - 1}\left(1 - \pi_a^{\frac{n_{s,a}-1}{-n_{s,a}}}\right)\right)^{\frac{-n_{s,ref}}{n_{s,ref}-1}} \text{, for turbines.} \tag{62}$$

Alsawy et al. [116] also state that the efficiency obtained by the performance maps should be corrected by a correction equation. This is however a novelty within literature and was therefore neglected. Further studies could determine the usefulness of such a correction equation as Alsawy et al. [116] show promising results regarding an error reduction in efficiency correction.

4.8.3 Power calculation

The combination of applicable performance maps, and correction factors for different inlet conditions, makes it possible to calculate the performance parameters of the turbomachinery. The turbomachinery models are created such that shaft speed, mass flow, pressure and enthalpy at the inlet side, will produce power, mass flow, pressure and enthalpy at the outlet side. First of all, it is assumed mass flow is equal at the inlet and outlet side according to Equation 63.

$$\dot{m}_i = \dot{m}_o \tag{63}$$

The actual inlet mass flow $\dot{m}_a$ and actual shaft speed N_a must first be corrected according to Equations 64 and 65 [116]. In these equations the mass correction factor MCF and shaft speed correction factor NCF are used to determine the corrected mass flow $\dot{m}_{corr}$ and corrected shaft speed N_{corr}.

$$\dot{m}_{corr} = MCF\,\dot{m}_a \tag{64}$$

$$N_{corr} = NCF\,N_a \tag{65}$$

In combination with the performance maps $f_{map}()$ and these correction factors, the pressure ratio π and efficiency η of the turbomachinery can be determined according to Equations 66-68 [116].

$$\eta = f_{map}(\dot{m}_{corr}, N_{corr}) \tag{66}$$

$$\pi_{corr} = f_{map}(\dot{m}_{corr}, N_{corr}) \tag{67}$$

$$\pi_a = f_{corr}(\pi_{corr}) \tag{68}$$

With the pressure ratio known, the outlet pressure can be determined according to Equation 69 for the compressors and Equation 70 for the turbine. Here, the pressure at the outlet of the compression $p_{C,o}$ is equal to the inlet pressure $p_{C,i}$ multiplied by the compression ratio π_C, while for the turbine the pressure at the outlet $p_{T,o}$ is equal to the inlet pressure $p_{T,i}$ divided by the expansion ratio π_T [91].

$$p_{C,o} = p_{C,i}\ \pi_C \tag{69}$$

$$p_{T,o} = \frac{p_{T,i}}{\pi_T} \tag{70}$$

To determine the outlet enthalpy of the turbomachinery Equations 71 and 72 can be used. Based on the efficiency of the turbomachinery, the inlet enthalpy h_i and the isentropic outlet enthalpy h_{isen}, the realised outlet enthalpy h_o can be calculated [91] [116].

$$h_{C,o} = h_{C,i} + \frac{h_{C,o,isen} - h_{C,i}}{\eta_C} \tag{71}$$

$$h_{T,o} = h_{T,i} - \eta_T(h_{T,i} - h_{T,o,isen}) \tag{72}$$

The isentropic enthalpy used in Equations 71 and 72 can be determined by realising the isentropic enthalpy states that entropy remains constant due to reversibility of the process. Therefore, entropy s can be determined at the inlet side of the turbomachinery and in a reversible process this would be equal to the entropy at the outlet. By using the already calculated outlet pressure, the isentropic enthalpy can be calculated as two thermodynamic properties are known. This has been presented in Equation 73.

$$s = f(h_i, p_i) \rightarrow h_{o,isen} = f(s, p_o) \tag{73}$$

The power consumed by the compressor, or produced by the turbine, is equal to the enthalpy difference between the inlet and outlet multiplied by the mass flow, which is presented in Equations 74 and 75. The power difference between these components, and the power consumed by the pumps and blower, will result in an overall electricity P_{elec} produced by the power conversion system. Here, it is assumed the generator does not impact the dynamic power behaviour of the power conversion and will only have an impact on the amount of power produced, which is accounted for by an overall generator efficiency η_{gen}. The power produced can be calculated by Equation 76 in which i is the amount of turbines, j is the amount of compressors and k is the amount of pumps or blowers in the power conversion cycle.

$$P_C = \dot{m}_C\,(h_{C,o} - h_{C,i}) \tag{74}$$

$$P_T = \dot{m}_T\,(h_{T,i} - h_{T,o}) \tag{75}$$

$$P_{elec} = (\sum_i P_T - \sum_j P_C)\,\eta_{gen} - \sum_k P_{P/B} \tag{76}$$

4.9 Rotating shaft model

4.9.1 Shaft inertia

The inertia I of the shaft limits the acceleration of the shaft and is therefore crucial in determining the change of shaft speed. For preliminary research purposes it is common to determine the inertia by applying a scaling analysis from a known power plant [108] [140]. Pope [167] determined the shaft inertia belonging to a 2400 MWth nuclear power plant connected to an sCO_2 power conversion cycle of which the values are given in Table 17. To determine the inertia values for the selected power conversion cycle the inertia values have been calculated according to Equation 77 [108]. Here, the cycle power P_{cycle} is equal to the reactor power output of 20 MWth and the reference power P_{ref} is equal to the reactor power output of 2400 MWth used by Pope [167]. The results of this scaling are visible in Table 17.

$$I_{scaled} = \frac{P_{cycle}}{P_{ref}} I_{ref} \tag{77}$$

The total shaft inertia is equal to the summation of the inertia of the individual machines and the shaft itself. The overall inertia can therefore be calculated according to Equation 78, which results in an overall shaft inertia for the selected cycle equal to 20.46 kgm^2.

$$I_{tot} = I_T + I_{MC} + I_{RC} + I_{gen} + I_{shaft} \tag{78}$$

Table 17: Moment of inertia (kg m^2) determined by Pope [167] and the scaled values for the selected power conversion cycle

Cycle power	Turbine	Main Compressor	Recompressor	Generator	Shaft	Total
2400 MWth	850	305.6	113.1	1000	186	2454.7
20 MWth	7.08	2.55	0.94	8.33	1.55	20.46

4.9.2 Shaft speed dynamics

The shaft speed dynamics of the power conversion cycle can be calculated according to the inertia I, the shaft speed N and the power of the different components connected to the shaft P. For a recompression cycle applying a TAC configuration, the rotating speeds of the turbine, compressor and external load are the same. As a result, the shaft speed will only change by a change in positive torque generated by the turbine or a negative torque generated by the compressors or external load [118]. Therefore, the dynamics of the shaft speed can be determined according to Equation 79 [101] [108] [134].

$$I_{tot} N \frac{dN}{dt} = P_T - P_{MC} - P_{RC} - \frac{P_{load}}{\eta_{gen}} - P_{loss} \tag{79}$$

Friction losses are accounted for by P_{loss}, but for simplicity it was assumed these losses are negligible. As the power load demand is an electrical power demand, the load must be divided by the efficiency of the generator, which was set to 98.7% [91]. The other power loads are determined by the enthalpy difference over, and the mass flow through, the turbomachinery.

4.10 Control valves

The pressure difference over a throttle and bypass valve is significantly different. Throttle valves are placed between pipes that contain similar pressure levels, resulting in low pressure differences over the valve. Bypass valves are connected between the high and low pressure side of the power conversion cycle, resulting in large pressure differences. For a throttle valve it is common that the pressure drop is equal to 0.3-0.6 of the total pressure drop over the piping in which it is located [133]. As explained in Section 3.5 the overall cycle pressure drop is 1.92 bar, which is the result of 6 heat exchanger passings. Assuming an equal pressure drop over each heat exchanger results in a 0.32 bar pressure drop, indicating that the pressure drop over the throttle valve should be related to this pressure drop. It was therefore decided that the valves are constructed in such a way, that a pressure drop of 0.1 bar occurs over the throttle valve in design conditions, as this is within the pressure drop range stated by Bian et al. [133]. For a bypass valve, the inlet and outlet pressure are equal to the high pressure side and low pressure side of the power conversion cycle, which are designed at 90 and 225 bar. Due to this large pressure difference, choke could occur within the valve and Bian et al. [133] therefore state that different equations should be used for describing the valves.

For a small pressure difference, the case of a throttle valve, Equation 80 can be used. For a bypass valve, the mathematical model of an orifice plate flow with a large pressure difference can be used, which is presented in Equation 81. In these equations the mass flow $\dot{m}$ is related to a discharge coefficient C_d, the relative opening area of the valve f_{open}, the geometrical flow area A, the flow density ρ, the pressure difference between the inlet p_i and outlet p_o of the valve and the specific heat ratio γ [133]. The specific heat ratio, in comparison with the isentropic exponent, can be used in the case of a bypass valve as the inlet of the valve is close to the turbine. At this point the operating conditions of CO_2 are far above its critical point, which results in a small difference between the specific heat ratio and isentropic exponent [166].

$$\dot{m} = C_d f_{open} A \sqrt{2\rho(p_i - p_o)} \tag{80}$$

$$\dot{m} = C_d f_{open} A \sqrt{\frac{2\gamma}{\gamma - 1}\rho_i p_i \left(\left(\frac{p_o}{p_i}\right)^{\frac{2}{\gamma}} - \left(\frac{p_o}{p_i}\right)^{\frac{\gamma+1}{\gamma}} \right)} \text{ , for } \left(\frac{2}{\gamma+1}\right)^{\frac{\gamma}{\gamma-1}} \leq \frac{p_o}{p_i} < 1 \tag{81}$$

$$\dot{m} = C_d f_{open} A \left(\frac{2}{\gamma+1}\right)^{\frac{\gamma+1}{2(\gamma-1)}} \sqrt{\gamma \rho_i p_i} \text{ , for } \frac{p_o}{p_i} < \left(\frac{2}{\gamma+1}\right)^{\frac{\gamma}{\gamma-1}}$$

These equations, and the boundary conditions stated for the throttle and bypass valves, make it possible to calculate the constant valve construction coefficient C_v, which is equal to the discharge coefficient multiplied by the geometrical flow area [133]. The results of this are presented in Table 18 and are used within the simulation as constants.

Table 18: Valve coefficients for the throttle and bypass valves

Valve number	V1	V2	V3	V4	V5	V6
Valve type	Throttle	Throttle	Throttle	Throttle	Bypass	Bypass
Valve coefficient C_v	0.0442	0.0662	0.0348	0.0464	0.0028	0.0024

5 Model validation

5.1 Point kinetics

Although the values for the point kinetic equation for the U-battery are displayed in Atkinson et al. [147], a validation possibility is not presented. Therefore, for the validation the values presented in Anglart [149] have been used, which are presented in Table 19. These values are presented as a Six-Group Point Kinetic Equation, but Anglart rewrites these values first to the One-Group Point Kinetic Equation before calculating the power change. In addition to the values presented in Table 19, the reactivity change set on the model is equal to $\rho = 0.0022$ at time t = 0, and the neutron generation time was set to $\Lambda = 10^{-3}$ s [149].

In Figure 60 a comparison is made between the relative power change calculated by the created model and presented by Anglart [149]. The two graphs are similar, but slightly differ at the end. However, this small difference is probably the result of rounding the numbers produced by Anglart [149]. For example, Anglart states that the total value for β_i/λ_i is equal to 0.084, while the model calculates a value of 0.0846. This small inaccuracy could explain the difference in Figure 60 and therefore the PKEs are deemed validated.

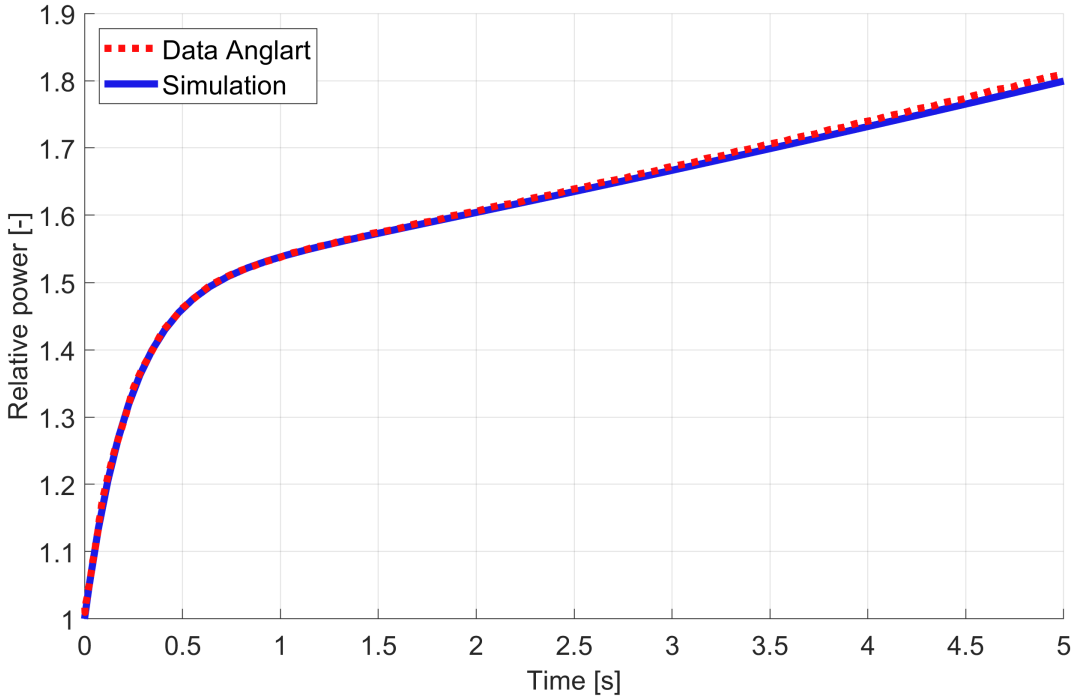

Figure 60: Comparison between the relative power change between the created model and Anglart [149]

Table 19: Input values used in the One-Group Point Kinetic equations [149]

Group	1	2	3	4	5	6	Total
Delayed neutron fraction (β_i)	0.000215	0.00142	0.00127	0.00257	0.00075	0.00027	0.0065
Decay constant (λ_i)	0.0124	0.0305	0.111	0.301	1.1	3.0	-
β_i/λ_i	0.0173	0.0466	0.0114	0.0085	0.0007	0.0001	0.084

5.2 Thermal-hydraulics

The thermal hydraulic (TH) model, created based on the design of the U-battery, applies a 1D heat transfer balance as model approach. Although this modelling approach has been used in literature, a detailed thermal hydraulic model and detailed information about the TH dynamics of a VHTR are lacking in literature. Therefore a validation approach based on dynamic values is not possible in the current research phase. To at least give an indication about the validity of the TH-model, it was decided to compare steady state temperatures of the U-battery during full power and to apply a sanity check about the dynamic results. Further research should focus on obtaining a detailed reactor design, including dynamic thermal hydraulic behaviour of an HTGR/VHTR.

The temperature distribution within the reactor of a 10 MWth U-battery design has been presented by Atkinson et al. [136] [122] and is presented in Table 20. However, some small temperature inconsistencies are present between the different sources. Atkinson et al. present a temperature for the insulation of 973.5 K [136] and 673 K [122], while for the RPV a temperature of 673.5 K [136] and 300 K [122] is given. An explanation for this could be the lack of stating which exact temperature point is used. A large temperature gradient, which is especially expected within the insulation, could result in large temperature deviations if wall or average temperatures are taken. Atkinson et al. [136] neglect stating for each material at which exact point the temperatures are calculated, which could therefore explain this difference.

Another inconsistency occurs between the different temperatures of several materials. Atkinson et al. [122] state that the outlet temperature of the coolant is equal to 1023.15 K, which is the exact temperature presented for the fuel and the matrix, as can be seen in Table 20. This therefore suggests that heat is transferred without a temperature gradient, which is not expected according to Fourier's law of thermal conduction. Travis and El-Genk [156] analysed the thermal hydraulics of a VHTR core and showed that a temperature gradient occurs within the matrix, as shown in Figure A5. An explanation could be that Atkinson et al. [136] chose to state general temperature values for the fuel and matrix, as the stated values are exactly 750°C. As the created model calculates average material temperatures, this could explain the large validation error up to 14.24%.

Table 20: Steady state temperature comparison of the U-battery

Material	Fuel	Matrix	Reflector	Insulation	Barrel	RPV
Atkinson et al. [136]	1023.15 K	1023.15 K	973.15 K	973.5 K	673.5 K	673.5 K
Model	1131.4 K	1127.5 K	1111.7 K	896.2 K	688.3 K	674.2 K
Error	10.58 %	10.20 %	14.24 %	-7.94 %	2.20 %	0.10 %

As detailed information about an HTGR/VHTR is lacking in literature, it is not possible to dynamically validate the TH-model. Still, a sanity check can be performed which has been done by performing a power transient and comparing the ramp rates with general values stated in literature. The results of a power increase and decrease between the power levels of 50% and 100% are presented in Figures 61 and 62. Here, a PID controller changes the height of the control rods to control the reactor power. The output of this PID controller is presented as rate-limited and unrestricted signal, of which the difference occurs due to the restricted control rod speed, as explained in Section 4.5.2. This clearly indicates that it is not possible to achieve faster reactor power transients.

During the decreasing power transient, the power level is reached after 290 seconds, resulting in a ramp rate of 10.34%/min. For the increasing power transient, the power level is reached after 250 seconds, resulting in a ramp rate of 12.00%/min. In Section 2.4 it was determined that for different types of HTGR/VHTR the ramp rate is between 5-10%/min, so the model produces dynamic results slightly above this range. As this range is based on a few selected reactors, the produced ramp rates are still within reason. In addition, if ramp rates

within literature are based on the time when the power stabilizes at the new power level, and not the first time the new power level is reached, than ramp rates of the model would fall within the range of 5-10%/min.[6]

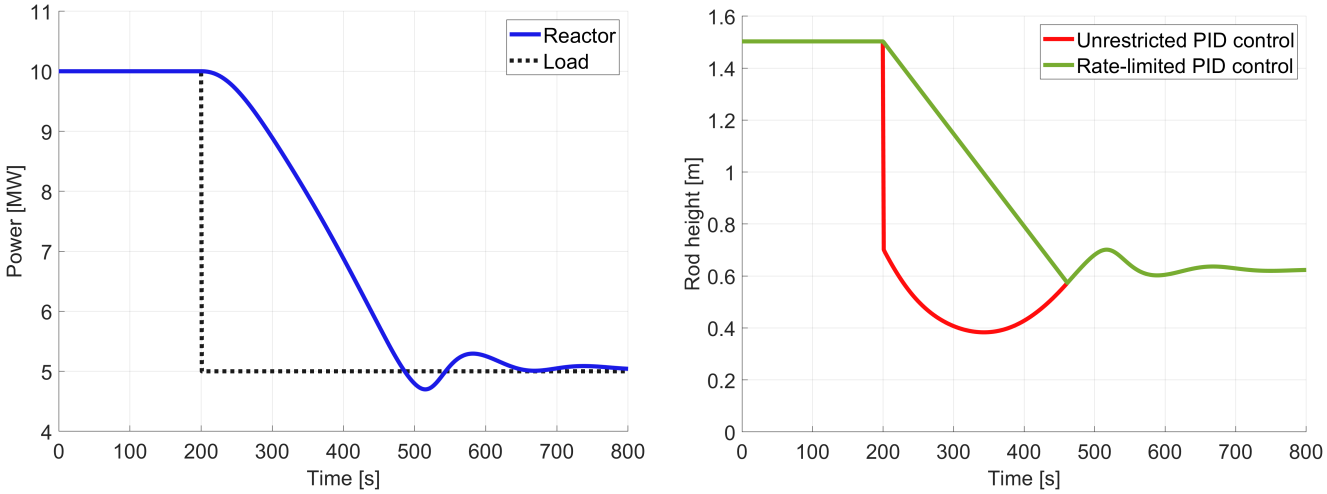

Figure 61: Power and control output during a power transient from 10 to 5 MWth

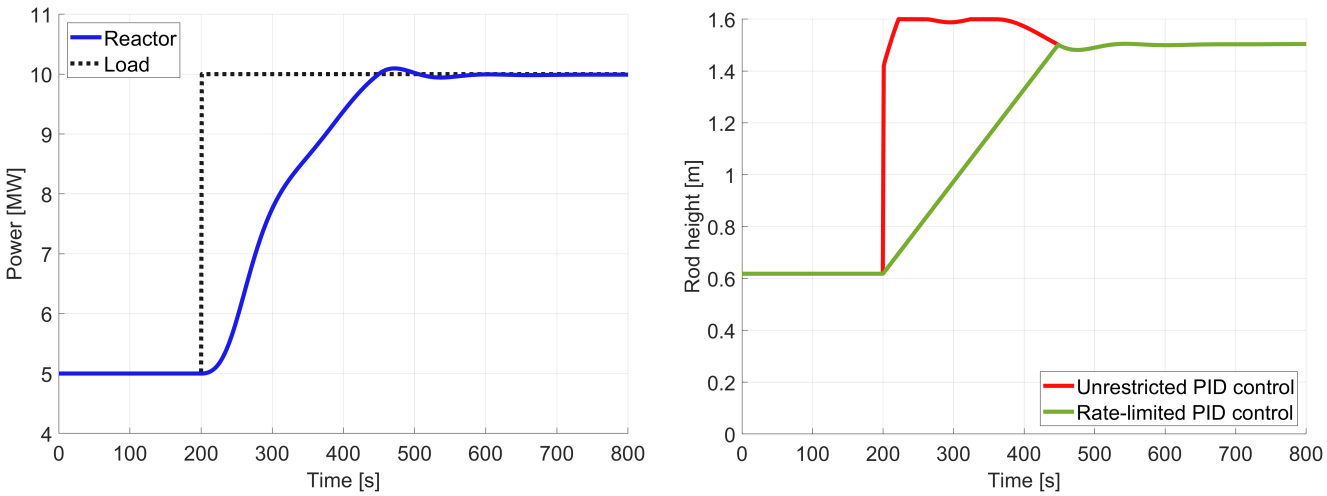

Figure 62: Power and control output during a power transient from 5 to 10 MWth

Further validation is required to determine if the created model is an accurate representation of an HTGR/VHTR. This however requires proper validation data that can be interpreted with full clarity, as current inconsistencies cannot explain if the temperature error of 14.24% is a model error or an interpretation error. Temperature is an important parameter for monitoring a safe environment within the reactor, but as the calculated temperatures of the model are higher than values of Atkinson et al. [122] it can be assumed that the model is capable to indicate a safe temperature environment. Furthermore, the sanity check of the dynamic power transient is within reason of ramp rates stated within literature of an HTGR/VHTR. The thermal-hydraulics model is therefore deemed acceptable for the preliminary dynamic analysis purpose of this study.

[6]The ramp rates of the model are based on the moment the reactor power reaches the desired power level for the first time and not the moment the reactor power stabilizes at the new power level. As this moment is 100–200 seconds later, this could reduce the overall ramp rate. Unfortunately, it is not clear at which exact moment the ramp rate of the reactor is calculated within literature.

5.3 Heat exchanger

The heat exchangers used in the created model are all wavy channeled printed circuit heat exchangers (PCHE) and are all modelled by the method discussed in Section 4.7. To dynamically validate this PCHE mode, a validation has been performed compared to the 630 kW sCO_2 recuperator of Marchionni et al. [138]. Here, Marchionni et al. [138] apply a dynamic heat exchanger model on experimental data of an sCO_2 PCHE.

For the transient simulation of the PCHE, the inlet conditions are presented in Figure 63. Appendix A11 provides the additional input values used by Marchionni et al. [138] for the sizing of the heat exchanger. Values not stated by Marchionni et al. [138] were assumed to be equal to general values of stainless steel 316L according to Table 9. Marchionni et al. [138] also state the inlet conditions of this simulation as text, but the values within the figure and in the text do not match[7]. As the output values of the transient simulation are displayed in a similar figure as the inlet conditions, it was decided to digitize the figure of the inlet conditions and use these as input values, neglecting any inlet values stated in the text.

The temperature and pressure results are presented in Figures 64 and 65 respectively, while Table 21 presents the error percentages at the end of the simulation. Here, multiple heat exchanger models are applied, which differ in the amount of nodes, to determine the impact on the accuracy of the model. The error for the pressure ranges between 0.12-0.22%, while the temperature error ranges between 0.63-1.5%. Although Marchionni et al. [138] also apply a 1D heat exchanger modelling approach, the exact modelling strategy and used equations are not clear, which could have an impact on the validation error. In addition, the uncertainty in inlet conditions due to the fact that values in figures and text do not match could also impact this error. With all these uncertainties, the error was deemed small enough to validate the heat exchanger model for the purpose of this study.

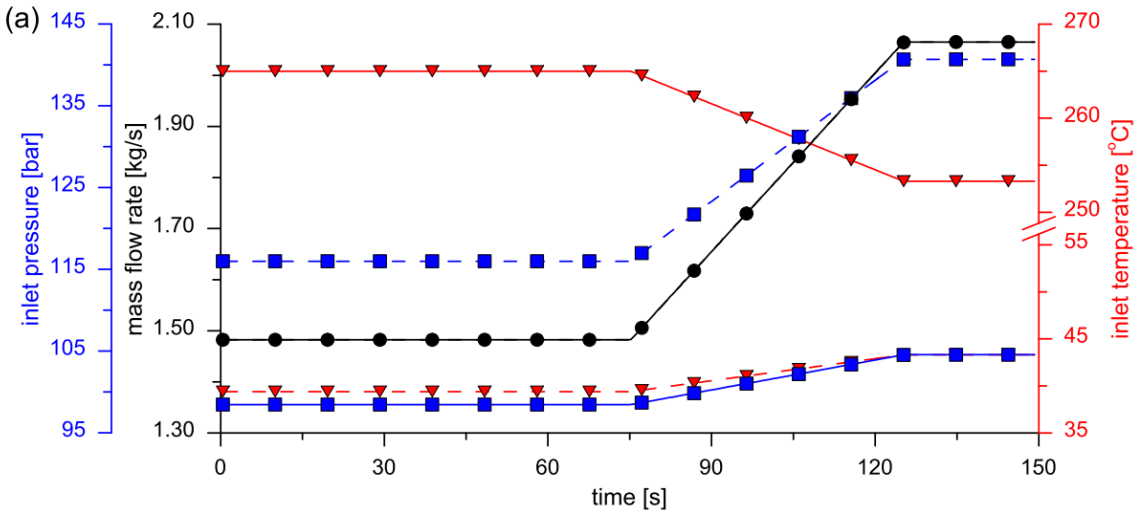

Figure 63: Inlet conditions during the transient simulation of Marchionni et al. [138]

Table 21 shows the impact of the amount of nodes used in the model on the accuracy and run time of the simulation. The run time is the time needed to simulate the 150 seconds duration of the simulation. Although a small number of nodes is still capable to produce accurate results (error of 1.5% for 5 nodes), it was decided to use a 20 node heat exchanger model. This number of nodes shows the most value regarding error reduction, while not resulting in significant increases in run time. For example, a 60 node structure increases the run time

[7] Marchionni et al. [138] state that the mass flow rate starts at 1.51 kg/s, while in the figure the line starts below 1.5 kg/s. The digitized value of the mass flow rate was equal to 1.48 kg/s, showing a clear inaccuracy between stated and visualized values.

by over 13 times compared to a 20 node structure, while only decreasing the error by 0.03%. The 20 node structure produces temperature and pressure errors smaller than 1.1%, which was deemed small enough for validation. The selected amount of nodes is higher compared to a more common 10 node structure [91] [111].

Table 21: Run time, pressure and temperature errors of models with different amount of nodes, compared to results presented in Marchionni et al. [138].

Number of nodes	Run time	Pressure cold/hot side error	Temperature cold/hot side error
5	5.00 s	-0.21/-0.14%	1.50/-1.07%
10	12.15 s	-0.22/-0.13%	1.17/-0.74%
20	35.97 s	-0.22/-0.13%	1.09/-0.66%
40	180.38 s	-0.22/-0.12%	1.07/-0.64%
60	480.45 s	-0.22/-0.12%	1.07/-0.63%

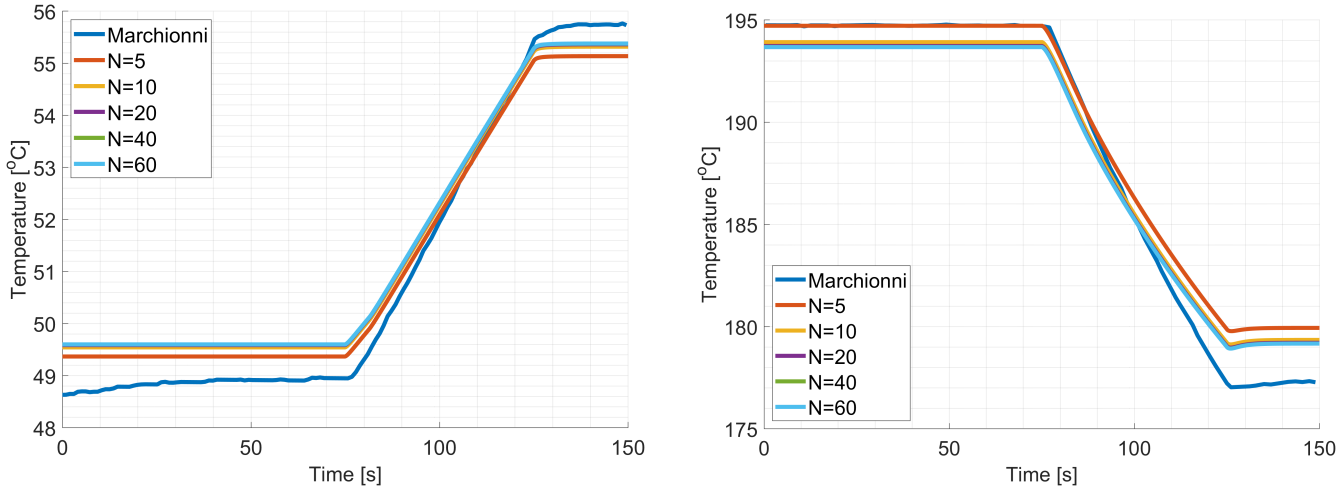

Figure 64: Temperature comparison between the model with different amount of nodes and values presented in Marchionni et al. [138]. Left side displays the hot HX side temperature and right side the cold HX side.

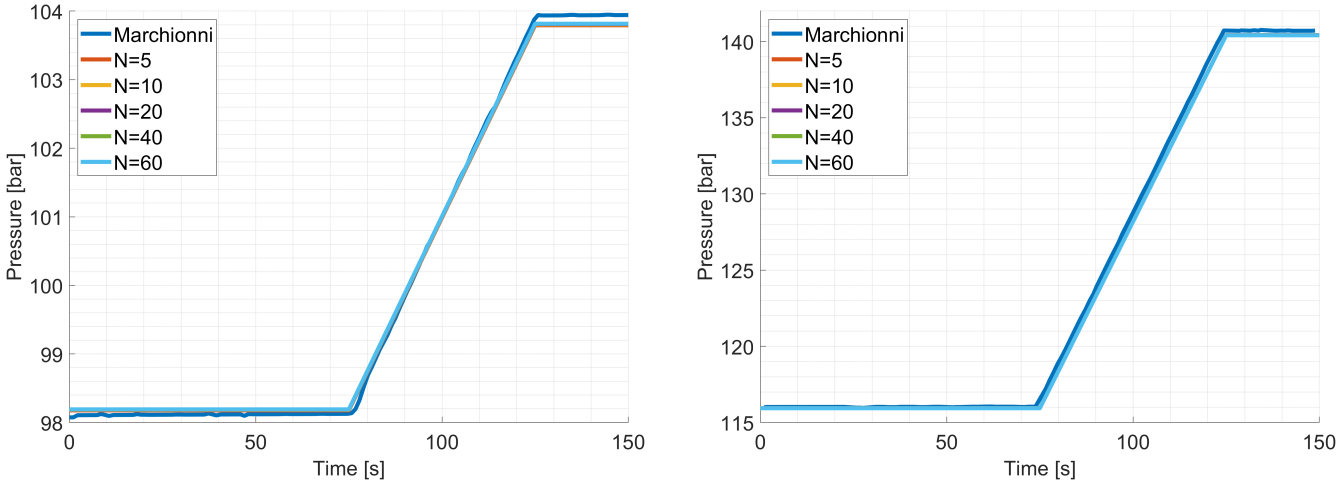

Figure 65: Pressure comparison between the model with different amount of nodes and values presented in Marchionni et al. [138]. Left side displays the hot HX side temperature and right side the cold HX side.

5.4 Turbomachinery

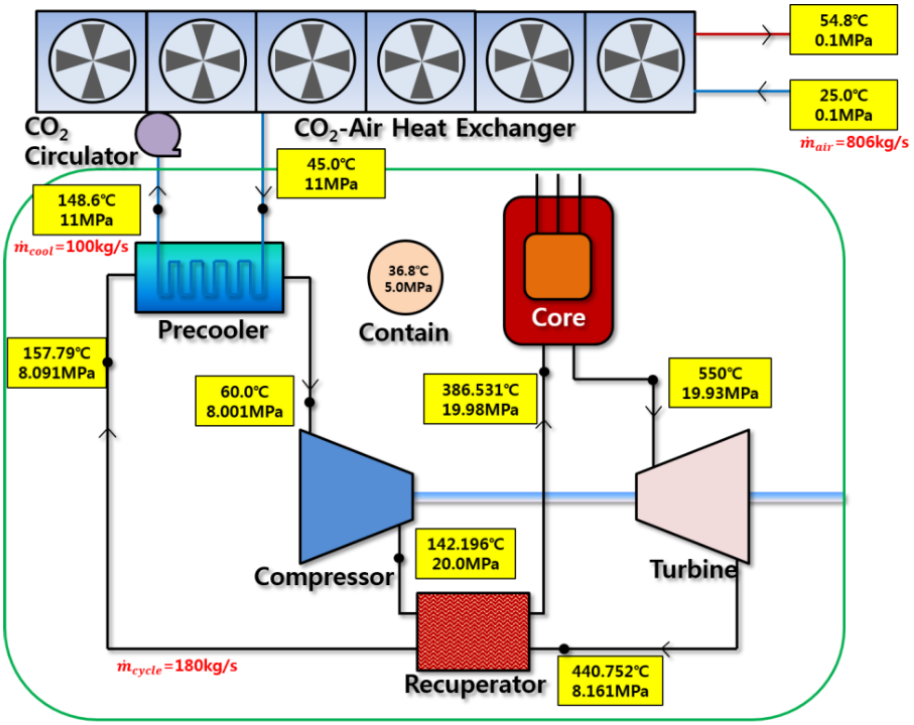

Figure 66: Designed cycle by Oh et al. [108]. Values used as input for turbomachinery validation

To validate the created turbomachinery model, the original performance maps presented by Oh et al. [108] will be used. Here, the input values stated by Oh et al. [108], as presented in Figure 66, have been used as input for the created compressor and turbine model. In Table 22 a comparison has been made between the different output values of the compressor and turbine. The errors of the outlet pressures and temperatures are all below 0.18%. The largest error occurs at the consumed/produced power as for the compressor this is 0.32%, while for the turbine -0.73%. The power errors are even smaller (compressor 0.09% and turbine -0.47%) if the power outputs from KAIST are determined by applying Equation 82, instead of the stated power values by Oh et al. [108], and inserting the input and output temperature and pressure presented by KAIST. This could indicate that values stated by KAIST are rounded, which impacts the exact error calculation. Still, all the errors are deemed small enough to validate the created turbomachinery model.

$$P = \dot{m}\Delta h, \text{ with } h = f_{cp}(T, p). \tag{82}$$

Table 22: Turbomachinery comparison between the created model and KAIST [108]

	Compressor			Turbine		
Output parameter	KAIST	Model	Error	KAIST	Model	Error
Pressure	20.000 MPa	20.005 MPa	0.03%	8.161 MPa	8.176 MPa	0.18%
Temperature	142.196 °C	142.236°C	0.03%	440.752°C	441.257°C	0.11%
Power	9.340 MW	9.372 MW	0.34%	21.750 MW	21.592 MW	-0.73%

6 Control

6.1 PID controller

For safe and optimal performance of the power conversion cycle, multiple control options should be included within the cycle. One of the most common and easily implemented ways of control is the Proportional-Integral-Derivative (PID) controller. As the aim for this research is not to provide a full control setup for a power conversion cycle, the PID controller will be selected to provide preliminary control results. The PID controller works based on the control function presented in Equation 83 [134]. Here the output value $u(t)$ of the PID is dependent on the error value $e(t)$, which is the difference between a desired setpoint and a measured variable during the simulation. The K_P, K_I and K_D denote the constants for the proportional, integral and derivative terms of the controller.

$$u(t) = K_P\, e(t) + K_I \int_0^t e(\tau)\, d\tau + K_d \frac{d\, e(t)}{dt} \tag{83}$$

There is a distinction between the different control purposes and control configurations can be classified under two control groups: disturbance rejection and setpoint tracking. Control based on disturbance rejection tries to maintain a certain desired output despite variable changes during the simulation. This control option therefore tries to minimize the impact of unexpected external inputs on the system. Setpoint tracking is based on the principle that during the simulation a certain value or trajectory should be reached (and maintained). This control option therefore tries to control changes in the desired output of the system.

6.2 Disturbance rejection

Disturbance rejection control systems are implemented to limit the impact of unwanted variable changes. These control systems are therefore always active within the power conversion cycle. For this research five disturbance rejection control systems were chosen, as these were deemed capable to maintain the stability of the power conversion cycle. The five types of parameters that are controlled are the main compressor inlet temperature, the in-/outlet pressure of the compressors and the in-/outlet temperature of the helium within the reactor.

6.2.1 Main compressor inlet temperature

Figure 67: Control system for the main compressor inlet temperature

The sCO_2 conditions at the inlet of the main compressor are the closest to the critical point of CO_2. To ensure the fluid conditions do not drop below the critical point of CO_2, and enter a two phase region, it is important to monitor and control the temperature at the inlet of the main compressor [133] [134]. The main compressor inlet temperature is regulated according to the control system presented in Figure 67. The PID controller acts based on a temperature difference for the inlet of the main compressor. By changing the seawater mass flow through the cooler, this error is adjusted [133]. In reality this change in mass flow can be realised with a seawater pump. It must be noted that other control mechanisms like a cooler bypass valve could also be used for main compressor inlet temperature control [85] [113], but these have been neglected for this study.

6.2.2 Compressor inlet pressure

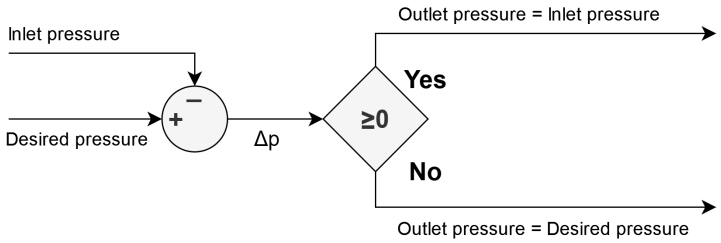

Figure 68: Valve control system for the compressor inlet pressure

The applied power conversion cycle is designed in such a way that the pressure losses over the heat exchangers are less than the difference in pressure ratio over the compressors and turbines (see Section 3). The pressure increase by the compressors is slightly higher than actually needed. The result of this is that the inlet pressure at the compressors is slightly higher than at the previous timestep, meaning that the pressure increases slightly over time. Throttle valves are used to maintain a certain compressor inlet pressure and prevent this pressure increase. However, it was decided to not implement PID controllers for these valves due to simplicity. As the response time of the valves is negligible compared to other components [133] it was decided to control the outlet pressure based on a limiter as displayed in Figure 68. This ensures that valve control acts instantly and therefore does not create simulation noise for other components. By using the pressure at the inlet as upper limit, the limiter will ensure that the desired pressure can never realise a pressure increase over the valve. The desired main compressor inlet pressures was set to 90 bar as this is the lower design pressure of the cycle. For the recompressor the design pressure is set slightly higher at 90.5 bar. This was done to ensure that the outlet pressure of the recompressor is slightly higher than the pressure after the LTR, which makes the outlet pressure of the recompressor controllable.

6.2.3 Compressor outlet pressure

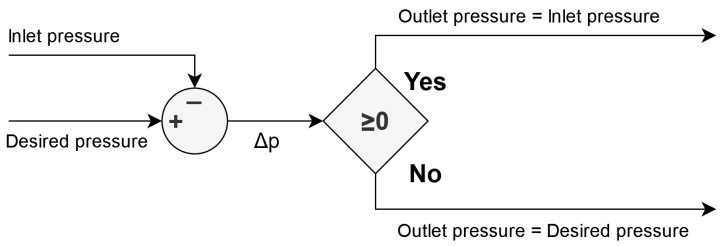

Figure 69: Valve control system for the compressor outlet pressure

As previously mentioned, the outlet pressure of the compressors should be controlled not only to prevent pressure increasing above the maximum pressure, but also to ensure that the two fluid streams entering the mixer after the recompressor contain the same pressure. To control the outlet pressure of the compressors, a throttle valve is implemented which applies the control system presented in Figure 69. This control system acts the same as for the inlet pressure of the compressor, but the only difference is the dependency of the desired compressor outlet pressure for the recompressor. For the main compressor the desired compressor outlet pressure is set to the maximum cycle pressure of 250 bar, but for the recompressor the desired pressure depends on the pressure after the LTR. As this changes during the simulation, the desired output pressure also changes for the recompressor.

6.2.4 Reactor outlet temperature

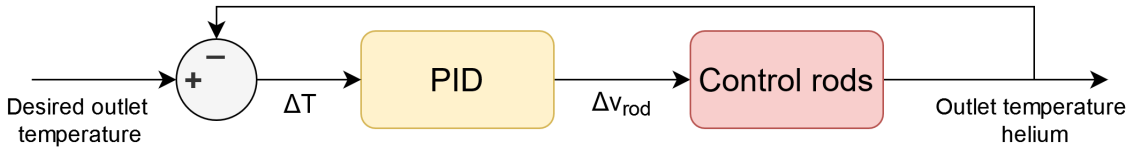

Figure 70: Control system for the reactor outlet temperature

Figure 70, presents the control configuration for the reactor outlet temperature. To ensure the temperatures in the reactor are maintained within a safe limit, the inlet and outlet temperature of the helium were selected as control parameters. However, in reality other temperatures, like fuel temperature, could be selected. The outlet temperature of the helium is of importance to ensure enough power is produced for the secondary cycle, as otherwise power demand cannot be achieved. A PID controller will act on a temperature difference by raising or lowering the control rods, which will account for the limitations in control rod speed as explained in Section 4.5.2. As the control rods produce a reactivity change within the reactor, this will result in a change in reactor outlet temperature, if inlet temperature is controlled.

6.2.5 Reactor inlet temperature

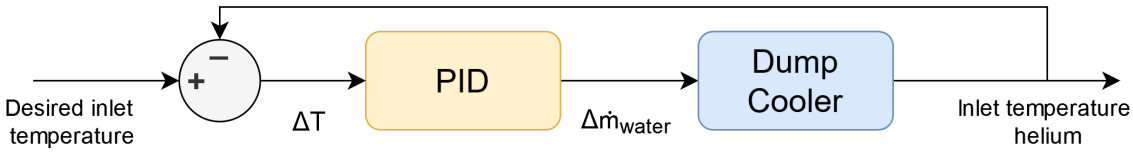

Figure 71: Control system for the reactor inlet temperature

As the outlet temperature is controlled by the control rods, and one control mechanism cannot control two output parameters, an additional control option has been implemented for controlling the reactor inlet temperature. This has been realised by implementing an additional cooler, the dump cooler, to the primary circuit of the system. This cooler operates similar to the cooler present within the secondary cycle, and controls the inlet temperature of the reactor according to Figure 71. Controlling the inlet temperature is of importance as a high inlet temperature results in material damage to the reactor, which must be prevented. For example, the barrel and RPV are made of steel which cannot reach a temperature above 425°C [136]. As these two materials are in direct contact with the inlet stream of the reactor, the inlet temperature of the helium must be maintained within safe limits.

6.3 Setpoint tracking

Setpoint tracking control systems aim to achieve and maintain a certain output value during the simulation. For this research the power load on the system changes and must therefore be controlled. This can be done in several ways of which reactor power control and bypass control are implemented for this research. In reality, a change in power cannot be monitored directly. However, according to Equation 79 will the shaft speed change due to a change in power load, and as the shaft speed can be monitored, this parameter will be used in setpoint tracking control.

6.3.1 Reactor power

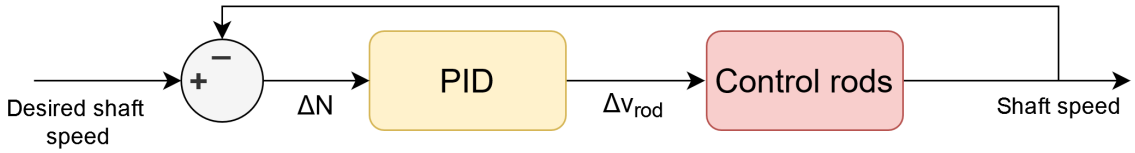

Figure 72: Control system for the reactor power

For controlling the power output of the reactor, the control system presented in Figure 72 is applied. Here, a PID controller monitors the difference in shaft speed compared to the desired shaft speed. Based on the error margin, the position of the control rods (and thus reactivity) is controlled by changing the speed of the control rods. For reactor control it is important that the reactor changes its power steady, to ensure a change in reactivity will not produce prompt critical conditions, as explained in Section 4.5.2. It must be noted that using this control method for setpoint tracking, reduces the possibility of controlling the reactor outlet temperature for disturbance rejection, as one control mechanism cannot control multiple parameters.

6.3.2 Bypass valve

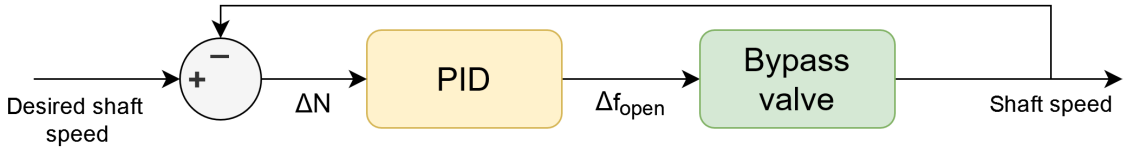

Figure 73: Control system for the bypass valve

Another power control method is by applying a bypass valve within the system. This bypass valve is applied according to control system presented in Figure 73. The PID controller will adjust the error in shaft speed by opening or closing the bypass valve. Flow entering the bypass valve will not enter the turbine, decreasing the power output of the turbine and this way stabilizing the shaft speed if the power load decreases. Vice versa occurs when the power load increases, until the valve is fully closed.

6.4 PID tuning

For this research it was decided to tune the PID controller manually by adjusting the PID constants until an acceptable controller response was realised. Due to a lack of time, additional complexities of PID tuning, like table based tuning, were neglected as perfect control conditions are not required for this research. The tuning results for the different PID controllers are presented in Table 23. For the reactor controller options, a normalization approach has been used on the parameter values, as this improved manually tuning the controller. The derivative terms were set to 0 for all PI(D) controllers as these were deemed unnecessary for stable reactor/cycle control.

Table 23: PI controller tuning values

Controller	K_p	K_i
Main comp. inlet temp.	-20	-5
Reactor inlet temp.	-3	-0.2
Reactor outlet temp.	1	0.02
Reactor power	1	0.02
Bypass valve	0.485	0.041

7 Results

7.1 Scenario overview

To determine the dynamic capabilities of a nuclear power plant, multiple different scenarios will be investigated. These scenarios will differ based on the specific control configuration and load transient, of which an overview is presented in Table 24. The results will present the following five different (steady state or dynamic) scenarios:

Scenario 0; presenting steady state results at full power,

Scenario 1; reactor dynamics, transient going as fast a possible,

Scenario 2; bypass control and constant reactor power output, power ramp rates comparable to a diesel engine,

Scenario 3; bypass control and additional dump cooler, power ramp rates comparable to a diesel engine,

Scenario 4; bypass control and additional dump cooler, power ramp rates comparable to a gas turbine.

Table 24: Control and power transient overview for the different scenarios

Category	Scenario 0	Scenario 1	Scenario 2	Scenario 3	Scenario 4
Control Overview					
Main compressor inlet temp.	Yes	Yes	Yes	Yes	Yes
Throttle valves	Yes	Yes	Yes	Yes	Yes
Reactor inlet temp.	No	No	No	Yes	Yes
Reactor outlet temp.	No	No	Yes	Yes	Yes
Reactor power	Yes	Yes	No	No	No
Bypass valve	Yes	Yes	Yes	Yes	Yes
Power Transients					
Lower power level	100% FP	10% FP	10% FP	10% FP	10% FP
Upper power level	100% FP	100% FP	100% FP	100% FP	100% FP
Transient speed	0%/min	13%/min	30%/min	30%/min	90%/min

The scenarios that will be investigated are based on ship manoeuvres. It was decided to only look at a full linear power demand going from the lowest power setting (10% FP) to the highest power setting (100% FP), back to the lowest power setting (10% FP), as this presents the most challenging power transient of a naval vessel. A 10% power level corresponds to the hotel load (base load) of a vessel, which includes the power of auxiliary systems such as the blower of the reactor. The increase of 90% corresponds to accelerating from zero propulsion power to full propulsion power. To determine if a nuclear power plant can achieve naval power dynamics, a comparison will be made with respect to conventional prime movers of a naval vessel. Section 2.1.3 determined that the diesel engine and gas turbine are the two most common prime movers of a naval vessel, being able to achieve a 10-100% load change in 180 and 60 seconds respectively (resulting in ramp rate of 30%/min and 90%/min). By applying these power transients, within different scenarios, it can be determined if a nuclear power plant can fulfill the power dynamics of a naval vessel.

Starting with scenario 0, the steady state results for operating at full power will be presented as reference condition. The dynamics of the nuclear power plant will then be investigated, starting with the limitation of reactor dynamics in scenario 1. The ramp rate of this scenario will go as fast as possible, resulting in a ramp

rate of 13%/min, based on a limitation for a change in shaft speed. The shaft speed is related to the frequency of the electrical grid, and this grid requires a relative stable frequency for all the electrical systems connected to the grid. Based on regulations of the International Electrotechnical Commission (IEC), it is assumed a frequency tolerance of 5% is acceptable [168]. As it is common for naval vessels to have a 60 Hz electrical grid, this results that a 3 Hz frequency drip is acceptable. As shaft speed and frequency are directly related to each other, this results that a shaft speed correction of 5% is acceptable.

The results of scenario 1 lead to the reactor being operated as a constant thermal power source in subsequent scenarios. Scenario 2, will further investigate if the reactor can be operated under constant thermal load, while changing the load with a ramp rate comparable to a diesel engine. Based on the results of this scenario, scenario 3 will activate the dump cooler, which can aid in maintaining a stable and safe reactor operation. Here, again the ramp rate of a diesel engine will be applied, to indicate the benefits of adding the dump cooler to the system. Finally, scenario 4 will apply the same operating conditions as scenario 3, but now the ramp rate is increased up to gas turbine level.

It must be noted that the implementation of the dump cooler was a later addition to improve cycle performance based on what was observed in the first few scenarios. The dump cooler is therefore, in contrary to the other heat exchangers present within the cycle, not modelled with a 1D node heat exchanger structure. The dump cooler is modelled as a simplified heat balance removing heat from the helium based on the energy conservation equation. In reality, the cooler cannot instantly remove the desired heat from the cycle, and therefore a PI controller and an additional filter have been added to introduce some simplified (first order) dynamics. The time constant of this filter was set to 5 seconds, simulating a slightly slower response rate compared to the time constant identified in the other modelled heat exchangers.

7.2 Scenario 0; steady state at full power

At first, the results belonging to a steady state scenario will be presented as reference conditions for the dynamic power scenarios. Here, the reactor and cycle are operating at full load, equal to a power demand of 20 MWth and 7.9 MWe. For these conditions, the turbomachinery is operating at its design point, as mass flow is equal to the design cycle mass flow, while shaft speed is equal to 100% of its rated speed. Figure 74 shows a power overview of the different components present within the power conversion cycle, of which the exact values are presented within Table A5. The temperature of the material sections present within the reactor are displayed in Figure 75. The colours used in this figure refer to the equivalent heat transfer scheme of the U-battery, as presented in Figure 50. Although the model only calculates the average temperature of the materials present within the reactor, an estimation can be made between the different average temperatures as overall heat transfer coefficients and heat transfer areas are known for each material. Finally, the performance of the IHX and HTR is presented in Figures 76 and 77. Here, the hot and cold fluid stream temperature and heat transfer coefficients are presented, while also presenting the temperature of the wall splitting the two fluid stream. For the LTR and CL similar figures are presented in appendix A12. The in-/outlet temperatures presented in these figures differ slightly from the design values presented in Table 10, which is expected as the design process does not account for pressure losses occurring within the cycle.

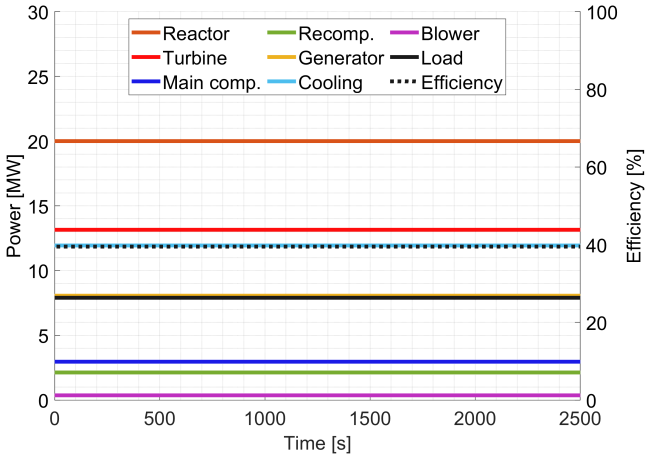

Figure 74: Cycle efficiency and power production/-consumption of different cycle components

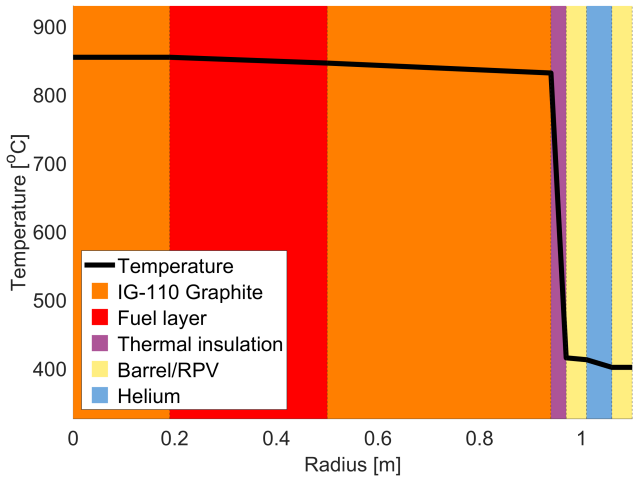

Figure 75: Temperature distribution within the reactor at full power load

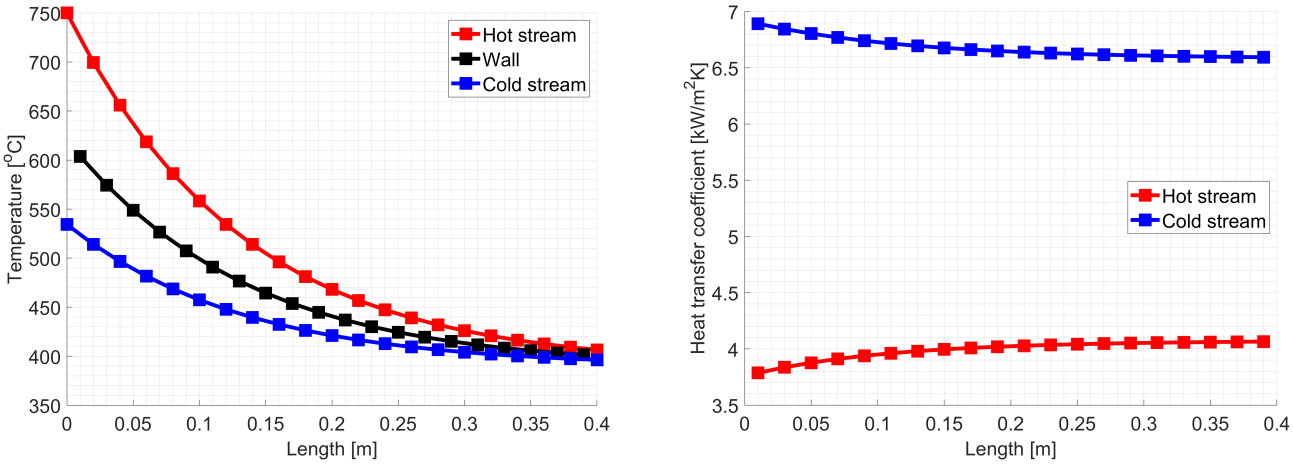

Figure 76: Temperature and heat transfer coefficient along the length of the IHX

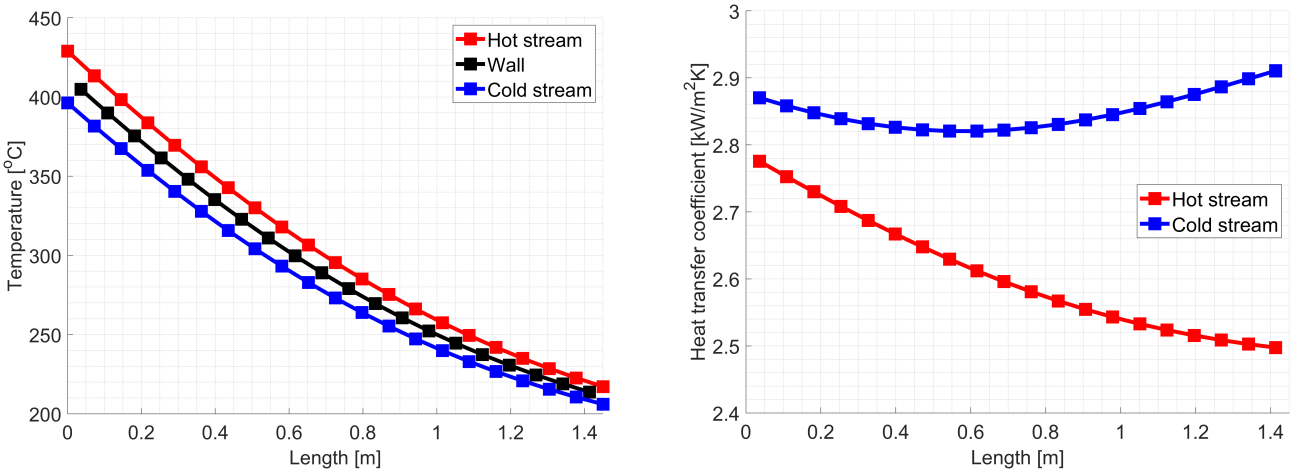

Figure 77: Temperature and heat transfer coefficient along the length of the HTR

7.3 Scenario 1; reactor dynamics

For scenario 1, the influence of the reactor dynamics on the maximum achievable power transient will be investigated. The power balance and cycle efficiency belonging to this scenario are visible in Figure 78, presenting the influence of different components onto the overall cycle power. As shown by the solid black line in Figure 78, the scenario starts at a low cycle load of 10% FP, increases up to 100% FP, before ending again at 10% FP. The power increase starts at 500 seconds and reaches full power at 900 seconds, resulting in a ramp rate of 13%/min. The same power transient, but than decreasing, occurs between 2500 and 2900 seconds. Furthermore, Figure 79 presents the temperature of the helium at the in-/outlet of the reactor while also presenting the change in rod height during the simulation. Finally, Figure 80 presents the shaft speed and bypass control during the power transient.

In theory it could be possible to fully neglect the bypass in this scenario and to only act on the reactor power during the power transient. However, this requires a load demand which accounts for the non-linear power behaviour of the reactor, as otherwise a power imbalance would affect the shaft speed. As the reactor control is not fast enough to stabilize the shaft speed for small power changes, it was not deemed feasible to create a power profile that ensures shaft speed is maintained within reasonable operating conditions. Bypass control is therefore added to the system to aid in a stable power control. The influence of the bypass is limited, visible in Figure 80, to ensure that mainly the impact of the reactor dynamics is presented. For this scenario, a 5% bypass valve opening at the start was deemed acceptable and overall bypass valve opening was limited to 15%, meaning that at least 85% of the mass flow enters the turbine.

Before the power transient occurs, the reactor is scaled down in power to still provide the 10% FP to the cycle, this way limiting the amount of waste heat and thus improving cycle efficiency. However, Figure 80 shows the bypass valve is still 5% open at the start of the simulation, indicating there is still waste heat present within the cycle. The bypass valve can still increase the mass flow through the turbine before being fully closed, meaning that the power transient is not reactor-dependent until the bypass fully closes, which occurs at 800 seconds. At this point, the shaft speed begins to decrease until the load demand reaches steady state at 900 seconds. Meanwhile, the reactor continues to increase in power until the control rods reach steady state at 1020 seconds, visible by the constant black line in Figure 79. This ensures shaft speed stabilizes again, resulting in an overall shaft speed dip of 2.5%. At this point, the reactor provides enough heat to the secondary cycle to meet the desired power demand. However, as shown by the blue and red lines in Figure 79, the temperature at the reactor inlet and outlet does not remain constant, even when the control rod position stays fixed. This is because the specific reactor temperatures are not directly controlled; instead, only the reactor's power output is regulated. As described by Equation 11, a specific rod height corresponds to a specific power output. If the rod height is not adjusted by a controller responding to for example the outlet temperature, a constant power output will be maintained by the reactor. A change in fuel temperature will also change the reactivity slightly as explained in Section 4.5.3, but this effect is small compared to the influence of a constant rod height.

At 2500 seconds, the power demand begins to decrease; however, as shown in Figure 80, the shaft speed remains relatively constant until the bypass reaches its 15% opening limit. At this moment, the bypass cannot open any further, limiting the reduction of turbine power. As the load is still decreasing, and the reactor is not capable to decrease faster in power, the shaft speed increases until the power demand stabilizes at 2900 seconds. At this moment, the decreasing reactor power output can start correcting the shaft speed, but this does result in an overall shaft speed increase of 5%.

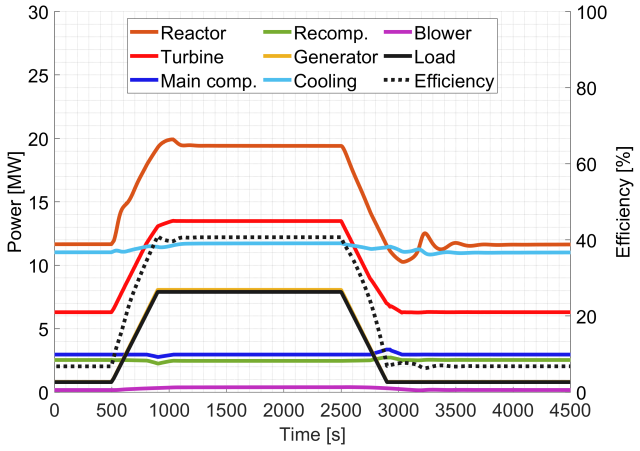

Figure 78: Cycle efficiency and power production/-consumption of different cycle components

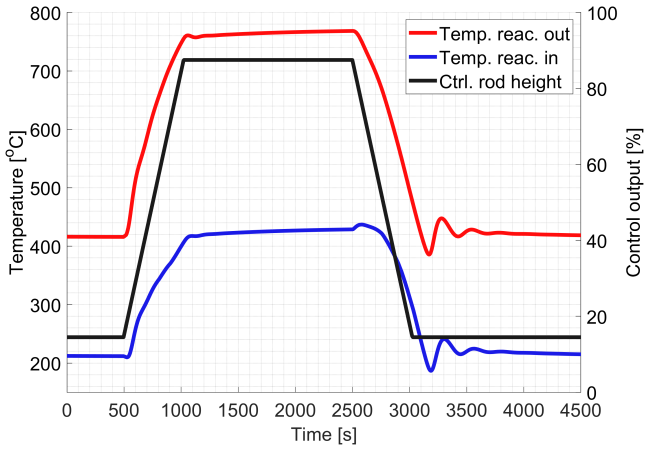

Figure 79: Temperature of the inlet and outlet flow of the reactor and control rod height

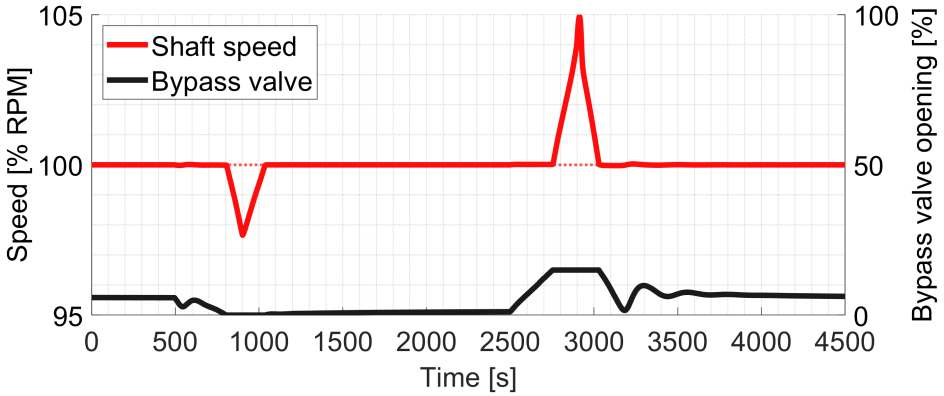

Figure 80: Shaft speed and opening of the bypass valve

The results of this scenario clearly indicate that, even with additional bypass support, the reactor is not capable to achieve faster power dynamics. If the power demand is set to 13%/min, a power increase still results in a shaft speed correction of 2.5%. During a power decrease, the limitation for opening the bypass, also results that the reactor produces more power than the power demand requires, resulting in a shaft speed correction of 5%. This scenario does however contain some specific arbitrarily chosen values. If the minimum reactor power output is increased during this scenario, the achievable power transient increases, but this requires additional bypass support in maintaining a stable shaft speed at part load. If the bypass is not limited in its maximum opening, the power decrease could also be achieved without significant shaft speed correction. However, these alternatives reduce the influence of the reactor on the power dynamics of the cycle. Even with small changes within this scenario, it is not deemed possible to increase the ramp rate of 13%/min to come close to the ramp rates of diesel engines (30%/min) or gas turbines (90%/min). Overall, it can therefore only be concluded that power transients with solely reactor control cannot provide the required power dynamics of a naval vessel. To ensure the reactor dynamics do not limit the cycle dynamics, further scenarios will aim to operate the reactor constantly at full power, applying solely bypass control for achieving desired power transients.

7.4 Scenario 2; bypass valve with a diesel engine ramp rate

For scenario 2, the influence of the reactor dynamics on the power load demand is minimized. This was realised by changing the control configuration from reactor power output control to reactor outlet temperature control. Here, the control rods aim to stabilize the reactor outlet temperature to 750°C. The ramp rate of this scenario is equal to the 30%/min ramp rate of a diesel engine, and the same load demand of 10-100-10% FP is applied. The bypass valve is used to maintain a stable shaft speed during the power increase or decrease.

The power balance and cycle efficiency of this scenario, presented in Figure 81, and the stable shaft speed, presented in Figure 83, indicate that the applied ramp rate can be realized if bypass control is used for power control. Figure 82 presents the temperature of the helium at the in-/outlet of the reactor. Here, the control rods are used for stabilizing the reactor outlet temperature and ensure a relative stable outlet temperature. However, as there is no control mechanism applied for controlling the reactor inlet temperature, the inlet temperature of the helium rises up to 550°C during low part load of the cycle. The steel used for the barrel and RPV is not capable to withstand temperatures above 425°C [136], and as these materials are in direct contact with the inlet helium stream, as visible in Figure 44, this violates the safety limits of the reactor. This scenario therefore indicates, that although the power dynamics could be achieved with bypass control, the current control configuration is not capable to achieve a safe working environment for the reactor.

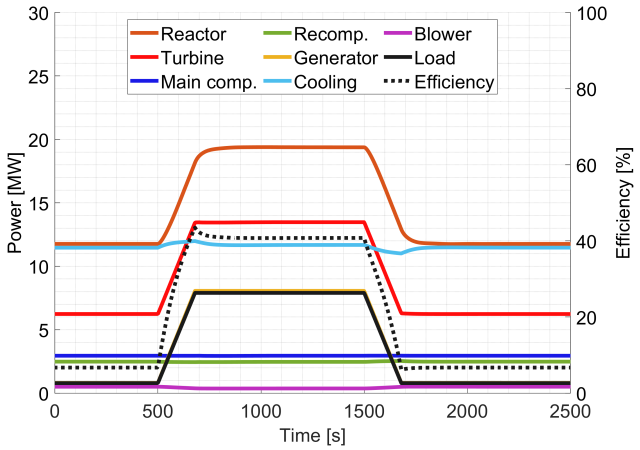

Figure 81: Cycle efficiency and power production/-consumption of different cycle components

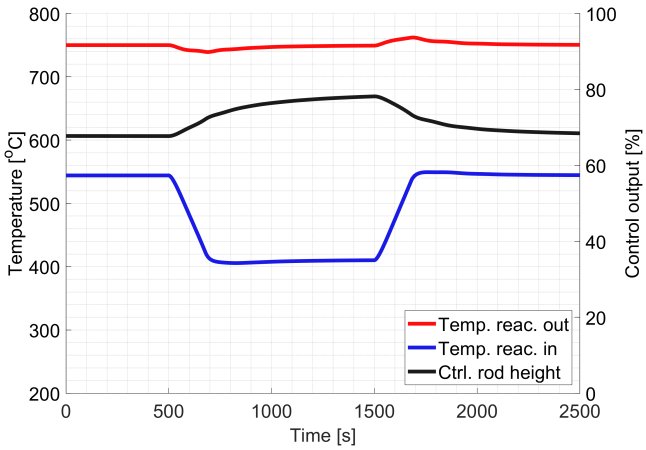

Figure 82: Temperature of the inlet and outlet flow of the reactor and control rod height

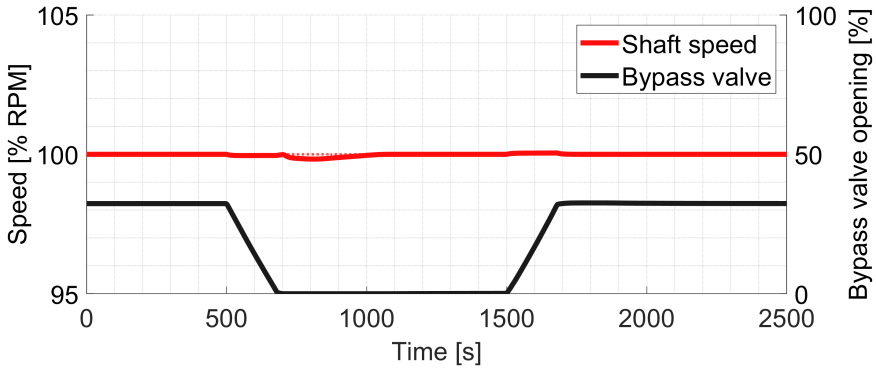

Figure 83: Shaft speed and opening of the bypass valve

7.5 Scenario 3; implementation of the dump cooler

In the previous scenario it was determined that without reactor inlet control the safety limits for the reactor are violated. To ensure the inlet and outlet temperature of the reactor are maintained, an additional control method is added, namely the primary circuit dump cooler. The control rods will still be used for controlling the outlet temperature, but the dump cooler will act as inlet temperature control for the reactor. The load demand within this scenario was set equal to the previous scenario, resulting in a ramp rate equal to the 30%/min and a load demand of 10-100-10% FP. The bypass valve is also still applied to maintain a stable shaft speed during the power increase or decrease, this way realizing only a difference in the implementation of the dump cooler.

The power balance and efficiency of this scenario, presented in Figure 84, and the stable shaft speed, presented in Figure 86, still indicate that the applied ramp rate is feasible. Figure 85 presents the temperature of the helium, combined with the control output of the rods and dump cooler. Here, the control of the dump cooler is expressed as a percentage, where 100% is equal to a cooling capacity of 10 MW. Although a slight change in inlet and outlet temperature is still present, the implementation of the dump cooler prevents that the inlet temperature exceeds 425°C. It was therefore deemed that the reactor can operate within a safe operating region during this scenario. Figure 84 shows that the cooling capacity is increased significantly at part load, resulting in a cycle efficiency of 4%. This is not beneficial, as a lot of heat is wasted, but it is deemed necessary to achieve fast power dynamics under the current cycle configuration. To determine if other components present within the cycle are operating within a safe environment an additional analysis regarding the turbomachinery and heat exchanger performance will be performed.

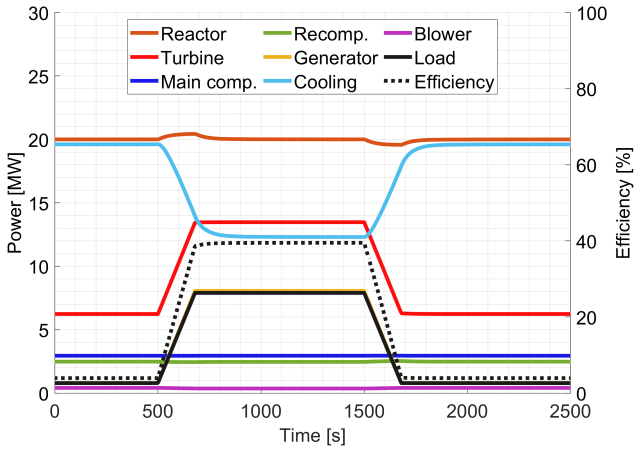

Figure 84: Cycle efficiency and power production/-consumption of different cycle components

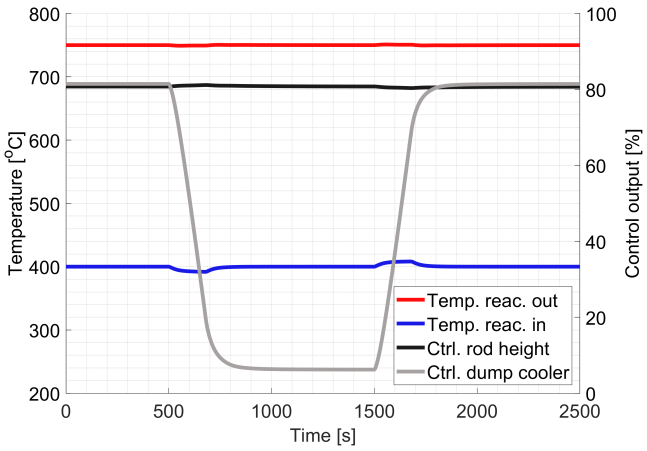

Figure 85: Temperature of the inlet and outlet flow of the reactor and control rod height

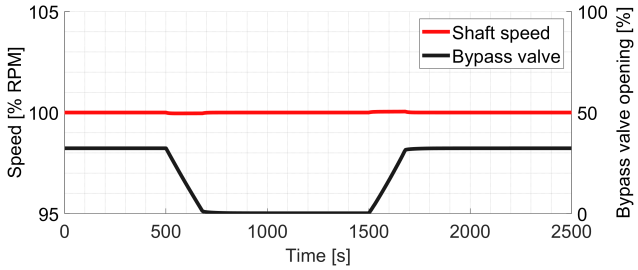

Figure 86: Shaft speed and opening of the bypass valve

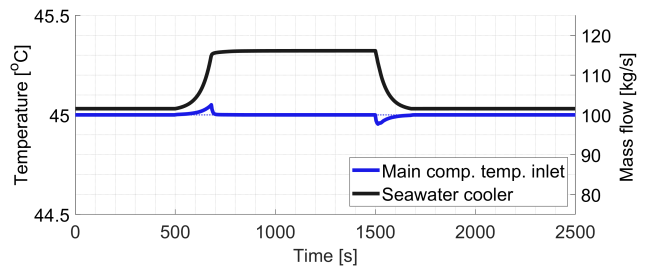

Figure 87: Main compressor inlet temperature and amount of seawater through the cooler

At first, Figures 88 and 89 present the performance maps of the recompressor and turbine, with the operating range during the simulation. Here, the corrected pressure ratio is presented based on the corrected mass flow and corrected shaft speed. Therefore, even if the shaft speed is constant during the power transient, a change in inlet temperature and pressure could result in a change in shaft speed as shown by the performance maps. It was decided to neglect the performance map of the main compressor as here only a black dot is present in the design point. This is the result of a controlled inlet pressure due to the throttle valve, and a controlled inlet temperature due to the cooler, of which the performance is presented in Figure 87. Figures 88 and 89 indicate that during the power transient, the recompressor stays relative constant at its design point. However, the performance of the turbine changes significantly, which is the result of the bypass changing the mass flow through the turbine. At part load, when less mass flow is entering the turbine, the pressure ratio of the turbine decreases, resulting in a higher temperature and pressure at its outlet side. Still, there is a sufficient margin between the choke, stall and surge areas of the turbomachinery, resulting in no safety violation regarding turbomachinery performance. Figures 90 and 91 present the change in temperature and pressure surrounding the turbomachinery. The results of operating at part load are a higher pressure at the outlet of the turbine, which is the result of the lower expansion ratio, as visualized in Figure 89. In addition, the temperature at the inlet of the turbine increases up to 615°C. This shows that for the design of the turbine the inlet temperature at full design power is not the limiting factor in design, but the inlet temperature at part load.

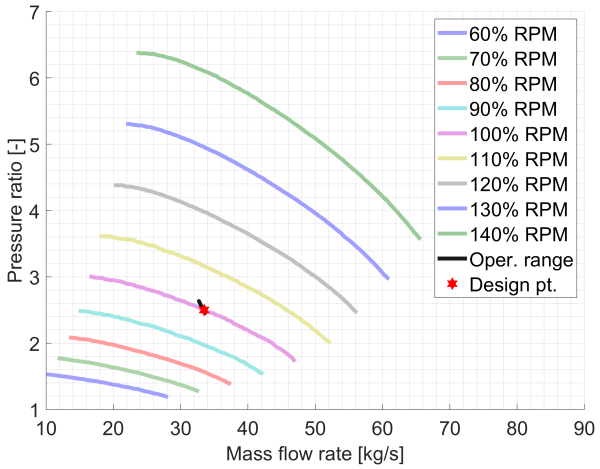

Figure 88: Recompressor performance map

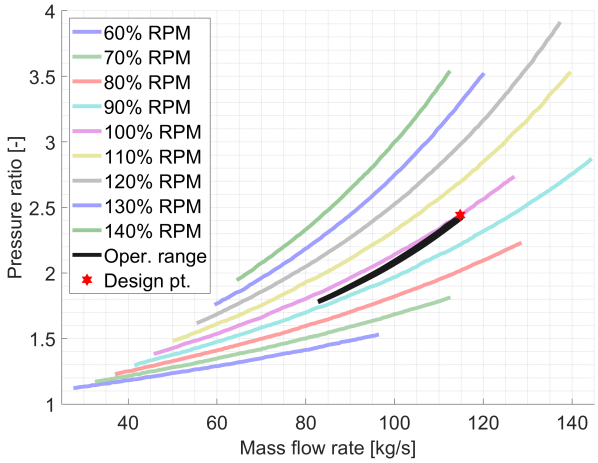

Figure 89: Turbine performance maps

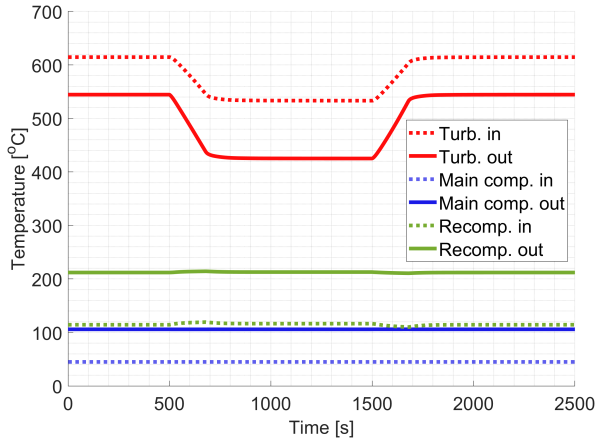

Figure 90: In-/outlet temp. of the turbomachinery

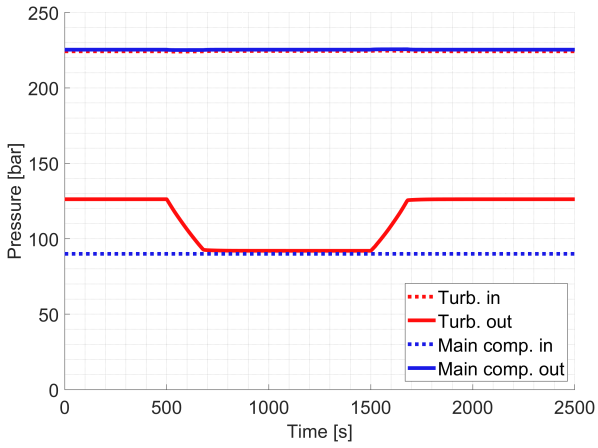

Figure 91: Outlet pressure of the turbomachinery

As the turbomachinery, mainly the turbine, changes the outlet pressure and temperature during part load, the operating conditions of the heat exchangers also differ. For the IHX and the HTR the temperature and pressure development is presented in Figures 92-95 as these present the most challenging operating conditions for the heat exchangers used within the cycle. Appendix A13 provides the change in temperature and pressure for the LTR and CL. As the pressure drop over the heat exchangers is negligible regarding the size of the figure, it was decided to only plot outlet pressures. The highest temperature present within the heat exchangers is related to the IHX, as here the outlet stream of the reactor enters the heat exchanger at 750°C. This temperature stays relative constant due to the control rods stabilizing the outlet temperature of the reactor. The maximum pressure within the cycle is 225 bar, which does not change significantly due to the relative stable compressor control and throttle valves used within the cycle. However, beside maximum temperatures and pressures, the change in temperature and pressure is also of importance. Fast changes in operating conditions could result in thermal shock, resulting in stress or fatigue within the materials of the heat exchangers. The fastest temperature and pressure gradients in this scenario occur within the HTR, reaching a temperature gradient up to $\pm$ 0.74°C/s and a pressure gradient up to $\pm$ 0.17 bar/s. These values were determined as the gradient occurring between 500 and 680 seconds, which belongs to the time interval of the increasing power load.

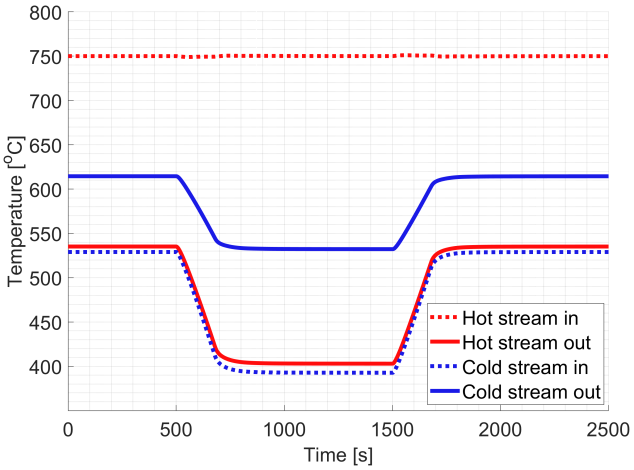

Figure 92: Temperature development of the IHX

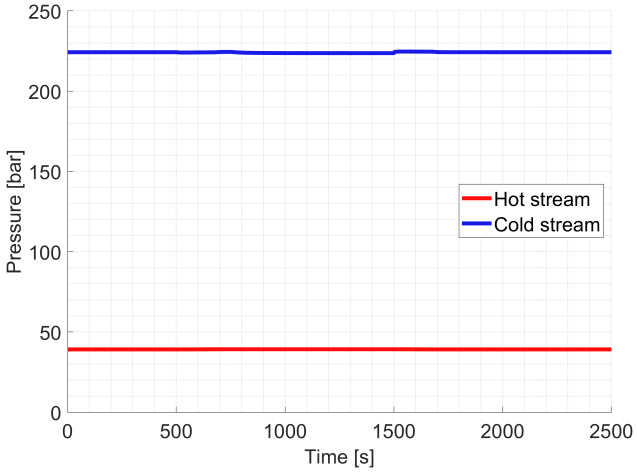

Figure 93: Pressure development of the IHX

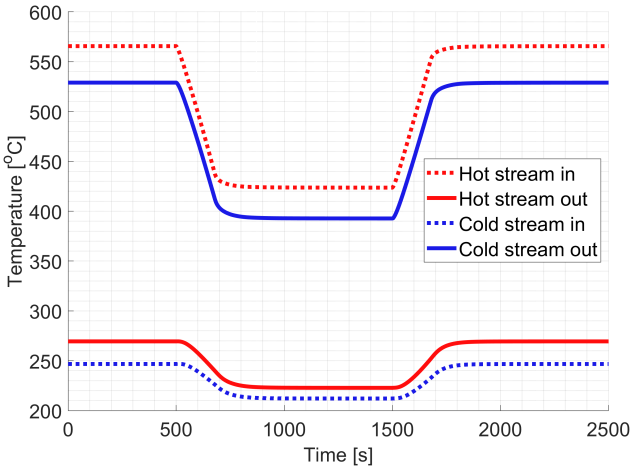

Figure 94: Temperature development of the HTR

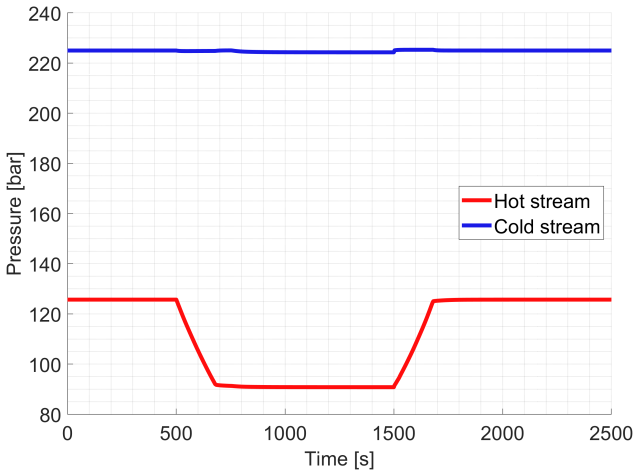

Figure 95: Pressure development of the HTR

7.6 Scenario 4; gas turbine ramp rate

In the previous scenario it was determined that the ramp speed of a diesel engine can be achieved with stable reactor control and cycle bypass control. In this scenario the influence of increasing the ramp rate to gas turbine level will be investigated. Therefore, a ramp rate equal to the 90%/min and a load demand of 10-100-10% FP is applied on the cycle. Here the bypass valve is still applied to maintain a stable shaft speed during the power increase or decrease, and the control rods and dump cooler are used for stable reactor control. This scenario therefore only increases the ramp rate from diesel engine to gas turbine level.

The power balance and cycle efficiency of this scenario, presented in Figure 96, and the stable shaft speed, presented in Figure 98, still indicate that the applied ramp rate can be realized. Figure 97 presents a small change in inlet and outlet temperature of the helium, but due to the control rods and dump cooler, the reactor is still operating within a safe working environment. To determine if the faster power transient changes the operating conditions of the cycle, the performance of the turbomachinery and heat exchanger will be investigated.

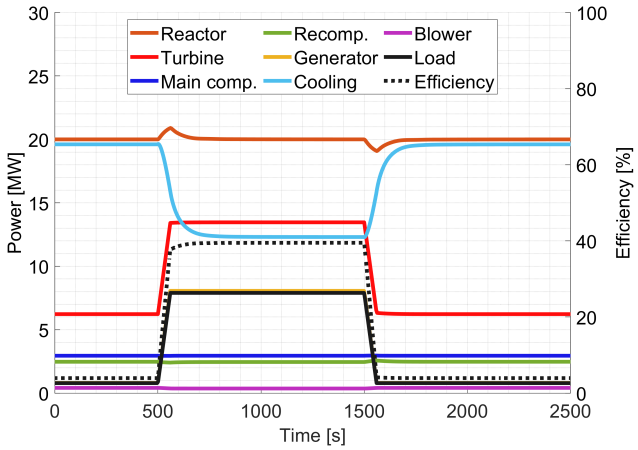

Figure 96: Cycle efficiency and power production/-consumption of different cycle components

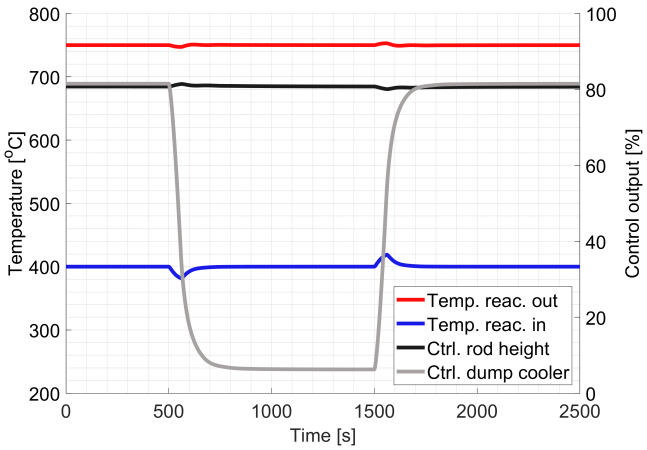

Figure 97: Temperature of the inlet and outlet flow of the reactor and control rod height

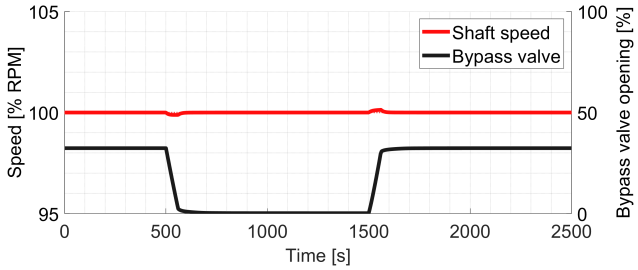

Figure 98: Shaft speed and opening of the bypass valve

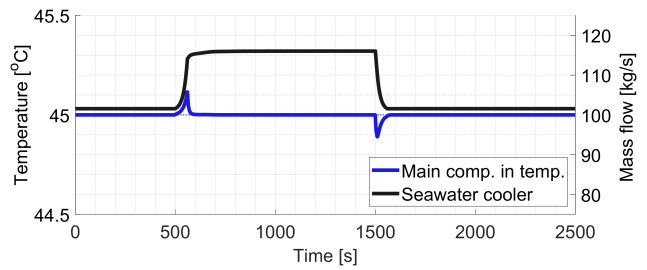

Figure 99: Main compressor inlet temperature and amount of seawater through the cooler

At first, Figures 100 and 101 present the performance maps of the recompressor and turbine, with the operating range during the simulation. It was again decided to neglect the performance map of the main compressor as the inlet conditions are still maintained and stable, as can be seen for the temperature in Figure 99. Figures 100 and 101 indicate that the recompressor stays relative constant at its design point, but that the performance of the turbine changes significantly. Compared to the previous scenario, the turbine covers a larger performance area within the map. Still, there is sufficient margin between the choke and surge areas of the turbomachinery,

resulting in no safety violation in turbomachinery performance. Figures 102 and 103 present the change in temperature and pressure surrounding the turbomachinery. Although relative similar temperature and pressure levels are reached, compared to the previous scenario, the rate of change differs. The increased ramp rate of the load opens the bypass faster to remove mass flow entering the turbine, ensuring a larger rate of change in pressure and temperature within the cycle.

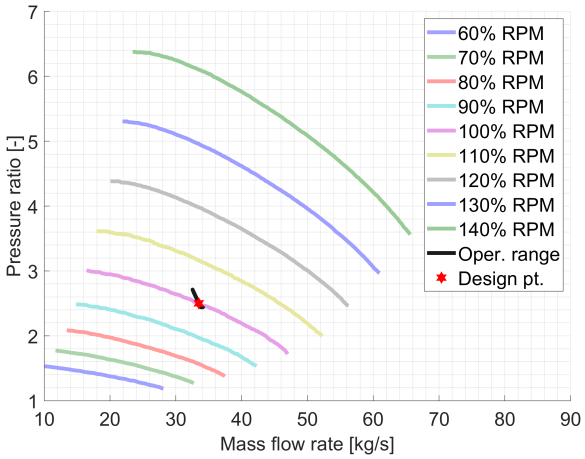

Figure 100: Recompressor performance map

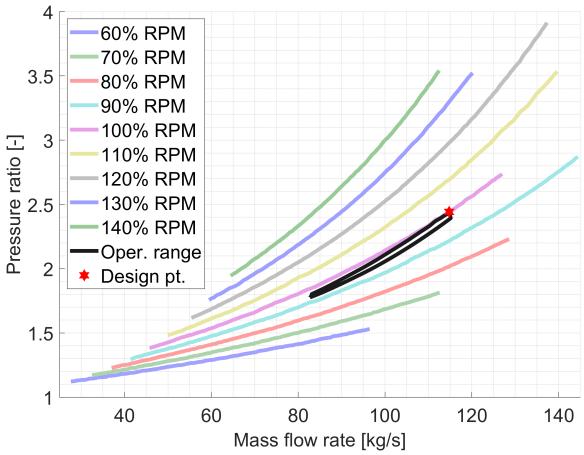

Figure 101: Turbine performance maps

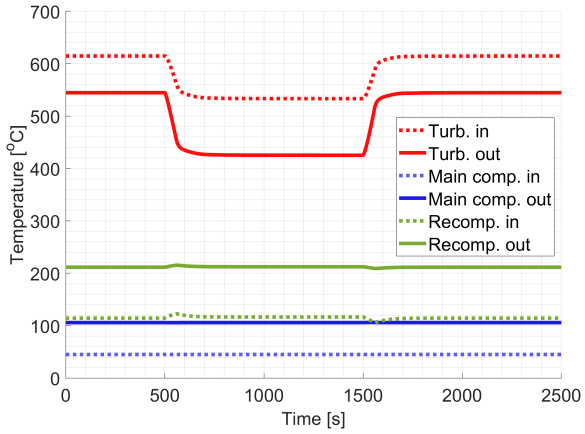

Figure 102: In-/outlet temp. of the turbomachinery

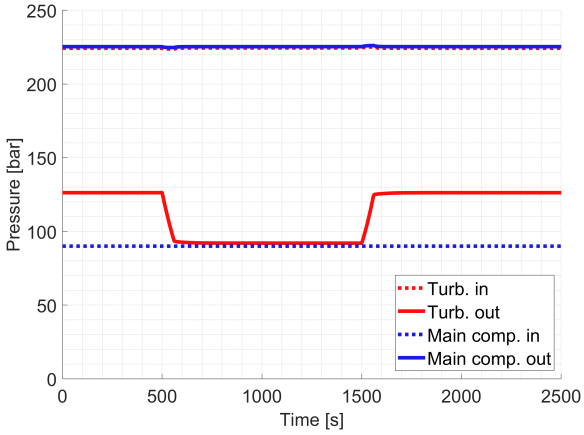

Figure 103: Outlet pressure of the turbomachinery

The pressure and temperature development within the heat exchanger differ significantly between full and part load. For the IHX and the HTR the temperature and pressure development is presented in Figures 104-107 as these present the most challenging operating conditions for the heat exchangers used within the cycle. Appendix A14 provides the change in temperature and pressure for the LTR and CL. As the pressure drop over the heat exchangers is negligible regarding the size of the figure, it was decided to only plot outlet pressures. Regarding absolute values of temperatures and pressures, this scenario is not significantly different compared to the previous scenario, as at 10% or 100% FP the same steady state is reached. However, a difference occurs between the rate of change of the different operating conditions. The fastest temperature and pressure gradients occur again within the HTR, but this time reaching a temperature gradient up to $\pm$ 1.48°C/s and a pressure gradient up to $\pm$ 0.38 bar/s. These values were determined as the gradient occurring between 500 and 560 seconds, which belong to the time interval of the increasing power load.

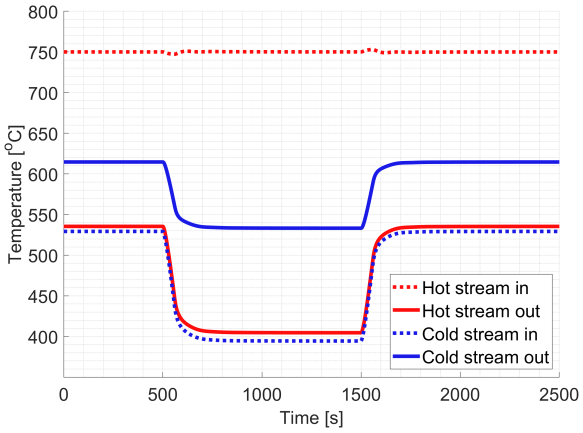

Figure 104: Temperature development of the IHX

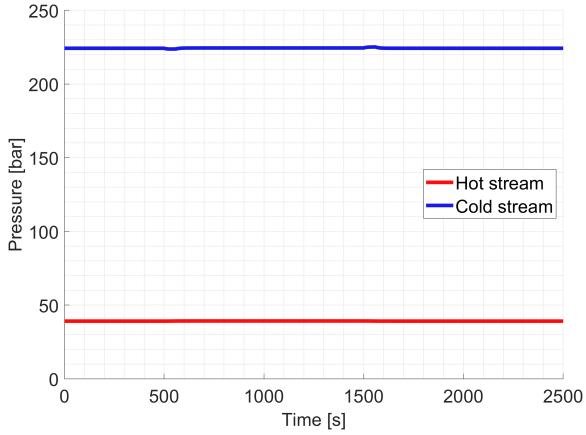

Figure 105: Pressure development of the IHX

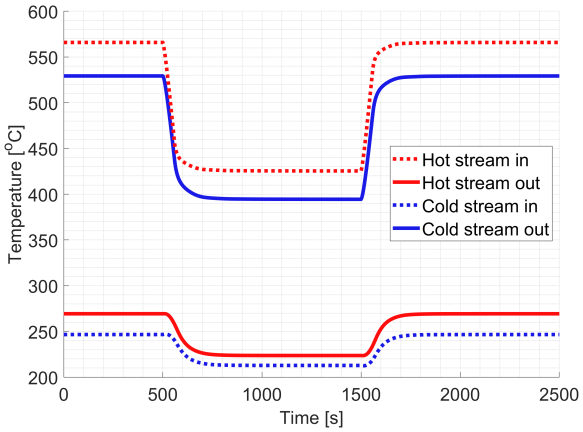

Figure 106: Temperature development of the HTR

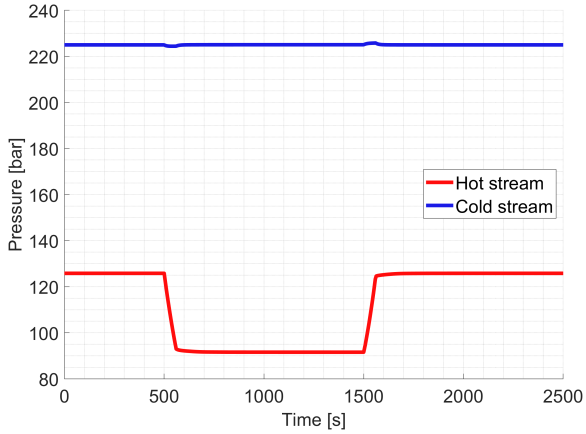

Figure 107: Pressure development of the HTR

7.7 Summary simulation results

The results of the different scenarios present multiple insights about the power dynamics of a nuclear-powered sCO_2 recompression cycle. At first, the power dynamics of naval vessels cannot be achieved with solely reactor control due to the limitations in control rod speed. However, using the reactor as a stable power source, and achieving the power dynamics with bypass control, presents a promising solution for achieving ramp rates up to gas turbine level. Here, it is of importance to control the in-/outlet fluid stream of the reactor to maintain a safe working environment within the reactor. Regarding component performance is the turbomachinery operating with sufficient margin between the choke and surge areas throughout the full power transient. However, at part load the inlet temperature of the turbine increases up to 615°C, which indicates that the turbomachinery should be capable to operate under these temperatures. Furthermore, the IHX experiences pressures up to 225 bar and temperatures up to 750°C, of which the latter is the result of the outlet temperature of the reactor. Finally, a faster rate of change in power increases the temperature and pressure gradients occurring within the heat exchangers. With a 30%/min ramp rate this results in temperature and pressure gradients up to $\pm$ 0.74°C/s and $\pm$ 0.17 bar/s. This increases even further with faster ramp rates, reaching gradients up to $\pm$ 1.48°C/s and $\pm$ 0.38 bar/s under power ramp rates of 90%/min. The current state of research does not provide insights regarding the limitations of temperature and pressure gradients for PCHEs and further research should therefore determine these limitations to decide if these pressure and temperature gradients are acceptable.

8 Discussion

Within this research the implementation of a nuclear power plant on a naval vessel has been investigated, specifically focusing on the dynamic possibilities of such a power plant. To provide an answer for this, a dynamic model simulation was performed based on a selected nuclear reactor and power conversion cycle. Results indicate that the power dynamics of common prime movers could be achieved with a nuclear power plant. However, these results are dependent on choices made during this research process. To determine the feasibility of these results a discussion will be performed based on the selected nuclear power plant and the developed model.

8.1 Selection nuclear power plant

8.1.1 Vessel selection

For this research, the Future Air Defender (FuAD) and the Amphibious Transport Ship (ATS) were selected as projects of interest for the integration of a nuclear power plant. An energy analysis of similar vessel types was conducted to determine key power levels, which were subsequently used to estimate the required power output for the nuclear power plant. However, the actual power demands of these vessels could vary significantly due to the potential addition of weapon or radar systems, which might influence overall power requirements. These variations could lead to different power demands on a single nuclear power plant. Nevertheless, if the power output of a single nuclear power plant is similar to the 7.9 MWe system analysed in this research, the overall dynamic power performance would likely remain consistent.

For the FuAD, the current power plant design requires the use of four nuclear power plants. Each installation applies two nuclear reactors, resulting in a total of eight reactors on board of the vessel. Such a configuration has been used before, by for example the aircraft carrier the USS Enterprise, but it raises questions about overall feasibility. Future research should focus on developing a cycle configuration that reduces the number of reactors required on board. A reduced-reactor configuration could enhance feasibility, simplify operations, and improve overall cycle efficiency.

8.1.2 Reactor selection

Based on a literature study towards multiple different reactor types, it was decided that the HTGR/VHTR is of interest for maritime implementation. However, other reactor types could be considered for implementation on a (naval) vessel. Historically, the PWR has been used wildly for maritime implementation, and an argument can be made that technological readiness should be favoured more if there is a desire to implement nuclear propulsion within a short time span. While selecting a different reactor type might affect overall reactor dynamics, it is unlikely that any alternative reactor type could bridge the significant gap between reactor dynamics and the operational requirements of a naval vessel.

The U-battery was selected for implementation as HTGR due to its relative mature design and public available design data. Compared to other HTGRs is the design of the U-battery not different enough to conclude it is not a representative technology for this reactor type. However, it can also not be concluded that the design of the U-battery is optimized for dynamic power performance. Based on the difference in reactor dynamics between different PWR designs, it seems possible that an HTGR could be designed with improved power dynamics. Still, the results show that the current HTGR design is not capable to come close to the power dynamics of a diesel engine, let alone a gas turbine. It is not expected that the large amount of thermal inertia present within an HTGR can be improved in such a way that an HTGR can provide the required cycle dynamics on its own.

8.1.3 Cycle selection

In combination with the HTGR, it was decided to implement an sCO_2 recompression cycle for power conversion. However, historically the Rankine steam cycle has been mainly used as nuclear power conversion cycle. This cycle is larger in size and less efficient than an sCO_2 cycle. Still, the technological feasibility and maturity could be favoured for cycle selection. The results of the cycle dynamics could differ if a Rankine cycle is applied. Not only is the cycle structure different, as a recompression cycle is a specific sCO_2 cycle configuration, but also operating conditions like temperature and pressure could differ significantly for steam or any other substance.

The recompression cycle was selected as cycle configuration for the sCO_2 power conversion cycle. This cycle configuration is deemed the most efficient sCO_2 cycle configuration, while staying relatively simplistic. However, it could be feasible to design a cycle which is favoured with a viewpoint towards cycle dynamics. Such a cycle could improve overall cycle dynamics, but also the operating conditions and gradients during these transients, this way ensuring a more thermal stable power cycle. Further research should focus on designing a cycle with beneficial power transient capabilities.

Within the cycle, printed circuit heat exchangers were selected as these provide large heat transfer capabilities for their size, and are capable to operate under high pressures and temperatures. Other type of heat exchangers can also be selected within nuclear power conversion cycles, as explained in Section 2.7. Another heat exchanger design, or a different design approach, could not only impact the required heat exchanger size, but also the limitations in operating conditions within the cycle. As a result, different temperature and pressure gradients could occur during the power transient, which could impact the materials of the heat exchanger.

8.1.4 Control configuration

The final design condition that impacts the power dynamics is the specific implemented control configuration. Several disturbance rejection control methods were selected and implemented to ensure a stable cycle output could be achieved. For example, in the case of the inlet temperature control of the main compressor, an adjustable cooler mass flow was selected as control method. It is however also possible to control the compressor inlet temperature with a bypass valve over the cooler, ensuring a relative stable cooler mass flow can be achieved. Other disturbance rejection control configurations could be implemented or designed, which could alter the specific power dynamics of the designed cycle. Still, as the disturbance rejection method is specifically implemented to limit the impact of system components on the overall cycle dynamics, it is expected that the selection of disturbance rejection control methods has a negligible impact on the power dynamics.

In addition, bypass control was implemented as main set point tracking control method. Bypass control is favored regarding power dynamics and this was deemed the most important for this research. However, as presented in the scenarios, the efficiency at part load decreases significantly due to the use of the bypass. It is therefore recommended within literature to also implement inventory control, as this provides a more stable efficient cycle control. Inventory control is dynamically unfavourable and could therefore result in slower power transients. Still, a combination between bypass and inventory control could apply benefits of both control configurations, but this can only be stated for certain by performing further research.

8.2 Model design

8.2.1 Neutronics

The point kinetics model is used dominantly for preliminary research goals, small reactor size and relative small power changes (not accident simulations) and was therefore deemed sufficient for this research. This model approach neglects any inconsistency of neutron/power production within the reactor. Not only is it expected that a sinusoidal power distribution is present within the reactor, as displayed in Figure 39, but also local power production could be higher due to the use of heterogeneous materials. Determining the maximum temperature according to the point kinetics model, without additional safety factors, is therefore insufficient, as local temperature spots could turn higher. As maximum temperatures impact the safe operation of the reactor, this could change the dynamics of the power cycle. Still, the results of this research indicate that a stable reactor control is the preferred control option, as then cycle dynamics are not influenced by reactor dynamics. It is therefore expected that the temperature changes within the reactor core are minimal. A more accurate reactor model would therefore probably not produce any insights into the limitation of the cycle dynamics. It could however change the perspective on the limitations in reactor dynamics.

The applied neutronic model only applies reactivity feedback from a temperature increase within the fuel. Changes in material temperature or long-term reactivity feedback phenomena, such as poisoning or burnup, could also influence reactor dynamics, but these effects were excluded from this research due to a lack of sufficient data. Although the final result of this research incorporates a constant power output from the reactor, and thus reactivity effects are negligible, further research should indicate the effect of long term feedback phenomena, even if this is only to verify that this does not impact the cycle dynamics significantly.

8.2.2 Thermal hydraulics

For the modelling of the thermal hydraulics (TH) of the nuclear reactor, a 1D thermal node structure was applied. This TH-model structure neglects any heat transfer at the top and bottom side of the reactor. Although the effects should be limited, as heat transfer must be dominant in the region between the fuel rods, matrix and coolant, the total effect of the top and bottom material could be an influence on the material temperatures within the reactor. Further research should therefore aim to model a 3D thermal hydraulic scheme as this could give insights in the heat transfer flows occurring within the HTGR.

In addition, constant property values for different material temperatures and irradiation values were assumed, which is unrealistic for actual reactor operation and could drastically impact the overall performance of the reactor. However, it was deemed not possible to accurately implement changing property values based on temperature and radiation as the appropriate correlations are not present within literature. Further research should therefore aim to find thermodynamic correlations of material properties like density, thermal conductivity and specific heat capacity for the materials present within an HTGR. A more accurate property database could present other insights towards the limitations in reactor dynamics, especially for long term reactor operations.

Finally, as discussed in Section 5, it was deemed difficult to perfectly validate the TH-model as sufficient data was lacking in literature about a dynamic HTGR. Additional research is required to obtain a dynamically validated TH-model as only then could the errors within the current model be explained. For now, the large errors were deemed acceptable as the model corresponds to steady state values if the inconsistencies within the validation source are accounted for, and the model produces dynamic power transients as expected when compared with literature. Therefore, although exact temperatures within the reactor could differ from actual values, it is still expected that the current model represents the dynamic capabilities of the reactor within reason.

8.2.3 Turbomachinery

The model method used for the turbomachinery is based on using performance maps to predict the performance of the turbomachinery. To obtain these maps a normalization approach is applied based on performance maps of the research group KAIST. However, to obtain a proper performance map a scaling approach seems more accurate. An attempt was made to implement a scaling method, but due to a lack of time, this scaling method was not implemented successfully. Still Appendix A7 presents the created scaling method based on the work of Jeong et al. [161] and Visser [162], which can be perfected and implemented in further studies. As the performance maps used in this research are related to performance maps of turbomachinery of similar type (centrifugal) and power size, the inaccuracy between scaling or normalization should be limited. Still, only a full sCO_2 turbomachinery design could produce accurate performance maps. Further research should opt for providing a tool to construct the performance map of turbomachinery for different power sizes, as this would indicate if scaling/normalization approaches are appropriate.

The performance maps used in the model are applied as a steady state modelling approach of the turbomachinery. Although it is expected that the dynamic effects of turbomachinery are negligible compared to the dynamics of a reactor or a heat exchanger, it is still important to confirm this assumption with a full dynamic turbomachinery design. Although the effect on cycle dynamics should be limited, it could still result in additional safety concerns regarding for example a temperature gradient at the inlet of the turbine.

8.2.4 Heat exchanger

The printed circuit heat exchangers used within the cycle are modelled by a 1D node model approach. This is a preliminary modelling approach suitable for dynamic power simulations, and it is therefore expected that results are within reason of actual heat exchanger performance. Still, small errors within the heat exchanger model could still drastically influence the operating conditions of the heat exchangers. The temperature and pressure levels and gradients occurring during the power transient influence the safety of the cycle and could result in limitations in the dynamics of the cycle. It is therefore recommended to design a 3D heat exchanger model which includes for example the in-/outlet channel effects on the flow regime, as then the exact material conditions of the heat exchangers can be determined.

9 Conclusion

Nuclear energy is a promising option for lowering the impact of the maritime/naval sector on climate change, as it provides a low carbon, high energy dense power source. However, naval vessels contain a dynamic power profile, which differs from the constant power load of land-based nuclear power plants. To make sure nuclear energy can be applied on naval vessels, this research investigates the following research question:

How can a nuclear power plant be implemented in a naval vessel to supply the required dynamic power behaviour?

To give an answer to this research question, the Future Air Defender (FuAD) and the Amphibious Transport Ship (ATS) were selected as projects of interest. Based on the important power levels of these vessels, it was decided that a single nuclear power plant should produce around 7-8 MWe. Dynamic power requirements were set to 30%/min and 90%/min respectively, corresponding to diesel engine and gas turbine ramp rates.

The high-temperature gas-cooled reactor (HTGR) was selected as reactor type of interest for (naval) nuclear propulsion. The design of the U-battery was chosen, and combining two of these helium cooled reactors for a single power conversion cycle results in 20 MWth of heat production. To convert this heat to electricity, a supercritical carbon dioxide (sCO_2) recompression power conversion cycle was implemented, which applies radial type turbomachinery and a coaxial turbine and compressor construction. So-called printed circuit heat exchangers (PCHE) were added to the cycle for heat transfer between the different fluids. To realize the required cycle dynamics, a turbine bypass valve was implemented.

It is of importance to apply two control methods for the inlet and outlet temperature of the reactor, as otherwise reactor material temperatures start to increase above safe operating limits. The implementation of control rods for regulating reactor outlet temperature and a dump cooler for inlet temperature control ensures that material temperatures remain within safe limits. A side effect is that at part load the amount of waste heat is drastically increased, resulting in a low cycle efficiency of 4% (compared to the 39.5% at full power).

Based on a created model of the selected nuclear power plant, dynamic power simulations were performed to analyse the dynamic possibilities of a nuclear power plant. The results indicate that ramping the reactor up and down when the power demand changes, is not a sufficient method of control, as a ramp rate of 13%/min already results in a shaft speed correction of 5%. When the reactor is ramped down in power, but a (sudden) increase in power demand follows, then the cycle dynamics are strictly limited by the dynamics of the nuclear reactor. As the reactor dynamics are not sufficient when compared to ramp rates observed in diesel engines or gas turbines, common ramp rates of naval vessels cannot be achieved by solely reactor control.

The results show that the nuclear power plant is capable to provide power dynamics up to diesel engine and gas turbine level if a bypass control configuration is implemented. Shaft speed is maintained stable and reactor and turbomachinery operate within their safe operating regions. However, large pressure and temperature gradients occur within the heat exchanger. In the case of a diesel engine ramp rate, a temperature gradient of $\pm$ 0.74°C/s and a pressure gradient of $\pm$ 0.17 bar/s are present. If the ramp rate is increased to gas turbine level, this gradient increases even more, reaching a temperature gradient of $\pm$ 1.48°C/s and a pressure gradient of $\pm$ 0.38 bar/s.

Current research does not provide limitations about temperature or pressure gradients within PCHE, and further research should therefore be performed on assessing these gradients. Even if these gradients are then deemed excessive, there is still possible room for cycle structure improvement due to the relative simplicity of the sCO_2 recompression cycle. Although the current research cannot state for certain the ramp rate of gas turbines can

be reached, the results clearly show that reaching gas turbine level power ramps are feasible. This research therefore concludes that an HTGR in combination with an sCO_2 recompression cycle, with implementation of bypass control, provides a promising option for providing dynamic power requirements of naval vessels. Further research about the implementation of nuclear propulsion should therefore not be limited by the assumption that nuclear energy can only be used for stable baseload operation.

10 Recommendations

Based on the obtained results, there are multiple topics which are of interest for further research. At first, due to limited data available about reactor design and dynamics, insights towards the true limitations of reactor dynamics could not be realized. Further research should aim to indicate what limits the dynamics of the reactor, but more specifically, what improvements could be made to increase the dynamics of a nuclear reactor. In addition, the long term effects of continuously cycling the power of the reactor regarding fatigue and stress should be determined, as this indicates if scaling the reactor down in power during sustained part load operation is beneficial.

Secondly, the current designed cycle configuration was implemented based on recommendations from literature. Besides the implementation of the dump cooler, no additional components were added to improve the performance of the cycle. As the current cycle is still simplistic in design, additional complexities could be added to improve cycle dynamics, (part load) efficiency and thermal stability. Points of improvement could be found in changing the shaft configuration, as now a simplistic TAC configuration was applied, adding additional turbomachinery stages for improved part load operation, implementing redundancy within the cycle to increase operational readiness and consider other bypass valve locations to reduce thermal stresses occurring on the system. Further research should therefore be focused on deciding which specific cycle configuration is beneficial for a nuclear sCO_2 power conversion cycle implemented on a naval vessel or other highly dynamic maritime applications.

Finally, it is important to perform research towards the material limitations of heat exchangers and turbomachinery during power transients. The results of this research indicate that not only high pressures and temperatures are reached during part load, but also that increased power dynamics result in increased pressure and temperature gradients. Within the current research phase it is not clear what the impact of these gradients are on the material integrity. Indicating the impact of these gradients on material fatigue and stress is of importance as only then could the feasibility of achieving power transients up to gas turbine level be confirmed. In addition, insights towards the limitations in material performance could also influence the considerations made within the design of the cycle, as additional options like coolers or (bypass) valves could be implemented to prevent large changes within temperature or pressure, if these were deemed too excessive.

Declaration of competing interest

The author declares that there are no conflicts of interest that could have influenced the work reported in this thesis. Furthermore, the author of this thesis wishes to emphasize that the views and beliefs expressed in this research are solely his own and do not necessarily represent those of Damen Naval and/or the Royal Netherlands Navy.

A Appendix

A1 Merchant ships sailing on nuclear energy

Ship	Lenin	NS Savannah	Otto Hahn	Mutsu	Arktika	Sibir	Rossiya	Sevmorput	Sovetskiy Soyuz	Taimyr	Vaygach	Yamal	50 Let Pobedy	Arktika	Sibir
Commission year-Decommission year	1959–1989	1962–1972	1968–1979	1974–1992	1975–2008	1977–1992	1985–2013	1988–present	1989–2014	1989–present	1990–present	1992–present	2007–present	2020–present	2021–present
Flag state	Soviet Union	United States	Germany	Japan	Russia	Russia	Russia	Russia	Russia	Russia	Russia	Russia	Russia	Russia	Russia
Type	Icebreaker	Cargo and passenger demonstration ship	Cargo and research ship	Cargo ship	Icebreaker	Icebreaker	Icebreaker	Cargo ship	Icebreaker	Icebreaker	Icebreaker	Icebreaker	Icebreaker	Icebreaker	Icebreaker
Length over all (m)	134	181.6	172	130	150	150	150	260.3	150	152	152	150	151	173	173
Beam (m)	27.6	23.8	23.4	19	30	30	30	32.2	30	29	29	30	30	34	34
Gross Tonnage	11,620	15,858	16,870	8240	20,646	20,646	20,646	38,226	20,646	20,791	20,791	20,646	23,440	33,540	33,540
Deadweight tonnage	3073	9570	14,079	2400	2750	2750	2750	26,480	2750	3550	3550	2750	3505	9000	9000
Displacement tonnage (t)	16,000	22,000	25,790	10,400	23,500	23,500	23,500	61,800	20,650	21,100	21,100	23,455	25,840	33,540	33,540
Speed (kn)	18	21	17	17.2	20.6	20.6	20.6	21	21	20	20	22	21	22	22
Engine (power)	OK-150→OK-900/A nuclear reactors (270 MW→342 MW)	"Babcock & Wilcox" pressurised water nuclear reactor (74 MW)	pressurised water nuclear reactor (38 MW)	pressurised water nuclear reactor (36 MW)	OK-900A nuclear reactors (342 MW)	OK-900A nuclear reactors (342 MW)	OK-900A nuclear reactors (342 MW)	KLT-40 nuclear reactor (135 MW)	OK-900A nuclear reactors (342 MW)	KLT-40M nuclear reactor (135 MW)	KLT-40M nuclear reactor (135 MW)	OK-900A nuclear reactors (342 MW)	OK-900A nuclear reactors (342 MW)	RITM-200 nuclear reactors (350 MW)	RITM-200 nuclear reactors (350 MW)
Propulsion power (MW)	34	16.4	8	7.5	52.8	52.8	52.8	29.4	52.8	74.8	74.8	52.8	52.8	110	110
Fuel (LEU = low-enriched uranium; HEU = highly enriched uranium)	LEU, 5% enriched→HEU, 20–90% enriched	UO2, 4% enriched	LEU, 3.5–6.6% enriched	LEU, 3.24–4.44% enriched	HEU, 90% enriched	HEU, 90% enriched	HEU, 90% enriched	HEU, either 30–40% or 90% enriched	HEU, 90% enriched	HEU, either 30–40% or 90% enriched	HEU, either 30–40% or 90% enriched	HEU, 90% enriched	HEU, 90% enriched	HEU, 20% enriched	HEU, 20% enriched

Figure A1: Table containing merchant ships that applied nuclear energy [169]

A2 Concept designs of the HTGR/VHTR

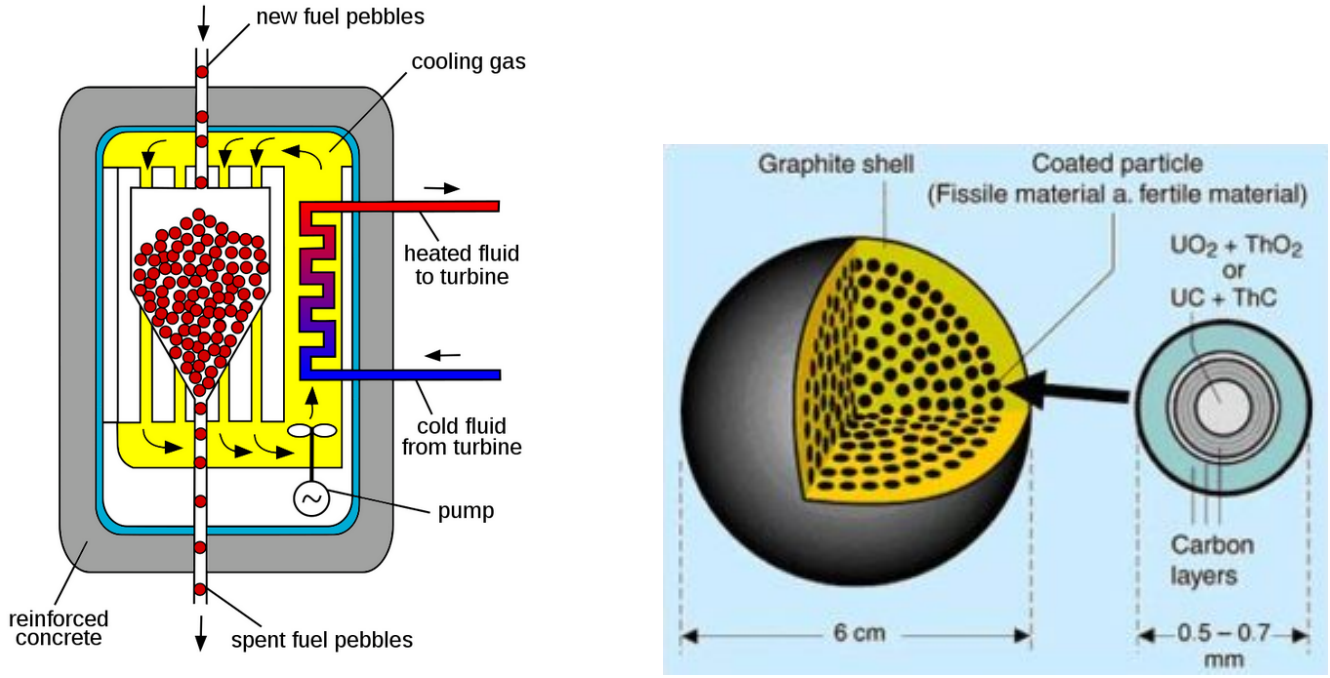

Figure A2: Concept of the pebble bed VHTR (left) [170] and the pebbles used in the reactor (right) [171]

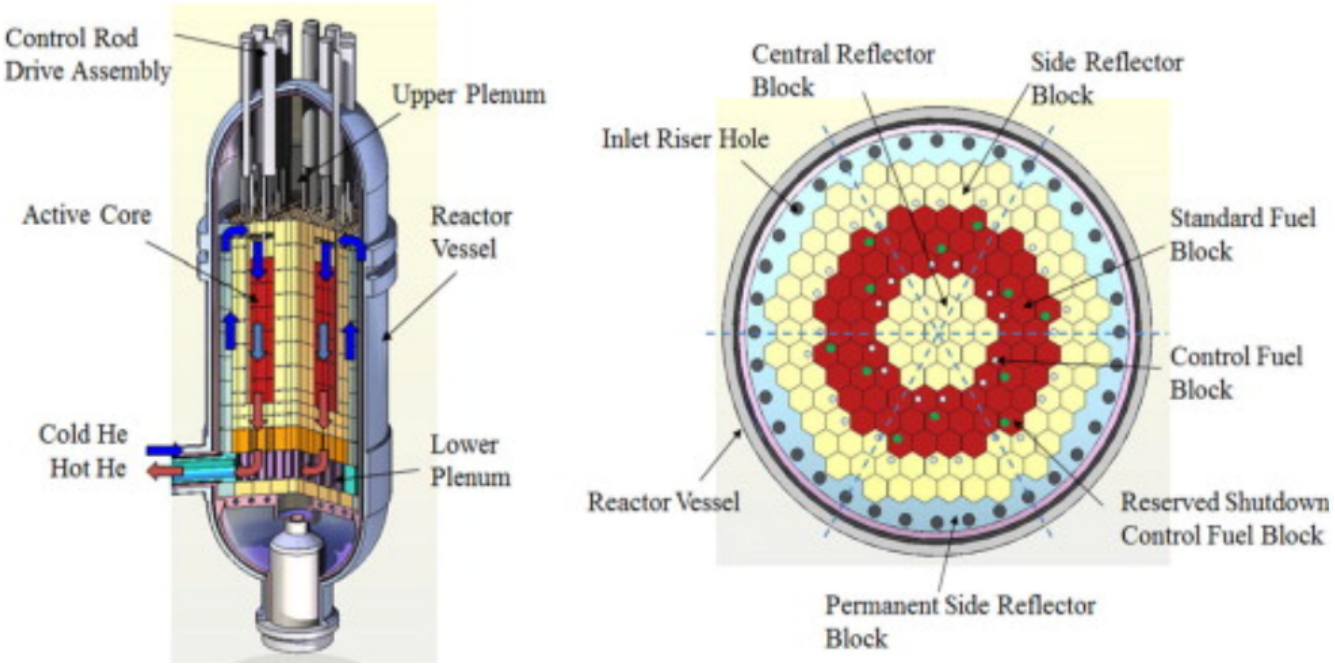

Figure A3: Concept of the prismatic VHTR [172]

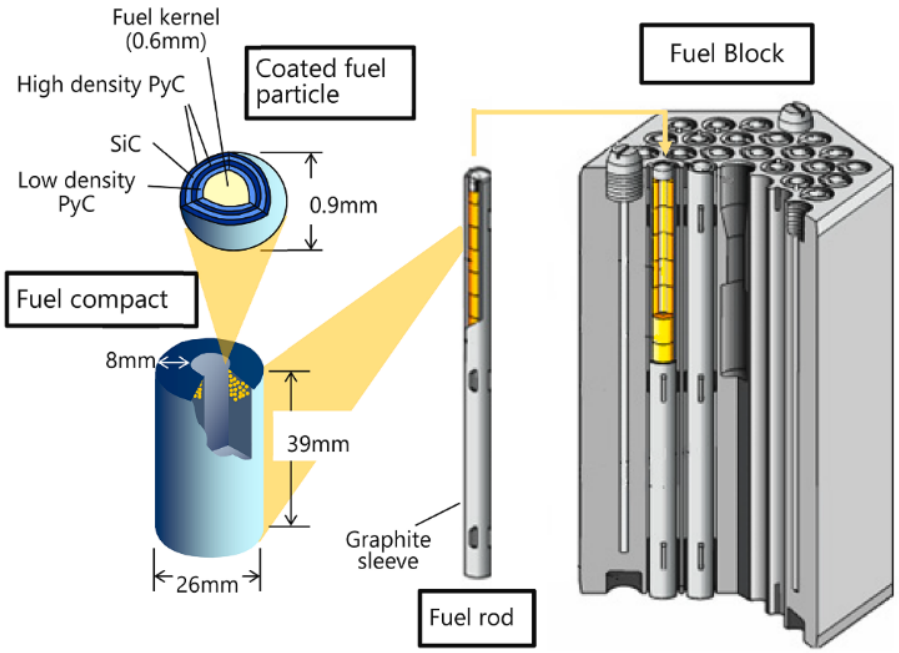

Figure A4: Concept of the prismatic VHTR [72]

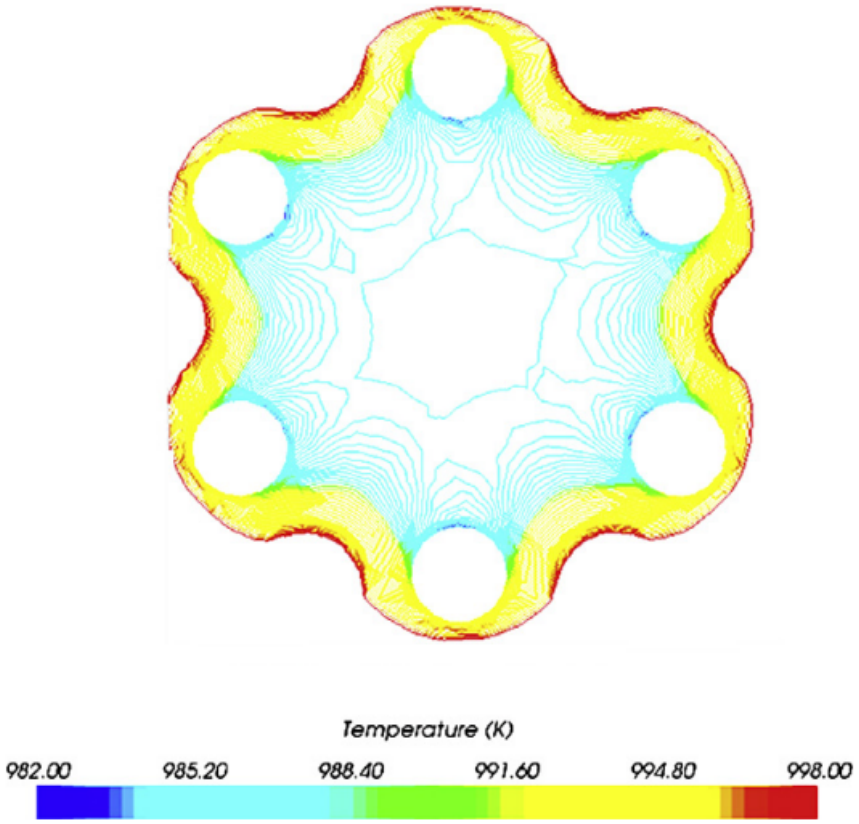

Figure A5: Temperature distribution in a part of the fuel block of a VHTR [156]

A3 Relative weight and sizing calculations

	Type	MWth	MWe	Efficiency	Diameter m	Height m	Weight tonne	Volume m^3	m^3/Mwe	ton/Mwe	Source
ACP100	PWR	385	125	32,47%	3,35	10	300	352,56606	2,82052848	2,4	SMR book
ACPR50S	PWR (mar)	200	50	25,00%	2,2	7,2		109,4784768	2,189569536		SMR book
ACP100S	PWR (mar)	385	125	32,47%	3,35	10	300	352,56606	2,82052848	2,4	SMR book
AP 1000	PWR	3400	1100	32,35%	4,0386	12,056		617,754346	0,56159486		ARIS
AP-600	PWR	1940	600	30,93%	3,988	11,708		584,9838835	0,974973139		ARIS
APR+	PWR	4290	1505	35,08%	6,4	23,1	795	2972,506522	1,97508739	0,528239203	ARIS
APR1000	PWR	2815	1000	35,52%	4,12	14,642		780,8106401	0,78081064		ARIS
APR1400	PWR	3983	1400	35,15%	6,4	23	781	2959,638528	2,11402752	0,557857143	ARIS
APWR	PWR	4466	1500	33,59%	5,2	13,6		1155,30455	0,770203034		ARIS
ATMEA1	PWR	3150	1150	36,51%	4,25						ARIS
Bandi-60	PWR (mar)	200	60	30,00%	2,8	11,2	110	275,8576128	4,59762688	1,833333333	SMR book
CAP200	PWR	660	200	30,30%	3,28	8,845	200	298,9485236	1,494742618	1	SMR book
Carem	PWR	100	30	30,00%	3,2	11	267	353,869824	11,7956608	8,9	SMR book
EPR	PWR	4590	1650	35,95%	4,87	13,083	520	974,8014176	0,590788738	0,315151515	ARIS
HAPPY200	PWR	200		0,00%	2,4	4,5	26	81,430272			ARIS
IMR	PWR	1000	350	35,00%	6	17		1922,6592	5,493312		SMR book
i-SMR	PWR	540	170	31,48%	5	23	650	1806,42	10,626	3,823529412	SMR book
KLT-40S	PWR (mar)	300	60	20,00%	1,92	3,892	70,5	45,07400798	0,751233466	1,175	ARIS
NUWARD	PWR	540	170	31,48%	4	13	310	653,4528	3,84384	1,823529412	ARIS
OPEN20	PWR	73	22	30,14%	2,3	9,1	89,3	151,2334824	6,8742492	4,059090909	SMR book
OPR1000	PWR	2815	1000	35,52%	4,14	14,642	-	788,4097257	0,788409726		ARIS
RITM-200	PWR	190	55	28,95%	3,4	7,5	164	272,37672	4,952304	2,981818182	SMR book
RITM-200M	PWR (mar)	175	50	28,57%	3,45	8,6	265	321,5788884	6,431577768	5,3	SMR book
Rolls-Royce	PWR	1358	470	34,61%	4,2	7,9	150	437,8008096	0,931491084	0,319148936	SMR book
SHELF-M	PWR (mar)	35,2	10	28,41%	2,6	4	75	84,948864	8,4948864	7,5	SMR book
SMART (KAERI)	PWR	365	107	29,32%	6,5	18,5	1070	2455,5531	22,94909439	10	SMR book
SMR-160	PWR	525	160	30,48%	3	15	295	424,116	2,650725	1,84375	SMR book
STAR	PWR	30	10	33,33%	2,3	7,6	20	126,3048864	12,63048864	2	SMR book
UK-SMR	PWR	1276	443	34,72%	4,5	11,3	220	718,87662	1,622746321	0,496613995	ARIS
VBER-300	PWR (mar)	917	300	32,72%	3,4	8,265	306,6	300,1591454	1,000530485	1,022	ARIS
VOYGR	PWR	250	77	30,80%	2,7	17,7		405,3700728	5,2645464		SMR book
VVER-1000 (V-466B)	PWR	3000	1011	33,70%	4,195	11,235	322	621,1377082	0,614379533	0,318496538	ARIS
VVER-1200 (V-392M)	PWR	3200	1082	33,81%	4,232	3,855	330	216,9035144	0,200465355	0,304990758	ARIS
VVER-1200 (V-491)	PWR	3200	1082	33,81%	4,232	3,855	330	216,9035144	0,200465355	0,304990758	ARIS
VVER-1500 (V-448)	PWR	4250	1560	36,71%	4,96	12,5	430	966,104832	0,619297969	0,275641026	ARIS
VVER-300 (V-478)	PWR	850	300	35,29%	3,145						ARIS
VVER-600 (V-498)	PWR	1600	600	37,50%	4,232	3,855	330	216,9035144	0,361505857	0,55	ARIS
VVER-640 (V-407)	PWR	1800	603	33,50%	4,132	10,655	288	571,5114925	0,947780253	0,47761194	ARIS
Westinghouse SMR	PWR	800	225	28,13%	3,7	28		1204,238112	5,352169387		SMR book
Unitherm	PWR	30	6,6	22,00%	2,9	9,8	32	258,9243888	39,230968	4,848484848	SMR book
	PWR total								**4,765367803**	**2,405688497**	
	PWR SMR <300		**<300**						**7,838563497**	**3,70061977**	
	PWR SMR <50		**<50**						**12,52105719**	**5,43459596**	
	PWR maritime								**3,755136145**	**3,205055556**	
	PWR maritime <50		**<50**						**5,705344568**	**6,4**	

Figure A6: Overview of the weight and sizing belonging to PWRs based on IAEA [45] or ARIS [68]

	Type	MWth	MWe	Efficiency	Diameter m	Height m	Weight tonne	Volume m^3	m^3/Mwe	ton/Mwe	Source
AMR	VHTR	10	3	30,00%	2,78	5,96	115	144,706067	48,23535566	38,33333333	SMR book
GTHTR300C	VHTR	600	274	45,67%	8	23	1000	4624,4352	16,87750073	3,649635036	ARIS/SMR book
GT-MHR	VHTR	600	288	48,00%	8,2	29	950	6125,994336	21,27081367	3,298611111	SMR book
HTMR100	VHTR	100	35	35,00%	5,6	15,7	155	1546,773043	44,19351552	4,428571429	SMR book
HTR-PM	VHTR	500	210	42,00%	5,7	25	800	2551,7646	12,15126	3,80952381	SMR book
MHR-T	VHTR	600	205,5	34,25%	6,9	32,8	950	4905,947693	23,87322478	4,622871046	SMR book
PBMR	VHTR	400	165	41,25%	6,2	30	1250	3622,89312	21,956928	7,575757576	SMR book
HOLOSQUAD	VHTR	22	10	45,45%			60			6	SMR book
Prismatic HTR	VHTR	350	150	42,86%	6,8	22		3195,886848	21,30591232		ARIS
SC-HTGR	VHTR	625	272	43,52%	8,5	24	880	5447,5344	20,0277	3,235294118	ARIS
U-Battery	VHTR	10	4	40,00%	2,2	5,5		83,629392	20,907348		SMR book
XE-100	VHTR	200	82,5	41,25%	4,88	16,4	274	1226,971232	14,87237857	3,321212121	SMR book
	VHTR total								**24,1519943**	**7,827480958**	
	VHTR SMR <300		**<300**						**24,1519943**	**7,827480958**	
	VHTR SMR <50		**<50**						**37,77873973**	**16,25396825**	

Figure A7: Overview of the weight and sizing belonging to VHTRs based on IAEA [45] or ARIS [68]

	Type	MWth	MWe	Efficiency	Diameter m	Height m	Weight tonne	Volume m^3	m^3/Mwe	ton/Mwe	Source
ALFRED	LFR	300	125	41,67%							ARIS
BREST-OD-300	LFR	700	300	42,86%							Aris
CLEAR-I	LFR	10									ARIS
ELECTRA	LFR	0.5									ARIS
ELFR	LFR	1500	630	42,00%							ARIS
G4M	LFR	70	25	35,71%							ARIS
LFR-AS-200	LFR	480	200	41,67%	6	6,2	42	701,20512	3,5060256	0,21	ARIS
LFR-TL-30	LFR	90	30	33,33%	3,7	5	35	215,04252	7,168084	1,166666667	SMR book
MYRRHA	LFR	100									ARIS
MicroUranus	LFR	60	20	33,33%	2,4	11	200	199,051776	9,9525888	10	SMR book
PEACER	LFR	850	300	35,29%							ARIS
SEALER	LFR	140	55	39,29%	4,8	6	50	434,294784	7,8962688	0,909090909	ARIS
SVBR-100	LFR	280	100	35,71%	4,53	8,2		528,6413674	5,286413674		ARIS
W-LFR	LFR	950	460	48,42%	3,9	7,5	35	358,37802	0,779082652	0,076086957	ARIS
	LFR total								**5,764743921**	**2,472368906**	
	LFR SMR <300		**<300**						**6,761876175**	**3,071439394**	
	LFR SMR <50		**<50**						**8,5603364**	**5,583333333**	

Figure A8: Overview of the weight and sizing belonging to LFRs based on IAEA [45] or ARIS [68]

	Type	MWth	MWe	Efficiency	Diameter m	Height m	Weight tonne	Volume m^3	m^3/Mwe	ton/Mwe	Source
4S	SFR	30	10	33,33%	3,4	25,5	86	926,080848	92,6080848	8,6	ARIS
ARC-100	SFR	286	100	34,97%	7,9	16,7	600	3274,323175	32,74323175	6	SMR book
	SFR total								**62,67565828**	**7,3**	
	SFR SMR <300		**<300**						**62,67565828**	**7,3**	
	SFR SMR <50		**<50**						**92,6080848**	**8,6**	

Figure A9: Overview of the weight and sizing belonging to SFRs based on IAEA [45] or ARIS [68]

A4 Impact main compressor inlet temperature

The inlet temperature of the main compressor and turbine have a significant effect on the total cycle efficiency. Brun et al. [85] presents the impact of the compressor inlet temperature as a function of different turbine inlet temperatures. It can be seen in Figure A10 that the lowest compressor inlet temperature, and the highest turbine inlet temperature, results in the highest overall cycle efficiency. For this research, the compressor inlet temperature was selected higher than Figure A10 even indicates, meaning that the cycle efficiency is not optimal regarding the main compressor inlet temperature. It was however decided for this research that efficiency is not the most important factor, and therefore no additional time was spent on improving this compressor inlet temperature. It must however be stated that if naval vessels want to operate globally, and an improved cycle efficiency is required, a solution must be found to operate the main compressor closer to a seawater temperature of 35 °C.

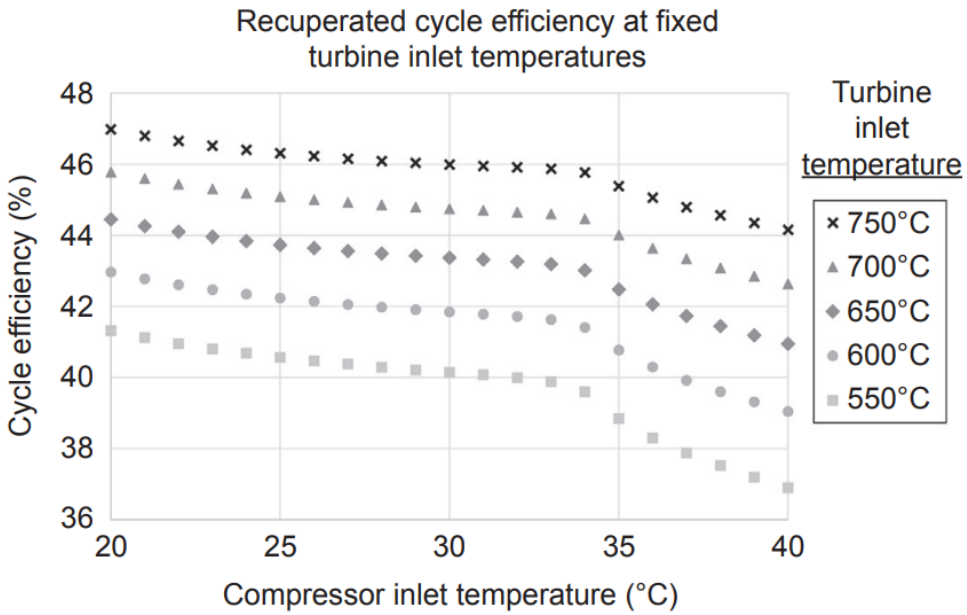

Figure A10: Impact of compressor and turbine inlet temperature on cycle efficiency [85]

A5 Lookup Tables

As explained in Section 4.4, directly calling CoolProp for each thermodynamic property during the simulation, slows down the simulation drastically. This is expected as Simulink must first call Matlab, which must then call Python which applies CoolProp to find the correct value. The found value must than be directed in reverse back to Simulink before the simulation can continue. To improve this, the values for each thermodynamic property have been calculated before running the simulation and are saved in datasets which can be used by Simulink to determine the value for the required property. This dataset is however limited by its data points, which decreases the accuracy of the requested property. To indicate the lack of accuracy, the sizing of the datasets will be presented. As there are three different fluids operating in the system, different datasets are created. The dataset for helium is presented in Table A1, for water in Table A2 and for sCO_2 in Table A3.

The range sizes of the dataset are based on the expected pressures during the simulation, including a margin below and above the maximum values. In addition, a range of temperatures for each working medium can be created, based on the designed cycle point. However, as the pressure and enthalpy are used in the model, the temperature must first be converted to a enthalpy range. For helium and water the minimum and maximum enthalpy are at a minimum temperature and pressure and maximum temperature and pressure. For sCO_2 this is not the case, due to operating above the critical point. The minimum enthalpy sCO_2 occurs at maximum pressure and minimum temperature, while the maximum enthalpy occurs at minimum pressure and maximum pressure. This approach therefore determines the range of the datasets and based on the values used during the simulation it was determined that the values do not exceed the ranges of the datasets. The accuracy is therefore only determined by the step size of the datasets. This step size has been based on the data size of the datasets, as smaller step sizes result in datasets that are too large to use within the Simulink environment (with the used computer capabilities).

Table A1: Created datasets for helium used by Simulink with Lookup Tables

Thermo. property	Property 1	Range	Step size	Property 2	Range	Step size
Density	Pressure	$38 - 42$ bar	0.1 bar	Enthalpy	$1955.4 - 6628.6 \frac{kJ}{kg}$	$0.1 \frac{kJ}{kg}$
Dynamic viscosity	Pressure	$38 - 42$ bar	0.1 bar	Enthalpy	$1955.4 - 6628.6 \frac{kJ}{kg}$	$0.1 \frac{kJ}{kg}$
Enthalpy	Pressure	$38 - 42$ bar	0.1 bar	Temperature	$100.0 - 1000.0$ °C	0.1°C
Specific heat capacity	Pressure	$38 - 42$ bar	0.1 bar	Enthalpy	$1955.4 - 6628.6 \frac{kJ}{kg}$	$0.1 \frac{kJ}{kg}$
Temperature	Pressure	$38 - 42$ bar	0.1 bar	Enthalpy	$1955.4 - 6628.6 \frac{kJ}{kg}$	$0.1 \frac{kJ}{kg}$
Thermal conductivity	Pressure	$38 - 42$ bar	0.1 bar	Enthalpy	$1955.4 - 6628.6 \frac{kJ}{kg}$	$0.1 \frac{kJ}{kg}$

Table A2: Created datasets for water used by Simulink with Lookup Tables

Thermo. property	Property 1	Range	Step size	Property 2	Range	Step size
Density	Pressure	$0.9 - 2.0$ bar	0.05 bar	Enthalpy	$84.0 - 251.3 \frac{kJ}{kg}$	$0.05 \frac{kJ}{kg}$
Dynamic viscosity	Pressure	$0.9 - 2.0$ bar	0.05 bar	Enthalpy	$84.0 - 251.3 \frac{kJ}{kg}$	$0.05 \frac{kJ}{kg}$
Enthalpy	Pressure	$0.9 - 2.0$ bar	0.05 bar	Temperature	$20.0 - 60.0$ °C	0.05°C
Specific heat capacity	Pressure	$0.9 - 2.0$ bar	0.05 bar	Enthalpy	$84.0 - 251.3 \frac{kJ}{kg}$	$0.05 \frac{kJ}{kg}$
Temperature	Pressure	$0.9 - 2.0$ bar	0.05 bar	Enthalpy	$84.0 - 251.3 \frac{kJ}{kg}$	$0.05 \frac{kJ}{kg}$
Thermal conductivity	Pressure	$0.9 - 2.0$ bar	0.05 bar	Enthalpy	$84.0 - 251.3 \frac{kJ}{kg}$	$0.05 \frac{kJ}{kg}$

Table A3: Created datasets for sCO_2 used by Simulink with Lookup Tables

Thermo. property	Property 1	Range	Step size	Property 2	Range	Step size
Density	Pressure	$80 - 250$ bar	0.5 bar	Enthalpy	$272.6 - 1228.4 \frac{kJ}{kg}$	$0.5 \frac{kJ}{kg}$
Density	Pressure	$80 - 250$ bar	0.5 bar	Temperature	$40.0 - 700.0$ °C	0.5°C
Dynamic viscosity	Pressure	$80 - 250$ bar	0.5 bar	Enthalpy	$272.6 - 1228.4 \frac{kJ}{kg}$	$0.5 \frac{kJ}{kg}$
Enthalpy	Pressure	$80 - 250$ bar	0.5 bar	Temperature	$40.0 - 700.0$ °C	0.5°C
Enthalpy	Pressure	$80 - 250$ bar	0.5 bar	Entropy	$1.5 - 2.9 \frac{kJ}{K}$	$0.01 \frac{kJ}{K}$
Entropy	Pressure	$80 - 250$ bar	0.5 bar	Enthalpy	$272.6 - 1228.4 \frac{kJ}{kg}$	$0.5 \frac{kJ}{kg}$
Specific heat capacity	Pressure	$80 - 250$ bar	0.5 bar	Enthalpy	$272.6 - 1228.4 \frac{kJ}{kg}$	$0.5 \frac{kJ}{kg}$
Temperature	Pressure	$80 - 250$ bar	0.5 bar	Enthalpy	$272.6 - 1228.4 \frac{kJ}{kg}$	$0.5 \frac{kJ}{kg}$
Thermal conductivity	Pressure	$80 - 250$ bar	0.5 bar	Enthalpy	$272.6 - 1228.4 \frac{kJ}{kg}$	$0.5 \frac{kJ}{kg}$
Volumetric heat capacity	Pressure	$80 - 250$ bar	0.5 bar	Enthalpy	$272.6 - 1228.4 \frac{kJ}{kg}$	$0.5 \frac{kJ}{kg}$

A6 Performance maps KAIST

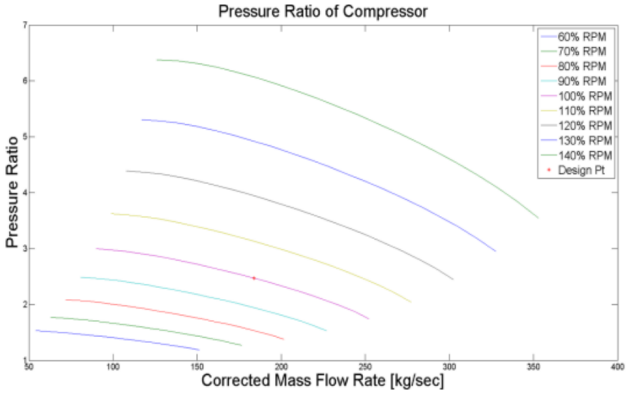

Figure A11: Pressure ratio compressor map [108]

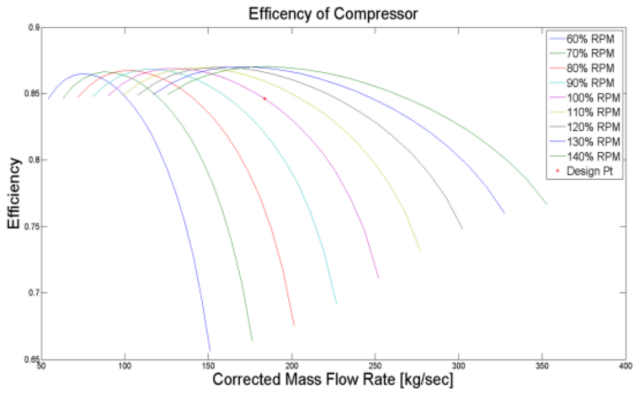

Figure A12: Efficiency compressor map [108]

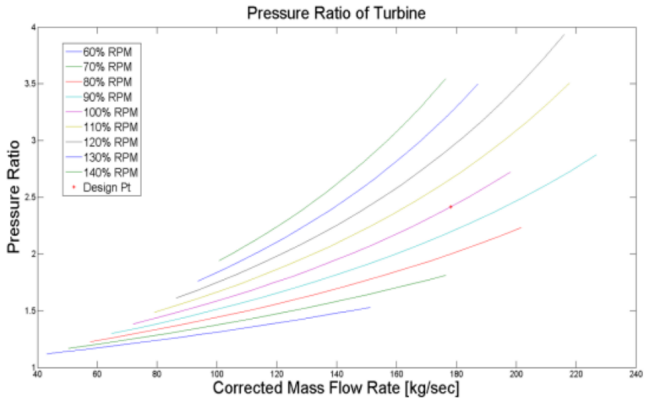

Figure A13: Pressure ratio turbine map [108]

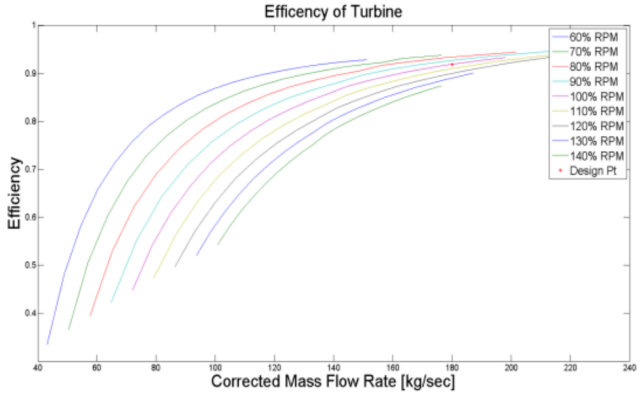

Figure A14: Efficiency turbine map [108]

A7 Scaling method performance maps

The selected performance map of the KAIST research group is not applicable to the selected turbomachinery as their turbomachinery has a higher than preferred power output. Therefore a scaling analysis must be done to convert the performance map to small power size turbomachinery. Due to a lack of time, it was not achieved to implement this scaling method successfully, and therefore a normalization approach was selected. Still, this scaling method gives insights for further studies regarding a scaling approach and will therefore still be presetend.

For the scaling analysis it is of importance to investigate the non-dimensional groups applicable for describing the performance of turbomachinery. Dixon and Hall [163] describe 7 non-dimensional groups Π for turbomachinery, which are described in Equations 84-90 [163] [161].

$$\Pi_1 = \frac{\dot{m}\sqrt{\gamma R T_{in}}}{D^2 \gamma P_{in}}, \text{ Flow parameter} \tag{84}$$

$$\Pi_2 = \frac{ND}{\sqrt{\gamma R T_{in}}}, \text{ Speed parameter} \tag{85}$$

$$\Pi_3 = \frac{\Delta h}{\gamma R T_{in}}, \text{ Head parameter} \tag{86}$$

$$\Pi_4 = \frac{p_{out}}{p_{in}} = \text{PR}, \text{ Pressure ratio} \tag{87}$$

$$\Pi_5 = \frac{T_{out}}{T_{in}} \rightarrow \eta, \text{ Efficiency} \tag{88}$$

$$\Pi_6 = \frac{\rho V D}{\mu} = \text{Re}, \text{ Reynolds number} \tag{89}$$

$$\Pi_7 = \frac{C_p}{C_v} = \gamma, \text{ Specific heat ratio} \tag{90}$$

These non-dimensional groups include the mass flow $\dot{m}$, the specific heat ratio γ, the specific gas constant R, the temperature T, the turbomachinery diameter D, the pressure p, the shaft speed N, the enthalpy change Δh, efficiency η, the density ρ, the volume V, the viscosity μ, the specific heat C_p and specific volume C_v.

For turbomachinery handling only one single gas, the specific heat ratio can be dropped as an independent non-dimensional group [163] [162]. In addition, the effect of the Reynolds number can also be neglected, as the effects of Reynolds on turbomachinery performance is small when $Re > 2 \cdot 10^5$ [163] due to the small effect of viscosity at high Reynolds numbers [161] [162]. As a result, only five dimensionless number groups are applicable for the case of sCO_2, which are Π_1-Π_5. It is furthermore common to drop the diameter from these groups if the diameter is fixed [163] [161] [162] , but this will be neglected as during scaling the diameter could change significantly.

When applying a scaling method between different sizes of turbomachinery, it is important to account for the above mentioned dimensionless groups. As can be seen by looking at the dimensionless groups, the pressure ratio Π_4 and efficiency Π_5 are already dimensionless and are therefore constant during the scaling method. Furthermore, neglecting the Reynolds number Π_6 and the specific heat ratio Π_7 results in that only three dimensionless numbers are of importance, which are the so called flow, speed and head parameter.

Besides the non-dimensional groups, it is important to ensure that the flow mechanism of the turbomachinery is still the same after scaling as this ensures that performance characteristic are maintained [163] [162]. To ensure the performance maps after scaling are still applicable, it is beneficial to ensure similar type of performance

between the turbomachinery. The flow mechanism can be assumed the same if the specific speed and diameter of the turbomachinery are equal. The specific speed N_s and specific diameter D_s are defined as follows:

$$N_s = \frac{\phi^{0.5}}{\psi^{0.75}} \tag{91}$$

$$D_s = \frac{\psi^{0.25}}{\phi^{0.5}} \tag{92}$$

, with the flow coefficient ϕ and the stage loading ψ defined as:

$$\phi = \frac{Q}{ND^3} \tag{93}$$

$$\psi = \frac{gH}{N^2D^2}. \tag{94}$$

N_s can also be defined by Equation 95 when the flow is compressible [163]. In this equation the specific speed is related to the shaft speed N, the mass flow $\dot{m}$, the exit density ρ_e and the isentropic enthalpy rise Δh_{0s}. It is stated by Dixon and Hall that the exit density can be guessed as the extra uncertainty introduced by this is small on the selected turbomachinery [163].

$$N_s = N\left(\frac{\dot{m}}{\rho_e}\right)^{0.5}\Delta h_{0s}^{-0.75} \tag{95}$$

By realizing the important dimensionless number, a scaling analysis can be performed. According to Equation 96 power P, mass flow $\dot{m}$ and diameter D are related for turbomachinery.

$$P \propto \dot{m} \propto D^2 \tag{96}$$

Due to this relation, the scale factor between the referenced and scaled turbomachinery can be determined according to Equation 97 [162].

$$SF = \frac{P_{des}}{P_{ref}} \propto \frac{\dot{m}_{des}}{\dot{m}_{ref}} \propto \frac{D_{des}^2}{D_{ref}^2} \tag{97}$$

This equation makes it possible to determine the design mass flow and diameter of the turbine if a reference turbine and a design power output is provided. For scaling the performance maps, there are four parameters which must be converted. These are the mass flow, shaft speed, pressure ratio and efficiency (see Section 4.8). As determined from the non-dimensional groups, the pressure ratio and efficiency are already dimensionless and are therefore constant during scaling. The mass flow and shaft speed do however change. Applying the Pham similitude method on the non-dimensional groups Π_1 and Π_2, the flow and speed parameter, results in the two scaling equations for the performance maps presented in Equations 98 and 99. By multiplying mass flow and shaft speed of the KAIST performance map according to these equation, while keeping pressure ratio and efficiency constant, the scaled performance maps can be obtained.

$$\dot{m}_{des} = \frac{\Pi_1 D_{des}^2 n_{s,des} P_{des}}{\sqrt{n_{s,des} Z_{des} R T_{des}}}, \text{ with } \Pi_1 = \frac{\dot{m}_{ref}\sqrt{n_{s,ref} Z_{ref} R T_{ref}}}{D_{ref}^2 n_{s,ref} P_{ref}} \tag{98}$$

$$N_{des} = \frac{\Pi_2 \sqrt{n_{s,des} R T_{des}}}{D_{des}}, \text{ with } \Pi_2 = \frac{N_{ref} D_{ref}}{\sqrt{n_{s,ref} R T_{ref}}} \tag{99}$$

In reality there are limitations to these relations as size effects of the turbomachinery impact the optimal mass flow rate, power and efficiency of a turbine [162]. Small turbomachinery always have lower efficiencies than larger geometrically similar machines [163]. However, as the reference power output and the scaled power output are within the same range, the assumption is made that these size effects can be neglected.

A8 Scaling impact on efficiency

The size of the turbomachinery impacts the optimal mass flow rate, power and efficiency of a turbomachinery [162]. Small turbomachinery always have lower efficiencies than larger geometrically similar machines [163]. To determine if large efficiency differences would occur between the designed power conversion cycle of 7.9 MWe, and the reference power conversion cycle of 12.5 MWe, a scaling impact analysis has been performed. An indication about the effect of scaling on efficiency has been made with Equation 100 [162] [163]. The exponent n used in this equation depends on the type of turbomachinery. Visser [162] states the range of n is between 0.12 to 0.5, but that $n = 0.2$ is the favored option. Dixon and Hall [163] also favor $n = 0.2$, but state the range is between 0.2 to 0.25. Therefore, $n = 0.2$ was selected as value for the exponent.

$$\frac{1 - \eta_{des}}{1 - \eta_{ref}} = \frac{{D_{ref}}^{n}}{D_{des}} \tag{100}$$

The effect of scaling on the efficiency has been investigated for specific cases of which a comparison can be seen in Table A4. This has been performed by applying the relation that holds between power, mass flow and diameter. As expected, the efficiency lowers with a smaller diameter and increases due to a larger diameter. However, the impact on scaling is small on the overall efficiency as the efficiency differs 0.2% and 1.1% for a power increase of 5 MW with the turbine and compressor respectively. As suggested by Visser [162], if a turbomachinery model with improvements in efficiency is required, than a fundamental turbomachinery design must be undertaken, but this is impractical for preliminary design analysis like this study. It was therefore decided to neglect this small change in efficiency.

Table A4: Efficiency comparison between the desired scaling power output and the realised power output

Compressor power	Mass flow	Diameter	Efficiency
9.34 MW (KAIST)	180 kg/s	0.2722 m	84.9%
5 MW	96.34 kg/s	0.1991 m	83.9%
7.5 MW	144.51 kg/s	0.2439 m	84.6%
10 MW	192.68 kg/s	0.2816 m	85.0%
Turbine power	**Mass flow**	**Diameter**	**Efficiency**
21.75 MW (KAIST)	180 kg/s	0.3254 m	91.9%
15 MW	124.14 kg/s	0.2702 m	91.6%
20 MW	165.52 kg/s	0.3120 m	91.8%
25 MW	206.90 kg/s	0.3489 m	92.0%

A9 Comparison interpolation and extrapolation method

To decide which inter-/extrapolation method should be used, a visual comparison has been performed towards the impact of each inter-/extrapolation method. In Figures A15-A17 a comparison between the different interpolation methods can be seen (without using any extrapolation method). The results differ slightly as it can be seen that the linear and natural interpolation methods result in smoother transitions between different data points compared to the nearest interpolation method. Between natural and linear interpolation no significant differences could be observed so natural interpolation was chosen as the preferred interpolation method as this method uses polynomial functions to create a smooth curve that passes through each data point ensuring a theoretically more smoother performance map.

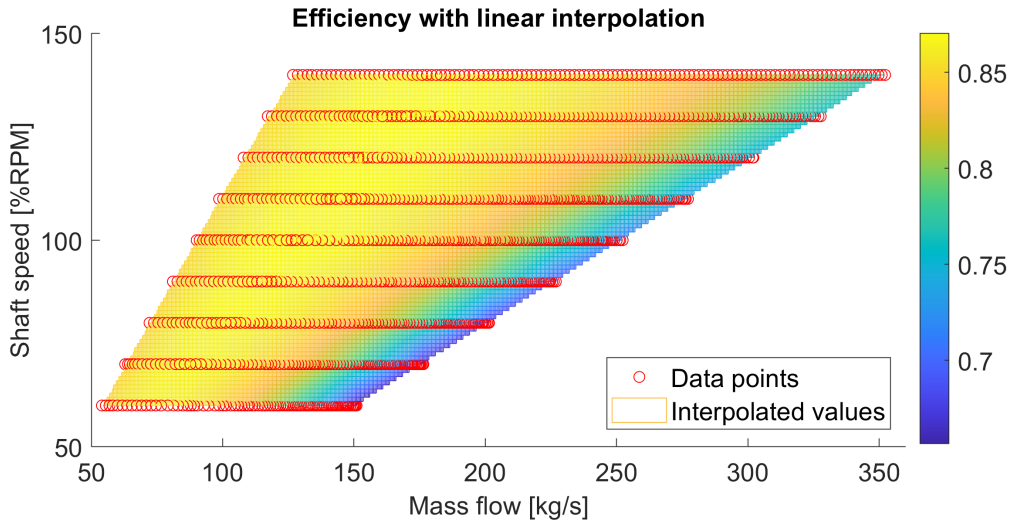

Figure A15: Comparison interpolation methods: effect of linear on the efficiency

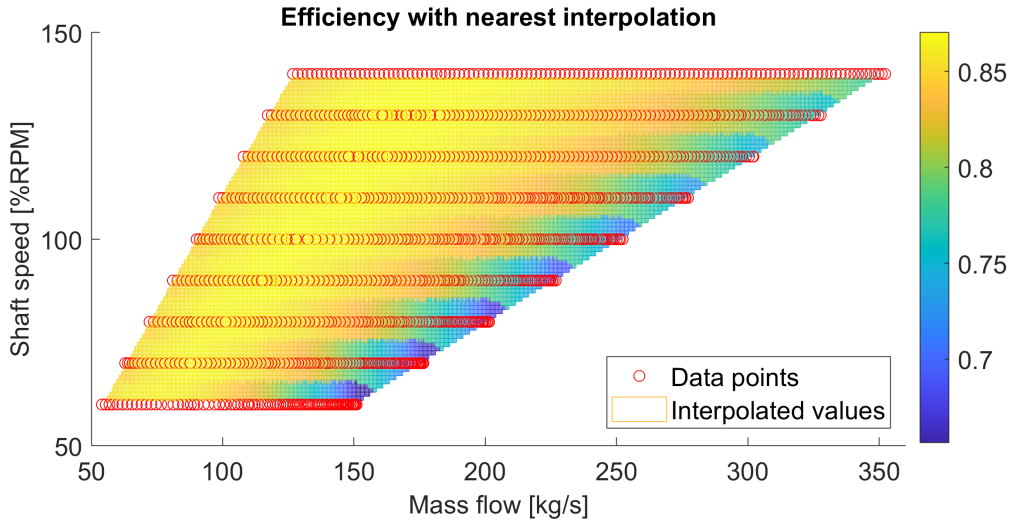

Figure A16: Comparison interpolation methods: effect of nearest on the efficiency

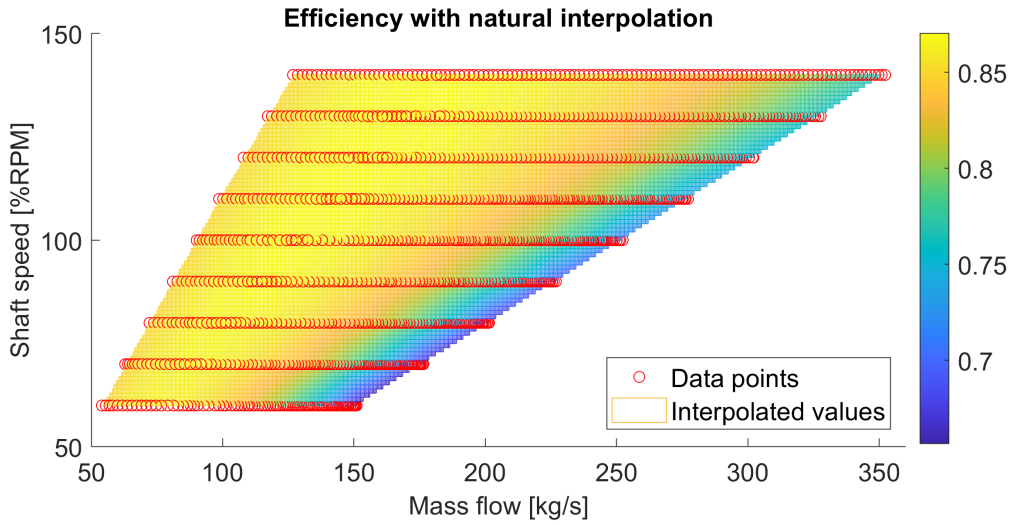

Figure A17: Comparison interpolation methods: effect of natural on the efficiency

There are also three options for extrapolation, which are linear, nearest and boundary. Although it is not preferred for the turbomachinery to enter these areas (as this results in surge or choke), it is model wise better to ensure this is possible, as this way the model will not immediately crash if these areas are entered. In Figures A18-A20 a comparison between the different extrapolation methods can be seen. It is clear that the linear extrapolation method results in inaccurate extrapolation data points and is therefore excluded. Between the nearest and boundary extrapolation method a small difference can be observed. It seems that the boundary method, which applies the values off the interpolation boundary as extrapolation values, produces a smoother performance map. As shown in Figure A19 the nearest extrapolation method results in inconsistent efficiency areas, while the boundary extrapolation method produces an efficiency area which increases/decreases consistently. The boundary extrapolation method is therefore the preferred extrapolation method for the performance maps.

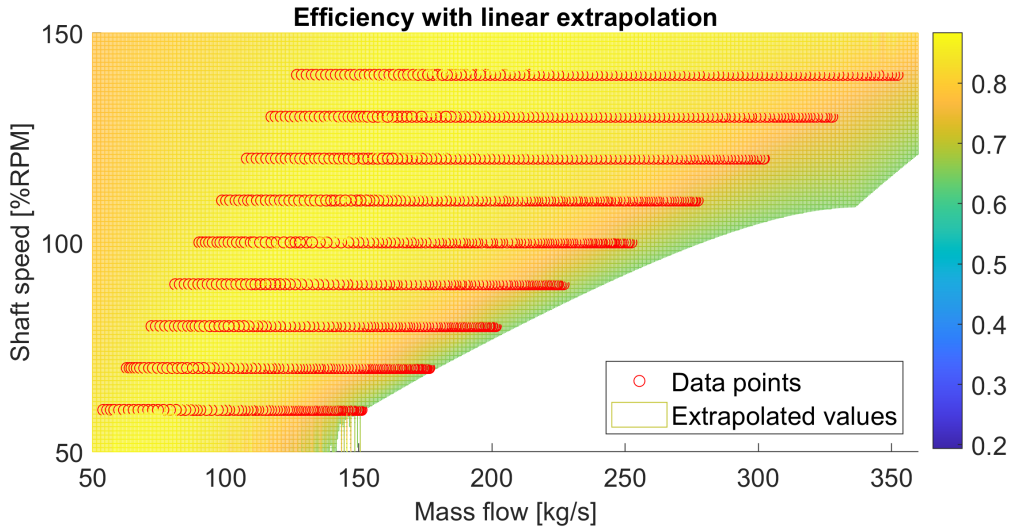

Figure A18: Comparison extrapolation methods: effect of linear on the efficiency

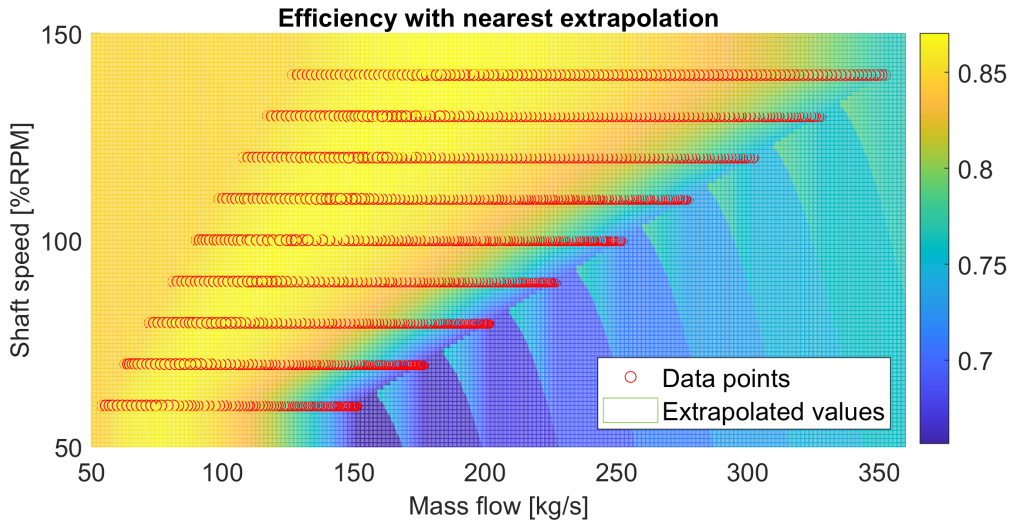

Figure A19: Comparison interpolation methods: effect of nearest on the efficiency

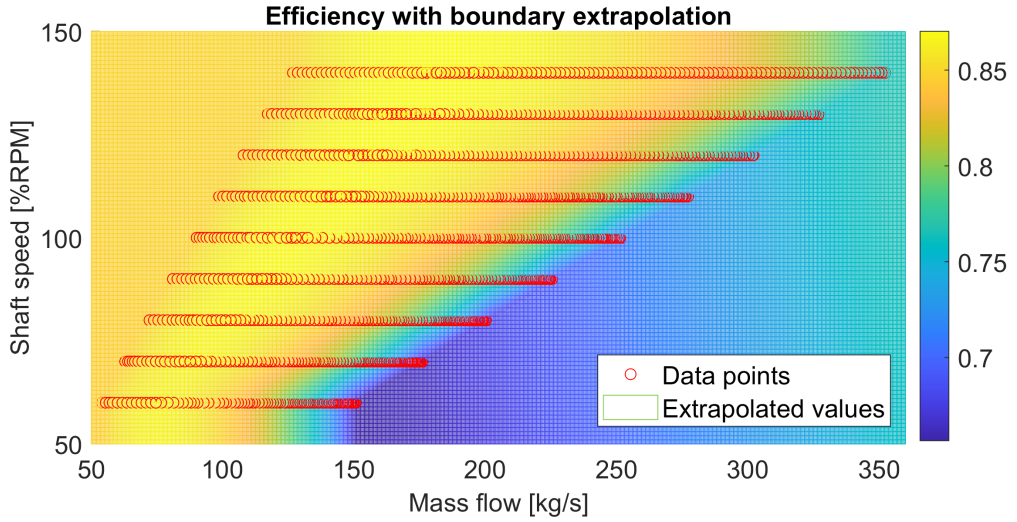

Figure A20: Comparison interpolation methods: effect of boundary on the efficiency

Finally, using these created performance maps with 2D Lookup Tables still requires some kind of interpolation method, as the created mesh is still a grid of data points. By changing the different methods of the 2D Lookup Table blocks an investigation has been done towards the effect of these interpolation methods. However, the output difference between these methods is negligible, which is probably the result of the already small mesh used in creating the performance maps. It was therefore decided to use the Linear point-slope interpolation, as this method is more accurate than methods that round values during operation (flat or nearest), but is still a less complex and faster interpolation method than methods using polynomial functions or other domains (Cubic spline, Linear Lagrange or Akima spline). [173]

A10 Impact correction equations

To indicate the impact of the correction equations, Figure A21 shows the obtained compression ratio for the main compressor for three different cases in which mass flow and shaft speed are kept constant, but pressure changes. At first the pressure ratio is obtained without using the correction equations, which shows an as expected constant obtained pressure ratio. In the second case, the pressure ratio is obtained by using the Pham correction equations for mass flow and shaft speed, but not applying the pressure correction equations. The third case applies the Pham correction equations while using the pressure ratio corrections. Although the impact of the pressure correction equation is small, the figure shows the correction equations do have a significant impact on the pressure within the system. Looking at for example a pressure inlet of 95 bar, a pressure ratio of 2.5 and 2.52 results in a pressure increase up to 237.5 and 239.4 bar, resulting in a 2 bar pressure difference. Figure A21 also shows that neglecting the pressure ratio correction equations is not applicable, as then the pressure ratio changes according to the 'partial corr' line, which shows clear deviations from design pressure ratio.

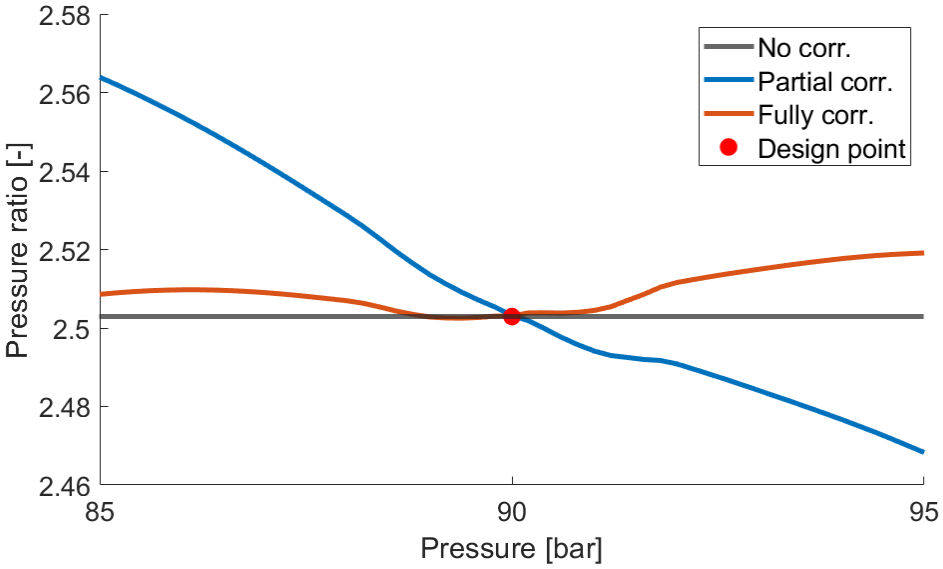

Figure A21: Impact of a pressure change and the correction equations on the obtained pressure ratio

A11 Heat exchangers values for validation

In addition to the heat exchanger design values presented in Figure A22 by Marchionni et al. [138], it is also stated that the plate thickness of the PCHE is equal to 1.63 mm. Figure 63 present the inlet conditions of the heat exchanger during the transient simulation.

Table 5
PCHE channel geometry.

Wetted perimeter [mm]	5.14
Hydraulic diameter [mm]	1.22
Cross-sectional area [mm^2]	1.57
Length [mm]	1012.00
Type	Zig-zag

Table 6
Additional PCHE features.

Material	SS 316L
Channel surface roughness	Not available
Channel discretization length [mm]	25.30
Number of channels per row	54
Number of rows	42

Figure A22: Design parameters for the heat exchanger used by Marchionni et al. [138]

A12 Scenario 0; Power balance, LTR and CL results

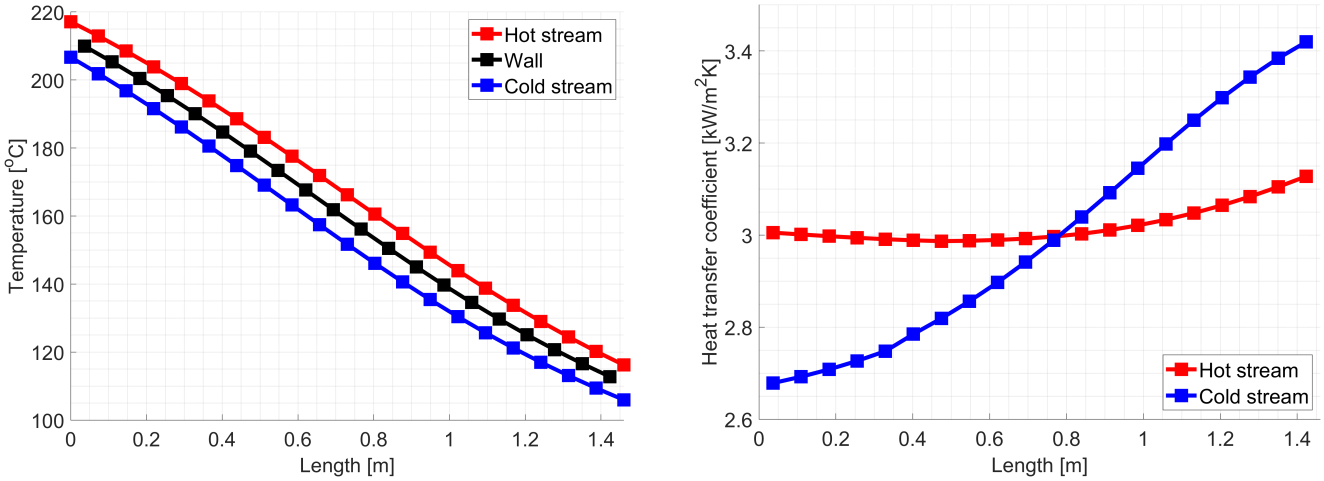

Figure A23: Temperature and heat transfer coefficient along the length of the LTR

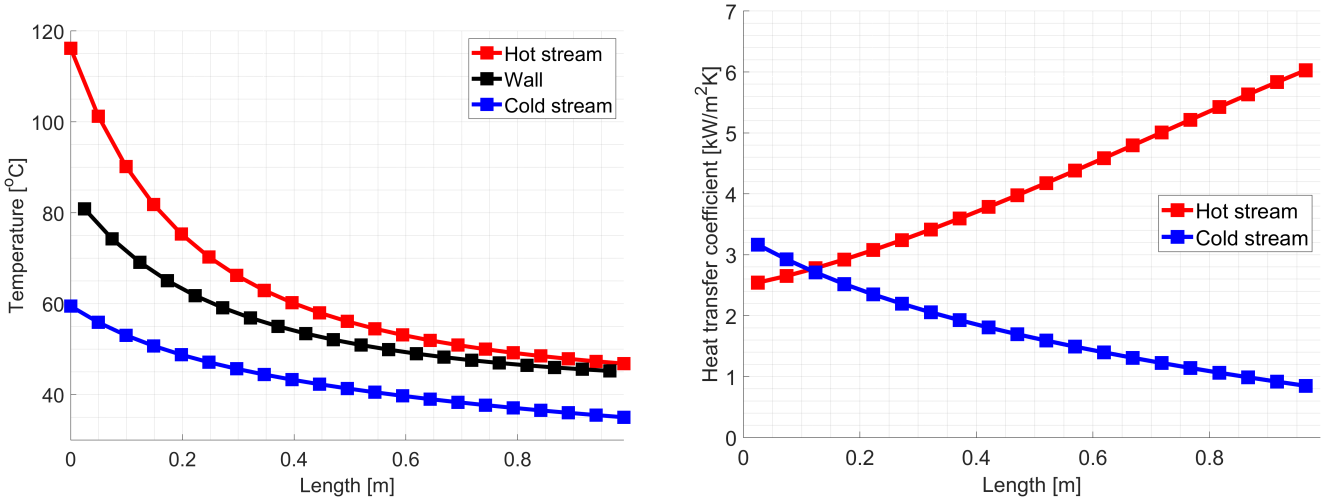

Figure A24: Temperature and heat transfer coefficient along the length of the CL

Table A5: Steady state power values

Component	Value
Reactor	20.00 MW
Turbine	13.15 MW
Main comp.	2.96 MW
Recomp.	2.13 MW
Generator	8.06 MW
Load	7.90 MW
Cooling	11.94 MW
Blower	0.36 MW
Efficiency	39.50%

A13 Scenario 3; LTR and CL results

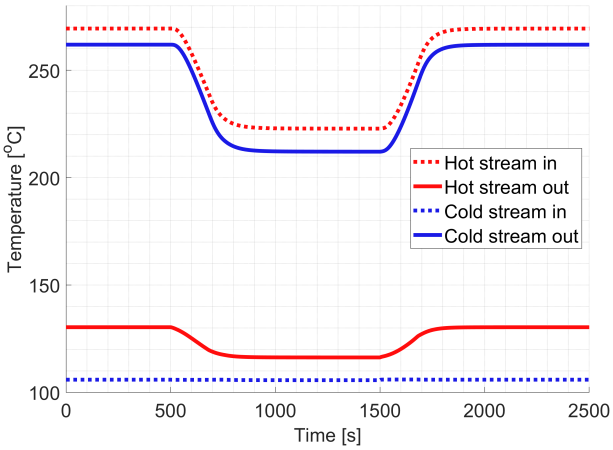

Figure A25: Temperature development of the LTR

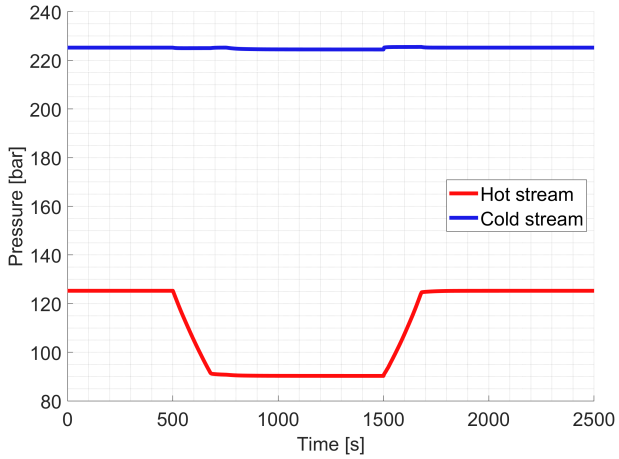

Figure A26: Pressure development of the LTR

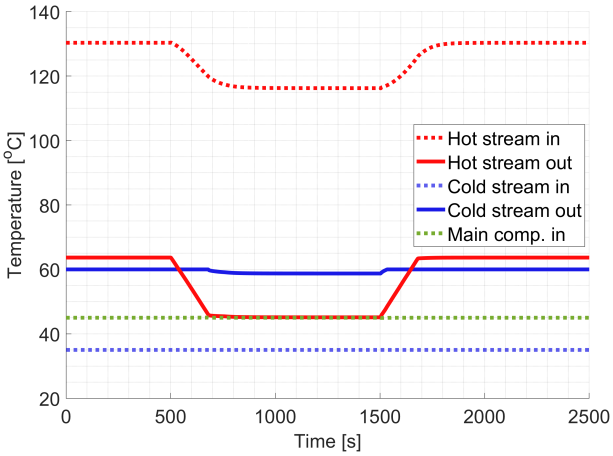

Figure A27: Temperature development of the CL

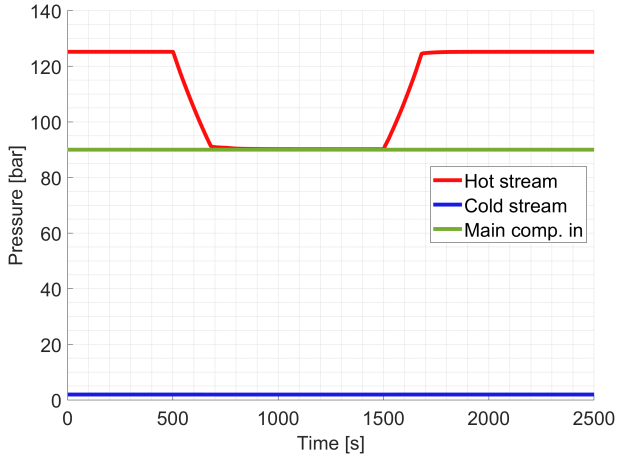

Figure A28: Pressure development of the CL

A14 Scenario 4; LTR and CL results

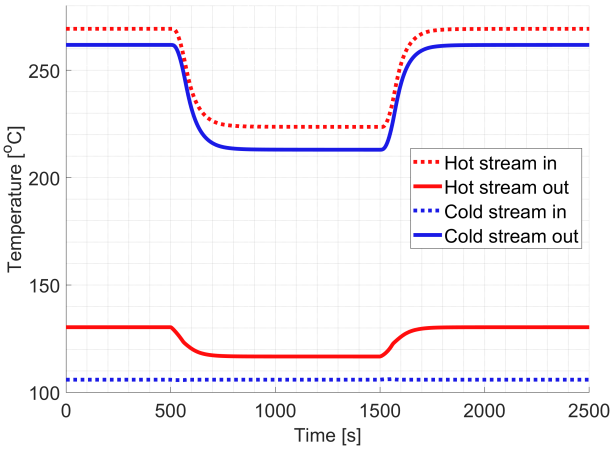

Figure A29: Temperature development of the LTR

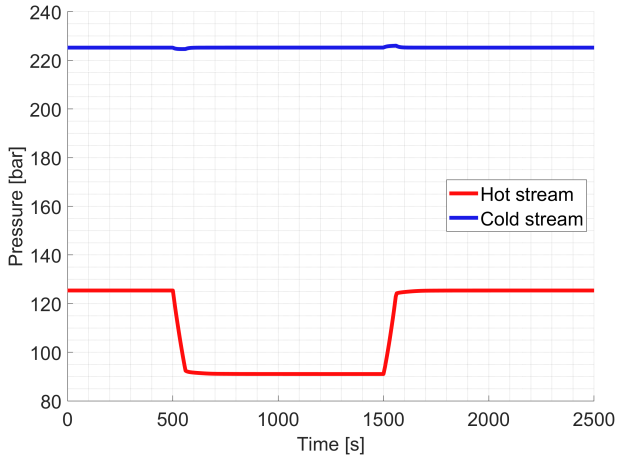

Figure A30: Pressure development of the LTR

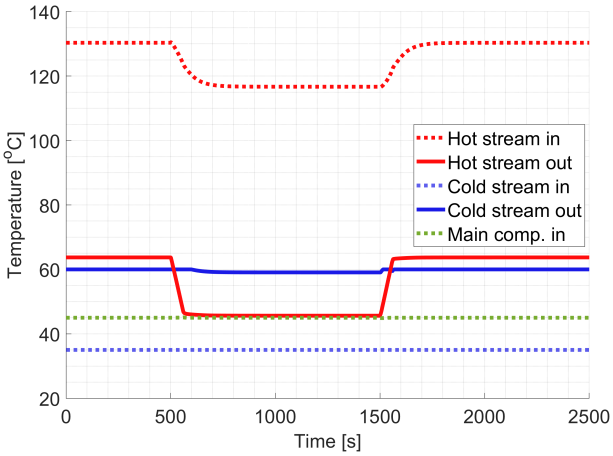

Figure A31: Temperature development of the CL

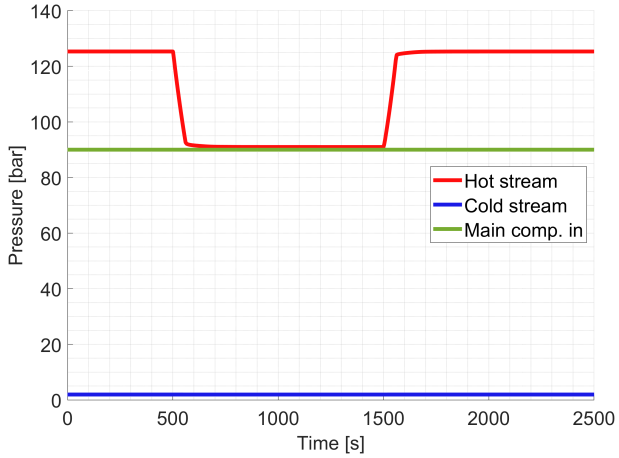

Figure A32: Pressure development of the CL

A15 3D turbomachinery performance map for simulation

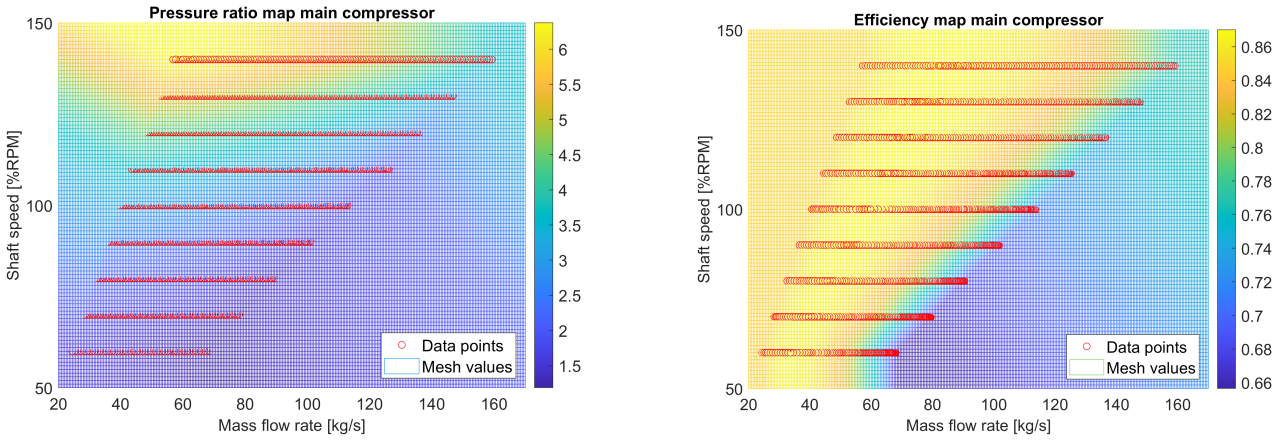

Figure A33: Main compressor performance maps

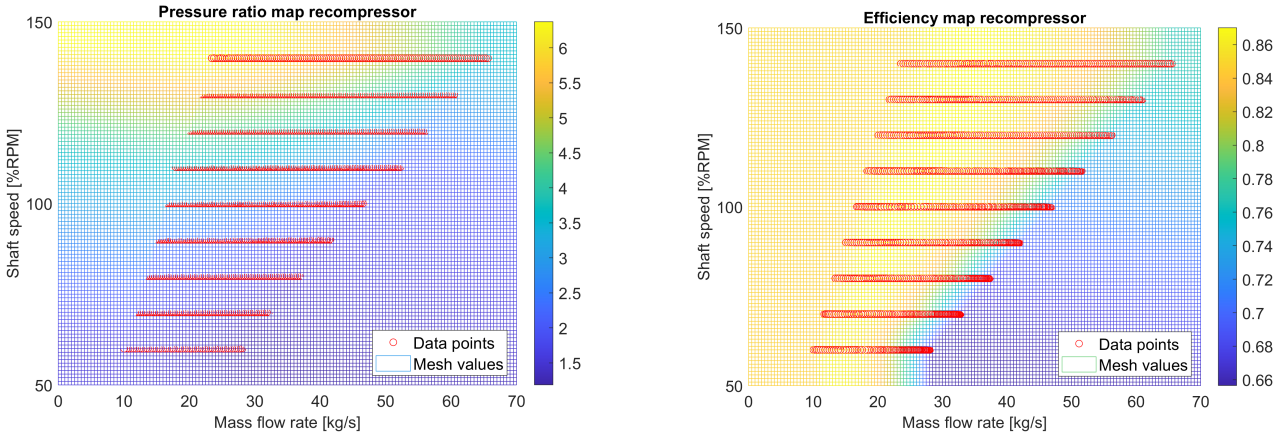

Figure A34: Recompressor performance maps

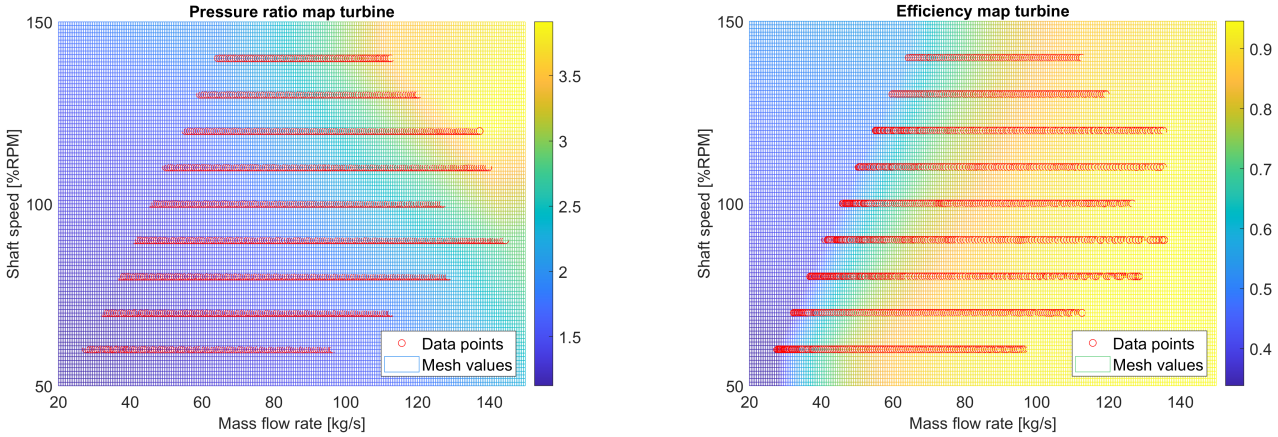

Figure A35: Turbine performance maps

References

[1] National Review. USS Gerald R. Ford. https://www.nationalreview.com/photos/uss-gerald-r-ford-aircraft-carrier-flight-operations/, 2022. Accessed on: 21-03-24.

[2] Dutch maritime sector. No guts, no Hollands Glorie! https://www.rijksoverheid.nl/documenten/rapporten/2023/10/26/sectoragenda-mmi, 2023. Accessed on: 21-03-24.

[3] Mphatso N. Nyanya, Huy B. Vu, Alessandro Schönborn, and Aykut I. Ölçer. Wind and solar assisted ship propulsion optimisation and its application to a bulk carrier. *Sustainable Energy Technologies and Assessments*, 47:101397, 2021.

[4] Green Maritime Methanol. Introduction. https://greenmaritimemethanol.nl/introduction/, 2024. Accessed on: 21-03-24.

[5] John van Zalk and Paul Behrens. The spatial extent of renewable and non-renewable power generation: A review and meta-analysis of power densities and their application in the u.s. *Energy Policy*, 123:83–91, 2018.

[6] U.S. Department of Energy. Fuel Properties Comparison. https://afdc.energy.gov/fuels/properties, 2024. Accessed on: 21-03-24.

[7] Royal Dutch Navy. Sail Plan Vooruit! https://open.overheid.nl/documenten/a45bdebd-7143-4a61-91f3-ebb357bf5d05/file, 2023. Accessed on: 21-03-24.

[8] World Nuclear Association. How can nuclear combat climate change? https://world-nuclear.org/nuclear-essentials/how-can-nuclear-combat-climate-change.aspx, 2023. Accessed on: 21-03-24.

[9] European Commission. Reducing emissions from the shipping sector. https://climate.ec.europa.eu/eu-action/transport/reducing-emissions-shipping-sector_en, 2023. Accessed on: 21-03-24.

[10] U.S. Department of the Navy and Department of Energy. The United States naval nuclear propulsion program. https://www.energy.gov/sites/prod/files/2017/08/f36/nuclear_propulsion_program_8-30-2016%5B1%5D.pdf, 2015. Accessed on: 21-03-24.

[11] World Nuclear Association. Nuclear-Powered Ships. https://world-nuclear.org/information-library/non-power-nuclear-applications/transport/nuclear-powered-ships.aspx, 2023. Accessed on: 21-03-24.

[12] Greg Jennett. Australia to acquire nuclear submarine fleet as part of historic partnership with US and UK to counter China's influence. https://www.abc.net.au/news/2021-09-16/australia-nuclear-submarine-partnership-us-uk/100465814, 2021. Accessed on: 21-03-24.

[13] Naval News. Brazil's Nuclear-Powered Submarine Project Reaches New Milestone. https://www.navalnews.com/naval-news/2023/10/brazils-nuclear-powered-submarine-project-reaches-new-milestone/, 2023. Accessed on: 21-03-24.

[14] Luciano Ondir Freire, Delvonei Alves de Andrade. Historic survey on nuclear merchant ships. *Nuclear Engineering and Design*, 293, 2015.

[15] Koen C.F. Houtkoop. Nuclear reactors for marine propulsion and power generation systems. https://repository.tudelft.nl/islandora/object/uuid%3Afb44c464-6936-4ec6-96b1-52333ff799e3, 2022. Accessed on: 21-03-24.

[16] Siddharth Kalra. An Exploratory Study on Nuclear-Powered Trailing Suction Hopper Dredgers. https://repository.tudelft.nl/islandora/object/uuid%3A73160842-08b7-4c60-a6bd-4a8f53919d63, 2020. Accessed on: 21-03-24.

[17] Z. Leurs. Design of a high-speed 20,000 TEU nuclear container vessel. https://repository.tudelft.nl/islandora/object/uuid%3Ab15d8ca0-ef54-4801-bc04-64818de3abaf, 2023. Accessed on: 21-03-24.

[18] R.D. Geertsma. Autonomous control for adaptive ships : with hybrid propulsion and power generation. https://repository.tudelft.nl/islandora/object/uuid%3Aad81b0ee-76be-4054-a7e8-bd2eeecdb156, 2019. Accessed on: 21-03-24.

[19] World Nuclear Association. Nuclear-powered ships. https://world-nuclear.org/information-library/non-power-nuclear-applications/transport/nuclear-powered-ships.aspx, 2023. Accessed on: 21-03-24.

[20] Jane's. Kirov (orlan) class (type 1144.1/1144.2) (cgn). https://web.archive.org/web/20090415230911/http://www.janes.com/defence/naval_forces/news/jfs/jfs000908_2_n.shtml, 2000. Accessed on: 21-03-24.

[21] R. Hill, C. G. Hodge, T. Gibbs. The potential of the molten salt reactor for warship propulsion. https://thoriumenergyalliance.com/wp-content/uploads/2020/02/bmtdsl-molten-salt-reactor-confpaper-inec-may12.pdf, 2012. Accessed on: 21-03-24.

[22] K.C.F. Houtkoop, K. Visser, J. Sietsmaa, N. de Vries. New potential for integration of nuclear power in marine propulsion systems. *International Naval Engineering Conference & Exhibition*, 2022.

[23] Nederlandse Omroep Stichting (NOS). Defensie krijgt miljarden extra te besteden, maar kan dat geld ook uitgegeven worden? https://nos.nl/artikel/2507722-defensie-krijgt-miljarden-extra-te-besteden-maar-kan-dat-geld-ook-uitgegeven-worden, 2024. Accessed on: 26-03-24.

[24] Marineschepen.nl. Overzicht toekomstige nederlandse marineschepen. https://marineschepen.nl/dossiers/nieuwe-marineschepen-Nederland.html, 2023. Accessed on: 21-03-24.

[25] Damen Naval. Man energy solutions to supply propulsion diesel engines and diesel generator sets for damen naval's asw-frigates. https://www.damen.com/insights-center/news/man-energy-solutions-to-supply-propulsion-engines-and-diesel-gensets, 2023. Accessed on: 21-03-24.

[26] Nederlandse Omroep Stichting (NOS). Kabinet wil voor miljarden onderzeeërs bestellen bij het Franse Naval. https://nos.nl/artikel/2512489-kabinet-wil-voor-miljarden-onderzeeers-bestellen-bij-het-franse-naval, 2024. Accessed on: 26-03-24.

[27] SWZ Maritime. Dutch navy's new support vessels will sail on methanol. https://swzmaritime.nl/news/2022/06/23/dutch-navys-new-support-vessels-will-sail-on-methanol/, 2024. Accessed on: 04-10-24.

[28] Harsh Sapra, Jelle Stam, Lindert van Biert, Peter de Vos, Klaas Visser, Gert-Jan Meijn. Potential of combined drive of fuel cell and internal combustion engine (cofaice) for naval ships. *International Naval Engineering Conference & Exhibition*, 2020.

[29] Marineschepen.nl. Weer een A-brief: zes amfibische transportschepen (LPX). https://marineschepen.nl/nieuws/A-brief-LPX-060324.html, 2024. Accessed on: 29-03-24.

[30] MAN. Project guides of engine types. https://www.man-es.com/marine/products/planning-tools-and-downloads/project-guides, 2023. Accessed on: 21-03-24.

[31] MAN. Man v28/33d stc, project guide – marine. https://man-es.com/applications/projectguides/4stroke/Propulsion/PG_P-III_V2833D%20STC.pdf, 2023. Accessed on: 21-03-24.

[32] General Electric. GE Marine Gas Turbines for Frigates. https://www.geaerospace.com/sites/default/files/2023-11/GE-Marine-Gas-Turbines-for-Frigates-2018-March.pdf, 2020. Accessed on: 21-03-24.

[33] GE Aerospace. Forty GE LM2500 Marine Gas Turbines to Power 10 Arleigh Burke-Class DDG51 Destroyers for United States Navy. https://www.geaerospace.com/news/press-releases/marine-industrial-engines/forty-ge-lm2500-marine-gas-turbines-power-10-arleigh-burke, 2018. Accessed on: 28-03-24.

[34] General Electric. LM2500 engine. https://www.geaerospace.com/military-defense/engines/lm2500, 2024. Accessed on: 21-03-24.

[35] General Electric. LM2500 Aeroderivative gas turbine. https://www.gevernova.com/content/dam/gepower-new/global/en_US/downloads/gas-new-site/products/gas-turbines/lm2500-fact-sheet-product-specifications.pdf, 2024. Accessed on: 21-03-24.

[36] James J. Duderstadt, Louis J. Hamilton. *Nuclear reactor analysis*. 1976.

[37] B.T. Smith. Introduction to radioactivity and radioactive decay. https://citeseerx.ist.psu.edu/document?repid=rep1&type=pdf&doi=ff751a11efaf4e67343a427d4e5815afc57e5148, 2010. Accessed on: 21-03-24.

[38] Max Born. Einstein's Theory of Relativity. https://books.google.nl/books?hl=nl&lr=&id=wUGKAAAAQBAJ&oi=fnd&pg=PP1&dq=The+Special+Theory+of+Relativity:+Einstein%27s+World+in+New+Axiomatic&ots=Di3m37OmxG&sig=dENdH3XGSRp33Tx8dVfXDY0BBhQ&redir_esc=y#v=onepage&q=The%20Special%20Theory%20of%20Relativity%3A%20Einstein's%20World%20in%20New%20Axiomatic&f=false, 1962. Accessed on: 21-03-24.

[39] Quizlet.com. Environmental Protection 10: (Neutron Interactions). https://quizlet.com/445338524/environmental-protection-10-neutron-interactions-flash-cards/, 2023. Accessed on: 21-03-24.

[40] atomicarchive.com. Nuclear Fission: Basics. https://www.atomicarchive.com/science/fission/index.html, 2023. Accessed on: 21-03-24.

[41] United States Nuclear Regulatory Commission. Fissile material. https://www.nrc.gov/reading-rm/basic-ref/glossary/fissile-material.html, 2023. Accessed on: 21-03-24.

[42] C. W. Forsberg, C. M. Hopper. Definition of weapons-usable uranium-233. https://web.archive.org/web/20131102011417/http://web.ornl.gov/info/reports/1998/3445606060721.pdf, 1998. Accessed on: 21-03-24.

[43] Magdi Ragheb. Nuclear naval propulsion. https://www.intechopen.com/chapters/19667, 2011. Accessed on: 21-03-24.

[44] Christian Schreinemachers. Preparation and characterization of U/Nd microspheres synthesized by internal gelation. https://www.researchgate.net/figure/Chain-yield-curves-for-233-U-235-U-239-Pu-and-241-Pu-fission-with-thermal-neutrons_fig7_255992204, 2013. Accessed on: 21-03-24.

[45] IAEA. Advances in Small Modular Reactor Technology Developments. https://aris.iaea.org/sites/Publications.html, 2022. Accessed on: 21-03-24.

[46] Gašper Žerovnik, Dušan Čalič, Samo Gerkšič, Marjan Kromar, Jan Malec, Anže Mihelčič, Andrej Trkov and Luka Snoj. An overview of power reactor kinetics and control in load-following operation modes. *Front. Energy Res*, 2023.

[47] Evans D. Kitcher and Sunil S. Chirayath. Neutronics and thermal hydraulics analysis of a small modular reactor. *Annals of Nuclear Energy*, 97:232–245, 2016.

[48] IAEA. Nuclear power reactors. https://www.iaea.org/topics/nuclear-power-reactors, 2023. Accessed on: 21-03-24.

[49] World nuclear association. World Nuclear Performance Report 2023. https://www.world-nuclear.org/world-nuclear-performance-report.aspx, 2023. Accessed on: 21-03-24.

[50] Westinghouse. Westinghouse Awarded Contract to Evaluate AP1000 Reactors in Support of Netherlands' Energy Future. https://info.westinghousenuclear.com/news/westinghouse-awarded-contract-to-evaluate-ap1000-reactors-in-support-of-netherlands-energy-future, 2024. Accessed on: 26-03-24.

[51] IAEA. What are Small Modular Reactors (SMRs)? https://www.iaea.org/newscenter/news/what-are-small-modular-reactors-smrs, 2023. Accessed on: 21-03-24.

[52] IAEA. Small Modular Reactors. https://www.iaea.org/topics/small-modular-reactors, 2023. Accessed on: 21-03-24.

[53] J.K. Shultis, R.E. Faw. *Fundamentals of Nuclear Science and Engineering*. Marcel Dekker Inc., first edition, 2002.

[54] Vecteezy. Nuclear power plant. https://www.vecteezy.com/vector-art/28155303-nuclear-power-plant-diagram-isolated-easy-to-understand-friendly-cartoon-concept-white-background, 2024. Accessed on: 21-03-24.

[55] D. Olander. Nuclear fuels – present and future. *Journal of Nuclear Materials*, 389(1):1–22, 2009.

[56] Bahman Zohuri. Generation iv nuclear reactors. *Nuclear Reactor Technology Development and Utilization*, pages 213–246, 2020.

[57] Ultra Safe Nuclear Corporation. TRISO Particle FUEL. https://www.usnc.com/triso/, 2023. Accessed on: 21-03-24.

[58] Alicat. Using fb-cvd for triso nuclear fuel particle manufacturing. https://www.alicat.com/knowledge-base/fb-cvd-triso-fuel/, 2024. Accessed on: 21-03-24.

[59] NRC. Reflector. https://www.nrc.gov/reading-rm/basic-ref/glossary/reflector.html, 2021. Accessed on: 21-03-24.

[60] Nigerian scholars. Control rods. https://nigerianscholars.com/tutorials/nuclear-chemistry/control-rods/, 2024. Accessed on: 18-09-24.

[61] NRC. Control rod. https://www.nrc.gov/reading-rm/basic-ref/glossary/control-rod.html, 2021. Accessed on: 21-03-24.

[62] NuclearNewswire. Small modular reactors at ans 2013 winter meeting. https://www.ans.org/news/tag-small%20modular%20reactors/step-1392341103/, 2013. Accessed on: 21-03-24.

[63] 360Science. Nuclear radiation and shielding. https://www.flinnsci.com/360-science-nuclear-radiation-and-shielding-3-year-access/ap10824/, 2023. Accessed on: 21-03-24.

[64] Y.Q. Chen and B.H. Yan. The technology of shielding design for nuclear reactor: A review. *Progress in Nuclear Energy*, 161:104741, 2023.

[65] Govatsa Acharya. Investigating the Application of Self-Actuated Passive Shutdown System in a Small Lead-Cooled Reactor. 2019. Accessed on: 21-03-24.

[66] Gen IV International forum. Technology roadmap update for generation iv nuclear energy systems. https://www.gen-4.org/gif/upload/docs/application/pdf/2014-03/gif-tru2014.pdf, 2014. Accessed on: 21-03-24.

[67] Rijksdienst voor Ondernemend Nederland. Technology readiness levels (trl). https://www.rvo.nl/onderwerpen/trl#4-fasen%2C-9-technology-readiness-levels, 2022. Accessed on: 21-03-24.

[68] IAEA. Advanced Reactors Information System(ARIS). https://aris.iaea.org/sites/overview.html, 2023. Accessed on: 21-03-24.

[69] World Nuclear Association. Fast Neutron Reactors. https://world-nuclear.org/information-library/current-and-future-generation/fast-neutron-reactors.aspx, 2021. Accessed on: 21-03-24.

[70] S.E. Hirdaris, Y.F. Cheng, P. Shallcross, J. Bonafoux, D. Carlson, B. Prince, and G.A. Sarris. Considerations on the potential use of nuclear small modular reactor (smr) technology for merchant marine propulsion. *Ocean Engineering*, 79:101–130, 2014.

[71] International Panel on Fissile Materials. Us study of reactor and fuel types to enable naval reactors to shift from heu fuel. https://fissilematerials.org/blog/2020/04/us_study_of_reactor_and_f.html, 2020. Accessed on: 21-03-24.

[72] Kentaro Nagatsuka, Hiroki Noguchi, Satoru Nagasumi, Yasunobu Nomoto, Atsushi Shimizu, Hiroyuki Sato, Tetsuo Nishihara, and Nariaki Sakaba. Current status of high temperature gas-cooled reactor development in japan. *Nuclear Engineering and Design*, 425:113338, 2024.

[73] U.S. NRC. Pressurized water reactors. https://www.nrc.gov/reactors/power/pwrs.html, 2023. Accessed on: 21-03-24.

[74] Marcin Karol Rowinski, Timothy John White, and Jiyun Zhao. Small and medium sized reactors (smr): A review of technology. *Renewable and Sustainable Energy Reviews*, 44:643–656, 2015.

[75] Y. Ismail, B.P. Bromley. Assessment of Small Modular Reactors (SMRs) for Load-Following Capabilities. *Transactions of the American Nuclear Society*, pages 121(1):1117–1120, 2019.

[76] Christopher Pistner. Sicherheitstechnische Analyse und Risikobewertung einer Anwendung von SMR-Konzepten (Small Modular Reactors). https://inis.iaea.org/collection/NCLCollectionStore/_Public/52/097/52097919.pdf?r=1, 2021. Accessed on: 21-03-24.

[77] NRG. Small Modular Reactors 2023. https://open.overheid.nl/documenten/ronl-7222d09bf81cec92c1c0b31f40133cf6fc7a6cea/pdf, 2023. Accessed on: 21-03-24.

[78] Björn Steigerwald, Jens Weibezahn, Martin Slowik, and Christian von Hirschhausen. Uncertainties in estimating production costs of future nuclear technologies: A model-based analysis of small modular reactors. *Energy*, 281:128204, 2023.

[79] Kuniyoshi Takamatsu and Rui Hu. New reactor cavity cooling system having passive safety features using novel shape for htgrs and vhtrs. *Annals of Nuclear Energy*, 77:165–171, 2015.

[80] C. Cabet, F. Rouillard. Corrosion of high temperature metallic materials in VHTR. *Journal of Nuclear Materials*, 392, 2009.

[81] Massachusetts Institute of Technology. The Future of Nuclear Energy in a Carbon-Constrained World. https://energy.mit.edu/research/future-nuclear-energy-carbon-constrained-world/, 2018. Accessed on: 21-03-24.

[82] IAEA. Status of Fast Reactor Research and Technology Development. https://www-pub.iaea.org/MTCD/Publications/PDF/te_1691_web.pdf, 2012. Accessed on: 21-03-24.

[83] Yoonhan Ahn and Jeong Ik Lee. Study of various brayton cycle designs for small modular sodium-cooled fast reactor. *Nuclear Engineering and Design*, 276:128–141, 2014.

[84] Tadashi Tanuma. *Advances in steam turbines for modern power plants*. 2022.

[85] Klaus Brun, Peter Friedman, Richard Dennis. *Fundamentals and Applications of Supercritical Carbon Dioxide (SCO2) Based Power Cycles*. Woodhead Publishing, 2017.

[86] H. Tian and G.Q. Shu. 17 - organic rankine cycle systems for large-scale waste heat recovery to produce electricity. In Ennio Macchi and Marco Astolfi, editors, *Organic Rankine Cycle (ORC) Power Systems*, pages 613–636. Woodhead Publishing, 2017.

[87] Sean M. Kissick and Hailei Wang. A comparative study of alternative power cycles for small modular reactors. *Energy Conversion and Management*, 247:114734, 2021.

[88] Olumide Olumayegun, Meihong Wang, and Greg Kelsall. Closed-cycle gas turbine for power generation: A state-of-the-art review. *Fuel*, 180:694–717, 2016.

[89] Seong Jun Bae, Jekyoung Lee, Yoonhan Ahn, and Jeong Ik Lee. Preliminary studies of compact brayton cycle performance for small modular high temperature gas-cooled reactor system. *Annals of Nuclear Energy*, 75:11–19, 2015.

[90] National Insititute of Standars and Technology (NIST). Thermophysical properties of fluid systems. `https://webbook.nist.gov/chemistry/fluid/`, 2024. Accessed on: 22-03-24.

[91] Olumide Olumayegun, Meihong Wang, and Greg Kelsall. Thermodynamic analysis and preliminary design of closed brayton cycle using nitrogen as working fluid and coupled to small modular sodium-cooled fast reactor (sm-sfr). *Applied Energy*, 191:436–453, 2017.

[92] Xiao Luo, Yifei Teng, Daogang Lu, Danting Sui, Hao Ding, Lu Zhang, and Yang Liu. Comparative analysis on high-efficiency energy conversion system with different working mediums matched with small lead-cooled fast reactor. *Progress in Nuclear Energy*, 164:104844, 2023.

[93] Joo Hyun Park, Jung Yoon, Jaehyuk Eoh, Hyungmo Kim, and Moo Hwan Kim. Optimization and sensitivity analysis of the nitrogen brayton cycle as a power conversion system for a sodium-cooled fast reactor. *Nuclear Engineering and Design*, 340:325–334, 2018.

[94] Matteo Marchionni, Giuseppe Bianchi, and Savvas A. Tassou. Transient analysis and control of a heat to power conversion unit based on a simple regenerative supercritical co2 joule-brayton cycle. *Applied Thermal Engineering*, 183:116214, 2021.

[95] Bong-Seong Oh, Jeong Ik Lee. Study of autonomous control system for s-CO2 power cycle. *3rd European supercritical CO2 Conference*, 2019.

[96] Bong-Seong Oh, Jeong Ik Lee. Control schemes of S-CO2 cooled KAIST Micro Modular Reactor as marine propulsion engine to treat rapid load change condition. *Korean Nuclear Society Spring Meeting*, 2019.

[97] Thiago Gotelip, Uwe Gampe, and Stefan Glos. Optimization strategies of different sco2 architectures for gas turbine bottoming cycle applications. *Energy*, 250:123734, 2022.

[98] Sungwook Choi, In Woo Son, Jeong Ik Lee. Comparative performance evaluation of gas brayton cycle for micro–nuclear reactors. *Energies, 16(4), 2065*, 2023.

[99] Ming Ding, Jan Leen Kloosterman, Theo Kooijman, Rik Linssen, Tim Abram, Barry Marsden, Tony Wickham. Design of a U-Battery. `https://www.janleenkloosterman.nl/reports/ubattery_final_201111.pdf`, 2011. Accessed on: 21-03-24.

[100] Chuntian Gao, Pan Wu, Weihua Liu, Yunduo Ma, and Jianqiang Shan. Development of a bypass control strategy for supercritical co2 brayton cycle cooled reactor system under load-following operation. *Annals of Nuclear Energy*, 151:107917, 2021.

[101] Yang Ming, Ruifeng Tian, Fulong Zhao, Chao Luo, and Sichao Tan. Control strategies and transient characteristics of a 5mwth small modular supercritical co2 brayton-cycle reactor system. *Applied Thermal Engineering*, 235:121302, 2023.

[102] A. Alenezi, L. Vesely, and J. Kapat. Exergoeconomic analysis of hybrid sco2 brayton power cycle. *Energy*, 247:123436, 2022.

[103] Pan Wu, Yunduo Ma, Chuntian Gao, Weihua Liu, Jianqiang Shan, Yanping Huang, Junfeng Wang, Dan Zhang, and Xu Ran. A review of research and development of supercritical carbon dioxide brayton cycle technology in nuclear engineering applications. *Nuclear Engineering and Design*, 368:110767, 2020.

[104] A. Gad-Briggs, P. Pilidis, T. Nikolaidis. Analyses of the load following capabilities of brayton helium gas turbine cycles for generation iv nuclear power plants. *ASME J of Nuclear Rad Sci.*, page 3(4): 041017, 2017.

[105] Vaclav Dostal. *A Supercritical Carbon Dioxide Cycle for Next Generation Nuclear Reactors*. PhD thesis, Massachusetts Institute of Technology, 2004.

[106] Ho Joon Yoon, Yoonhan Ahn, Jeong Ik Lee, and Yacine Addad. Potential advantages of coupling supercritical co2 brayton cycle to water cooled small and medium size reactor. *Nuclear Engineering and Design*, 245:223–232, 2012.

[107] Bong Seong Oh and Jeong Ik Lee. Control schemes of S-CO2 cooled KAIST Micro Modular Reactor as marine propulsion engine to treat rapid load change condition. *Transactions of the Korean Nuclear Society Spring Meeting Jeju*, 2019.

[108] Bong Seong Oh, Jeong Ik Lee, Seong Gu Kim, Seong Kuk Cho, Hwanyeol Yu. Transient analyses of s-co2 cooled kaist micro modular reactor with gamma+ code. *The 11th International Topical Meeting on Nuclear Reactor Thermal Hydraulics, Operation and Safety Gyeongju*, 2016.

[109] Miguel Angel Gonzalez-Salazar, Trevor Kirsten, and Lubos Prchlik. Review of the operational flexibility and emissions of gas- and coal-fired power plants in a future with growing renewables. *Renewable and Sustainable Energy Reviews*, 82:1497–1513, 2018.

[110] James Spelling, Markus Jöcker, Andrew Martin. Thermal Modeling of a Solar Steam Turbine With a Focus on Start-Up Time Reduction . *ASME J. Eng. Gas Turbines Power*, 134(1):013001, 2012.

[111] Nathan A. Carstens. *Control Strategies for Supercritical Carbon Dioxide Power Conversion Systems*. PhD thesis, Massachusetts Institute of Technology, 2007.

[112] Hao Zheng, Tao Yu, Chengtun Qu, Wanjing Li, and Yanfei Wang. Basic characteristics and application progress of supercritical water. *IOP Conf. Series: Earth and Environmental Science 555*, 2020.

[113] Xuan Wang, Rui Wang, Xingyan Bian, Jinwen Cai, Hua Tian, Gequn Shu, Xinyu Li, and Zheng Qin. Review of dynamic performance and control strategy of supercritical co2 brayton cycle. *Energy and AI*, 5:100078, 2021.

[114] Apostolos A. Gkountas, Anastassios M. Stamatelos, and Anestis I. Kalfas. Recuperators investigation for high temperature supercritical carbon dioxide power generation cycles. *Applied Thermal Engineering*, 125:1094–1102, 2017.

[115] Bo Wang, Jiafei Shen, Jindong Chen, Yaliang Wang. Numerical Improvement Using Flow and Heat Transfer Calculations of the Zigzag Geometry for Carbon Dioxide PCHEs . *Energies 2022, 15(8), 2831*.

[116] Tariq Alsawy, Ramy H. Mohammed, Osama Mesalhy, and Mohamed L. Elsayed. Dynamic performance of supercritical co2 brayton cycle and its relationship to the correction of turbomachinery performance maps: A comparative analysis. *Applied Thermal Engineering*, 242:122364, 2024.

[117] Yuan Jiang, Eric Liese, Stephen E. Zitney, and Debangsu Bhattacharyya. Design and dynamic modeling of printed circuit heat exchangers for supercritical carbon dioxide brayton power cycles. *Applied Energy*, 231:1019–1032, 2018.

[118] Yang Ming, Kai Liu, Fulong Zhao, Huawei Fang, Sichao Tan, Ruifeng Tian. Dynamic modeling and validation of the 5 MW small modular supercritical CO2 Brayton-Cycle reactor system. *Energy Conversion and Management*, 253, 2022.

[119] Tianrui Deng, Xionghui Li, Qiuwang Wang, and Ting Ma. Dynamic modelling and transient characteristics of supercritical co2 recompression brayton cycle. *Energy*, 180:292–302, 2019.

[120] M. Chen. Design, fabrication, testing, and modeling of a high-temperature printed circuit heat exchanger (MSc thesis) The Ohio State University. https://www.researchgate.net/publication/322056688_DESIGN_FABRICATION_TESTING_AND_MODELING_OF_A_HIGH-TEMPERATURE_PRINTED_CIRCUIT_HEAT, 2015. Accessed on: 16-04-24.

[121] Katrine Bennett and Yi tung Chen. Printed circuit heat exchanger performance analysis using non-uniform segmental design method. *Applied Thermal Engineering*, 153:69–84, 2019.

[122] S. Atkinson, D. Litskevich, and B. Merk. Small modular high temperature reactor optimisation part 2: Reactivity control for prismatic core high temperature small modular reactor, including fixed burnable poisons, spectrum hardening and control rods. *Progress in Nuclear Energy*, 111:233–242, 2019.

[123] World Nuclear Association. Nuclear Power in France. https://world-nuclear.org/information-library/country-profiles/countries-a-f/france.aspx, 2023. Accessed on: 21-03-24.

[124] Nuclear Energy Agency. Technical and Economic Aspects of Load Following with Nuclear Power Plants. https://www.oecd-nea.org/upload/docs/application/pdf/2021-12/technical_and_economic_aspects_of_load_following_with_nuclear_power_plants.pdf, 2011. Accessed on: 22-03-24.

[125] D. Gosset. 15 - absorber materials for generation iv reactors. In Pascal Yvon, editor, *Structural Materials for Generation IV Nuclear Reactors*, pages 533–567. Woodhead Publishing, 2017.

[126] Seddon Atkinson and Takeshi Aoki. The development of a fuel lifecycle reactivity control strategy for a generic micro high temperature reactor. *Nuclear Engineering and Technology*, 56(3):785–792, 2024.

[127] B. Boer, J.L. Kloosterman, D. Lathouwers, and T.H.J.J. van der Hagen. In-core fuel management optimization of pebble-bed reactors. *Annals of Nuclear Energy*, 36(8):1049–1058, 2009.

[128] Nicholas Dunkle and Ondrej Chvala. Effect of xenon removal rate on load following in high power thermal spectrum molten-salt reactors (msrs). *Nuclear Engineering and Design*, 409:112329, 2023.

[129] Ming Ding and Jan Leen Kloosterman. Thermal-hydraulic design and transient evaluation of a small long-life htr. *Nuclear Engineering and Design*, 255:347–358, 2013.

[130] Rodica Loisel, Victoria Alexeeva, Andreas Zucker, and David Shropshire. Load-following with nuclear power: Market effects and welfare implications. *Progress in Nuclear Energy*, 109:280–292, 2018.

[131] World Nuclear Association. Nuclear Power Reactors. https://world-nuclear.org/information-library/nuclear-fuel-cycle/nuclear-power-reactors/nuclear-power-reactors.aspx, 2023. Accessed on: 23-03-24.

[132] Anton Moisseytsev, James J. Sienicki. Dynamic Control Analysis of the AFR-100 SMR SFR With a Supercritical CO2 Cycle and Dry Air Cooling: Part I — Plant Control Optimization. *26th International Conference on Nuclear Engineering*, Volume 1: Operations and Maintenance, Engineering, Modifications, Life Extension, Life Cycle, and Balance of Plant; Instrumentation and Control (IC) and Influence of Human Factors; Innovative Nuclear Power Plant Design and SMRs, 2018.

[133] Xingyan Bian, Xuan Wang, Rui Wang, Jinwen Cai, Hua Tian, Gequn Shu, Zhimin Lin, Xiangyu Yu, and Lingfeng Shi. A comprehensive evaluation of the effect of different control valves on the dynamic performance of a recompression supercritical co2 brayton cycle. *Energy*, 248:123630, 2022.

[134] Olumide Olumayegun and Meihong Wang. Dynamic modelling and control of supercritical co2 power cycle using waste heat from industrial processes. *Fuel*, 249:89–102, 2019.

[135] Seddon Atkinson. *Design variances and optimisation of the U-Battery*. PhD thesis, University of Sheffield, 2018.

[136] S. Atkinson, T.J. Abram, D. Litskevich, and B. Merk. Small modular high temperature reactor optimisation – part 1: A comparison between beryllium oxide and nuclear graphite in a small scale high temperature reactor. *Progress in Nuclear Energy*, 111:223–232, 2019.

[137] Seatemperature.org. World Sea Temperatures. `https://www.seatemperature.org/`, 2024. Accessed on: 26-06-24.

[138] Matteo Marchionni, Lei Chai, Giuseppe Bianchi, and Savvas A. Tassou. Numerical modelling and transient analysis of a printed circuit heat exchanger used as recuperator for supercritical co2 heat to power conversion systems. *Applied Thermal Engineering*, 161:114190, 2019.

[139] Thyssenkrupp. Stainless Steel 316L 1.4404. `https://www.thyssenkrupp-materials.co.uk/stainless-steel-316l-14404.html`, 2024. Accessed on: 27-06-24.

[140] Tri Q. Trinh. Dynamic Response of the Supercritical CO2 Brayton Recompression Cycle to Various System Transients, Massachusetts Institute of Technology. `https://dspace.mit.edu/handle/1721.1/53527`, 2009. Accessed on: 21-03-24.

[141] T.H. Wien, G.J. Meijn. Dynamic power behavior of a nuclear power plant integrated in naval vessels. *International Naval Engineering Conference*, 2024.

[142] Yulin Wang, Weiran Chen, Linxuan Zhang, Xinyu Zhao, Yiming Gao, Venkata Dinavahi. Small Modular Reactors: An Overview of Modeling, Control, Simulation, and Applications. *IEEE Access*, 4, 2016.

[143] Samet E. Arda and Keith E. Holbert. Nonlinear dynamic modeling and simulation of a passively cooled small modular reactor. *Progress in Nuclear Energy*, 91:116–131, 2016.

[144] Mohamed S. El-Genk and Jean-Michel P. Tournier. A point kinetics model for dynamic simulations of next generation nuclear reactor. *Progress in Nuclear Energy*, 92:91–103, 2016.

[145] Leilei Qiu, Shengyong Liao, Sui Fan, Peiwei Sun, and Xinyu Wei. Dynamic modelling and control system design of micro-high-temperature gas-cooled reactor with helium brayton cycle. *Energy*, 278:128030, 2023.

[146] L.C. Ju arez-Martínez, G. Espinosa-Paredes. Development of a zero-dimensional dynamic simulator of a power conversion system with a high-temperature gas reactor. *International Journal of Energy Research*, 45:16984–16994, 2021.

[147] S. Atkinson, T. Aoki, D. Litskevich, B. Merk, and Y. Xing. Part 3: Evaluating a small modular high temperature reactor design during control rod withdrawal and a depressurised loss of coolant accidents. *Progress in Nuclear Energy*, 134:103689, 2021.

[148] S.D. Hamieh and M. Saidinezhad. Analytical solution of the point reactor kinetics equations with temperature feedback. *Annals of Nuclear Energy*, 42:148–152, 2012.

[149] Henryk Anglart. *Nuclear Reactor Dynamics and Stability*. 2011.

[150] Thomas W. Kerlin, Beller R. Upadhyaya. *Dyanmics and control of Nuclear Reactors*. Elsevier, 2019.

[151] Ankit Rohatgi. Webplotdigitizer. `https://automeris.io/WebPlotDigitizer.html`, 2024.

[152] Zhe Dong and Yifei Pan. A lumped-parameter dynamical model of a nuclear heating reactor cogeneration plant. *Energy*, 145:638–656, 2018.

[153] Haipeng Li, Xiaojin Huang, and Liangju Zhang. A simplified mathematical dynamic model of the htr-10 high temperature gas-cooled reactor with control system design purposes. *Annals of Nuclear Energy*, 35(9):1642–1651, 2008.

[154] Anthony F. Mills, Carlos F. M. Coimbra. *Basic Heat and Mass Transfer: Third Edition*. Temporal Publishing, LLC, 2015.

[155] The Engineering Toolbox. Fluid Flow - Hydraulic Diameter . `https://www.engineeringtoolbox.com/hydraulic-equivalent-diameter-d_458.html`, 2024. Accessed on: 05-10-24.

[156] Boyce W. Travis and Mohamed S. El-Genk. Thermal–hydraulics analyses for 1/6 prismatic vhtr core and fuel element with and without bypass flow. *Energy Conversion and Management*, 67:325–341, 2013.

[157] National Institute of Standards and Technology. Silicon carbide. `https://webbook.nist.gov/cgi/cbook.cgi?ID=C409212&Units=SI&Type=JANAFS&Plot=on#JANAFS`, 2024. Accessed on: 24-09-24.

[158] The Engineering Toolbox. Stainless Steel - Specific Heat and Thermal Conductivities vs. Temperatures . `https://www.engineeringtoolbox.com/stainless-steel-specific-heat-thermal-conductivity-vs-temperature-d_2225.html`, 2024. Accessed on: 24-09-24.

[159] Boyce W. Travis. An effective methodology for thermal-hydraulics analysis of a vhtr core and fuel elements. `https://digitalrepository.unm.edu/cgi/viewcontent.cgi?article=1029&context=ne_etds`, 2013. Accessed on: 16-07-24.

[160] Andrew J. Furlong, Hongtian Ge, Robin W. Hughes, Arturo Macchi, and Jan B. Haelssig. Dynamic modelling of cross-flow printed circuit heat exchangers for multistage reactor intercooling. *Applied Thermal Engineering*, 239:122010, 2024.

[161] Yongju Jeong, Seong Kuk Cho, In Woo Son, and Jeong Ik Lee. Evaluation of off-design scaling methods of supercritical co2 compressor with experimental data. *Energy*, 278:127730, 2023.

[162] Wilfried Visser. *Generic Analysis Methods for Gas Turbine Engine Performance*. PhD thesis, TuDelft, 2015.

[163] S.L. Dixon and C.A. Hall. *Fluid Mechanics and Thermodynamics of Turbomachinery, 6th ed.* Butterworth-Heinemann, 2010.

[164] Yongju Jeong, Seongmin Son, Seong Kuk Cho, Seungjoon Baik, and Jeong Ik Lee. Evaluation of supercritical co2 compressor off-design performance prediction methods. *Energy*, 213:119071, 2020.

[165] H.S. Pham, N. Alpy, J.H. Ferrasse, O. Boutin, M. Tothill, J. Quenaut, O. Gastaldi, T. Cadiou, and M. Saez. An approach for establishing the performance maps of the sc-co2 compressor: Development and qualification by means of cfd simulations. *International Journal of Heat and Fluid Flow*, 61:379–394, 2016.

[166] Pim Nederstigt and Rene Pecnik. Generalised isentropic relations in thermodynamics. *Energies*, 16(5), 2023.

[167] Michael A. Pope. *Thermal hydraulic design of a 2400 MWth direct supercritical CO2 cooled fast reactor*. PhD thesis, Massachusetts Institute of Technology, 2006.

[168] Muhammad Imam Sudrajat, Niek Moonen, Hans Bergsma, Frank Leferink. Behavior of cots-based equipment under ship mains supply frequency tolerance requirements. *IEEE International Joint EMC/SI/PI and EMC Europe Symposium*, 2021.

[169] Qiuwen Wang, Hu Zhang, Puxin Zhu. Using nuclear energy for maritime decarbonization and related environmental challenges: Existing regulatory shortcomings and improvements. `https://www-ncbi-nlm-nih-gov.tudelft.idm.oclc.org/pmc/articles/PMC9966280/`, 2023. Accessed on: 21-03-24.

[170] Wikipedia. Pebble bed reactor scheme. `https://commons.wikimedia.org/wiki/File:Pebble_bed_reactor_scheme_(English).svg`, 2023. Accessed on: 21-03-24.

[171] European Nuclear Society. Pebble bed reactor. `https://www.euronuclear.org/glossary/pebble-bed-reactor/`, 2023. Accessed on: 21-03-24.

[172] NAM-IL TAK, SUNG NAM LEE, MIN-HWAN KIM, HONG SIK LIM, and JAE MAN NOH. Development of a core thermo-fluid analysis code for prismatic gas cooled reactors. *Nuclear Engineering and Technology*, 46(5):641–654, 2014.

[173] MathWorks. Methods for Approximating Function Values. `https://nl.mathworks.com/help/simulink/ug/methods-for-estimating-missing-points.html#bqi6gig`, 2024. Accessed on: 15-05-24.